

# **INVESTIGATIONS OF RADIO-FREQUENCY, CAPACITIVELY-COUPLED LARGE AREA INDUSTRIAL REACTOR: COST-EFFECTIVE PRODUCTION OF THIN FILM MICROCRYSTALLINE SILICON FOR SOLAR CELLS**

THÈSE N° 3895 (2007)

PRÉSENTÉE LE 19 OCTOBRE 2007

À LA FACULTÉ DES SCIENCES ET TECHNIQUES DE L'INGÉNIEUR  
CRPP ASSOCIATION EURATOM  
PROGRAMME DOCTORAL EN SCIENCE ET GÉNIE DES MATÉRIAUX

ÉCOLE POLYTECHNIQUE FÉDÉRALE DE LAUSANNE

POUR L'OBTENTION DU GRADE DE DOCTEUR ÈS SCIENCES

PAR

**Benjamin STRAHM**

ingénieur en science des matériaux diplômé EPF  
de nationalité suisse et originaire de Leysin (VD)

acceptée sur proposition du jury:

Prof. M. Rappaz, président du jury  
Dr C. Hollenstein, directeur de thèse  
Prof. C. Ballif, rapporteur  
Dr F. Finger, rapporteur  
Prof. P. Muralt, rapporteur



ÉCOLE POLYTECHNIQUE  
FÉDÉRALE DE LAUSANNE

Suisse  
2007



*A mon frère et à mon père.*



# Abstract

The constant energy consumption and world-wide demography expansion add to the potential risks of ecological and human disaster associated with global warming. This makes it a necessity to develop renewable energy technologies such as photovoltaic energy. These technologies already exist, but their cost has to be reduced in order to compete with well-established energies based on natural resources such as oil, coal or natural gas.

A first step has been performed successfully in recent years in the field of low cost photovoltaic (PV) solar cells. Manufacturing equipment for large area ( $> 1 \text{ m}^2$ ) amorphous silicon thin film solar cell production is now available. Even if this type of PV cell has lower energy conversion efficiencies ( $\approx 9 - 10 \%$ ) than other types of cells such as crystalline silicon cells ( $\approx 25 \%$ ), it has lower financial and ecological costs. Nevertheless, the next generation of large area silicon thin film PV cells promise higher conversion efficiencies ( $\approx 12 \%$ ) and stability under light exposure. This new type of PV cell is based on microcrystalline silicon grown on large glass substrates by plasma-enhanced chemical vapor deposition from silane ( $\text{SiH}_4$ ) and hydrogen ( $\text{H}_2$ ) gas, as for the previous amorphous silicon generation. Amorphous/microcrystalline silicon PV multi-junction cells require a thick ( $\approx 2 \mu\text{m}$ ) microcrystalline intrinsic light absorber layer because of the need to fit the photo-generated current of the two stacked cells. This increases the cost of the final product since the deposition rate of microcrystalline silicon achieved nowadays is limited to a few  $\text{\AA}/\text{s}$ , making the processing time very long. The enhancement of the deposition rate while maintaining a good material quality, i.e. at the boundary between amorphous and microcrystalline growth, is difficult because the phenomena involved in the deposition of microcrystalline silicon are not well understood, and the optimization is then generally performed empirically.

The plasma composition is measured using Fourier transform infrared absorption spectroscopy and optical emission spectroscopy. It is shown that the deposited films can be classified into three categories (amorphous, transitional and microcrystalline) as a function of silane concentration *in the plasma*, while it is impossible to do so as a function of all other process parameters (silane input concentration, RF power, pressure, etc...) if they are all varied simultaneously. This means that the common way to deposit microcrystalline silicon by strongly diluting the silane with hydrogen ( $< 5 \%$ ) is not unique. This is because the plasma composition does not depend only on the gas composition, but also on the fraction of silane depleted in the plasma. Analytical and numerical plasma chemistry modeling show that this is because the silane concentration in the plasma determines the species flux towards the growing film surface. Hence, in agreement with existing phenomenological models of microcrystalline growth, the lower the silane concentration

in the plasma, the higher the H to  $\text{SiH}_x$  flux ratio towards the surface and the higher the crystallinity.

This is used to demonstrate the feasibility of the growth of microcrystalline silicon in large area reactors using radio-frequency excitation (40 MHz) even from pure silane gas. Moreover, it is shown that the optimum in terms of deposition rate and deposition efficiency tends towards pure silane and not to the common  $\text{H}_2$ -diluted regime. Following this conclusion, an optimization strategy is constructed by varying only the hydrogen flow rate and the working pressure. Guidelines for the selection of the initial process parameters are given in order to achieve high deposition rate ( $> 10 \text{ \AA/s}$ ) and high gas utilization efficiency ( $> 80 \%$ ) of good quality microcrystalline silicon with a high input silane concentration ( $> 10 - 20 \%$ ) by using the optimization strategy.

Furthermore, it is shown by using time-resolved plasma composition measurement and modeling that the time necessary to reach chemical steady-state is about 1 second in large area Plasma-Box<sup>TM</sup> reactors. This time is much shorter than times reported for small laboratory reactors, which are typically of about 1 minute. It is demonstrated by using two-dimensional modeling that this is due to back-diffusion of the silane molecules from the vacuum chamber to the plasma zone in laboratory reactors, whereas the plasma fills the whole volume in large area Plasma-Box<sup>TM</sup> reactors, making the plasma composition quasi-instantaneously uniform at plasma ignition. This is of importance for the film microstructure uniformity across the thickness of the layer. In large area Plasma-Box<sup>TM</sup> reactors, it is not necessary to use strategies such as  $\text{H}_2$ -dilution profiling in order to eliminate the plasma-induced amorphous incubation layer at plasma ignition, because plasma composition suitable to grow microcrystalline silicon is reached directly from ignition.

Finally, it is shown that the Telegraph effect and the standing-wave, which are the two necessary and sufficient distinct electromagnetic modes to determine the electromagnetic fields in a RF reactor, affects the film thickness and microstructure uniformity. It is shown that the film thickness variation at the reactor edges due to the Telegraph effect can be eliminated by symmetrizing the two electrodes. It is also shown that the standing-wave affects significantly the film microstructure of microcrystalline silicon deposited from discharges with a silane input concentration about 10 %, whereas for low input silane concentrations ( $< 4 - 5 \%$ ) the microstructure is more or less uniform. This means that the higher the silane concentration, the better has to be the design of the lens-shaped electrode to compensate for the standing-wave in large area reactors.

#### KEYWORDS

photovoltaic solar cells, plasma enhanced chemical vapor deposition of thin films, microcrystalline silicon, capacitively-coupled large area reactors.

# Résumé

La démographie mondiale galopante associée à la demande énergétique toujours plus forte augmentent considérablement les risques d'un désastre écologique et humain provoqué par le réchauffement global du climat. Il est donc impératif de développer les technologies d'énergie renouvelables telles que l'énergie photovoltaïque (PV). De telles sources d'énergie verte sont déjà disponibles, mais leur coût est encore trop élevé pour pouvoir concurrencer les énergies basées sur les ressources fossiles, telles que le pétrole, le charbon ou le gaz naturel.

Un pas important a été effectué récemment avec l'introduction sur le marché de cellules solaires photovoltaïques de grande surface ( $> 1 \text{ m}^2$ ). Ces cellules sont basées sur la technologie des couches minces de silicium amorphe permettant des taux de rendement de l'ordre de 9 à 10 %. Ces rendements sont nettement inférieurs à ceux des cellules existant déjà sur le marché ( $\approx 25 \%$  pour les cellules en silicium cristallin), mais les coûts, tant de production que sur l'environnement, des cellules de grande surface en silicium amorphe sont aussi beaucoup plus faibles. Toutefois, la nouvelle génération de cellules PV en couches minces de silicium promet des rendements de l'ordre de 12 % et surtout une meilleure stabilité lors du fonctionnement. Ces nouvelles cellules sont basées sur du silicium microcristallin déposé sur des verres de grande surface par déposition par vapeur chimique assistée par plasma (PECVD) à partir de silane ( $\text{SiH}_4$ ) et d'hydrogène ( $\text{H}_2$ ), comme pour le silicium amorphe. Les cellules PV multi-jonctions silicium amorphe/silicium microcristallin nécessitent une couche épaisse ( $\approx 2 \mu\text{m}$ ) de silicium microcristallin pour accorder les courants générés dans les deux cellules superposées. Cette condition augmente le prix du produit final en raison des faibles vitesses de déposition (quelques Å/s) atteintes aujourd'hui, ce qui demande un temps excessivement long à la production de ces couches. L'amélioration de la vitesse de déposition tout en gardant une bonne qualité des films est difficile à accomplir en raison du manque de compréhension des phénomènes impliqués lors de la croissance de silicium microcristallin et les techniques d'optimisation empiriques généralement utilisées.

Dans ce travail, la composition du plasma est mesurée par spectroscopie d'absorption infrarouge et d'émission optique. Il est montré que les films en silicium déposés par PECVD avec une fréquence d'excitation de 40 MHz peuvent être classés en trois catégories (amorphe, transitionnel et microcristallin) en fonction de la concentration de silane *dans le plasma*, alors que ce n'est pas possible de le faire en fonction des autres paramètres du procédé (concentration initiale, puissance, pression, etc.) lorsqu'ils sont tous variés simultanément. Ces résultats démontrent que la technique consistant à diluer fortement le silane avec de l'hydrogène ( $< 5 \%$ ) n'est pas nécessaire pour déposer du silicium mi-

crocristallin. En effet, la composition du plasma ne dépend pas que de la composition initiale du gaz, mais également de la fraction de silane dissocié dans le plasma. Il est montré avec des modèles analytiques et numériques de la chimie du plasma que ceci est dû au fait que la composition du plasma détermine le flux des radicaux vers la surface du film. De ce fait, en accord avec les modèles phénoménologiques existant, plus le flux d'hydrogène atomique est important par rapport au flux de radicaux de silane, plus la fraction cristalline du dépôt est importante.

Cette conclusion est utilisée pour démontrer que du silicium microcristallin peut être déposé à partir de silane pur dans des réacteurs de grande surface. De plus, il est démontré que l'optimum en termes de vitesse de déposition et de fraction de gaz utilisé est du côté du silane pur, plutôt que du régime conventionnel très fortement dilué en hydrogène. Une stratégie d'optimisation de la déposition de silicium microcristallin en variant uniquement la pression et le flux d'hydrogène est proposée. Un dépôt de bonne qualité avec une grande vitesse de déposition ( $> 10 \text{ Å/s}$ ) et une grande utilisation du gaz ( $> 80 \%$ ) a ainsi été déposé à partir d'une concentration initiale en silane importante ( $> 10 - 20 \%$ ).

Il est également montré en se basant sur de la modélisation et des mesures résolues en temps de la composition du plasma que le temps nécessaire à atteindre l'équilibre chimique dans des réacteurs de type Plasma-Box<sup>TM</sup> est de l'ordre de la seconde. Cette période est nettement plus courte que celles observées dans de petits réacteurs de laboratoire, et il est montré que la rétro-diffusion du silane depuis le volume mort vers le plasma en est la cause. La composition adéquate pour la croissance de silicium microcristallin est atteinte de manière quasi-instantanée à l'allumage du plasma dans les réacteurs de type Plasma-Box<sup>TM</sup>. Il n'est donc pas nécessaire avec ces réacteurs d'utiliser des stratégies telles que la pré-dilution en hydrogène pour éliminer la couche d'incubation en silicium amorphe provoquée par l'évolution temporelle du plasma jusqu'à l'équilibre chimique.

Finalement, il est montré que les effets Telegraph et d'onde-stationnaire, qui sont les deux modes électromagnétiques nécessaires et suffisants pour décrire les champs électromagnétiques dans les réacteurs RF, influencent l'uniformité tant de l'épaisseur que de la microstructure du film déposé. Il est démontré que l'effet Telegraph peut être éliminé en symétrisant les électrodes et que l'effet d'onde-stationnaire influence la microstructure des dépôts seulement lorsque la concentration initiale de silane est importante ( $\approx 10\%$ ). Cela implique que plus la concentration initiale de silane est importante, plus la construction de l'électrode incurvée pour compenser l'effet d'onde stationnaire doit être précise.

## MOTS CLÉS

cellule solaire photovoltaïque, déposition de couches minces assistée par plasma, silicium microcristallin, réacteur capacitif de grande surface.



# Contents

<b>Abstract</b>	<b>i</b>
<b>Résumé</b>	<b>iii</b>
<b>Introduction</b>	<b>1</b>
<b>1 Microcrystalline silicon thin film photovoltaic solar cells</b>	<b>7</b>
1.1 Radio-frequency plasma enhanced chemical vapor deposition . . . . .	7
1.2 Silicon thin film solar cells . . . . .	9
1.2.1 Structure of thin film solar cells . . . . .	9
1.2.2 From amorphous to microcrystalline silicon solar cells . . . . .	10
1.3 Microcrystalline silicon growth . . . . .	15
1.3.1 Surface diffusion model . . . . .	15
1.3.2 Selective etching model . . . . .	16
1.3.3 Chemical annealing model . . . . .	17
1.4 Foundations of the present work . . . . .	18
<b>2 Experimental arrangement &amp; method</b>	<b>21</b>
2.1 Plasma reactor . . . . .	21
2.2 Plasma diagnostics . . . . .	24
2.2.1 Deposition rate monitoring . . . . .	24
2.2.2 Plasma composition determined by infrared spectroscopy . . . . .	25
2.2.3 Optical emission spectroscopy . . . . .	29
2.3 Material characterization . . . . .	35
2.3.1 Micro-Raman spectroscopy . . . . .	35
2.3.2 Infrared spectroscopy . . . . .	38
2.3.3 Film thickness . . . . .	39
<b>3 Plasma composition as the relevant plasma parameter</b>	<b>43</b>
3.1 Crystallinity & plasma composition . . . . .	44
3.2 Analytical plasma chemistry model . . . . .	50
3.2.1 Model I: The simplest . . . . .	50
3.2.2 Towards more realistic chemical models . . . . .	52
3.3 Plasma and process characteristics . . . . .	59

3.4	Silane depletion as a function of the plasma parameters . . . . .	60
3.5	Dissociation efficiency and deposition rate . . . . .	62
3.6	Are there other interesting deposition regimes ? . . . . .	64
3.7	Conclusion . . . . .	66
<b>4</b>	<b><math>\mu</math>c-Si:H deposition optimization: Towards pure silane plasmas</b>	<b>67</b>
4.1	From highly H <sub>2</sub> -diluted to pure silane regime . . . . .	67
4.1.1	Effect of H <sub>2</sub> -dilution on the deposition rate and silane gas utilization fraction . . . . .	68
4.1.2	Pure silane regime optimization . . . . .	71
4.1.3	Estimation of the polysilane or powder quantity . . . . .	73
4.2	Deposition optimization . . . . .	76
4.2.1	Initial process parameter selection: A short review . . . . .	77
4.2.2	Optimization strategy . . . . .	80
4.2.3	Flow diagram . . . . .	83
4.3	Conclusion . . . . .	87
<b>5</b>	<b>Plasma and film growth at discharge ignition</b>	<b>89</b>
5.1	Time-resolved plasma composition measurement . . . . .	89
5.2	Highly-diluted silane . . . . .	90
5.3	Time-resolved models . . . . .	93
5.3.1	Solution for constant pumping speed . . . . .	94
5.3.2	Solution for constant pressure . . . . .	95
5.3.3	Comparison of model boundaries . . . . .	96
5.3.4	Comparison of the model with OES measurements . . . . .	97
5.4	High concentrations and pressures . . . . .	98
5.4.1	30 % silane concentration . . . . .	99
5.4.2	Higher pressures . . . . .	100
5.4.3	Pure silane . . . . .	102
5.4.4	Optimized conditions for microcrystalline silicon deposition . . . . .	103
5.5	Large industrial vs small laboratory reactors . . . . .	104
5.5.1	Silane back-diffusion . . . . .	104
5.5.2	Hydrogen dilution profiling strategies . . . . .	110
5.6	H <sub>2</sub> background subtraction . . . . .	111
5.7	Conclusion . . . . .	113
<b>6</b>	<b>Polysilane formation:</b>	
	<b>Analytical model and process limitations</b>	<b>115</b>
6.1	Disilane model . . . . .	116
6.2	Numerical model . . . . .	122
6.3	Gap reduction . . . . .	123
6.4	Flux ratio dependence on pressure . . . . .	128
6.5	Conclusion . . . . .	131

<b>7</b>	<b>Reactor geometry and uniformity</b>	<b>133</b>
7.1	Theory on electromagnetic uniformity . . . . .	134
7.1.1	The Telegraph effect . . . . .	134
7.1.2	The standing-wave effect . . . . .	135
7.2	Results . . . . .	137
7.2.1	Edge uniformity: the Telegraph effect . . . . .	137
7.2.2	RF voltage non-uniformity . . . . .	140
7.3	Conclusion . . . . .	146
	<b>Final conclusion and outlook</b>	<b>146</b>
	<b>Appendix</b>	<b>151</b>
A	Two-dimension numerical modeling	151
	<b>Bibliography</b>	<b>155</b>
	<b>Acknowledgments/Remerciements</b>	<b>171</b>



# Introduction

Energy... This concept is now discussed in all spheres: In public media, in politics, in the economic community and, of course, in the scientific community. This growing interest has many origins. The everyday price increase at the gas station acts as a psychological activator for all of us. The growing energy consumption per capita [1] coupled with the galloping world demography is a promising playground for huge financial benefit. And last but not least, global warming [2] forces us to develop green energy production solutions and to increase our energy consumption efficiency in order to avoid a programmed ecological, economic and human disaster [2, 3].



**Figure 1:** Global warming already has dramatic consequences in climate sensitive regions.

However, many different technical solutions exist for the production of energy without carbon dioxide emission such as hydraulic, geothermic, wind, bio-gas and solar energies, but they represent only 7 % of the total world energy production, and even less than 1 % without hydraulic energy as shown in Fig. 2. This marginal contribution of the renewable energies when compared to the well-established energy sources based on the natural resources (coal, oil, gas, uranium) is mainly due to the still too high cost of these new technologies, but also to the immobility of the politicians in front of huge multinational energy companies. Nevertheless, some clear signals of a current change can now be observed such as the new energy policy in Germany with the introduction of the "feed-in laws" leading to a huge development of green energies in that country or the recent interest of the economic class in the consequence of global warming [3].

The solar energy technology also benefits from this recent trend for renewable energy,

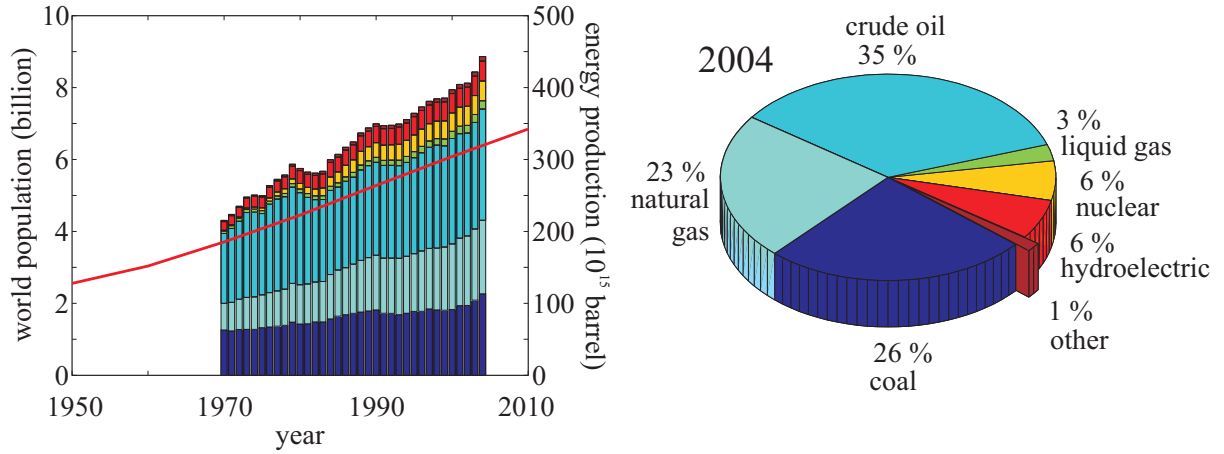


**Figure 2:** (left) Evolution of the world population (solid line) and energy production (bar plot) in barrel equivalent (data taken from Refs. [4, 5]). (right) Energy production in 2004 by type: renewable energy production is less than 1 % without taking into account hydroelectricity (data taken from Ref. [5]). Colors of the bar plot correspond to energy sources of the pie plot.

and the associated market segment has an annual growth of about 40 % as shown in Fig. 3. Germany is the world's largest market with a photovoltaic electricity production capacity of 968 MW installed during the year 2006 [8], whereas 645 MW were installed during 2005 in the whole European Union [9]. One of the major factors for this success is the continuous decrease in PV system cost as shown in Fig. 3(b) [7] for Japan and the USA. However, the cost disadvantage of the PV is still significant compared to fossil-based and nuclear energies [10]. This is partly due to the fact that the actual PV market is

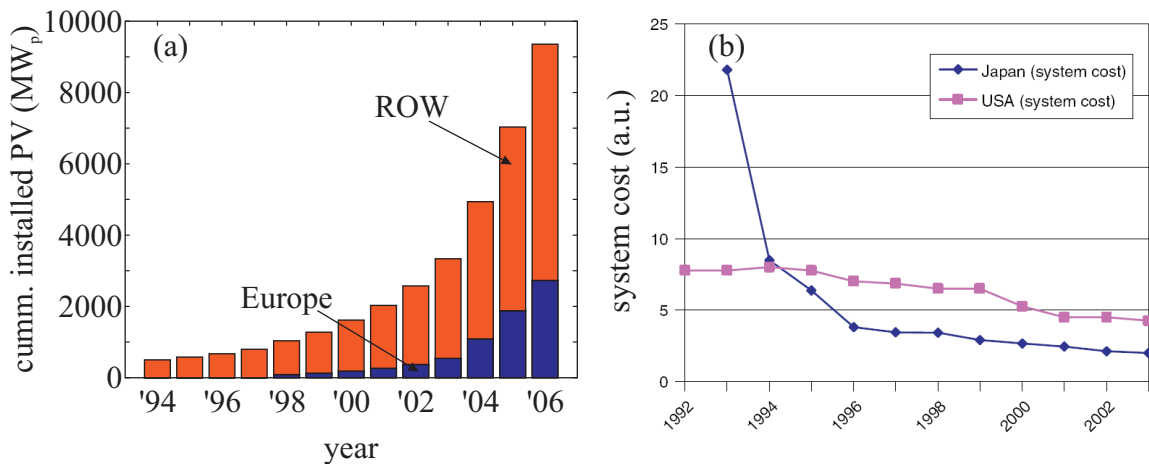


**Figure 3:** (a) Cumulative Photovoltaic installation in Europe and the rest of the world (ROW) from 1994 to 2006 (from Ref. [6]). (b) Price reduction of PV systems in Japan and in the USA from 1992 to 2003 (from Ref. [7]).

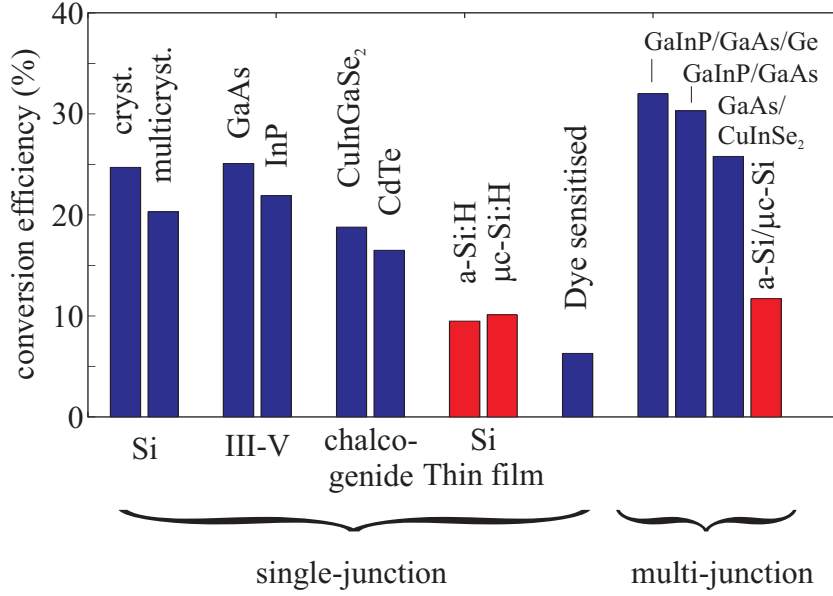


**Figure 4:** Panel of the different PV technologies with their conversion efficiencies, from high performance multi-junction GaInP/GaAs/Ge to very low cost chemical dye sensitized cells (data from Ref. [13]).

dominated by solar cells based on expensive crystalline silicon with a market share above 90 % [11], despite the great variety of PV technologies. Indeed, there are many different types of PV design using different type of materials or structures as shown in Fig. 4. Additionally to the common crystalline and multi-crystalline silicon cells which have high conversion efficiencies, there are the III-V and the chalcogenide cells composed of more exotic compounds (As, Sb, Ga, In,...) which have also high conversion efficiencies of about 20 %. But these latter are less environmentally friendly than cells based on silicon because of the toxicity of their constituents. All these types of cells can be combined into multi-junction cells which present very high conversion efficiencies of up to 30 %. The main disadvantage of these cells is that they are all deposited on crystalline silicon wafers making them economically and environmentally expensive. On the other hand, chemical dye sensitized cells are very cheap, but show poor conversion efficiency, about 5 - 7 % [12]. PV solar cells based on silicon thin film technology lie between these two limits. The silicon does not come from expensive monocrystalline ingots but is grown by chemical vapor deposition (CVD) on inexpensive substrates such as glass or polymer. The deposited silicon can present either an amorphous (a-Si:H) or a microcrystalline ( $\mu$ c-Si:H) structure and the resulting PV solar cells have a conversion efficiency of about 10 %. Combining these two materials into a multi-junction a-Si:H/ $\mu$ c-Si:H solar cell increases the conversion efficiency up to 11.7 % [13], but one hopes to reach an efficiency near 15 % [11]. These types of multi-junction a-Si:H/ $\mu$ c-Si:H cells are called *Tandem* or *Micromorph* cells.

Silicon thin film solar cells have many advantages compared to the other PV technologies, even if their conversion efficiency is lower than solar cells based on crystalline silicon or III-V compounds. First, it can be deposited on large area substrates having typical



**Figure 5:** (a) Traditional silicon thin film solar cells can be produced on low cost substrates 40 times larger than 20 cm diameter crystalline wafers. (b) This considerably reduces the cost of PV systems compared to solar modules composed of inter-connected cells having the size of silicon wafers. Pictures taken from Oerlikon-Solar AG [16].

size of  $1 \text{ m}^2$  [14] as shown in Fig. 5(a), or it can be deposited continuously on flexible substrate in a roll-to-roll configuration [15]. The large size of the final cells eliminates the assembly of the small size cells into modules, which is necessary when 20 cm diameter crystalline silicon wafers are used. Second, the quantity of raw material used to produce a thin film solar cell is much lower than for  $\approx 300 \text{ }\mu\text{m}$  thick crystalline silicon wafers, since the total thickness of the deposited films is less than  $10 \text{ }\mu\text{m}$ . Therefore, thin film silicon solar cells are less expensive and the economical and energy pay-back times are shorter than for the other PV technologies.

The actual commercially-available generation of thin film silicon solar cells is based on amorphous silicon. Typical manufacturing equipment (Fig. 5(b)) produces  $1.4 \text{ m}^2$  amorphous silicon solar cells with a yearly production volume of 20 MW/yr [14]. Similar equipment using plasma-enhanced CVD (PECVD) is currently in development to achieve the passage to the next generation based on microcrystalline silicon thin film. This second generation will make it possible to increase the efficiency of the solar cells and the annual production volume.

The technique used to deposit silicon thin films is a common technology which is employed in many fields as shown in Fig. 6. Some common examples (Fig. 6) are plasma sterilization, plasma TV, fluorescent plasma lighting or plasma processing for microelectronics. The plasma state is produced by applying an electric field to a gas. One can differentiate plasmas and gases by the density of charged particles (electrons and ions) which is larger in plasmas than in gases. There exist different types of plasmas which can be classified as a function of their electron density and temperature. The electron density could range from  $10^9$  to  $10^{26} \text{ m}^{-3}$  and the electron temperature from  $10^{-2}$  to  $10^5 \text{ eV}$  (1 eV corresponds to 11605 K) [17]. The plasmas which are studied in this work are called *glow discharges* and have an electron density about  $10^{15} \text{ m}^{-3}$  and an electron temperature of a few eV.

Since the end of the XIX<sup>th</sup> century, the development of plasma processing for industrial





**Figure 6:** Plasma in everyday life: 1-plasma TV, 2-plasma-coated jet turbine blades, 3-plasma-manufactured LEDs in panel, 4-diamond-like plasma CVD eyeglass coating, 5-plasma ion-implanted artificial hip, 6-plasma laser cut cloth, 7-plasma HID headlamps, 8-plasma-produced  $H_2$  in fuel cell, 9-plasma-aided combustion, 10-plasma muffler, 11-plasma ozone water purification, 12-plasma-deposited LCD screen, 13-plasma-deposited silicon solar cells, 14-plasma-processed microelectronics, 15-plasma-sterilization in pharmaceutical production, 16-plasma-treated polymers, 17-plasma-treated textiles, 18-plasma-treated heart stent, 19-plasma-deposited diffusion barriers for containers, 20-plasma-sputtered window glazing, 21-compact fluorescent plasma lamp (taken from Ref. [18]).

applications has been made principally by empirical methods. However, since the 80's the use of plasma processing in microelectronics has become a necessity instead of wet chemistry to permit the microfabrication of integrated circuits which are smaller from year to year. To achieve this goal, complex process equipment and techniques have been developed and they have necessitated a better comprehension of the physics standing behind the plasma and a strong collaboration between industry and academic institutions. The key-point to achieve efficient studies of plasma processing is to perform a multidisciplinary approach of this complex tool. One needs to intermix a wide knowledge in physics, chemistry and material sciences which play major roles in the plasma generation and properties, gas phase and surface reactions and film growth and properties, respectively.

## Purpose and structure of this work

Silicon thin film deposition by PECVD for photovoltaic application is interesting in order to reduce the price of solar cells systems. An intense research activity is performed in many groups all around the globe in this field to increase the silicon deposition rate on inexpensive large area substrates. In parallel, important efforts are invested in the passage from the amorphous silicon generation to the microcrystalline silicon generation. This promising material needs higher growth rate than the ones reported nowadays and a uniformity better than  $\pm 10\%$  over large areas. However, most of the research groups involved in this field generally concentrate on the solar cell itself and not on the plasma characteristics.

The *objective* of this work was to study the inter-relation between the plasma and the deposited silicon films. This was achieved by the characterization of both the plasma and the resulting films, as opposed to the conventional comparison between the plasma input parameters and the deposited materials. The motivation of this approach was to evidence the plasma properties needed to grow microcrystalline silicon. This understanding may then be used to help the passage from amorphous to microcrystalline silicon thin film solar cells, and optimize the process parameters and reactors to get closer to a cost-effective solar cell production.

The work presented in this thesis has been performed in collaboration with Oerlikon-Solar AG through the CTI (Commission of Technology and Innovation) project n° 6947 entitled: "*A new large area very high frequency (VHF) reactor for the high rate deposition of microcrystalline silicon for thin film solar cell applications*". Thin film characterization and solar cell manufacturing have been performed in collaboration with the Photovoltaic Laboratory of the Institut de Microtechnique of the University of Neuchâtel (Switzerland).

This work is organized as follows: Chapter 1 introduces plasma-enhanced chemical vapor deposition of microcrystalline silicon and the foundations of this thesis. Chapter 2 presents the experimental setup and the techniques used to characterize the plasma and the deposited layers. Chapter 3 exposes the main results on the inter-relation between the plasma properties and the film microstructure. This is used to optimize the deposition rate and the gas utilization efficiency in Chapter 4 and to study the plasma and the film growth at plasma ignition in Chapter 5. Chapter 6 discusses the influence of polysilane formation in the discharge on the process window and on the film growth. The effect of the reactor geometry on the film uniformity over the substrate area in terms of thickness and crystallinity is presented in Chapter 7, before concluding this work.

# Chapter 1

## Microcrystalline silicon thin film photovoltaic solar cells

This chapter briefly presents the deposition technique used to grow silicon films used in the present study. Amorphous silicon solar cells and the current knowledge on microcrystalline silicon growth are also introduced. Finally, the work of Howling *et al* [19], which is the foundations of this thesis, is reviewed.

### 1.1 Radio-frequency plasma enhanced chemical vapor deposition

Plasma-enhanced chemical vapor deposition (PECVD) is a common technique used during the manufacturing of most microelectronic devices. It consists in the excitation of a gas, or a mix of gases, by an electric field between two electrodes as sketched in Fig. 1.1. The electric field accelerates free electrons naturally present in the reactor and molecules start to dissociate by electron impact, creating more free electrons: The glow discharge is

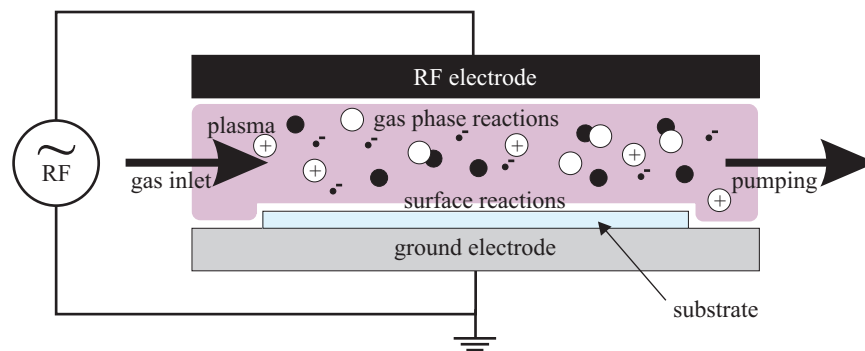


**Figure 1.1:** Schematic representation of a RF capacitively-coupled, parallel plate PECVD system, with gas inlet and pumping, gas phase reactions induced by the RF electric field applied between the two electrodes and surface reactions at the origin of the film growth.

ignited.

The dissociation of stable molecules by electron impact provides reactive radicals which may react between themselves through gas phase reactions, or react with the reactor walls, including the substrate, through surface reactions. The pressure is generally maintained in the 0.01 – 1 mbar range, which favors the surface reactions instead of the gas phase reactions. The excitation source could be either direct or alternative current, but the use of alternative excitation in the radio-frequency (RF) range offers some advantages. First, insulating films which are used in most of electronic devices can be grown because the current between the electrode and the plasma is dominated by displacement current. Second, the use of RF excitation makes it possible to increase the energy of the electrons while keeping the energy of the ions at low level. This is due to the fact that only light electrons can follow the RF electric field. Therefore, the energy transferred from the electrical excitation continuously accelerates the electrons. Such type of discharges are not in thermal equilibrium, with a high electron temperature - typically  $T_e$  is about 1 eV - and a low ion temperature - about room temperature. However, the ions are much heavier than the electrons, and the plasma temperature is determined by the temperature of the heavy particles. Therefore, RF-PECVD is generally compatible with most of substrate materials, even polymers. In other words, PECVD is a technique which gives access to high-temperature-chemistry while remaining at room temperature.

The deposition of amorphous (a-Si:H) and microcrystalline ( $\mu$ c-Si:H) hydrogenated silicon is generally performed from silane ( $\text{SiH}_4$ ) and hydrogen ( $\text{H}_2$ ) discharges. The dissociation products are mainly silicon radicals,  $\text{SiH}_x$  ( $x = 1-3$ ), and atomic hydrogen, H. These reactive species interact with the reactor walls through complex surface reactions, which result in the deposition of a silicon film with a low content of hydrogen (generally < 10 at.%) and the rejection of hydrogen into the gas phase. In RF discharges, the radical densities are much lower than the molecular densities (Fig. 1.2(a)) [20, 21, 22] because of the low dissociation rate of RF capacitive sources and of the high reactivity of the radicals which are "lost" on reactor walls.

The generally used RF excitation frequency is 13.56 MHz. However, the use of higher frequencies increases the gas dissociation [24] and hence the deposition rate as shown by Howling *et al* [23] (Fig. 1.2(b)). The use of very-high frequencies (VHF) also reduces the energy of the ions [25] since the DC sheath voltage is smaller. The bombardment of the growing film by energetic ions is then reduced, increasing the deposited material quality, because of the lower defect density.

RF-PECVD discharges are experimentally controlled by external variables. These are

- the RF excitation frequency,
- the RF power density,
- the substrate temperature,
- the total pressure,
- the total flow rate,
- the gas mixture composition and

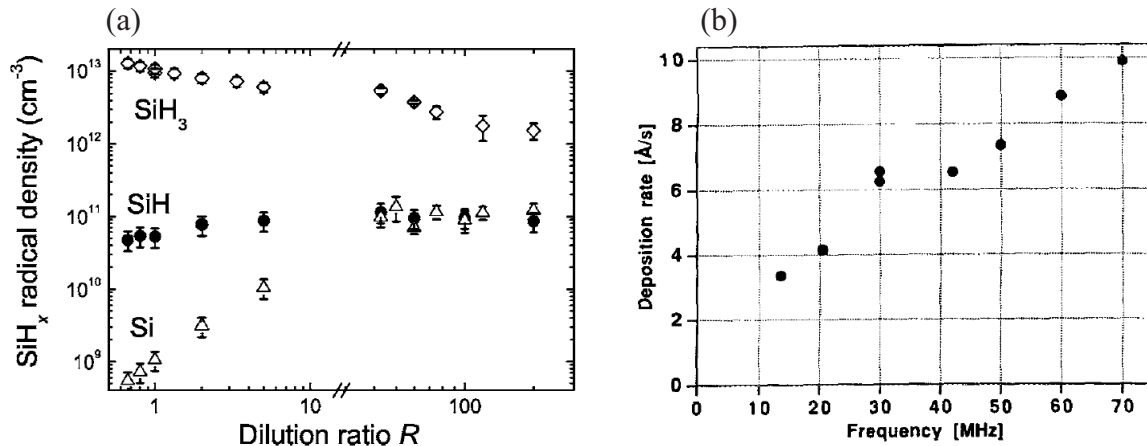


**Figure 1.2:** (a) Silane radical number densities as a function of the dilution ratio (from Kessels *et al* [20]). The total gas density is  $\approx 3 \cdot 10^{15} \text{ cm}^{-3}$ . (b) a-Si:H deposition rate as a function of the excitation frequency at constant RF power (from Howling *et al* [23]).

- the reactor geometry.

The process characteristics are the result of the phenomena occurring in the plasma and at the plasma-surface boundary. They are typically characterized by the deposition rate, the film uniformity over the substrate area, or the deposited material properties. The relations between the input parameters and the film properties are complex. The complexity of the physical and chemical processes involved in gas phase reactions and in the interactions between the plasma and the growing film surface adds to the engineering difficulties of PECVD systems which includes the reactor geometry, the gas flows, the RF power feeding, etc. The large quantity of parameters and their interactions are the reason why empirical developments are generally performed when studying film growth by PECVD. In order to efficiently optimize deposition processes, it is therefore necessary to have an inter-disciplinary approach, which includes plasma physics as well as chemical engineering and material sciences.

## 1.2 Silicon thin film solar cells

### 1.2.1 Structure of thin film solar cells

Thin film photovoltaic (PV) solar cells are generally deposited on a transparent substrate which can be either rigid, such as a thick glass, or flexible, such as a polymer sheet [26]. Some exceptions can be found in the literature such as the temporary superstrate concept, where the film is deposited on a metallic substrate which is removed after the deposition of the films by wet chemical etching [27]. The substrate is generally coated with an anti-reflective layer on the illuminated side to avoid light collection losses at the entrance of the cell.

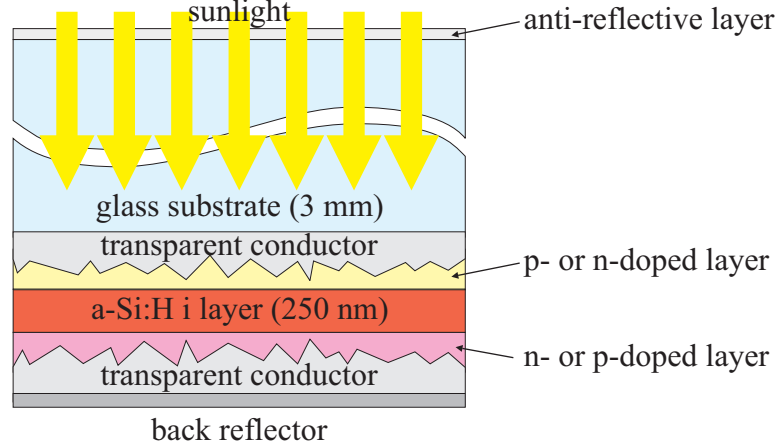


**Figure 1.3:** Schematic representation of the structure of a single-junction amorphous silicon thin film PV solar cell. It is composed of a thick glass substrate on which have successively been deposited a front transparent conducting contact, a p- (or n-) doped layer, an a-Si:H intrinsic layer, a n- (or p-) doped layer, a back transparent conducting contact and a back reflector.

The first layer of the cell deposited on the substrate is an electrical contact which has to be transparent to let the light enter in the PV cell as shown in Fig. 1.3. These contacts are transparent conductive oxide (TCO), which are typically zinc oxide (ZnO) [11] or tin oxide ( $\text{SnO}_2$ ) [28] deposited by sputtering. They have generally a textured surface in order to enhance the light trapping within the active part of the PV solar cell [11]. The intrinsic layer (i-layer) where most of the light is converted into electrons and holes is placed between two doped layers, a p- (hole acceptor) and a n-doped (electron acceptor) layer [29]. These create an electric field across the thickness of the i-layer forcing photo-generated electrons to drift towards the n-doped layer and the holes towards the p-doped layer. This p-i-n (or n-i-p) configuration has the advantage of increasing the collection of the photo-generated free-carriers by increasing their travel distance compared to a purely diffusive case, where no electric field is applied across the i-layer [15]. At the bottom part of the cell structure, there is another transparent contact and a metallic (Ag or Al) back-reflector, which both reflect the light back into the active part of the cell to increase the fraction of the absorbed light.

The present work focuses on the deposition of the intrinsic layer which is the thickest layer of the cell structure. This i-layer necessitates particular care, as shown in the next section, in order to have good light conversion capability and to transport efficiently the photo-generated free-carriers to the electrical contacts.

### 1.2.2 From amorphous to microcrystalline silicon solar cells

The light absorber intrinsic layer of a PV solar cell can be made of hydrogenated amorphous silicon deposited by PECVD. The first use of hydrogenated amorphous silicon in a photovoltaic solar cell was reported by Carlson and Wronski in 1976 [30]. The conversion efficiency was 2.4 % at AM-1 (one sun illumination). Shortly after this first work on

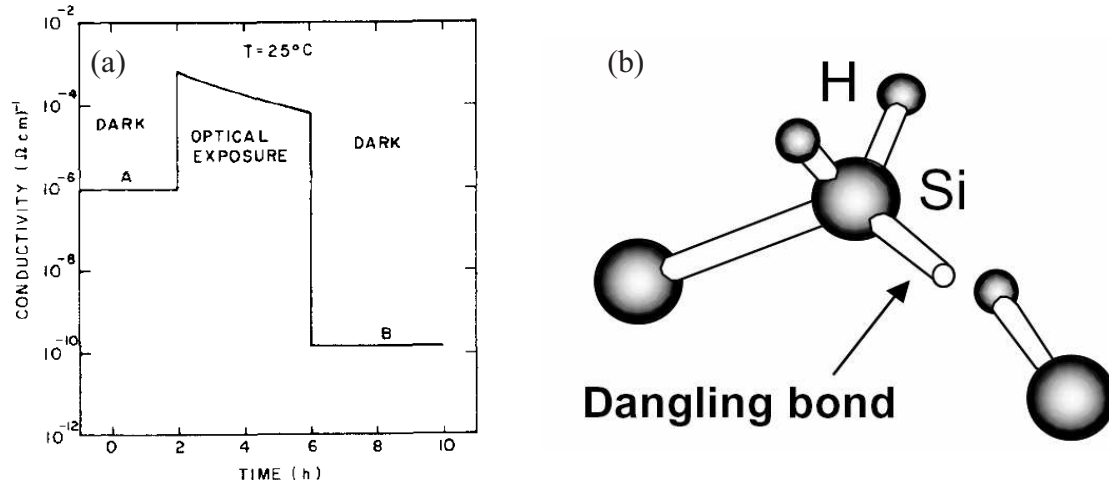


**Figure 1.4:** (a) Photo-induced degradation of amorphous silicon thin film conductivity (from Ref. [31]). (b) Silicon dangling bond which is a very efficient recombination center (from Ref. [32]).

a-Si:H PV solar cell, a degradation of the solar cell performance under light exposure was reported by Staebler and Wronski [31]. This has been evidenced by a reduction of the dark conductivity after light exposure as shown in Fig. 1.4(a) and this effect is known as the *Staebler-Wronski effect*.

Even if the mechanisms involved in the Staebler-Wronski effect are still not fully understood, it is assumed that the photodegradation of the conductivity is associated with the creation of defects which act as carrier recombination centers. The photoconductivity is defined as [33]

$$\sigma_p = e\mu n = e\mu\tau G, \quad (1.1)$$

where  $e$  is the elementary charge,  $\mu$  the mobility of the free carriers,  $n$  the density of the free electrons in the conduction band,  $\tau$  the free carrier life-time and  $G$  the electron-hole pair generation rate. During light exposure, the free carrier mobility,  $\mu$ , and the photogeneration of electron-hole pairs,  $G$ , are constant. Therefore, the photodegradation is caused by a change of the free carrier life-time,  $\tau$ , which is caused by the increase in the defect density acting as recombination centers and to their recombination capability.

The recombination centers can be associated with three different types of defects [33]. The *soft defects* having very high recombination capability are due to small structural imperfections such as mechanical stresses. However, their low activation energy makes them unstable at standard working temperature of PV solar cells, and therefore they are not the origin of the photo-induced degradation of PV cells. The *hard defects* having moderate recombination capability are due to more serious structural imperfections such as silicon dangling bonds as shown in Fig. 1.4(b). These defects have high activation energy and therefore are stable at standard working temperature of PV cells. These defects play a major role in the photo-induced degradation of a-Si:H PV solar cells, even if they can be annealed at high temperature [33]. The third type of recombination centers

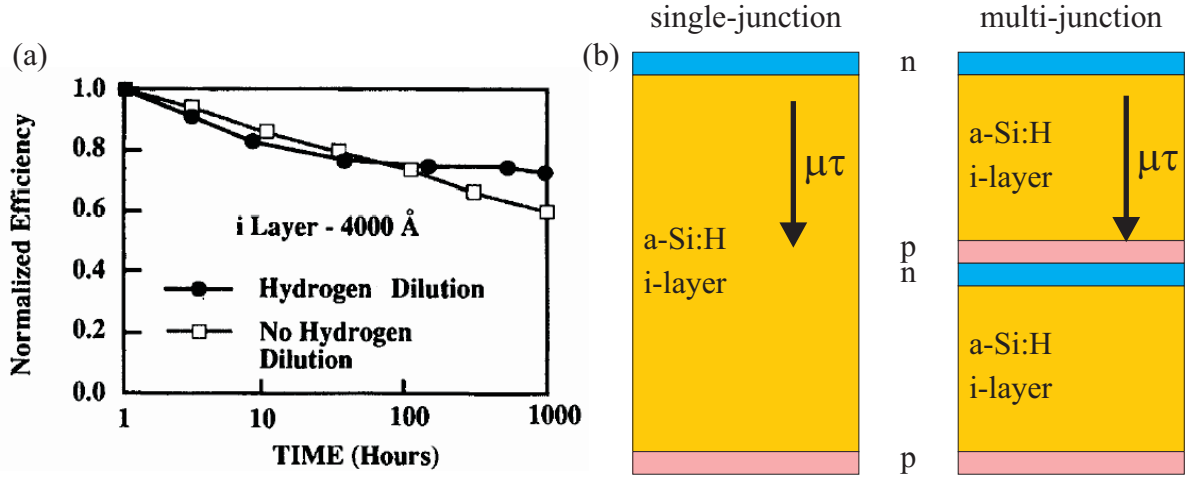


**Figure 1.5:** Strategies to reduce the effect of the photo-induced degradation of a-Si:H: (a) processing of a-Si:H from  $H_2$  diluted silane gas (from Ref. [34]), and (b) multi-junction PV solar cell to make the thickness of the i-layer thinner than the diffusion length of the free carriers, while keeping the same total absorber thickness

are the *stable defects* which are due to microstructural defects such as micro-voids. Their recombination capability is very low and their very high activation energy makes them stable at working temperature as at higher temperatures.

In summary, the most important recombination centers are the hard defects since they are active at the standard working temperature of PV solar cells and have a non-negligible recombination capability.

Different strategies have been developed in order to limit the photo-induced degradation of a-Si:H or at least to limit its impact on the loss of conversion efficiency of the final PV solar cell. The common way to reduce the photo-induced degradation of a-Si:H is to deposit the film from silane gas diluted by hydrogen. This technique reduces the defect density within the film, hence reducing the recombination center density. This technique does not completely eliminate the photo-induced loss of conversion efficiency of a-Si:H PV solar cells as shown in Fig. 1.5(a), but a-Si:H deposited from  $H_2$  diluted silane shows stable efficiency after degradation, while a-Si:H from pure silane continues to degrade [34]. Another technique is to reduce the collection length of the free-carrier by appropriate cell engineering. Indeed, if the diffusion length of the free carriers after photodegradation,  $\mu\tau$ , is larger than the collection length, i.e. the film thickness, the probability of carrier recombination is reduced. Therefore, multi-junction PV solar cells (Fig. 1.5(b)) can be produced in order to reduce the loss of free carriers without affecting the light absorption. This design adds losses at the interfaces between the different layers, but the great improvement in the collection of the free carriers makes multi-junction cells more efficient than thick single-junction cells [35].

This work concerns another technique which acts directly on the recombination center density as for the passivation of the silicon dangling bonds by hydrogen. The defect density can be greatly reduced if the microstructure is ordered. Indeed, in the extreme case of



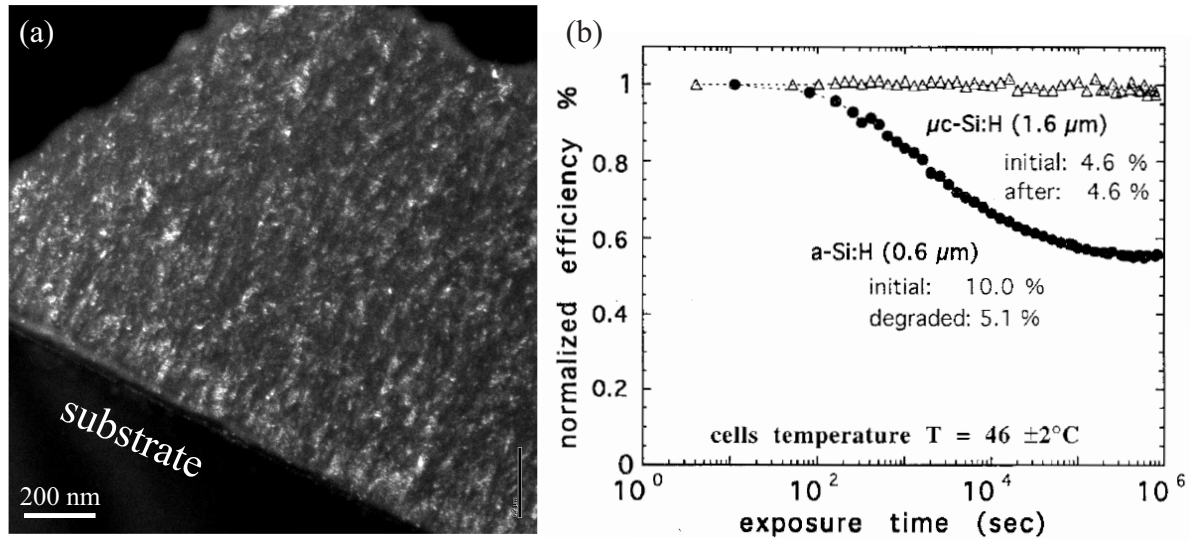


**Figure 1.6:** (a) Transmission electron micrograph of a  $\mu\text{c-Si:H}$  layer deposited on a crystalline silicon wafer. (b) Light soaking experiments on  $\mu\text{c-Si:H}$  and a-Si:H single junction PV solar cells (from Ref. [36]).

monocrystalline silicon, the defect density is very low and corresponds to the concentration of impurities. Between the fully amorphous hydrogenated silicon and monocrystalline silicon lies microcrystalline hydrogenated-silicon ( $\mu\text{c-Si:H}$ ). It consists of grains of crystalline silicon embedded in an amorphous silicon matrix as shown in Fig. 1.6(a). The size of the crystalline grains is about 100-300 nm, therefore the name nanocrystalline hydrogenated-silicon is sometimes also associated with this material. The defect density is higher in  $\mu\text{c-Si:H}$  than in a-Si:H, but the defects are located at grain boundaries or in the amorphous matrix [36]. The well-ordered structure in the crystallites effectively eliminates, at least in the crystalline phase, the hard defects. Since the electronic transport properties in  $\mu\text{c-Si:H}$  are dominated by the properties of the crystalline phase [36], no photo-degradation can be observed in  $\mu\text{c-Si:H}$  PV solar cells as shown by Meier *et al* [37] (Fig. 1.6(b)). However, the crucial point to reach solar grade quality  $\mu\text{c-Si:H}$  is to have good quality grain boundaries containing a low amount of unstable defects. Indeed, low quality amorphous silicon grain boundaries or cracks along grain boundaries which can be observed in highly-crystalline microcrystalline silicon make the material unusable for stable, high-efficiency solar cells [38].

Microcrystalline silicon has not only the advantage of a better stability under light exposure than amorphous silicon. Microcrystalline silicon has a different sunlight absorption spectrum than a-Si:H as shown in Fig. 1.7.  $\mu\text{c-Si:H}$  absorbs the light more in the infrared range. This difference between a-Si:H and  $\mu\text{c-Si:H}$  has been used to increase the sunlight energy conversion efficiency by performing a so-called Tandem cell, which consists in a multi-junction cell with a top-cell made of a-Si:H and a bottom-cell of  $\mu\text{c-Si:H}$  [36] as sketched in Fig. 1.7. The thickness of the a-Si:H intrinsic layer is generally thin (about 250 nm) in order to collect a maximum of the photo-induced electrons. The  $\mu\text{c-Si:H}$  in-

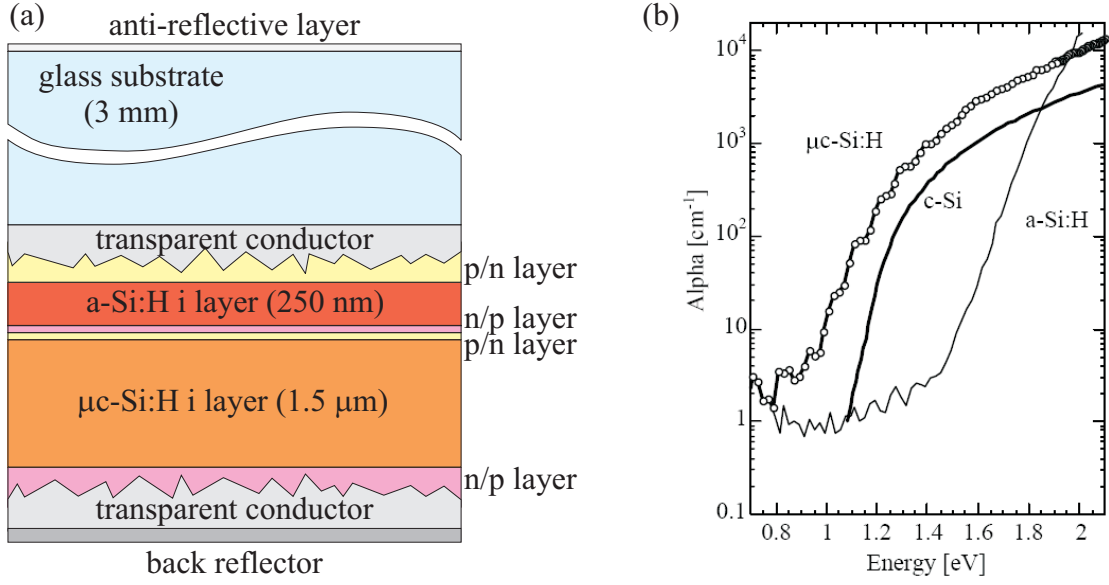


**Figure 1.7:** (a) Tandem or Micromorph PV solar cell structure with its top a-Si:H and bottom  $\mu c$ -Si:H cells. (b) Optical absorption spectra of a-Si:H,  $\mu c$ -Si:H and crystalline silicon (from Ref. [38]).

intrinsic layer has to be thicker (about 1.5 - 2  $\mu m$ ) because of its indirect band-gap and the necessity to match the photo-current generated by the two stacked cells [39].

From the point of view of the manufacturing technique,  $\mu c$ -Si:H is fully compatible with a-Si:H. Indeed, it can be deposited using the same reactor at the same substrate temperature of about 200 °C. The source gases are silane and hydrogen as for the deposition of a-Si:H. Generally, the hydrogen dilution is increased to change from the amorphous to the microcrystalline silicon deposition regime. When  $\mu c$ -Si:H is deposited in RF capacitively-coupled parallel plate reactors, the deposition rate is generally less than for a-Si:H, and is in the 1 - 5 Å/s range. This low deposition rate is a limiting factor for the use of  $\mu c$ -Si:H in PV solar cells, because it involves a too long time to deposit the  $\sim 2 \mu m$  thick  $\mu c$ -Si:H intrinsic layer. Typically, about 1 1/2 hours are necessary to deposit a 2  $\mu m$  thick layer with a 4 Å/s deposition rate. In order to achieve low-cost Tandem PV solar cells, the deposition rate of the intrinsic  $\mu c$ -Si:H layer has to be improved to rates higher than 10 Å/s.

High deposition rates are not the only condition for  $\mu c$ -Si:H films to achieve low-cost Tandem PV solar cells. Vetterl *et al* [40] have shown that the best material quality to be integrated in a Tandem solar cell is at the limit between amorphous and microcrystalline silicon. Therefore, the deposition conditions have to be perfectly controlled in order to have a material crystallinity in the 40 - 60 % range, and not to fall into the fully amorphous or strongly microcrystalline deposition region. Moreover, the material quality and the deposition rate have to be uniform within a range of  $\pm 10$  % over the whole substrate area [41] which is generally larger than 1 m<sup>2</sup>. This is in order to guarantee a

uniform light conversion efficiency, but also a uniform color of the final product which is of importance for the final customer.

### 1.3 Microcrystalline silicon deposition: Phenomenological models

The mechanisms involved in the growth of hydrogenated microcrystalline silicon are complex. They include chemical aspects such as the hydrogen and silicon dangling bonds and reactions in the film, and physical aspects such as the species ( $\text{SiH}_x$  and H) bulk diffusion. The heterogeneous microstructure composed by crystalline grains embedded in an amorphous matrix adds to the system complexity. Moreover, the surface and sub-surface chemistry and physics depend on both the growing film properties and on the plasma. This complexity is the reason why the  $\mu\text{c-Si:H}$  growth is not yet understood, making its quality improvement difficult. However, some phenomenological models have been proposed [32, 41, 42, 43, 44, 45, 46, 47, 48, 49, 50, 51] to explain the difference between amorphous and microcrystalline silicon growth from silane and hydrogen discharges. The three most important models are the *surface diffusion model*, the *selective etching model* and the *chemical annealing model*, which are reviewed in this section.

#### 1.3.1 Surface diffusion model

The surface diffusion model was developed after the importance of the surface diffusion of growth precursors ( $\text{SiH}_x$ ) was experimentally demonstrated. As shown by Matsuda [46], the crystalline volume fraction of deposited films strongly depends on the surface diffusivity of  $\text{SiH}_x$  which is improved when the silane concentration is reduced or the substrate temperature increased. This is due to the hydrogen surface coverage improvement making the  $\text{SiH}_x$  surface diffusion length long enough to permit  $\text{SiH}_x$  to attach at favorable sites to create a flat film surface. This has been confirmed by the abrupt fall of the film crystallinity for substrate temperature higher than 400 °C [46], caused by the desorption of hydrogen adsorbed on the surface at such high temperatures [45]. Moreover, some of the hydrogen atoms coming from the plasma recombine with surface bonded-hydrogen heating locally the surface, which enhances the surface diffusion of  $\text{SiH}_x$  as sketched in Fig. 1.8. The role of the surface diffusion in flattening the film surface is of particular importance for the nucleation of crystallites as shown by *in-situ* spectroscopic ellipsometry studies [52]. They have shown that silicon crystallite nucleation needs a smooth surface [44] and occurs only after a reduction of the initial surface roughness.

This shows that to promote the crystallinity of the deposited silicon film, a sufficiently high atomic hydrogen flux towards the growing film surface has to be delivered with respect to the silicon radicals flux. However, the role of the  $\text{SiH}_x$  surface diffusion in  $\mu\text{c-Si:H}$  growth may not be dominant for depositions performed at high rates, because of the shorter time allowed for  $\text{SiH}_x$  radicals to find adequate sites to attach.

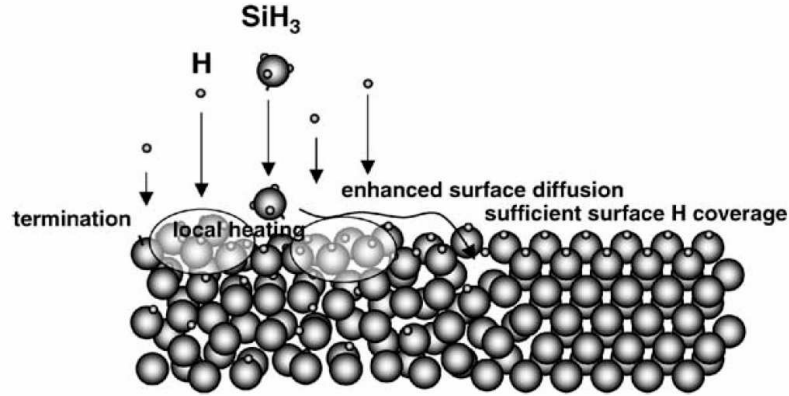
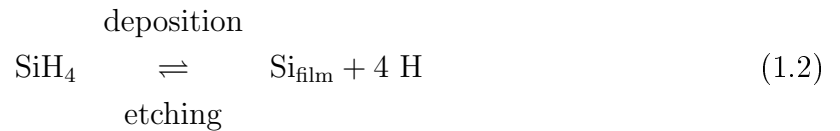


**Figure 1.8:** Schematic representation of the surface diffusion model. The hydrogen atoms from the plasma passivate all the surface silicon dangling-bonds, hence enhancing the surface diffusion length of silicon radicals, which could find an adequate site to attach (from Ref. [32]).

### 1.3.2 Selective etching model

The diffusion model was able to explain  $\mu c$ -Si:H deposition for substrate temperatures lower than  $400^\circ\text{C}$ , but  $\mu c$ -Si:H deposition at higher temperatures [48] shows that this model is not sufficient. Terasa *et al* [48, 49] have proposed that a combination of the surface diffusion model with a selective etching model may explain the deposition of microcrystalline silicon. This selective etching model is based on the experimental observation of silicon etching by hydrogen [53] by the reverse chemical reaction leading to silicon deposition from silane discharge [47].



This model is called *selective* because of the different etching rate of amorphous and microcrystalline silicon [53]. Indeed, the high lattice defect density in the amorphous structure facilitates the atomic hydrogen to etch the silicon atoms which are weakly bonded to their neighbors, whereas the well-arranged silicon atoms of the crystallites resist better to hydrogen etching [32]. The resulting difference in etching rate is about a factor 10, with an etching rate of  $\mu c$ -Si:H similar than for monocrystalline silicon [53]. The selective etching model sketched in Fig. 1.9 is based on the hypothesis that both amorphous and microcrystalline silicon are deposited and etched simultaneously, but with an etching rate much higher for the amorphous phase, hence increasing the crystalline volume fraction of the growing film. This model has to be combined with the surface diffusion model in order to explain the nucleation of the crystallites to initiate the microcrystalline growth from the initial amorphous incubation layer.

As for the surface diffusion model, the crucial physical consideration is the atomic

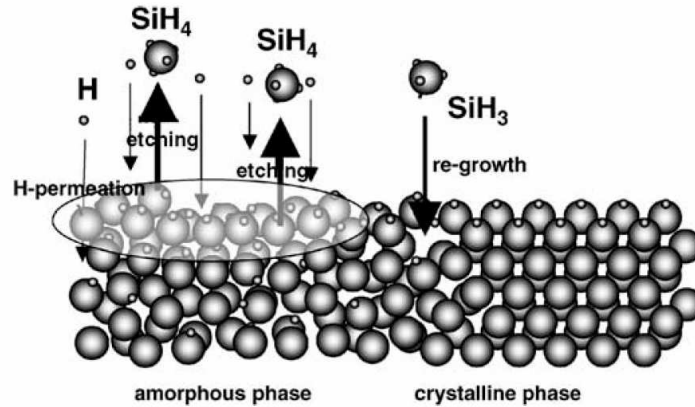


**Figure 1.9:** Schematic representation of the selective etching model. The hydrogen atoms from the plasma etch preferentially the amorphous silicon, favoring the growth of  $\mu c$ -Si:H (from Ref. [32]).

hydrogen flux towards the film surface with regard to the silicon radical flux, in order to etch efficiently the amorphous phase to promote the film crystallinity.

### 1.3.3 Chemical annealing model

The chemical annealing model has been constructed in order to explain the crystallization of amorphous silicon when exposed to a pure  $H_2$  plasma [54]. Indeed,  $\mu c$ -Si:H can be produced by using a layer-by-layer technique by alternatively depositing a thin a-Si:H layer and expose it to a pure  $H_2$  discharge which crystallizes the thin layer. Neither the etching model, nor the surface diffusion model, can explain this phenomenon, even if during the  $H_2$  plasma treatment the film is slightly etched [54]. This third model is based on the chemical reaction of atomic hydrogen coming from the plasma with hydrogen bonded to silicon at the film surface or sub-surface as depicted in Fig. 1.10. The reaction creates a silicon dangling bond and a hydrogen molecule. This reaction is exothermic, and the resulting structure thermal vibration promotes surface and bulk structural rearrangement leading to the energetically more favorable  $\mu c$ -Si:H [32]. The Si dangling bond created is then transformed into a more stable and rigid Si-Si bond or, if placed at the film surface, re-hydrogenated by atomic hydrogen from the plasma.

As for the selective etching model, the atomic hydrogen from the discharge can react with the surface or sub-surface of the film, but the reactions are different. In the etching model, the H atoms attach to silicon and re-hydrogenate the bulk silicon until silane desorption, and on the other hand, in the chemical annealing model, the H atoms recombine with surface or sub-surface hydrogen. As shown by the crystallization of a-Si:H with a low etching rate when exposed to pure  $H_2$  plasma [54], the crystallization by chemical annealing is more effective than by etching. This is due to the branching ratio between the two reaction channels which favors the hydrogen recombination with a branching ratio of the hydrogen flux which reacts on the surface of about 0.95:0.05 [55].

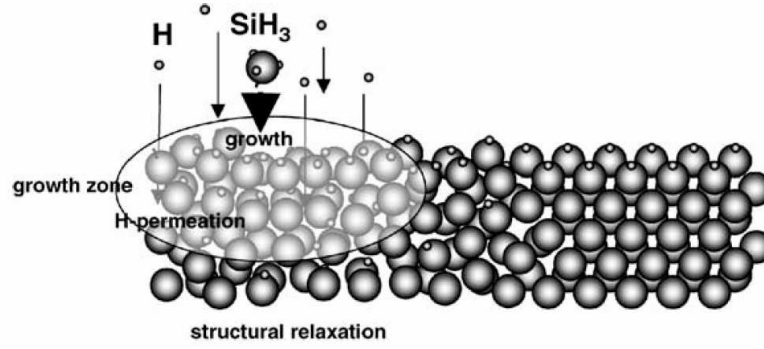


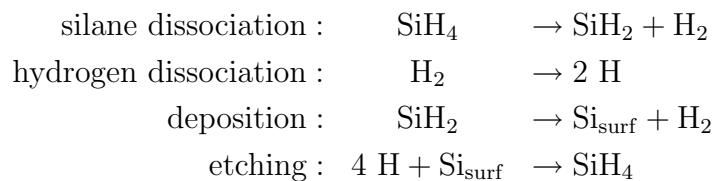
**Figure 1.10:** Schematic representation of the chemical annealing model. The hydrogen atoms from the plasma recombine with hydrogen bonded to surface or sub-surface silicon atoms, delivering vibrational energy which favors silicon crystallization (from Ref. [32]).

Consequently, the atomic hydrogen flow rate towards the surface has to be large compared to the silicon radical flux to promote the growth of  $\mu c$ -Si:H instead of the common a-Si:H. This is to increase the surface diffusivity by a fully H-covered surface, to remove undesirable a-Si:H by selective etching by H atoms, or to generate vibrational energy by hydrogen surface or sub-surface recombination, according to the surface diffusion, the selective etching or the chemical annealing models, respectively.

## 1.4 Foundations of the present work

The present work is based on the conference paper "*The influence of plasma chemistry on the deposition of microcrystalline silicon for large area photovoltaic solar cells*" presented in Glasgow (UK) at the 16<sup>th</sup> European Photovoltaic Solar Energy Conference in 2000 by Howling *et al* [19]. This seeding work is resumed in this section.

This work introduces a simple plasma chemistry model which describes a silane-hydrogen discharge. Its aim is to discuss the relation between the plasma properties and the resulting microstructure of the deposited silicon film. The flux ratio towards the growing film surface of atomic hydrogen to silane radicals was analytically deduced from a reduced set of chemical reactions including molecule dissociation by electron impact, silane radical deposition on reactor walls and etching of surface silicon by atomic hydrogen.



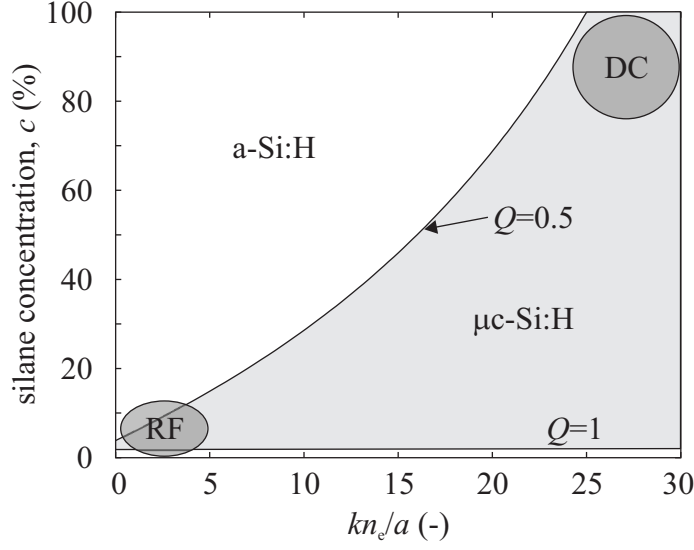


**Figure 1.11:** Film microstructure as a function of the dissociation rate to pumping rate ratio,  $kn_e/a$ , and of the input silane concentration,  $c$  [19].

More complex surface reactions such as surface diffusion or hydrogen surface recombination were not taken into account. The flux ratio,  $Q$ , physically represents the ratio of the etching rate to the deposition rate. It was assumed that for a low etching rate ( $Q < 0.5$ ) the deposited film microstructure was amorphous, and that for a high etching rate ( $0.5 < Q < 1$ ) the microstructure was microcrystalline according to the selective etching model and experimental observations. For ratio higher than unity, no deposition occurs since the etching rate is larger than the deposition rate. The analytical model has shown that the flux ratio could be expressed as a function of the silane input concentration and of the ratio of the silane dissociation rate to the gas pumping rate,  $kn_e/a$ , where  $k$  is the silane dissociation rate constant in  $\text{m}^3 \cdot \text{s}^{-1}$ ,  $n_e$  the electron density in  $\text{m}^{-3}$  and  $a$  the effective pumping rate in  $\text{s}^{-1}$ . The limit values of  $Q = 0.5$  and  $Q = 1$  as a function of  $kn_e/a$  and of the silane concentration,  $c$ , are presented in Fig. 1.11. It shows that microcrystalline silicon can be deposited only if the dissociation rate to the pumping rate ratio,  $kn_e/a$ , is sufficiently high, i.e. at high RF power or low pumping speed. For conventional deposition using RF excitation, the silane concentration has to be kept at low values since the poor dissociation efficiency of such plasma sources limits  $kn_e$  to low values. On the other hand, much more powerful sources such as the DC arc technique permit to deposit  $\mu\text{c-Si:H}$  from pure silane plasmas [56].

Moreover, Howling *et al* [19] have proposed on the basis of this plasma chemistry model that the plasma composition is determined by  $Q$ , and hence that plasmas suitable for the deposition of  $\mu\text{c-Si:H}$  are "composed almost entirely of hydrogen, independently of the flow rates used". As a consequence, the plasma composition of RF discharges performed from highly  $\text{H}_2$ -diluted silane is similar to the plasma composition of a DC discharge performed from pure silane gas. This makes possible the deposition of  $\mu\text{c-Si:H}$  from pure silane, as shown by Franz *et al* [56].

The work of Howling *et al* [19] will be investigated in more detail and further developed in the present thesis. Experiments will be compared to a more realistic model including additional plasma and surface reactions.



## Chapter 2

# Experimental setup, plasma diagnostics and material characterization

This chapter introduces the details of the experimental arrangement and method. Section 2.1 is dedicated to the deposition reactor and Sections 2.2 and 2.3 describe briefly the techniques used to characterize the plasma and the deposited films.

### 2.1 Plasma reactor

The plasma reactor used in this work was a modified KAI-S large area industrial reactor from Oerlikon-Solar AG. This type of reactor was initially designed for the flat display industry and is based on the Plasma-Box<sup>TM</sup> concept developed by J.P.M. Schmitt [41, 57] in the 80's. This vessel configuration consists of a differential pumping of the closed plasma reactor in which the deposition occurs, and the large vacuum chamber which contains the plasma reactor as shown in Fig. 2.1. The risks of contamination of the deposition area with particles (dust, powder,...) and chemical impurities (O<sub>2</sub>, N<sub>2</sub>,...) flowing from the vacuum chamber as observed in conventional open geometries is eliminated by maintaining a lower pressure in the vacuum chamber than the working pressure in the plasma reactor.

The RF plasma reactor was a grounded aluminum box with internal dimensions of 47 cm in width and 57 cm in length. Even if this area is large compared to conventional laboratory reactors, it is much smaller than industrial reactors used nowadays having sizes larger than 1 m<sup>2</sup> [58, 59]. However, it is much more convenient to perform academic research in such a "small" area reactor and it is less problematic to upscale results to industrial size reactors from this type of reactor than from small (< 20 cm in diameter) laboratory reactors. This is mainly due to the fact that studying plasmas and thin films produced in reactors such as the KAI-S ensures that the observed phenomena are not dominated by edge effects, making the comparison with performances of large industrial reactors easier.

In KAI reactors, the substrate (37 x 47 cm<sup>2</sup> for KAI-S) is laid on the grounded floor and the RF excitation is made by an electrode which is suspended in the grounded box (see Fig. 2.2). The standard interelectrode distance between the grounded floor and the RF electrode is 25 mm. The RF electrode is also used as a gas showerhead as sketched

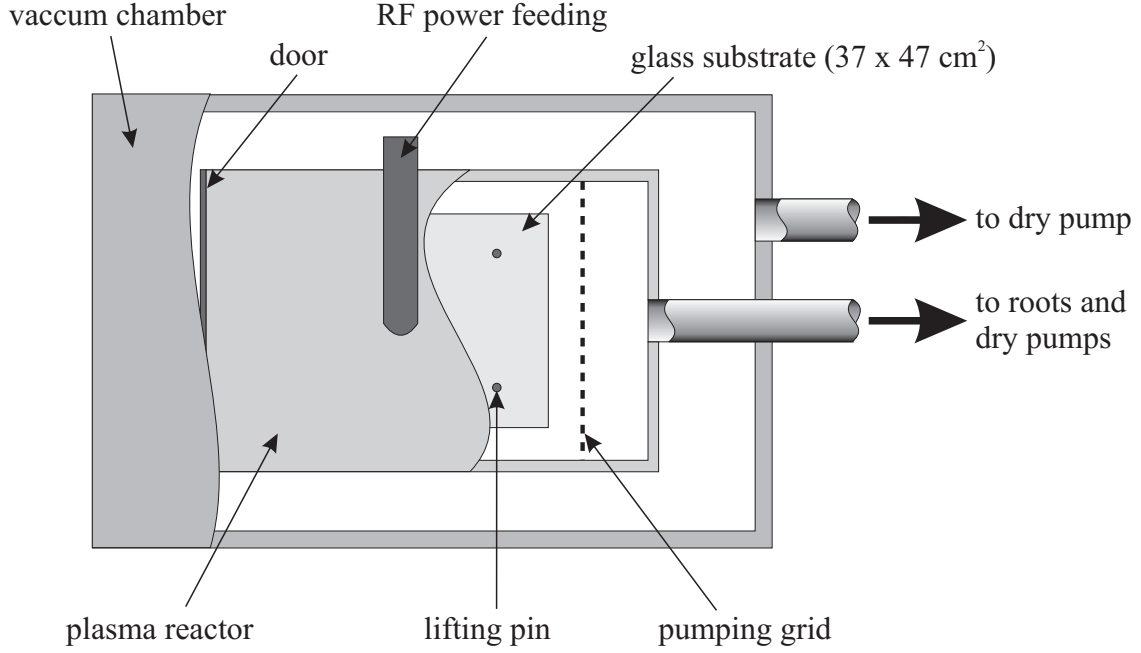


**Figure 2.1:** Deposition apparatus: The plasma reactor is placed in a large vacuum chamber which is differentially pumped. Glass substrates ( $37 \times 47 \text{ cm}^2$ ) are inserted via a load-lock through the door and are placed on the grounded electrode by using four lifting pins. The RF electrode is connected to the generator via a RF power feeding stripline with a connection point at the center of the RF electrode. Exhaust gases are pumped out by a roots pump and a dry pump through a pumping grid.

in Fig. 2.2. The process gas is pumped out from one side through a pumping grid having a high gas conductance (see Fig. 2.1). Therefore, the pumping grid acts only as an electrically conducting sidewall without affecting the gas outflow. This configuration which combines a uniform gas showerhead and a unilateral pumping guarantees a uniform pressure and gas distribution and composition over the whole substrate area, as demonstrated by Sansonnens *et al* [60]. The pressure was measured in the exhaust line by a baratron gauge and controlled by a butterfly valve (MKS type 653-B) positioned before the process pumping unit consisting of a roots pump (Pfeiffer WKP500,  $500 \text{ m}^3 \cdot \text{hour}^{-1}$ ) and a dry pump (Edwards QDP40,  $44 \text{ m}^3 \cdot \text{hour}^{-1}$ ). The whole deposition reactor was heated by using a resistive heater in close contact with the grounded box as described in Fig. 2.2. The temperature was controlled by a thermocouple inserted in the grounded box and was maintained at  $230 \text{ }^\circ\text{C}$  for all the experiments presented in this work.

The RF power delivered by a 40.68 MHz generator (Comdel CX-4000) was guided by a coaxial cable to a home-made matching box [61] directly connected to the vacuum feed-through. Inside the vacuum chamber, the RF power was guided by a stripline to the RF connection placed at the center of the RF electrode (see Fig. 2.1). The stripline has a sandwich structure composed of a powered aluminum strip embedded between two external grounded aluminum strips as shown in Fig. 2.2. The empty spaces in the stripline

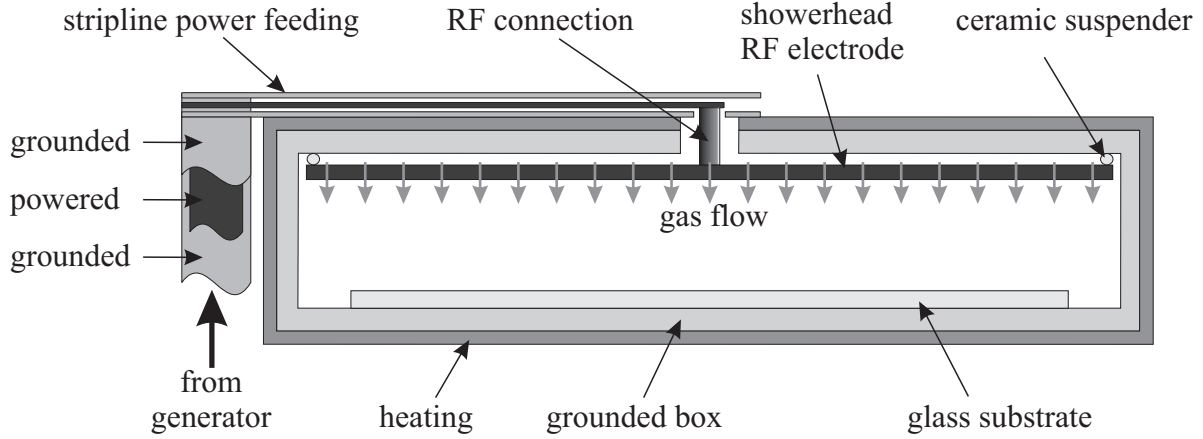


**Figure 2.2:** Lateral view of the plasma reactor (not to scale): The RF electrode is suspended in the grounded box and connected to a three layer sandwich power stripline. The RF electrode acts also as a gas showerhead which permits a uniform distribution of the process gases over the whole deposition area. The Plasma-Box<sup>TM</sup> is uniformly heated by a resistive heating wire covering the whole grounded box.

were filled with silicon rubber to avoid parasitic plasmas and corrosion of the stripline due to aggressive gases ( $\text{SF}_6$  and its decomposed byproducts) used for reactor cleaning. The injected and the reflected RF power were measured by a power meter (Bird power meter 4421 and sensor 027A35M) placed between the RF generator and the matching box. The resulting voltage between the RF electrode and the grounded box was measured by a voltage probe [62].

All gas flows were controlled by mass-flowmeters. Silane and hydrogen flowmeters were calibrated once per day in order to avoid errors in flow rates due to silicon oxide particles which can form in gas lines and flowmeters in the presence of silane and oxygen. This calibration was performed by measuring the rate of pressure rise in a calibrated volume at room temperature. The flow rates  $F$  can be calculated as following:

$$F \text{ (sccm)} = \frac{\Delta p}{\Delta t} V, \quad (2.1)$$

where  $\Delta t$  is the measured time in minutes during a pressure rise of  $\Delta p$  in mbar in the calibration volume  $V = 4.955 \text{ l}$ . This calibration can also be performed by using the large vacuum chamber as a calibration volume. However, the use of an independent calibration volume allows to calibrate or check flow rates even when the reactor is hot.

To avoid a decrease of the reactor temperature and to prevent the reactor from contamination with water vapor, substrates were loaded and unloaded by using a load-lock, while keeping the whole deposition vessel under vacuum. Once the substrate unloaded, the deposition chamber was cleaned by dry etching using a gas mixture of argon ( $\text{Ar}$ ), oxygen ( $\text{O}_2$ ) and sulfur hexafluoride ( $\text{SF}_6$ ) with flow rates of 250, 20 and 136 sccm, respectively. The input RF power was 600 W and the pressure 0.4 mbar.

## 2.2 Plasma diagnostics

### 2.2.1 Deposition rate monitoring

One of the major concerns of this work was to improve the deposition rate of  $\mu\text{c-Si:H}$  and therefore it had to be measured. The technique used in this work was an *in situ* optical diagnostic allowing real-time deposition rate monitoring at the center of the substrate. It consists in measuring the interaction of an incident monochromatic ( $\lambda = 640 \text{ nm}$ ) light with the growing film. The light emitted by a photodiode was guided through an optical fiber to the back of the substrate through a hole in the grounded bottom electrode as sketched in Fig. 2.3. The light was sent into the reactor perpendicularly to the substrate by a small tilted mirror before interacting with the growing film. The intensity of the reflected light,  $I_r$ , depends on the film thickness and optical properties as follows [62]

$$I_r = I_0 \left( 1 - \frac{T^2}{(1 - R^2)} \cdot \frac{1}{1 + \frac{4R}{1-R^2} \cdot \sin^2\left(\frac{2\pi d_{\text{film}} n_f}{\lambda}\right)} \right), \quad (2.2)$$

where  $n_f$  is the refractive index of the deposited material,  $d_{\text{film}}$  the film thickness,  $R$  and  $T$  the reflection and transmission coefficients, respectively, and  $\lambda$  the wavelength of the incident light. The reflected light was then collected in the same way as the incident light was injected, i.e. via the tilted mirror and an optical guide as sketched in Fig. 2.3. The signal was amplified by a photomultiplier and transformed by a current-voltage converter before being monitored as a function of time.

The reflected intensity,  $I_r$ , follows a sinusoidal-like behavior as a function of the layer thickness. The period of this oscillation is given by

$$\Delta L = \frac{\lambda}{2n_f} \quad (2.3)$$

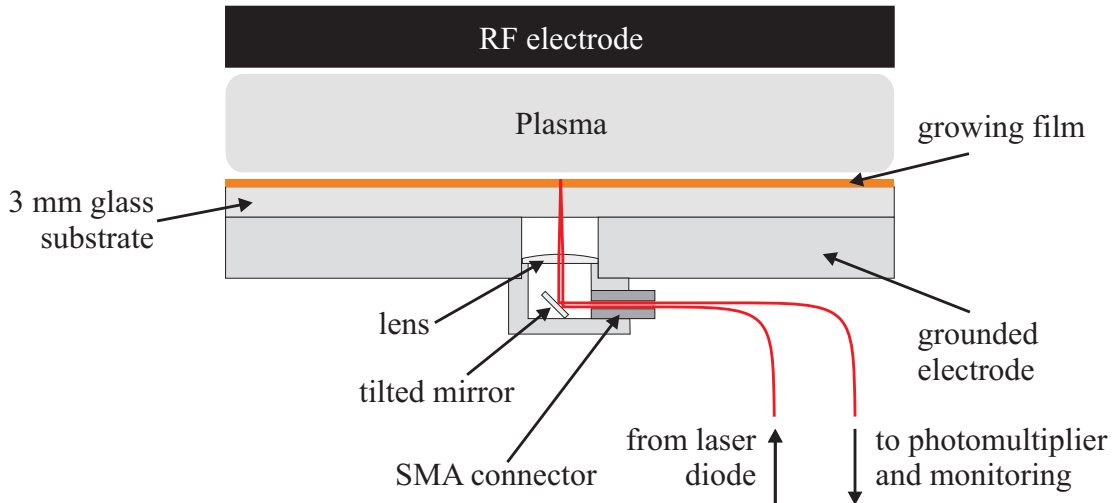


**Figure 2.3:** Monochromatic light interferometry setup to measure *in situ* the deposition rate.

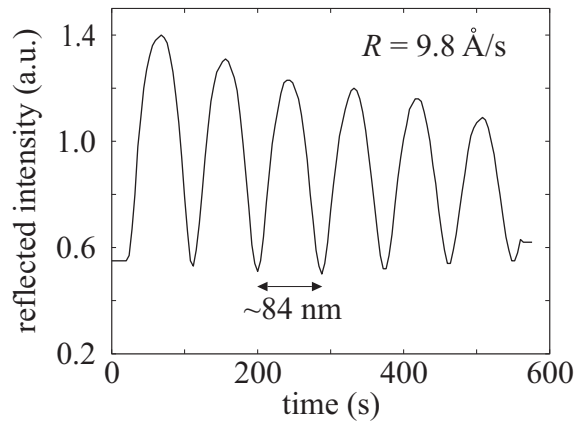


**Figure 2.4:** Output signal of a reflection interferometry measurement during an a-Si:H film deposition. The total thickness corresponds approximately to 500 nm and the resulting deposition rate is 9.8 Å/s.

For silicon compounds such as amorphous or microcrystalline silicon, a period  $\Delta L$  corresponds approximately to 84 nm, depending on the hydrogen content which influences the refractive index,  $n_f$ , which could vary between 3.7 and 4.1.

This *in situ* diagnostic allowed to control in real-time the thickness of the growing film by counting the fringes as shown in Fig. 2.4. The deposition rate was determined by dividing  $\Delta L$  by the time between two minima of the reflected intensity.

### 2.2.2 Plasma composition determined by infrared spectroscopy

Fourier transform infrared (FTIR) spectroscopy is based on the two-beam interferometer designed by Michelson in 1891. It is a widely used chemical analysis technique since its commercialization in the late 1960's simultaneously with minicomputers that made this technique much faster than originally [63]. One of the reasons of the success of this technique is that it is well suited to analyze solids, liquid solutions and gases (see Table 2.1) in a rapid way with little sample preparation. In this work, FTIR technique was used for gas analysis and hydrogenated silicon thin film characterization which is detailed in Section 2.3.2.

The principle of infrared (IR) analysis is to measure the absorption of an incident

type of sample	example of utilization
solid	organic materials characterization [64, 65]
liquid	petroleum [66] and powder technology [64, 67]
gas	gas and plasma analysis [64, 68, 69]

**Table 2.1:** Examples of the use of FTIR spectroscopy analysis.

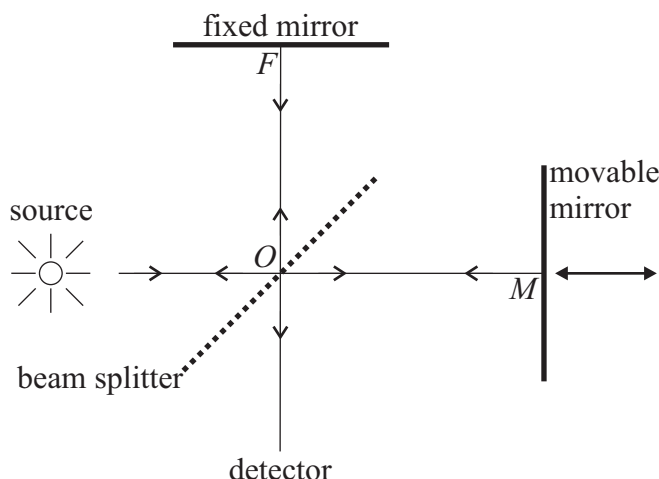


**Figure 2.5:** Schematic representation of a Michelson interferometer: The IR beam emitted by the source is separated by a beam splitter. A retardation is introduced by a difference in the two paths  $\overline{OF}$  and  $\overline{OM}$  before the recombination of the two beams. The resulting beam reaching the detector is the inverse Fourier transform of the source emission when the movable mirror is scanned.

IR beam by a material. IR in the wavenumber range  $400 - 4000 \text{ cm}^{-1}$  are absorbed by covalent bonds, hence excluding the analysis of materials such as pure metallic alloys or ceramics that contain only metallic or ionic bonds, respectively. Absorptions are associated with fundamental vibrations of molecules or functional groups. These vibrations can be either stretching vibrations, i.e. vibrations involving bond-length changes, or deformation vibrations, i.e. vibrations involving bond-angle changes.

Most FTIR spectroscopy experiments used nowadays are based on the design of Michelson presented in Fig. 2.5. The IR beam generated by the source is split into two beams ideally with the same intensity that are recombined after the introduction of a path difference  $\delta$ . The length of this path, called *retardation*, corresponds to twice the difference between the distances from a beam splitter (O) and two mirrors, one fixed (F) and one movable (M),  $\delta = 2(\overline{OM} - \overline{OF})$ . The intensity of the so-generated IR beam depends on  $\delta$  because of constructive or destructive interferences between the two beams. Hence, with a monochromatic IR source, the signal which reaches the detector is a cosine function as a function of the retardation [64]. The initial signal can be deduced by making the Fourier transform of the detected signal. When a sample to be analyzed is placed between the interferometer and the detector, the measured signal after Fourier transformation is the spectrum of the intensity emitted by the source after absorption by the sample. The difference between this spectrum and a reference spectrum measured without sample (without absorption) gives the IR absorption of the sample.

The arrangement for gas analysis used in this work is presented in Fig. 2.6. The sampling path stands in the pumping line of the plasma reactor between an IR interferometer (Bruker Equinox 55) and an external detector (Graseby type FTIR-W24) cooled with liquid nitrogen. The path length was 1 m between two IR transparent windows made of

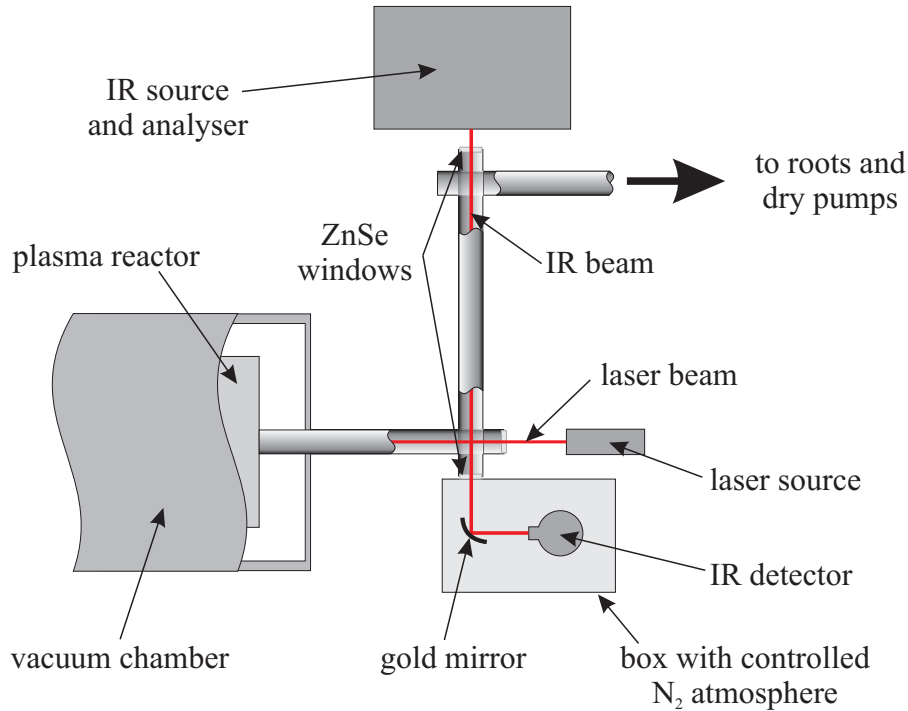


**Figure 2.6:** FTIR measurement arrangement: The IR absorption of the gas mixture is measured in the pumping line between two ZnSe windows. The IR beam is collected by an external detector standing in a box with a controlled  $N_2$  dry atmosphere. A visible laser beam in the pumping line is used to check if the discharge is powder free or not.

ZnSe. The detection setup was placed in a box under dry nitrogen atmosphere in order to avoid IR absorption by water vapor. The IR beam was focused on the detector by a paraboloid gold mirror. Acquisitions were performed within a  $400 - 4000\text{ cm}^{-1}$  range with a resolution of  $0.5\text{ cm}^{-1}$  and using a Blackman-Harris 3 term apodization function and a Mertz phase correction mode. Backgrounds and samples were averaged over 10 scans in order to improve the signal-to-noise ratio.

Figure 2.7(a) shows measured absorption spectra with plasma off (solid line) and plasma on (dashed line). The reduction in absorption when the plasma is on is due to plasma dissociation of silane molecules which are then deposited inside the reactor, hence not contributing to the absorption in the exhaust line. Due to a non-linear pressure dependence of the IR absorption, the silane partial pressure cannot be directly calculated from absorption measurements. To permit a quantitative analysis, a calibration curve presented in Fig. 2.7(b) was established between the pressure of pure silane gas (without  $H_2$  dilution) and the IR absorption. This calibration curve was performed by integrating the absorption spectrum between  $2163$  and  $2199\text{ cm}^{-1}$  for pure silane samples within the pressure range from  $0.005$  to  $6\text{ mbar}$ , and is valid only for the spectrometer parameters stated in the previous paragraph. This curve was then used to determine the silane partial pressure from its absorption without and with plasma in the reactor.

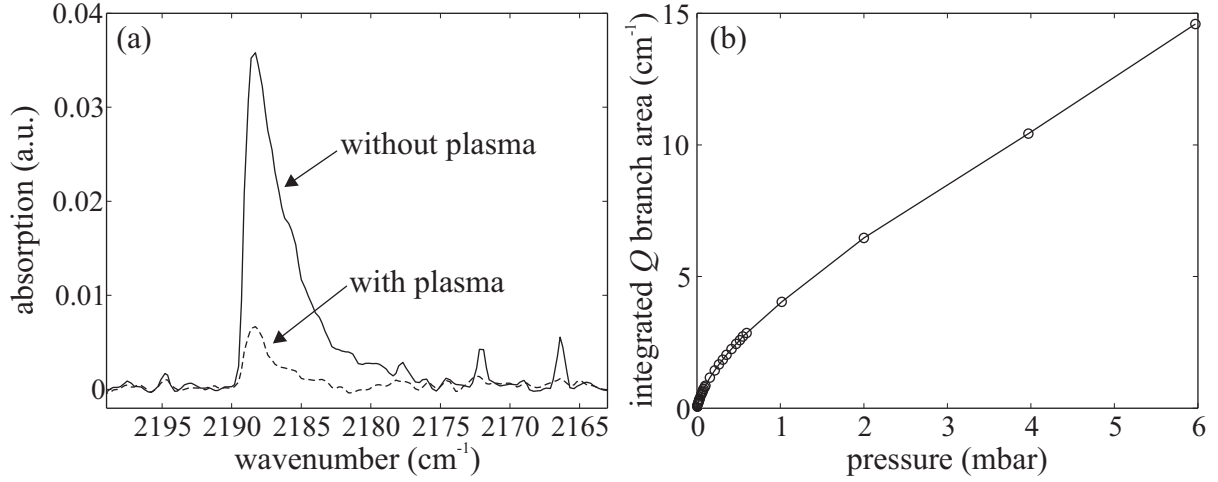


**Figure 2.7:** (a) IR absorption spectra without (solid line) and with (dashed line) plasma for a mixture of 2 %  $\text{SiH}_4$  in  $\text{H}_2$  at 4 mbar. The abscissa limits correspond to the integration limits (2163-2199  $\text{cm}^{-1}$ ). (b) Measured absorption of pure silane as a function of pressure. This calibration curve was used to convert silane absorption into silane partial pressure with and without plasma in the reactor.

The methodology used for this study was the following: First, a background spectrum was acquired without any gas flow and a pressure in the reactor below  $10^{-2}$  mbar. The flow rates of the process gases ( $\text{SiH}_4$  and  $\text{H}_2$ ) were established and the desired pressure was set by adapting the pumping rate by varying the butterfly valve position (Fig. 2.1) using a pressure feedback control from the baratron gauge. For these experiments, pressure equilibrium was set between the plasma reactor and the vacuum chamber to avoid differential silane and hydrogen leak rates from the plasma reactor to the vacuum chamber. Therefore, all molecules flowing into the reactor are pumped out through the exhaust line. A first spectrum acquisition was performed without plasma (solid line in Fig. 2.7(a)), hence giving a measurement of the silane initial partial pressure,  $p_{\text{SiH}_4}^0$ , by using the calibration curve. In the literature, the silane concentration is conventionally defined as the flow rate ratio  $\Phi_{\text{SiH}_4}/(\Phi_{\text{SiH}_4} + \Phi_{\text{H}_2})$ . However, the pumping speeds of silane and hydrogen may not necessary be the same depending on the flow regime and the way the pressure is regulated, hence the pressure ratio in the reactor may differ from the input flow rate ratio. Since we are concerned here with pressure measurements, the silane input concentration,  $c$ , is therefore defined in this work by the pressure ratio without plasma

$$c = \frac{p_{\text{SiH}_4}^0}{p_{\text{SiH}_4}^0 + p_{\text{H}_2}^0} = \frac{p_{\text{SiH}_4}^0}{p}, \quad (2.4)$$

where  $p_{\text{SiH}_4}^0$  and  $p_{\text{H}_2}^0$  are the silane and hydrogen initial partial pressures, respectively, and  $p = p_{\text{SiH}_4}^0 + p_{\text{H}_2}^0$  is the total pressure.

The plasma was then ignited with the required RF power, the same process pressure  $p$  (automatically adjusted by the butterfly valve) and unchanged input flow rates. A second spectrum was acquired (dashed line in Fig. 2.7(a)) and the silane partial pressure *in the*



$p_{\text{plasma}}$ ,  $p_{\text{SiH}_4}$ , was measured using the same method. Hence, the silane concentration in the plasma can be calculated as

$$c_p = \frac{p_{\text{SiH}_4}}{p}. \quad (2.5)$$

The fractional depletion of silane,  $D$ , which is at the origin of the decrease of the absorption in Fig. 2.7(a) can be defined as

$$D = \frac{p_{\text{SiH}_4}^0 - p_{\text{SiH}_4}}{p_{\text{SiH}_4}^0}. \quad (2.6)$$

The silane depletion is a direct measurement of the reduction of silane pressure due to the dissociation by the plasma. The fact that the total pressure is kept constant before and after plasma ignition by an adjustment of the butterfly valve position means that the  $\text{H}_2$  partial pressure increases because of the reduction in  $\text{SiH}_4$  partial pressure, so that  $p = p_{\text{SiH}_4}^0 + p_{\text{H}_2}^0 = p_{\text{SiH}_4} + p_{\text{H}_2}$  if we consider that all other species have a negligible contribution to the total pressure [20]. The silane concentration in the plasma,  $c_p$ , is then related to the input silane concentration,  $c$ , and to the fractional depletion,  $D$ , by

$$c_p = c(1 - D). \quad (2.7)$$

Note that Eq. 2.7 is valid only if the pressure is maintained constant before and after ignition and if the gas composition is independent of position in the reactor. This latter assumption is valid for a uniform showerhead reactor in the presence of a uniform plasma as shown by Sansonnens *et al* [60]. The molecular gas composition is the same in the pumping line as in the reactor. The radicals, which have comparably negligible density [20], are lost by gas and surface reactions in the reactor and do not enter the pumping line. For other gas distribution configurations or in the presence of strong plasma non-uniformities, the silane concentration in the plasma would have to be measured locally and Eq. 2.7 would no longer be valid.

### 2.2.3 Optical emission spectroscopy

Optical emission spectroscopy (OES) is very well adapted to diagnose process discharges because it permits real-time measurement which does not perturb the plasma. Moreover, the experimental simplicity of OES makes it a widely-used technique for various plasma chemistry including  $\text{SiH}_4$ - $\text{H}_2$  discharges [70, 71]. OES measurement can collect information about the plasma composition of the species formed in the discharge and also plasma characteristics such as the electron density and electron temperature [72]. In this work, time-resolved optical emission spectroscopy measurements have been used to investigate the plasma behavior following the plasma ignition until plasma equilibrium.

Emission of a photon can occur when the energy of an excited molecule decreases to a lower state. Another channel for a molecule to lower its energy is to dissociate. Photons can be emitted by transition between electronic, vibrational or rotational levels, corresponding to radiations within the optical, infrared or microwave frequency range, respectively. Generally, each transition can be associated to a characteristic wavelength as for argon (Ar) and atomic hydrogen (H) in Fig. 2.8. For polyatomic molecules the

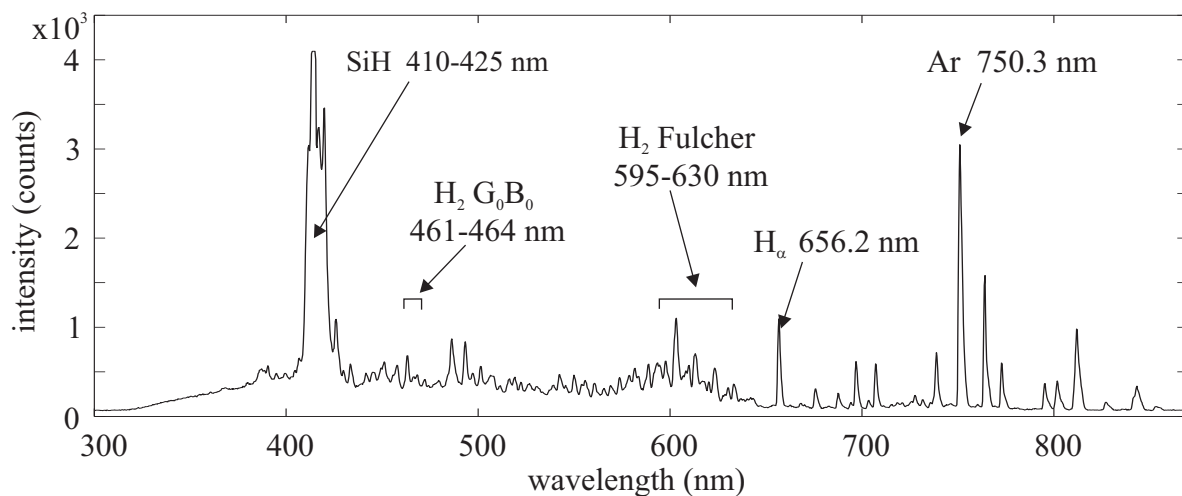


**Figure 2.8:** Emission spectrum of a discharge of silane and argon.

large quantity of electronic transitions due to the many different possible vibrational and rotational states at the initial and final levels makes the emission spectrum much more complex as shown for  $H_2$  in Fig. 2.8. The case of the SiH molecule stands in between the two previous extrema with a well-defined but wide peak from 410 to 425 nm.

The emission lines and bands of interest in this work were the ones emitted by the used molecules and atoms present in hydrogen ( $H_2$ ), silane ( $SiH_4$ ) and argon (Ar) discharges and are summarized in Table 2.2.

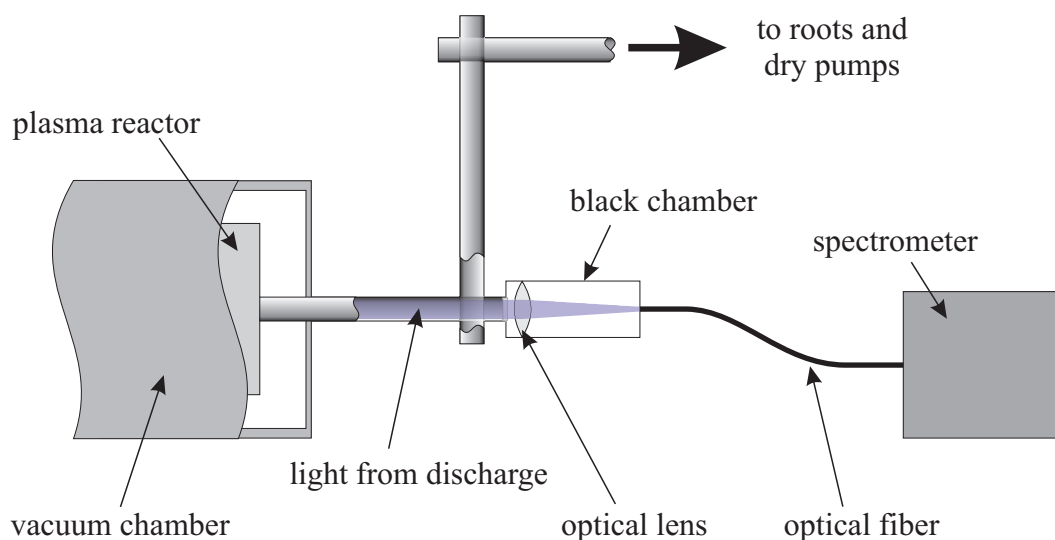


**Figure 2.9:** OES measurement arrangement: the light emitted by the plasma is focused by an optical lens into an optical guide before being analyzed by a spectrometer.

line/band	source	transition	wavelength (nm)
H $_{\alpha}$	e $^{-}$ + H $_2$ e $^{-}$ + SiH $_4$	3d $^2$ D $\rightarrow$ 2p $^2$ P $^0$	656.2
H $_2$ Fulcher	e $^{-}$ + H $_2$	d $^3$ $\Pi_u \rightarrow$ a $_3$ $\Sigma_g^+$ $v' = v'' = 0 - 2$	595 - 630
H $_2$ G $_0$ B $_0$	e $^{-}$ + H $_2$	G $^1$ $\Sigma_g^+ \rightarrow$ B $^1$ $\Sigma_u^+$ $v' = v'' = 0$	461 - 464
SiH	e $^{-}$ + SiH $_4$	A $^2$ $\Delta \rightarrow$ X $^2$ $\Pi$	410 - 425

**Table 2.2:** Emission origins and wavelengths from Ref. [70] for the chemical compounds used in this study.

The arrangement of the OES setup for the KAI-S reactor is presented in Fig. 2.9. It consists first of a light collection step, and second in an analyzing step. The light emitted by the plasma was collected from a glass window facing the plasma placed in the exhaust line, where an optical lens focused the incoming light into an optical guide (see Fig. 2.9). The light was sent directly into a spectrometer (Ocean Optics S2000) which permit spectrum acquisition within a 180 - 870 nm range with a spectral resolution of 1.7 nm (6 or 7 pixels) and a time resolution up to 20 ms. With such a configuration, the collected spectra do not represent a local information, but represent the emitted light integrated along the length of the reactor from the door to the pumping grid in the central part of the reactor.

### Choice of spectral lines of interest

In order to study the time evolution of the molecular densities of silane and hydrogen in the plasma, the spectral line selection is a crucial point. The choice made in this work is based on the spectroscopic work of Fantz in "*Spectroscopic diagnostics and modeling of silane microwave plasmas*" [70] and the spectrum analysis technique is based on the work of Howling *et al* [73].

**Molecular hydrogen number density:** Figure 2.8 shows that hydrogen presents emission from excited molecular state (H $_2^*$ ) and from atomic state (H $_{\alpha}$ , H $_{\beta}$ , etc...). The main difference between these two types of emission is that the emission from the molecular state results only from electron impact excitation of H $_2$  ground state [70, 73], and on the other hand, atomic emission results from dissociative emission of hydrogen and silane. Because of this dual source of atomic hydrogen emission, only the H $_2^*$  spectrum was used in this work to determine the hydrogen molecular density.

Emission due to the Fulcher transition (triplet transition d $^3$  $\Pi_u \rightarrow$  a $_3$  $\Sigma_g^+$ ,  $v' = v'' =$

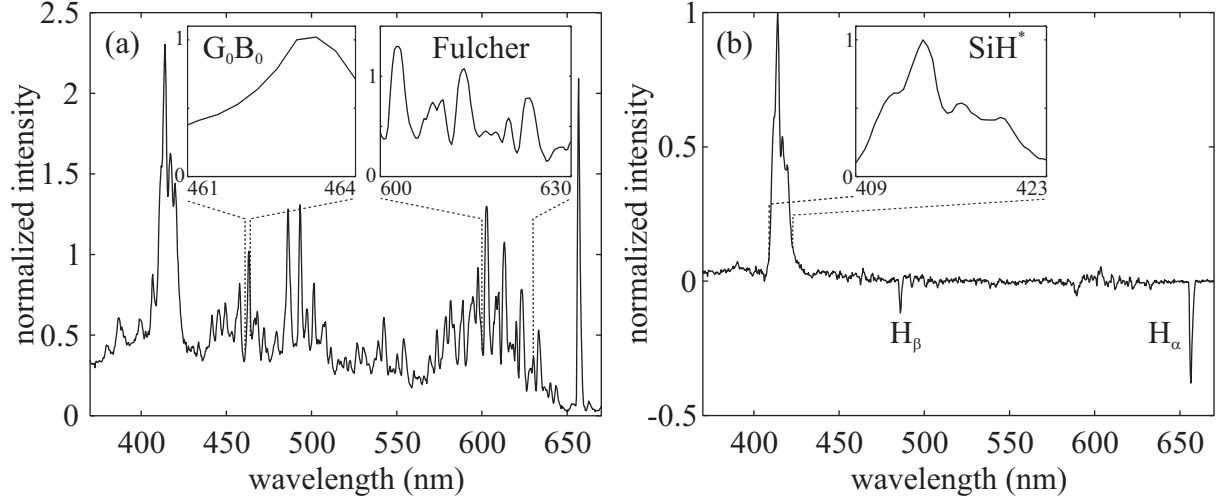


**Figure 2.10:** Ranges of spectral integration for (a)  $\text{H}_2^*$  (singlet and triplet) and (b)  $\text{SiH}^*$  after  $\text{H}_2^*$  background subtraction.

0 – 2) has been summed over the 600-630 nm range, and the time-dependent measured intensity can be written as

$$I_{\text{Ful}}^t = K_{\text{Ful}} \cdot X_{\text{Ful}}(T_e^t) \cdot n_e^t \cdot n_{\text{H}_2}^t, \quad (2.8)$$

where the constant  $K_{\text{Ful}}$  accounts for the collection, transmission and detection efficiencies of the emitted light,  $X_{\text{Ful}}(T_e^t)$  is the emission rate coefficient for electron impact excitation of molecular hydrogen depending on the electron temperature  $T_e$ ,  $n_e^t$  is the time-dependent electron number density and  $n_{\text{H}_2}^t$  is the time-dependent number density of molecular hydrogen.

The emission of the R-branch (singlet transition  $\text{G}^1\Sigma_g^+ \rightarrow \text{B}^1\Sigma_u^+$ ,  $v' = v'' = 0$ ) has been summed over the 461-464 nm range, and the time-dependent measured intensity can be written as

$$I_{\text{G}_0\text{B}_0}^t = K_{\text{G}_0\text{B}_0} \cdot X_{\text{G}_0\text{B}_0}(T_e^t) \cdot n_e^t \cdot n_{\text{H}_2}^t. \quad (2.9)$$

Even if both emissions originate from electron impact excitation of ground state molecular hydrogen, their emission rate coefficients  $X$  have a different dependence on electron temperature as shown in Fig. 2.11 using the emission rate coefficients averaged over a Maxwellian electron energy distribution by Fantz [70]. This relative variation between these two transitions can be used for a qualitative check on the variation of the electron temperature during the time of observation.

As shown by Howling *et al* [73], the normalized emission spectra for both singlet and triplet transitions do not vary from ignition to steady-state, i.e. the shapes of the spectra in the Fulcher and  $\text{G}_0\text{B}_0$  ranges are invariant even if the total intensity varies, meaning that the choice of the wavelength limits for intensity integration is not a crucial point.

**Silane number density:** The  $\text{SiH}^*$  emission is assumed to be dominated by electron impact dissociation of  $\text{SiH}_4$ , which is correct for low pressures where powder formation is

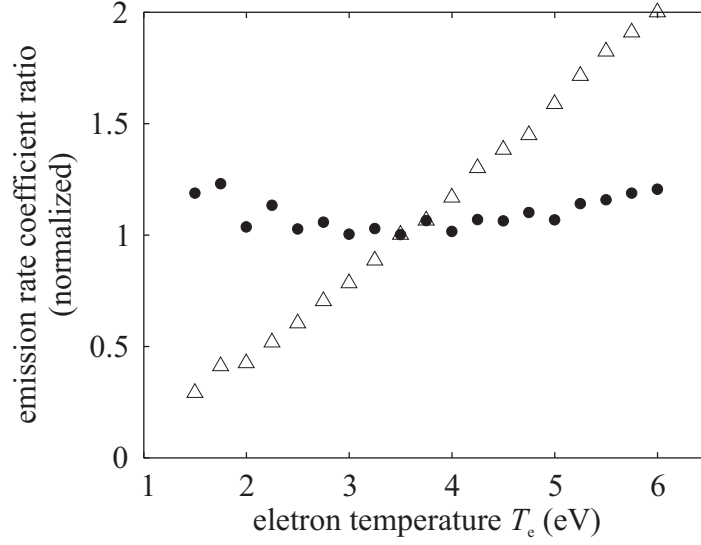


**Figure 2.11:** Variation of the emission rate coefficient ratio  $X_{G_0B_0}/X_{Ful}$  (△) and  $X_{SiH}/X_{Ful}$  (●) as a function of the electron temperature. The ratio are arbitrary normalized at 3.5 eV. Data are taken from Fantz [70].

avoided [74]. The contribution to the SiH\* intensity of electron impact dissociation of SiH<sub>x</sub> radicals ( $x = 1, 2, 3$ ) can be neglected because of their much lower density compared to SiH<sub>4</sub> in RF plasmas [20]. The SiH\* emission band is superposed with H<sub>2</sub>\* emission over the same wavelength range. This necessitates a H<sub>2</sub>\* background subtraction by removing the spectrum of a pure H<sub>2</sub> plasma with the same parameters (pressure, RF power, total flow rate) normalized to the intensity at 463 nm, standing next to the SiH\* peak (Fig. 2.10(b)). After background subtraction, the intensity has been integrated over the 409-423 nm range, giving the time-dependent SiH\* intensity

$$I_{SiH}^t = K_{SiH} \cdot X_{SiH}(T_e^t) \cdot n_e^t \cdot n_{SiH_4}^t. \quad (2.10)$$

The Si\* emission at 390.6 nm can also be analyzed in the same way, but its intensity is much lower compared to the one of SiH\* emission in RF plasmas, and so it is not reported here.

Note that the H<sub>2</sub>\* background subtraction does not eliminate the H<sub>α</sub> and H<sub>β</sub> lines. These is due to the fact that the  $H \leftrightarrow H_2$  chemical equilibrium does not depend on the H<sub>2</sub> dissociation rate alone. This will be treated in more detail in Section 5.6.

### Spectral analysis method

The measured emission intensities of silane,  $I_{SiH_4}^t$ , and molecular hydrogen,  $I_{Ful}^t$  and  $I_{G_0B_0}^t$ , have to be post-treated to obtain information about the silane density evolution from plasma ignition to steady-state [73]. First, the ratio  $I_{G_0B_0}^t/I_{Ful}^t$  has to be calculated to check if we can assume a constant  $X_{G_0B_0}/X_{Ful}$  ratio, respectively a constant electron temperature. Since this ratio is nearly constant as will be shown in Chapter 5, we can

assume that the ratio  $X_{\text{SiH}}/X_{\text{Ful}}$  also is constant, because of its even weaker  $T_e$  dependence than for the ratio  $X_{\text{G}_0\text{B}_0}/X_{\text{Ful}}$  as shown in Fig. 2.11. Furthermore, the effect of any time variation of the electron density is eliminated by dividing  $I_{\text{SiH}_4}^t$  (Eq. 2.10) by  $I_{\text{Ful}}^t$  (Eq. 2.8). Finally, this ratio,  $R^t$ , normalized to the initial value at plasma ignition, depends only on molecular number densities:

$$R^t = \frac{I_{\text{SiH}_4}^t}{I_{\text{Ful}}^t} / \frac{I_{\text{SiH}_4}^0}{I_{\text{Ful}}^0} = \frac{n_{\text{SiH}_4}^t}{n_{\text{H}_2}^t} / \frac{n_{\text{SiH}_4}^0}{n_{\text{H}_2}^0}. \quad (2.11)$$

Hence, all unknowns disappear by normalizing to the value at plasma ignition, and the remaining variables are known since  $n_{\text{SiH}_4}^0 + n_{\text{H}_2}^0 = n_{\text{tot}}^0 = p/(k_B T_{\text{gas}})$ , and  $c = n_{\text{SiH}_4}^0/n_{\text{tot}}^0$  is the initial concentration in the gas before ignition, assumed to be equal to the input flux ratio  $\Phi_{\text{SiH}_4}/\Phi_{\text{tot}}$ .

If the time-dependence of the total pressure is known, the silane and molecular hydrogen densities can be deduced from  $R^t$  (Eq. 2.11). Typically, if the pressure is assumed to be constant during plasma transient until steady-state and that radicals have a negligible participation to the total pressure ( $n_{\text{tot}}^t = n_{\text{H}_2}^t + n_{\text{SiH}_4}^t = n_{\text{H}_2}^0 + n_{\text{SiH}_4}^0 = n_{\text{tot}}^0$ ), the silane and hydrogen density time development are given by

$$n_{\text{SiH}_4}^t = \frac{n_{\text{SiH}_4}^0}{c + (1-c)/R^t} \quad \text{and} \quad n_{\text{H}_2}^t = \frac{n_{\text{H}_2}^0}{1/c + R^t/(1-c)}. \quad (2.12)$$

A value of the steady-state silane depletion fraction,  $D$ , can be then estimated for the limit case of  $t \rightarrow \infty$  using Eqs 2.6 and 2.12

$$D_{\text{OES}} = \frac{1 - R^\infty}{1 + \left(\frac{c}{1-c}\right) R^\infty}. \quad (2.13)$$

The time-development of the silane density given in Eq. 2.12 can be used to determine the relative time variation of the electron density by normalizing it to the initial value at ignition:

$$\frac{n_e^t}{n_e^0} = \frac{I_{\text{SiH}}^t}{n_{\text{SiH}_4}^t} \cdot \frac{n_{\text{SiH}_4}^0}{I_{\text{SiH}}^0} = \frac{I_{\text{SiH}}^t}{I_{\text{SiH}}^0} \cdot \left( c + \frac{1-c}{R^t} \right). \quad (2.14)$$

To summarize, time-resolved optical emission spectroscopy can be used to determine absolute values of  $n_{\text{SiH}_4}^t$  and  $n_{\text{H}_2}^t$ , and therefore the silane depletion fraction,  $D$ . Information on the relative variation of the electron density,  $n_e^t$ , and on qualitative behavior of the electron temperature,  $T_e^t$ , can also be measured using this simple and inexpensive technique. The only restrictions are that the emission has to be measured from the plasma ignition until steady-state is reached, and that the electron temperature has to remain stable within this interval.

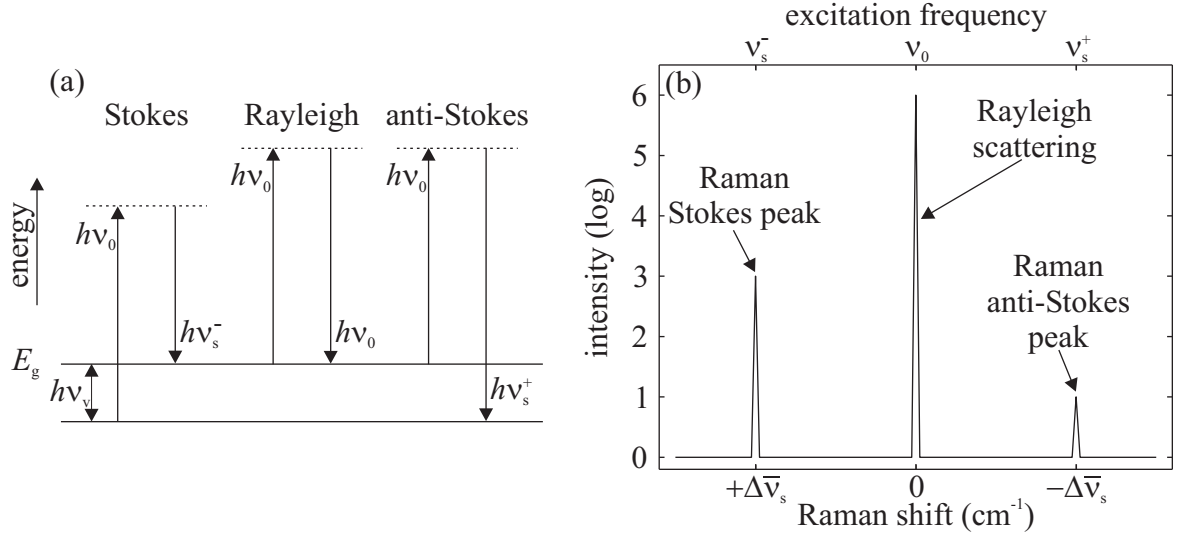


**Figure 2.12:** (a) Energy diagram of Stokes, Rayleigh and anti-Stokes transitions under the excitation of energy  $h\nu_0$ . (b) Schematic representation of a Raman spectrum with Stokes ( $\nu_s^-$ ), anti-Stokes ( $\nu_s^+$ ) peaks and Rayleigh elastic scattering ( $\nu_0$ ) peaks. Note that elastic collision (Rayleigh) probability is much higher than of inelastic collision (Raman).

## 2.3 Material characterization

### 2.3.1 Micro-Raman spectroscopy

Raman spectroscopy consists in the observation of inelastic scattering of an incident light beam by a media which could be a gas, a liquid or a solid. The Raman effect, first reported by Raman and Krishna in 1928 [75], has been used in this work to evaluate the degree of crystallinity of the deposited silicon layers.

Raman scattering differs from Rayleigh scattering which is related to elastic interactions between the incoming light and the sample. It can occur because of the Boltzman law which permits a small fraction of molecules to be in another energy state than in the ground state ( $E_g$ ). Hence, if radiation with a frequency  $\nu_0$  excites a molecule with an initial energy lower than  $E_g$  to a higher state than  $E_g$ , it may result in a radiation with a frequency  $\nu_s^-$ , associated with the energy  $h\nu_s^-$  released when the molecule transits from the excited state to the ground state, as sketched in Fig. 2.12(a). This phenomenon gives a Raman Stokes peak at a frequency  $\nu_s^-$  smaller than  $\nu_0$  presented in Fig. 2.12(b). The inverse phenomena may also occur as sketched in Fig. 2.12(a) but with a much lower probability and gives a small Raman anti-Stokes peak at a frequency  $\nu_s^+$  as shown in Fig. 2.12(b). These two frequencies ( $\nu_s^-$  and  $\nu_s^+$ ) are in perfect symmetry centered at the frequency of the initial excitation  $\nu_0$  due to Rayleigh scattering (see Figs. 2.12(a) and (b)). The much stronger intensity of the Rayleigh scattering is due to the Boltzman distribution of the initial energy state of the molecules forming the sample. Conventionally, Raman spectra are plotted as a function of the *Raman shift*, which is the shift from the

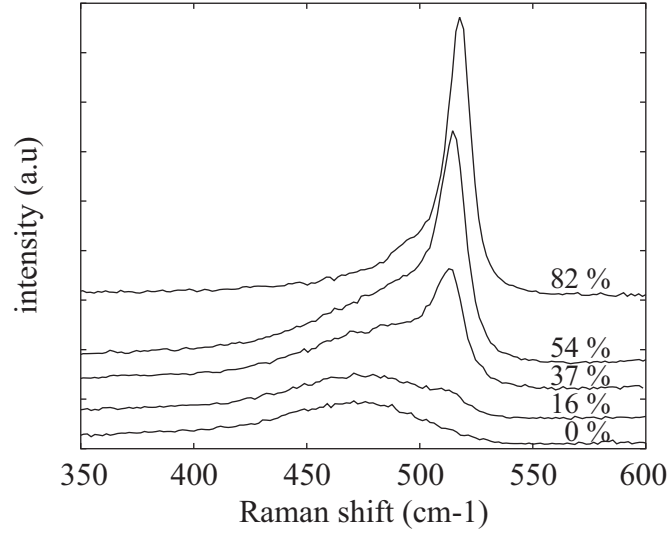


**Figure 2.13:** Raman spectra of films having crystalline fraction from 0 (bottom) to 82 % (top). Spectra are vertically displaced for clarity.

incident radiation wavenumber given by

$$\Delta\bar{\nu} = \bar{\nu}_0 - \bar{\nu}, \quad (2.15)$$

where  $\bar{\nu}_0$  and  $\bar{\nu}$  are the wavenumber in  $\text{cm}^{-1}$  associated to the frequencies of the incident radiation,  $\nu_0$ , and the output signal,  $\nu$ . The relation between the wavenumber  $\bar{\nu}$  and the frequency  $\nu$  is given by

$$\bar{\nu} = \frac{\nu}{c}, \quad (2.16)$$

where  $c = 2.998 \cdot 10^{10} \text{ cm} \cdot \text{s}^{-1}$  is the speed of light. This definition of the Raman shift (Eq. 2.15) implies that the shift of the Raman Stokes lines are positive and they are preferably plotted compared to anti-Stokes lines as shown in Fig. 2.13 because of their much higher ( $\sim \times 10^3$ ) intensity. Figure 2.12(a) shows that the choice of the incident radiation frequency,  $\nu_0$ , is very important, because it has to be higher than the frequency of the vibrational transition ( $\nu_v$ ) to allow Raman scattering to happen. Moreover,  $\nu_0$  has to be lower than the frequency of the electronic transition ( $\nu_e$ ). However, if  $\nu_0$  approaches  $\nu_e$ , the intensity of the Raman scattering is greatly improved by resonance. This effect is called *resonance Raman effect* [76].

As shown in Fig. 2.13, Raman spectroscopy is very well suited to study the phase transitions of hydrogenated-silicon and also of other chemical systems [77]. This sensitivity of Raman scattering on microstructural phase is due to the fact that the lattice vibration strongly depends on the microstructure. Hence, the Raman shift of silicon slides from a narrow peak at  $520 \text{ cm}^{-1}$  for a 82 % crystalline film (top of Fig. 2.13) to a wide peak at  $480 \text{ cm}^{-1}$  for fully amorphous silicon film (bottom of Fig. 2.13). In between stands microcrystalline silicon that contains both crystalline and amorphous phases.

However, even though Raman spectroscopy is a unique tool, it has not always been as user-friendly as today. Before 1986, it was confined to research laboratory dedicated to it,



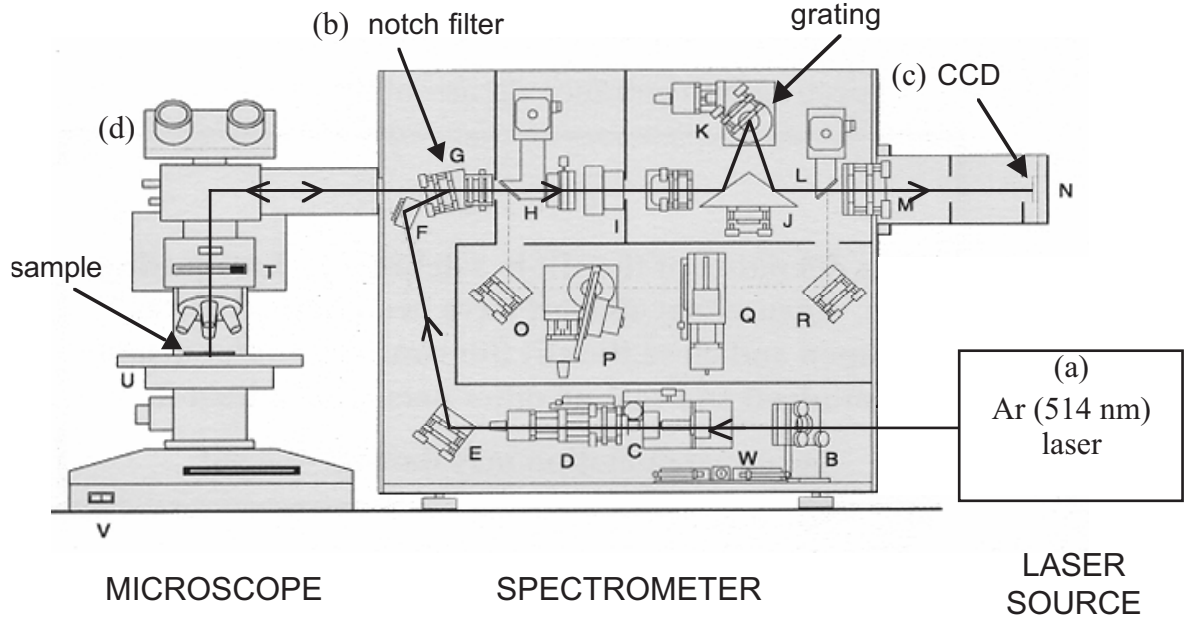


**Figure 2.14:** Micro-Raman spectrometer composed of an Ar laser source, a microscope, a notch filter, a grating and a CCD camera.

and only after several technical advances it became widely used [75]. These improvements are now all integrated in commercial "plug and play" Raman spectrometers as the one sketched in Fig. 2.14. Generally: (a) a compact laser source is much more practical and cheaper than before, (b) an efficient notch filters rejecting the very strong light from Rayleigh scattering, (c) a charged-coupled devices (CCD's) permitting multi-wavelength detection and great improvement of signal-to-noise ratio, and last but not least, personal computers (PC's) which are necessary to pilot CCD cameras and interferometers in a rapid way at low cost. Micro-Raman which consists in focusing the laser beam on the surface of the sample with an optical microscope (d) is generally used because it improves the output signal. Indeed, the Raman radiation is inversely proportional to the diameter of the laser beam at the sample [76]. In this work, the microscope magnification was  $50\times$  resulting in a 2 mm diameter laser spot. The Raman apparatus was a Renishaw RM serie with an Ar laser source (514 nm). Final spectra were obtained by summing 20 acquisitions with a single time of illumination of 1 s.

Spectra were fitted using three peaks with Gaussian shapes. Two peaks are associated with the silicon crystalline phase. The first one at  $518\pm 1\text{ cm}^{-1}$  ( $\text{FWHM} = 10\pm 1\text{ cm}^{-1}$ ) is due to defect-free crystallites and the second one at  $510\pm 5\text{ cm}^{-1}$  ( $\text{FWHM} = 26\pm 2\text{ cm}^{-1}$ ) is associated with crystallites which contain some structural defects. The peak associated with the amorphous silicon phase is centered at  $480\text{ cm}^{-1}$  ( $\text{FWHM} = 53\pm 7\text{ cm}^{-1}$ ) [78].

In this work, the Raman crystallinity is defined as

$$\phi_c = \frac{A_{518} + A_{510}}{A_{518} + A_{510} + A_{480}}, \quad (2.17)$$

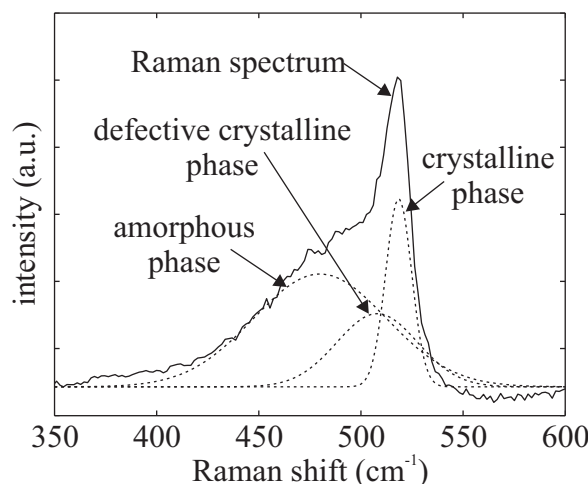


**Figure 2.15:** Gaussian fitting of a Raman spectrum with three peaks centered at 480, 510 and 518  $\text{cm}^{-1}$  associated with amorphous, defective crystalline and crystalline silicon phases, respectively. The sample presented here has a Raman crystallinity of 42 %.

where  $A_j$  is the area of the peak centered at  $j \text{ cm}^{-1}$ . This generally accepted [78, 79] definition gives a rough estimation of the real crystallinity, which is sufficient for the purpose of this work. Further details on Raman crystallinity versus real crystallinity can be found in the literature [78, 80].

### 2.3.2 Infrared spectroscopy

As mentioned previously, infrared (IR) spectroscopy can be used to determine the chemical bonds within the thin films. The experimental and theoretical principles are exactly the same as for gaseous samples described in Section 2.2.2. The only difference is that the sample placed between the interferometer and the IR detector is now solid instead of gaseous. In this work, IR absorption spectroscopy has been used to evaluate the microstructure parameter of the deposited films.

For this characterization, sample preparation is a crucial point and particular care has to be taken. To improve the absorption, the films have to have a thickness in the 1.5 - 2  $\mu\text{m}$  range leading often to film peeling, because of the high internal stresses in the film which breaks the weak film/substrate interface, especially for material deposited near the amorphous to microcrystalline silicon transition [81]. The substrates were double-sided polished crystalline Si wafer (p-doped, 300  $\mu\text{m}$  thick) instead of common glass, because this latter fully absorbs light in the IR range. The wafers were cut and cleaned in ultrasonic baths with alkaline and acidic solutions. A 50 nm thick adhesion layer of silicon carbide (SiC) was deposited ( $\text{SiH}_4/\text{CH}_4/\text{H}_2=20/40/500 \text{ sccm}$ ,  $p = 0.4 \text{ mbar}$ ,  $P_{\text{RF}} = 200 \text{ W}$ ) by PECVD just before the Si:H layer deposition in the same reactor. IR spectra were acquired as soon as the Si:H layers were deposited. This precaution was taken to avoid IR absorption modification due to oxygen absorption during exposure to ambient [82]. Spectra were acquired with a Bruker Equinox 55 FTIR spectrometer from 400 to 4000

$\text{cm}^{-1}$ . A background subtraction was performed in order to eliminate the absorption of the c-Si substrate. The sample used for background subtraction was always a piece of the same c-Si wafer as the one on which the Si:H film of interest was deposited in order to be independent of possible variation in thickness between different wafers. To improve the signal-to-noise ratio, background and sample spectra were averaged over 200 acquisitions. The resolution was  $8 \text{ cm}^{-1}$  to avoid interference fringes due to the film/substrate interface.

The microstructure parameter  $\hat{R}$  [83] was defined as

$$\hat{R} = \frac{A_{2080}}{A_{2000} + A_{2080}}, \quad (2.18)$$

where  $A_j$  is the area of the Gaussian peak centered at  $j \text{ cm}^{-1}$ . The absorption at  $2080 \text{ cm}^{-1}$  is due to the stretching vibration of the Si-H bond when the silicon atom is bonded to two hydrogen atoms ( $\text{SiH}_2$ ). The absorption at  $2000 \text{ cm}^{-1}$  is due to the stretching vibration of the same Si-H bond, but when the silicon atom is bonded to only one hydrogen atom ( $\text{SiH}$ ) [84]. The  $\text{SiH}_2$  configuration is located in majority on internal surfaces. On the other hand, single hydrogen bonded Si atoms are located in the bulk of the Si:H film. In hydrogenated microcrystalline silicon,  $\text{SiH}_2$  can be found at grain boundaries which are taken as internal surfaces. Hence, the interpretation of the microstructure parameter  $R$  (note the absence of  $\hat{\phantom{R}}$ ) commonly used for hydrogenated amorphous silicon is not valid in the case of microcrystalline silicon. The microstructure parameter  $\hat{R}$  for  $\mu\text{c-Si:H}$  cannot be associated with the porosity of the film as in the case of a-Si:H.  $\hat{R}$  gives an indication of the preferential location of hydrogen in the film: In bulk silicon or on internal surfaces, i.e. micro-voids *or* grain boundaries [81].

### 2.3.3 Film thickness

The thickness of the deposited films was characterized by using different techniques. First of all, alpha-step was used to determine precisely the thickness of single layers, but this technique is inadequate when one needs to characterize film thickness over large areas. For such a purpose, optical interference techniques were used. These are based on light interference with a film deposited on a substrate. The resulting light intensity after having interfered with the film depends on the optical properties of both the film and substrate, but also on the film thickness and the light wavelength. This can be used in two different ways: (i) Film thickness imaging or (ii) film thickness measurement which are described briefly in this section.

Film thickness imaging by white light interferometry has been performed exclusively by transmission through films deposited on glass substrates. First, the intensity of the incident white light source was homogenized by using diffusors between the source and the transparent substrate as shown in Fig. 2.16(a). The transmitted light was then filtered by a interference filter at  $707 \text{ nm}$ , and the resulting two-dimensional picture (Fig. 2.16(b)) was then acquired by a CCD camera. The interference picture presents dark zones and bright zones corresponding, respectively, to destructive and constructive interferences which depend on the film thickness. Therefore, the interference pattern represents the film uniformity over the substrate area, and the thickness difference between consecutive

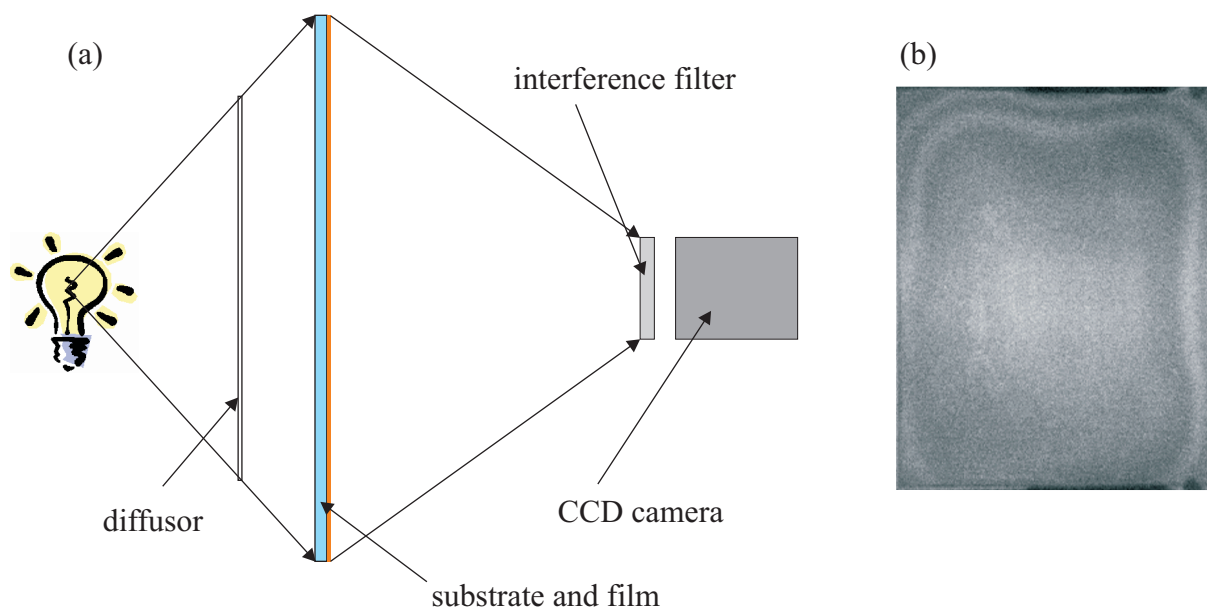


**Figure 2.16:** (a) White light transmission interferometry arrangement and (b) resulting interferometry pattern with destructive (dark zone) and constructive (bright zone) interferences.

destructive and constructive interferences corresponds to about 45 nm for the interference filter used.

However, this technique does not provide any information about the gradient of the film thickness, and to determine if the film thickness increases or decreases from a dark

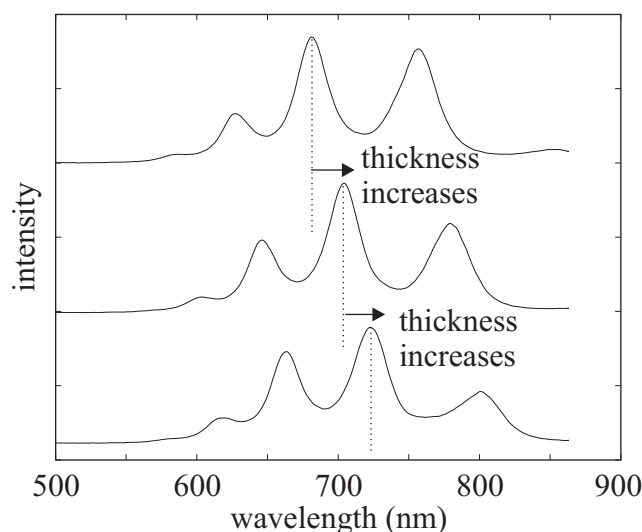


**Figure 2.17:** reflection spectra of a  $\mu\text{c-Si:H}$  film on a glass substrate. When the light collection head is moved to a zone where the film is thicker, the spectra shifts to higher wavelength. The spectra are vertically displaced for clarity.

zone to a bright zone, we have to make a local measurement of the transmitted light. To perform this, the transmitted light is collected by an optical fiber without using an interference filter, and the light is then sent to a spectrometer. The resulting spectrum presents maxima and minima as a function of the wavelength corresponding, respectively, to constructive and destructive interferences as shown in Fig. 2.17. If the head of the optical fiber is now moved, the spectrum is shifted to higher wavelengths if the film thickness increases, and to lower wavelengths if the film thickness decreases as shown in Fig. 2.17. Hence, the two-dimensional film profile over the whole substrate can be obtained by combining these two techniques.

The same technique can be used by reflectance instead of transmittance to estimate the film thickness when it is deposited on an opaque substrate. The only difference is that the incident light comes from the same side of the film as it is collected after having interfered with the film. The resulting spectra can be simulated by adjusting the film thickness  $d_{\text{film}}$  in the expression [85]

$$I_{\text{refl}} = \left| \frac{r_{\text{af}} + r_{\text{fs}}\varphi^2}{1 - r_{\text{fa}}r_{\text{fs}}\varphi^2} \right|^2, \quad (2.19)$$

where  $\varphi = \exp(j\omega n_{\text{f}}d_{\text{film}}/c)$ ,  $r_{ik} = (n_i - n_k)/(n_i + n_k)$  and  $n_{\text{a}}$ ,  $n_{\text{f}}$  and  $n_{\text{s}}$  are the refraction index of the ambient, the film and the substrate, respectively.



## Chapter 3

# Plasma composition as the relevant plasma parameter

The introduction to microcrystalline silicon deposition in Chapter 1 has shown that optimal deposition is difficult to achieve, since high deposition rate, optimal material quality and good uniformity over the substrate have to be combined. This difficulty is due to the fact that the transition zone from a-Si:H to  $\mu$ c-Si:H cannot be simply defined as a function of the deposition process parameters (pressure, RF power, excitation frequency, flow rates, interelectrode distance and substrate temperature) because of their inter-dependence on the plasma physical properties and chemistry [86]. For example, high dilution of silane with hydrogen is a well-known technique to reach the transition zone, however, depending on the different deposition process parameters and on the reactor configuration, the phase transition can occur between silane input concentration as low as 3 % [87] and as high as 10 % [88] and covers the whole intermediate concentration range [48, 38, 89, 90]. Franz *et al* [56] have shown that using a low energy plasma (LEP) DC source it was possible to deposit  $\mu$ c-Si:H from pure silane at 10 nm/s and recently, van den Donker *et al* [91] have even shown that good  $\mu$ c-Si:H at reasonable deposition rate (4 Å/s) can be deposited with RF PECVD from pure silane input flow. Nowadays, most of the  $\mu$ c-Si:H PECVD optimization has essentially been done by empirical parameter studies, due to the difficulty of applying relevant and simple plasma diagnostics in real deposition conditions. In parallel, self-consistent numerical plasma models including a large number of species (up to 50 [92]) and chemical reactions (up to 224 [92]) have been developed in order to achieve the closest simulation of the complex phenomena occurring in the plasma [55, 92, 93, 94, 95]. However, they are not systematically used, since such models remain very complicated to use, validate and interpret, and are very time consuming, so that they require dedicated plasma modeling specialists. Taking this into account, there is therefore a need to develop a simple methodological approach based on simple plasma measurements in order to better understand the behavior of the transition zone from a-Si:H to  $\mu$ c-Si:H as a function of the deposition parameters. The aim of this chapter is to show that the measurement of the silane concentration in the plasma can be used for such a purpose.

### 3.1 Crystallinity & plasma composition

The Raman crystallinity of samples,  $\phi_c$ , silane input concentration,  $c$ , and silane concentration in the plasma,  $c_p$ , were systematically measured using the techniques detailed in Chapter 2 for a large number of different plasma process parameters within the following ranges:

- silane concentration,  $c$ , from 0.7 to 10 %
- RF power,  $P_{\text{RF}}$ , from 250 to 2000 W
- pressure,  $p$ , from 0.75 to 10 mbar
- total flow rate,  $F_{\text{tot}}$ , from 2000 to 5000 sccm
- interelectrode distance from 11 to 25 mm

Only the substrate type (3 mm thick conventional glass), the substrate temperature (230 °C) and the excitation frequency (40.68 MHz) were kept constant. The only restriction imposed on the combination of the different process parameters was that the plasma should be in powder-free conditions, as far as could be judged by the absence of powder visible in a HeNe laser beam ( $\lambda = 632.8$  nm) in the pumping line just behind the pumping grid (see Fig. 2.6). The deposition rate during this parameter scan was between 1 and 20 Å/s for both a-Si:H and  $\mu$ c-Si:H sample types.

The Raman crystallinity of samples deposited with all the different experimental parameters plotted as a function of the silane input concentration  $c = p_{\text{SiH}_4}^0/p$  in Fig. 3.1(a) shows that the silane concentration alone does not determine the material crystallinity if the other plasma process parameters are not held constant, as performed in many works [48, 87, 88, 38, 89, 90]. It results in a mix of amorphous ( $\circ$ ,  $\phi_c < 50$  %) and microcrystalline ( $\blacktriangle$ ,  $\phi_c > 50$  %) layers over the whole silane concentration range from 0.7 to 10 % in Fig. 3.1(a). A similar dispersion of the Raman crystallinity is also observed if the results are plotted as a function of any other plasma process parameter (RF power, pressure, total gas flow or interelectrode distance) as shown in Figs. 3.1(b)-(e). This is due to the inter-relation between the different plasma process parameters and their effects on the transition zone from a-Si:H to  $\mu$ c-Si:H. A clear transition from a-Si:H to  $\mu$ c-Si:H can only be observed as a function of one of the plasma process parameters if all the others are held constant [48, 87, 88, 38, 89, 90]. On the other hand, if the same crystallinity results are plotted as a function of the measured silane concentration *in the plasma*,  $c_p$ , (Fig. 3.2), they are arranged into three distinct regions. A microstructure transition zone ( $\blacksquare$ ) separates a zone of highly crystalline material ( $\blacktriangle$ ,  $\phi_c > 50$  %) for  $c_p < 0.5$  %, from a zone of amorphous material ( $\circ$ ,  $\phi_c \approx 0$  %) for  $c_p > 1.2$  %. The material deposited in the transition zone ( $0.5\% < c_p < 1.2\%$ ) has a range of crystalline fraction from 0 to 75 %. In fact, the silane concentration in the plasma appears to account for the combined effect of all the plasma process parameters (silane input concentration, input power, pressure, total flow rate, interelectrode distance and excitation frequency) on the film crystallinity.

In our case of a large area reactor with uniform gas showerhead, the silane concentration in the plasma,  $c_p$ , can be expressed as a function of the silane input concentration,  $c$ ,



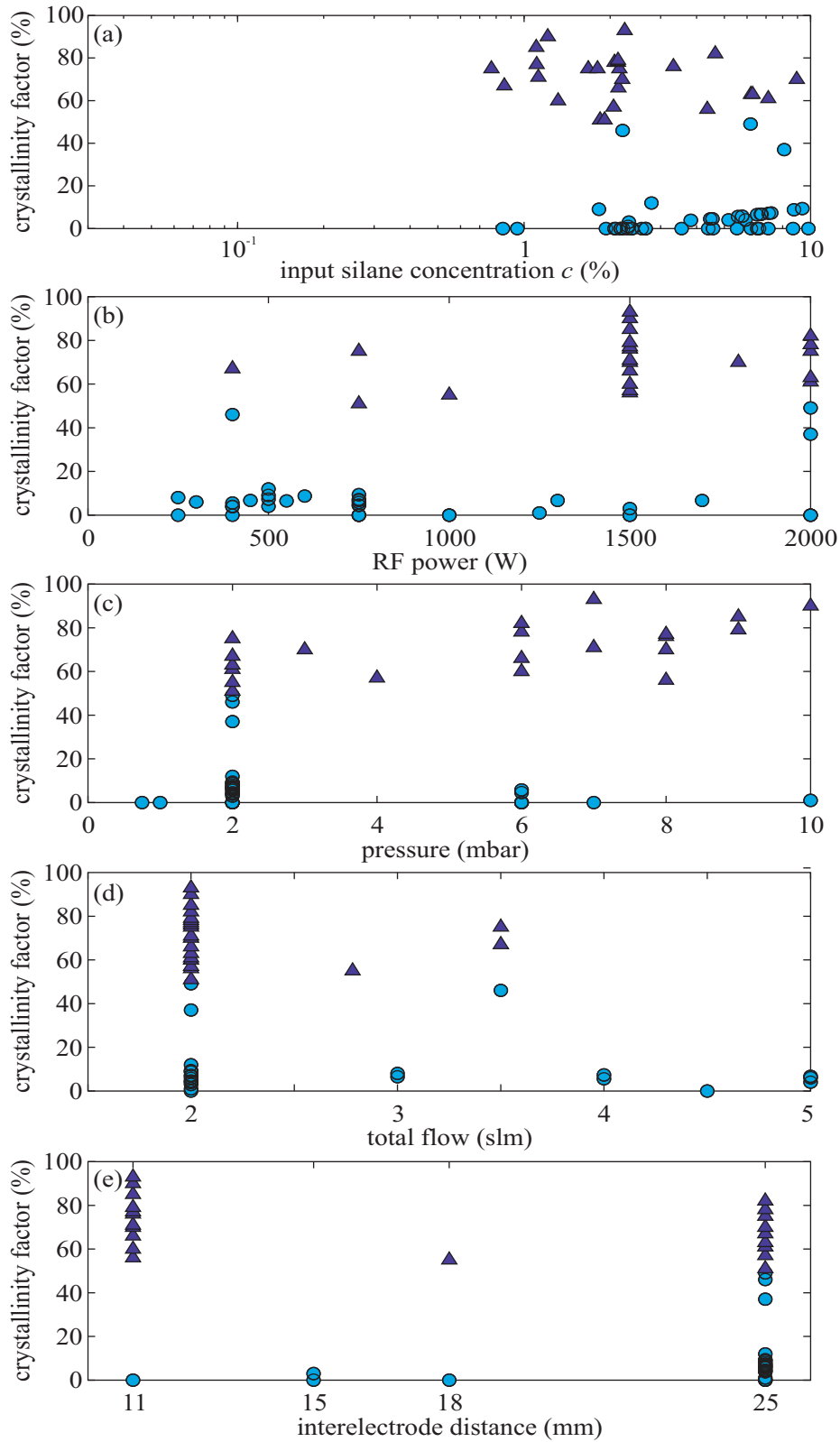


**Figure 3.1:** Plot of the Raman crystallinity of samples deposited with various parameters as a function of (a) the silane input concentration, (b) the RF power, (c) the pressure, (d) the total flow and (e) the inter-electrode distance.  $\blacktriangle$  correspond to samples with a Raman crystallinity higher than 50 %, and  $\circ$  to samples with  $\phi_c < 50$  %.

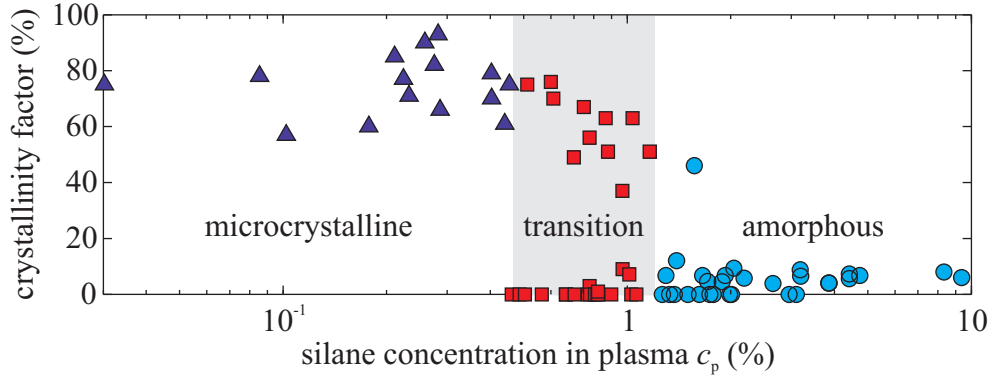


**Figure 3.2:** Plot of the Raman crystallinity of samples deposited with various parameters (see Fig. 3.1) as a function of the silane concentration *in the plasma*. The material microstructure is then separated into three well defined zones: Microcrystalline, transitional and amorphous.

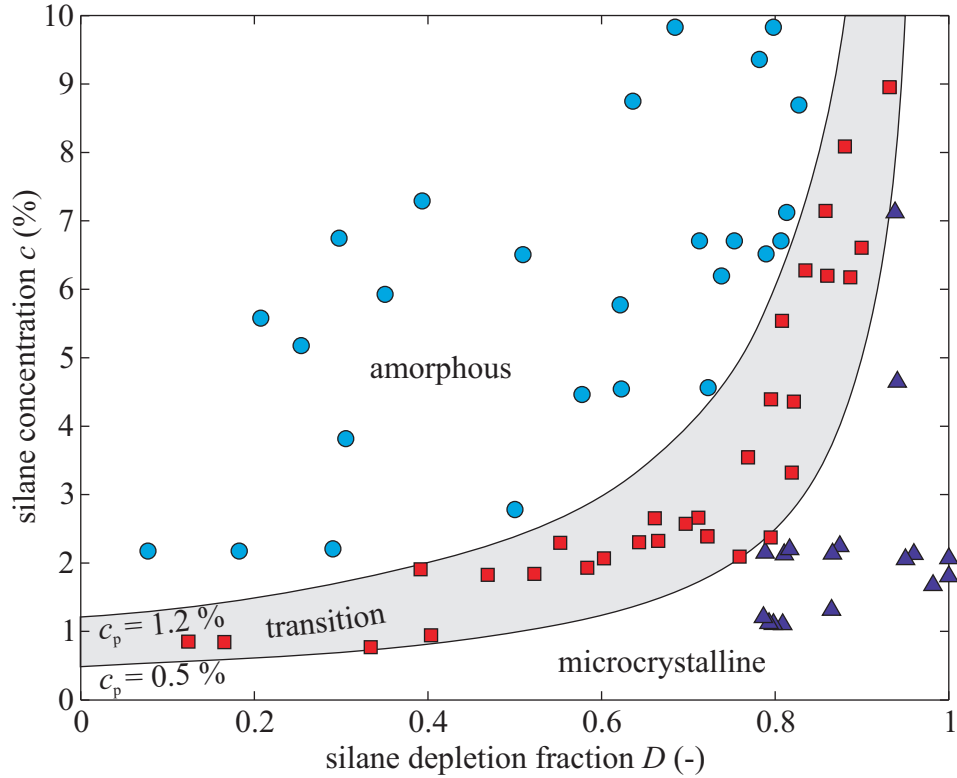


**Figure 3.3:** Plot of the transition zone (shaded) and experimental data as a function of the silane depletion fraction,  $D$ , and the silane input concentration,  $c$ . Experimental data of  $\mu$ c-Si:H ( $\blacktriangle$ ) and a-Si:H ( $\circ$ ) have been used to define the transition zone ( $\blacksquare$ ) between the amorphous and microcrystalline deposition regions. This transition zone is only valid for the substrate temperature used ( $T_s = 230$  °C).

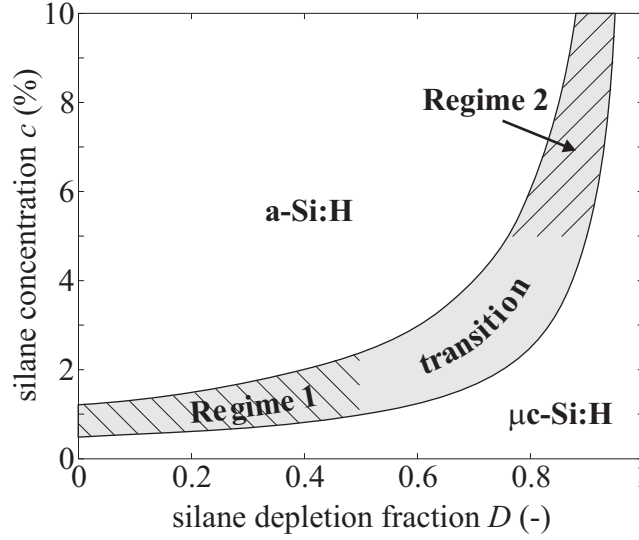


**Figure 3.4:** The transition zone can be roughly separated into two regimes. One at low silane concentration and depletion (Regime 1) where the microstructure is governed by the silane concentration, and another at high silane concentration and depletion (Regime 2) where the microstructure is governed by the depletion fraction.

and the silane depletion,  $D$ , through Eq. 2.7,  $c_p = c(1 - D)$ . This dependence on two parameters ( $c$  and  $D$ ) can be used to transform Fig. 3.2 into Fig. 3.3 which is a two-dimensional representation of the three regions separated by contours of constant silane concentration in the plasma,  $c_p = 0.5$  % and  $c_p = 1.2$  %. This two-dimensional representation may be more convenient for understanding the effect of the different plasma process parameters on the transition zone, because  $c$  is directly the initial gas composition, and the behavior of  $D$  as a function of the other process parameters can be estimated from simple arguments: In general,  $D$  should increase if either the dissociation rate or the gas residence time are increased (see Sec. 3.4). These results have implications for solar cell technology because solar cells made with silicon films produced at the boundary between the two microstructures (amorphous and microcrystalline) show the best performances [39, 40, 96, 97]. Thus, the transition zone in Fig. 3.4 represents the optimum plasma process window for producing  $\mu c$ -Si:H layers for high performance solar cells. Furthermore, the transition zone can be roughly separated into two different regimes: Regime 1 at low input concentration of silane ( $c < 2.5$  %) and low depletion ( $D < 0.5$ ), where the film microstructure is governed by the low silane input concentration, i.e. the crystallinity is dependent strongly on  $c$  and weakly on  $D$  (see Fig. 3.4); and Regime 2 at high silane input concentration ( $c > 5$  %) and high depletion ( $D > 0.8$ ), where the film microstructure is governed by the high depletion fraction, i.e. the crystallinity is strongly dependent on  $D$  and weakly on  $c$  (see Fig. 3.4). These regimes correspond to experimental observations in the literature, where  $\mu c$ -Si:H can be deposited with low RF power density and low silane concentration (Regime 1) [98, 99], or with high RF power density and high silane concentration (Regime 2) [48, 56, 78, 96, 100]. This means that there is no unique silane input concentration

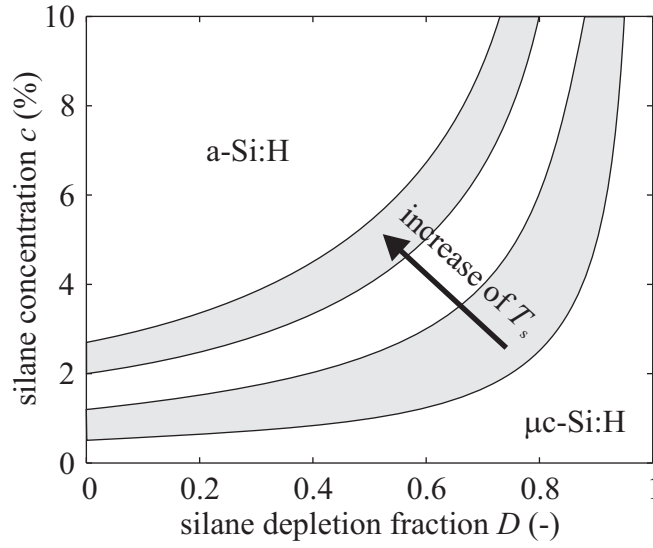


**Figure 3.5:** Shift of the microstructure transition zone to higher value of  $c_p$  for an increase of the substrate temperature.

which defines the a-Si:H to  $\mu$ c-Si:H transition, because the effective concentration in the plasma itself depends both on the input silane concentration and on the level of silane depletion. The common link between the two regimes is that the silane concentration in the plasma is the same.

A factor which does not depend on the plasma parameters is the substrate temperature,  $T_s$ . Indeed, high  $T_s$  is favorable for  $\mu$ c-Si:H deposition [89] and in the extreme case a-Si:H can be annealed by thermal treatment ( $T_s > 600$  °C) to obtain a crystalline structure [101]. Even below the annealing temperature,  $T_s$  plays an important role in supplying vibrational energy to the a-Si:H structure and as a consequence the need for supplementary energy - supplied by chemical annealing - necessary to crystallize the film is reduced when  $T_s$  is increased. Hence, the transition contour values of  $c_p$  have to be re-calibrated if the deposition temperature  $T_s$  is changed. For example, increasing  $T_s$  will shift the transition region to higher values of  $c_p$  as sketched in Fig. 3.5.

The position of the transition region from a-Si:H to  $\mu$ c-Si:H may also be affected by the type of substrate on which the films are deposited, since some materials are more favorable to nucleation of crystallites than others [102, 103, 104], hence varying the thickness of the amorphous incubation layer. As shown in Fig. 3.6, the crystallinity depends on the thickness of the deposited layer, because of the already-mentioned incubation layer and of the conical shape of the crystallites. In our case, to avoid such effects, the depositions were always performed on 3 mm glass substrates with a minimum approximate thickness of 200 nm.

The crystallinity is not the only property of the deposited silicon films which is influenced by the plasma composition. As shown in Fig. 3.7, the microstructure parameter of the film depends on the plasma silane concentration. Hence, the lower the silane plasma concentration, the higher the microstructure parameter. This translate the fact that the

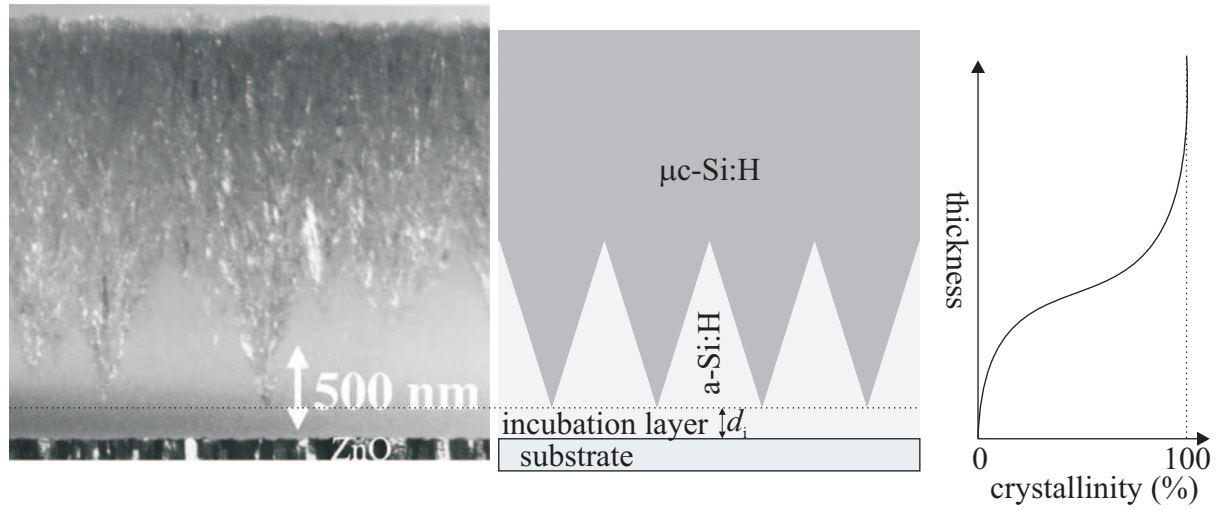


**Figure 3.6:** Crystallinity evolution as a function of the film thickness due to the amorphous incubation layer and the conical shape of the crystallites. TEM picture from Ref. [38].

hydrogen contained in the film takes place in the bulk when the material is amorphous at high  $c_p$  and at the grain boundaries, which is an internal surface, when the material is microcrystalline at low  $c_p$ . In fact, this variation of the microstructure parameter with the plasma composition is related to the variation of the film crystallinity. Therefore, any physical, chemical or mechanical property of the film which is influenced by the crystalline fraction of the layer such as the electrical properties [78, 90, 105, 106] will be determined by the plasma composition.

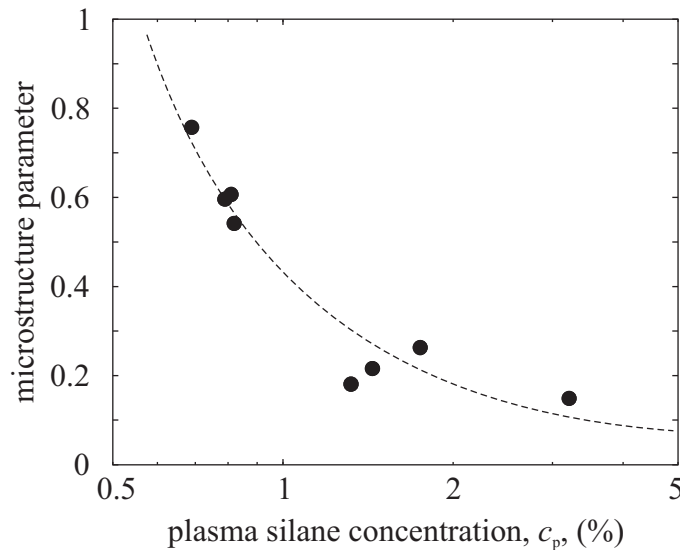


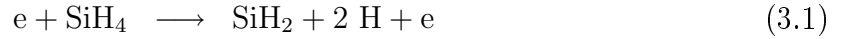
**Figure 3.7:** Microstructure parameter determined by IR absorption as a function of the plasma silane concentration. The dashed line is to guide the eye.

## 3.2 Analytical plasma chemistry model

### 3.2.1 Model I: The simplest

In this section, we develop a plasma chemistry model in order to investigate why the silane concentration in the plasma,  $c_p$ , appears to determine the film crystallinity. It is based on a set of important reactions taking place in silane-hydrogen discharges using the approach in Ref. [19] described in Section 1.4. The model is zero-dimensional (no spatial dependence), since each species density is laterally everywhere the same in an ideal uniform showerhead reactor [60] and the species densities are average over the interelectrode gap. We assume that the radical densities are much smaller than the silane and hydrogen gas densities in the plasma [20, 32] because their reactions with the surfaces, and also that the gas phase radical reactions (hydrogen abstraction, silane polymerization, etc.) are dominated by electron impact dissociation and surface reactions. This latter condition limits the validity of this simple model to low pressure. Due to the low degree of ionization in capacitively coupled plasmas, we assume that the contribution of the ionic species to the film growth can be neglected compared to the contribution of the neutral species.

For simplicity, this model considers only hydrogen molecules, hydrogen atoms, silane molecules, and one type of silane radical,  $\text{SiH}_2$ . Here, the radical  $\text{SiH}_2$  represents the sum of the radicals  $\text{SiH}_x$  ( $x = 0 \rightarrow 3$ ) from the different channels of silane electron impact dissociation. In Section 3.2.2, the effect of other silane radicals, ions, and several dissociation channels is considered. Dissociation of both  $\text{SiH}_4$  and  $\text{H}_2$  is driven by electron impact (Eqs. 3.1 and 3.2) with rate constants  $k$  and  $k_H$ , respectively:



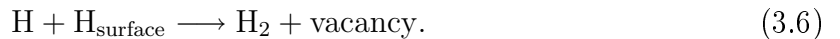
The interactions between the plasma and the reactor surfaces are represented by (i) deposition of silicon radicals  $\text{SiH}_2$  with release of  $\text{H}_2$  (Eq. 3.3), and (ii) hydrogen recombination on the surface (Eq. 3.4) having surface reaction rates  $S$  and  $R^{\text{I1}}$ , respectively:



Here, Eq. 3.4 for the hydrogen surface recombination represents the two step recombination which can be described as



and



Following the same reasoning, silicon deposition (reaction 3.3) is the sum of the  $\text{SiH}_2$  sticking onto the surface and H surface recombination. The steady-state equilibrium

---

<sup>1</sup>The superscript (I) refers to the model I.

which conserves the overall stoichiometry of all chemical species in the plasma gives the following equations:

$$\text{SiH}_4 : \quad \Phi_{\text{SiH}_4} - (kn_e + a_{\text{SiH}_4})n_{\text{SiH}_4} = 0 \quad (3.7)$$

$$\text{SiH}_2 : \quad kn_en_{\text{SiH}_4} - Sn_{\text{SiH}_2} = 0 \quad (3.8)$$

$$\text{H}_2 : \quad \Phi_{\text{H}_2} + 1/2 R^{\text{I}}n_{\text{H}} + Sn_{\text{SiH}_2} - (k_{\text{H}}n_e + a_{\text{H}_2})n_{\text{H}_2} = 0 \quad (3.9)$$

$$\text{H} : \quad 2kn_en_{\text{SiH}_4} + 2k_{\text{H}}n_en_{\text{H}_2} - R^{\text{I}}n_{\text{H}} = 0, \quad (3.10)$$

where  $a_{\text{SiH}_4}$  and  $a_{\text{H}_2}$  are the inverse of the gas (silane and hydrogen, respectively) effective residence times in  $\text{s}^{-1}$ , i.e. the effective pumping speed which is independent of position in the case of a uniform showerhead [60],  $n_j$  is the density of the  $j$  specie in  $\text{molecules}\cdot\text{m}^{-3}$  and  $\Phi_{\text{H}_2}$  and  $\Phi_{\text{SiH}_4}$  are the input molecular flow rates per unit of volume of  $\text{H}_2$  and  $\text{SiH}_4$ , respectively, in  $\text{molecules}\cdot\text{m}^{-3}\cdot\text{s}^{-1}$ . Assuming that no radicals (neither of silane nor hydrogen) leave the reactor because of their high reaction probability with the reactor walls, the pumping terms  $a_{\text{SiH}_2}$  and  $a_{\text{H}}$  have been neglected compared to  $S$  and  $R^{\text{I}}$ , respectively, in Eqs. 3.8 and 3.10. In this equation system,  $\Gamma_{\text{SiH}_2} = Sn_{\text{SiH}_2}$  is the rate of film growth per unit volume of plasma in  $\text{radicals}\cdot\text{m}^{-3}\cdot\text{s}^{-1}$ , and  $\Gamma_{\text{H}} = R^{\text{I}}n_{\text{H}}$  is the rate of H surface recombination per unit of volume of plasma on the film surface in  $\text{atoms}\cdot\text{m}^{-3}\cdot\text{s}^{-1}$ . By this definition,  $S$  and  $R^{\text{I}}$  are the inverse confinement times for loss of silane radicals by deposition, and hydrogen atoms by surface recombination, respectively. These rates can be expressed as a function of the neutral species density in the plasma using Eqs. 3.8 and 3.10 only:

$$\Gamma_{\text{SiH}_2} = Sn_{\text{SiH}_2} = kn_en_{\text{SiH}_4} \quad (3.11)$$

$$\Gamma_{\text{H}} = R^{\text{I}}n_{\text{H}} = 2k_{\text{H}}n_en_{\text{H}_2} + 2kn_en_{\text{SiH}_4}. \quad (3.12)$$

We have seen in Chapter 1 that a relevant factor for  $\mu\text{c-Si:H}$  deposition is the atomic hydrogen to silane radical flux ratio towards the growing film surface

$$\frac{\Gamma_{\text{H}}}{\Gamma_{\text{SiH}_2}} = 2\kappa \frac{n_{\text{H}_2}}{n_{\text{SiH}_4}} + 2, \quad (3.13)$$

where  $\kappa = k_{\text{H}}/k$  is the ratio of the hydrogen and silane electron impact dissociation rate constants. This ratio is independent of the pumping speeds  $a_{\text{SiH}_4}$  and  $a_{\text{H}_2}$ . In principle,  $\kappa$  is a function of electron temperature  $T_e$ , but since the dissociation of hydrogen and silane by electron impact have almost the same energy threshold, the dependence on  $T_e$  remains relatively weak. Using the definition of the silane concentration in the plasma  $c_{\text{p}} = p_{\text{SiH}_4}/(p_{\text{SiH}_4} + p_{\text{H}_2})$  (Eq. 2.5) and the perfect gas law ( $p = nk_{\text{B}}T$ , where  $n$  is the total number density), Eq. 3.13 can be rearranged giving:

$$\frac{\Gamma_{\text{H}}}{\Gamma_{\text{SiH}_2}} = 2\kappa \left( \frac{1}{c_{\text{p}}} - 1 \right) + 2, \quad (3.14)$$

Therefore, Eq. 3.14 shows that the silane concentration in the plasma,  $c_{\text{p}}$ , determines the flux ratio of hydrogen atoms and silicon radicals to the growing film surface. This

shows why the film crystallinity is a function of  $c_p$  in Fig. 3.2 and why contours of iso- $c_p$  delimit the zones of a-Si:H and  $\mu$ c-Si:H deposition in Fig. 3.3.

As stated above, this model should be valid only at low pressure where the radical gas phase reactions can be neglected. Giving an upper limit for the pressure is difficult because of the different types of radical gas phase reactions. However, this model is still useful as it gives the phenomenological basis to understand why  $c_p$  plays a dominant role in the determination of the film crystallinity. From the experimental results, no strong effect of the pressure on the position of the transition zone as a function of  $c_p$  was observed. This may be because the process parameter space was restricted to conditions where no powder was observed in the pumping line. Since the presence of powder is certainly a sign of strong polymerization reactions, this condition may have fortuitously restricted the process conditions to where the model remains essentially valid. The effect of pressure on polymerization processes and on the model is discussed further in Sec. 3.2.2 and in Chapter 6.

Another plasma characteristic that is not taken into account here is the ion bombardment energy at the substrate. Even if the ion flux to the surface remains lower than the neutral flux, ions can influence the film growth through their high bombardment energy at the substrate. Indeed, very energetic ions ( $> 20$  eV) can sputter the deposited layer or at least amorphize a crystalline structure [107]. On the other hand, ions with low energy ( $< 20$  eV) can help to crystallize a structure [107, 108]. Thus, increasing the excitation frequency - which reduces the sheath voltage and therefore the maximum ion energy for a given plasma power [109] - is favorable to improve the crystallinity, but amorphization by high energy ions can be a limiting factor to high power  $\mu$ c-Si:H deposition.

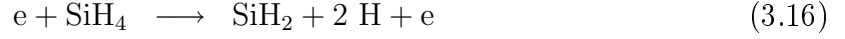
To summarize the results of this simple model, together with the experimental results of Fig. 3.2, we have shown that the silane concentration in the plasma,  $c_p$ , appears to be the main parameter which determines the flux ratio of hydrogen atoms and silicon radicals to the growing film surface, and that this flux ratio is determinant for the crystallinity of the film. In particular, for very low values of  $c_p$  ( $c_p < 0.5$  %), this flux ratio is always sufficiently high to ensure that the growing film is always microcrystalline, and on the other hand, for high values of  $c_p$  ( $c_p > 1.2$  %), this flux ratio is always sufficiently low so that the growing film is always amorphous. In the transition zone ( $0.5$  %  $< c_p < 1.2$  %), the film crystallinity is not uniquely determined by the value of  $c_p$ , leading to films having crystallinity as high as 75 % and as low as 0 %. This may be due to the fact that in this transition zone, other effects such as secondary radical gas phase reactions or ion energy bombardment to the surface may also play a role in determining the film microstructure. Understanding such effects in the transition zone would require the use of more complicated plasma and chemistry models.

### 3.2.2 Towards more realistic chemical models

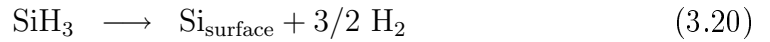
#### Model II: Analytical model development

The simple plasma chemistry model in Section 3.2.1 can further be generalized by considering other electron impact dissociation channels with dissociation rate constants  $k_1$ ,  $k_2$ ,  $k_3$  and  $k_H$  for reactions 3.15 - 3.18, respectively:





The interactions between the plasma and the walls of the reactor (including the substrate) are assumed to be (i) deposition of silicon radicals  $\text{SiH}_2$  and  $\text{SiH}_3$  (Eqs. 3.19 and 3.20), (ii) etching by H atoms (Eq. 3.21) and (iii) hydrogen recombination on the surface (Eq. 3.22) having reaction rates  $S_1$ ,  $S_2$ ,  $G$  and  $R^{\text{II}2}$ , respectively, which conserve overall stoichiometry assuming no hydrogen content in the film:



where the last reaction is a combination of surface reactions with an overall reaction rate  $R^{\text{II}}$ , as in Sec. 3.2.1. Note that here, the etching reaction (Eq. 3.21) is in fact not a five body reaction, but is, like hydrogen surface recombination, the sum of two body reactions ( $\text{H} + \text{SiH}_{x,\text{surface}} \rightarrow \text{SiH}_{x+1,\text{surface}}$  with  $x = 0, 1, 2$ ) until  $\text{SiH}_4$  leaves the surface creating a Si dangling bond on the surface ( $\text{SiH}_{3,\text{surface}} \rightarrow \text{SiH}_4 + \text{vacancy}$ ). The steady-state equilibrium of all chemical species present in the plasma gives the following equations:

$$\text{SiH}_4 : \Phi_{\text{SiH}_4} - (kn_e + a_{\text{SiH}_4})n_{\text{SiH}_4} + 1/4 G n_{\text{H}} = 0 \quad (3.23)$$

$$\text{SiH}_3 : k_3 n_e n_{\text{SiH}_4} - S_2 n_{\text{SiH}_3} = 0 \quad (3.24)$$

$$\text{SiH}_2 : (k_1 + k_2) n_e n_{\text{SiH}_4} - S_1 n_{\text{SiH}_2} = 0 \quad (3.25)$$

$$\text{H}_2 : \Phi_{\text{H}_2} + k_1 n_e n_{\text{SiH}_4} + 3/2 S_2 n_{\text{SiH}_3} + S_1 n_{\text{SiH}_2} + \quad (3.26)$$

$$+ 1/2 R^{\text{II}} n_{\text{H}} - (k_{\text{H}} n_e + a_{\text{H}_2}) n_{\text{H}_2} = 0 \quad (3.27)$$

$$\text{H} : (2k_2 + k_3) n_e n_{\text{SiH}_4} + 2k_{\text{H}} n_e n_{\text{H}_2} - (G + R^{\text{II}}) n_{\text{H}} = 0, \quad (3.28)$$

where  $k = k_1 + k_2 + k_3$ , and the other terms have the same definition as in Sec. 3.2.1. The ratio of the H atom flux,  $\Gamma_{\text{H}}$ , to silane radical fluxes reacting on the surface,  $\Gamma_{\text{SiH}_x}$ , becomes:

$$\frac{\Gamma_{\text{H}}}{\Gamma_{\text{SiH}_2} + \Gamma_{\text{SiH}_3}} = \frac{(G + R^{\text{II}}) n_{\text{H}}}{S_1 n_{\text{SiH}_2} + S_2 n_{\text{SiH}_3}} = 2\kappa \frac{n_{\text{H}_2}}{n_{\text{SiH}_4}} + \frac{2k_2 + k_3}{k} \quad (3.29)$$

$$= 2\kappa \left( \frac{1}{c_{\text{p}}} - 1 \right) + \frac{2k_2 + k_3}{k}, \quad (3.30)$$

which is the same solution as Eq. 3.14 for the simple model, except for the additive constant which is less than 2 for this more general case. The silane dissociation channels

---

<sup>2</sup>The superscript (II) refers to the model II.

	reaction	rate constant (m <sup>3</sup> ·s <sup>-1</sup> )	Ref.
Model I			
1.	SiH <sub>4</sub> + e → SiH <sub>2</sub> +2 H	1.87 · 10 <sup>-17</sup>	[92]
2.	H <sub>2</sub> + e → 2 H	4.49 · 10 <sup>-18</sup>	[92]
Model II			
1.	SiH <sub>4</sub> + e → SiH <sub>2</sub> +2 H	1.87 · 10 <sup>-17</sup>	[92]
2.	SiH <sub>4</sub> + e → SiH <sub>3</sub> +H	1.59 · 10 <sup>-16</sup>	[92]
3.	H <sub>2</sub> + e → 2 H	4.49 · 10 <sup>-18</sup>	[92]

**Table 3.1:** Rate constants of the gas phase reactions used for numerical evaluation of the two first plasma chemistry models.

can be supplemented by silane ionization reactions with no general change to the final expression. In this way, silane radical ions as well as neutral radicals can also be accounted for in the flux ratio.

This result shows that adding species and/or reactions to the simple model presented in Section 3.2.1 does not change the general solution and the ratio of hydrogen to silane radical flux to the surface still has the same dependence on  $c_p$ . This is because the species and reactions chosen for the simple model dominate all secondary species and reactions due to higher densities and reaction frequencies, respectively, in the range of experimental parameters considered here.

### Model III: Non-linear numerical model

To show the effect of additional chemical reactions on the final results, simple analytical models can no longer be used because of non-linearities introduced by radical-radical gas phase reactions. To permit the resolution of such a system, a numerical model has been developed using a commercially available software (COMSOL Reaction Engineering Lab<sup>TM</sup>).

First of all, zero dimensional numerical versions of the two analytical models presented in Sections 3.2.1 and 3.2.2 have been compared to the analytical models (Model I and II) in order to validate this approach. Table 3.1 presents the gas phase reaction rate constants used to solve numerically both the analytical and numerical solutions.

The rate constants of the surface reactions presented in Table 3.2 can not be directly found in the literature, because of their dependence on the reactor geometry and on the pressure. Therefore, they have been estimated on the basis of the work of Chantry [110].

The local net density variation due to the diffusion of particles can be expressed as

$$\left| \frac{1}{n_i} \frac{dn_i}{dt} \right| = \frac{D_{i/j}}{\Lambda^2}, \quad (3.31)$$

where  $n_i$  is the number density of the  $i$  specie in m<sup>-3</sup>,  $D_{i/j}$  is the binary diffusion coefficient of the  $i$  specie in the media  $j$  in m<sup>-2</sup>·s<sup>-1</sup>, and  $\Lambda$  is the diffusion length of  $i$  in m. The

	reaction	rate constant
Model I		
3.	$\text{SiH}_2 \rightarrow \text{Si}_{\text{surf.}} + \text{H}_2$	$S$
4.	$\text{H} \rightarrow 1/2 \text{H}_2$	$R^{\text{I}}$
Model II		
4.	$\text{SiH}_2 \rightarrow \text{Si}_{\text{surf.}} + \text{H}_2$	$S_1$
5.	$\text{SiH}_3 \rightarrow \text{Si}_{\text{surf.}} + 3/2 \text{H}_2$	$S_2$
6.	$\text{H} \rightarrow 1/2 \text{H}_2$	$R^{\text{II}}$
7.	$\text{H} + 1/4 \text{Si}_{\text{surf.}} \rightarrow 1/4 \text{SiH}_4$	$G$

**Table 3.2:** Rate constants of the surface reactions used for numerical evaluation of the two first plasma chemistry models.

binary diffusion coefficient  $D_{i/j}$  can be calculated either from the kinetic theory or from the binary diffusivity theory resumed by Perrin *et al* [111] and giving for a given pressure  $p$  and gas temperature  $T$

$$D_{i/j} = \frac{3}{16} \frac{(4\pi k_B T / 2m_{ij})^{1/2}}{p / k_B T \cdot \pi \sigma_{ij}^2 \Omega_D(T^*)}, \quad (3.32)$$

where  $m_{ij} = m_i m_j / (m_i + m_j)$  is the reduced mass in kg,  $\sigma_{ij} = (\sigma_i + \sigma_j)/2$  the binary collision diameter in m and  $T^* = T / \epsilon_{ij}$  with  $\epsilon_{ij} = \sqrt{\epsilon_i \epsilon_j}$ , where  $(\sigma_i, \epsilon_i)$  are the Lennard-Jones parameters given in Table 3.3 for the species used in this work.  $\Omega_D(T^*)$  can be calculated from the expression [111]:

$$\Omega_D(T^*) = \frac{A}{T^* B} + \frac{C}{e^{D \cdot T^*}} + \frac{E}{e^{F \cdot T^*}} + \frac{G}{e^{H \cdot T^*}}, \quad (3.33)$$

with  $A = 1.06036$ ,  $B = 0.1561$ ,  $C = 0.193$ ,  $D = 0.47635$ ,  $E = 1.03587$ ,  $F = 1.52996$ ,  $G = 1.76474$  and  $H = 3.89411$ .

The diffusion length  $\Lambda$  in Eq. 3.31 can be approximated according to Chantry [110] as follows

$$\Lambda^2 = \Lambda_0^2 + l_0 \lambda, \quad (3.34)$$

where  $\Lambda_0 = d_{\text{gap}} / \pi$ ,  $l_0$  the reactor volume to surface ratio and  $\lambda = (N \sigma_m)^{-1}$  the linear

specie	$\sigma$ (Å)	$\epsilon / k_B$ (K)
H <sub>2</sub>	2.827	59.7
H	2.50	30
SiH <sub>4</sub>	4.084	207.6
SiH <sub>3</sub>	3.943	170.3
SiH <sub>2</sub>	3.803	133.1

**Table 3.3:** Lennard-Jones parameters of the species used. (taken from Ref. [111].)

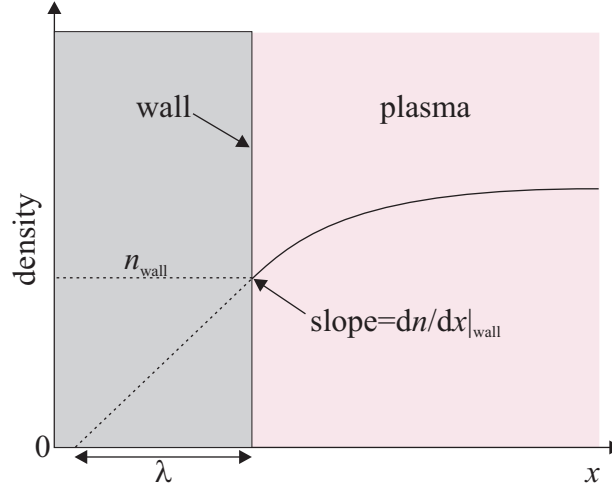


**Figure 3.8:** Effect of a wall on the radical density gradient in its vicinity.

extrapolation length of the density gradient at the wall (see Fig. 3.8), with  $N = p/k_B T$  the background gas density and  $\sigma_m$  the momentum transfer cross-section. Using these definitions, the pressure dependent radical surface reaction rates can be estimated and are given by

$$S_1 = \frac{17.2}{(d_{\text{gap}}/\pi)^2 \cdot p + 0.0201l_0} \quad (3.35)$$

$$S_2 = \frac{16}{(d_{\text{gap}}/\pi)^2 \cdot p + 0.0193l_0} \quad (3.36)$$

$$S_3 = \frac{11.92}{(d_{\text{gap}}/\pi)^2 \cdot p + 0.0155l_0} \quad (3.37)$$

$$R^{\text{II}} = 0.95 \cdot \frac{52.7}{(d_{\text{gap}}/\pi)^2 \cdot p + 0.0372l_0} \quad (3.38)$$

$$G = 0.05 \cdot \frac{52.7}{(d_{\text{gap}}/\pi)^2 \cdot p + 0.0372l_0} \quad (3.39)$$

$$(3.40)$$

where  $p$  is the total pressure in Pa, and  $l_0 = d_{\text{gap}}/(2 + 2d_{\text{gap}})$  for a closed parallel plate reactor. Note that the sum of H atom surface reaction rate constants ( $R^{\text{II}} + G$ ) in the model II correspond to the single reaction rate constant ( $R^{\text{I}}$ ) in the model I. Physically it corresponds to an identical loss rate of H atoms on the surfaces, but the utilization follows a branching ratio  $R : G = 0.95 : 0.05$  corresponding to values found in the literature [55].

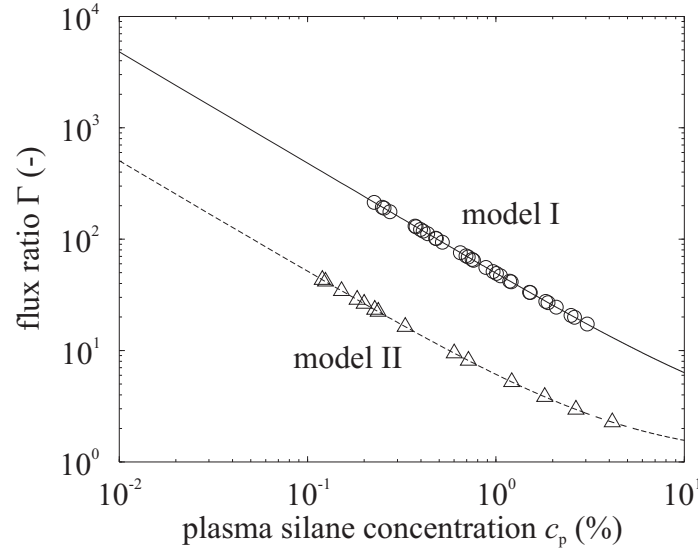


**Figure 3.9:** Comparison of analytical (lines) and numerical (points) solutions of the 1<sup>st</sup> (Section 3.2.1) and 2<sup>nd</sup> (Section 3.2.2) models.

Figure 3.9 compares the results of the numerical models to the analytical curves from Eqs. 3.14 and 3.30 using the reaction rate constants from Tables 3.1 and 3.2. First it shows that there is perfect agreement between analytical and numerical models as expected. Second, it shows that the value of the flux ratio is about ten times smaller in the case of the model II, which includes the silicon etching by atomic hydrogen and the presence of  $\text{SiH}_3$  radicals. The model II is much more in agreement with the value  $\Gamma_{\text{H}}/\Gamma_{\text{SiH}_x} = 5.2$  proposed by Klein *et al* [106] for transitional material deposition. This difference between the two models does not come from the introduction of the silicon chemical etching reaction because its importance is relatively small ( $< 5\%$ ) compared to the hydrogen surface recombination. This shift comes from the introduction of the  $\text{SiH}_3$  radical that boosts in a significant manner the silicon dissociation rate due to the high electron impact dissociation rate constant ( $1.59 \cdot 10^{-16} \text{ m}^3 \cdot \text{s}^{-1}$ ) compared to the one leading to  $\text{SiH}_2$  radicals ( $1.87 \cdot 10^{-17} \text{ m}^3 \cdot \text{s}^{-1}$ ). However, even if the values of the ratio of the fluxes towards the surface are different, both models are qualitatively equivalent and relevant because of their monotonic behavior as a function of  $c_p$ , meaning that the lower  $c_p$ , the higher the hydrogen to silicon radical flux ratio towards the surface  $\Gamma_{\text{H}}/\Gamma_{\text{SiH}_x}$ .

Figure 3.9 shows that the zero dimensional numerical routine gives correct solutions and it can be used for more complex chemical reaction systems including radical-molecule and radical-radical reactions. This third numerical model includes the reactions presented in Table 3.4. The surface reaction rates have been calculated as for the model II using  $(\sigma_i, \epsilon_i) = (4.42, 230)$  and  $(4.717, 306.9)$  [111] for  $\text{Si}_2\text{H}_5$  and  $\text{Si}_2\text{H}_6$ , respectively.

Figure 3.10 compares the two analytical models (I and II) with the numerical model III including non-linear reactions. The results of this model is no longer only a function of the silane concentration in the plasma as for the two first models. The scattering of

the numerical results is due to the non-zero effect of the pressure at iso-plasma silane concentration on the plasma chemistry, as will be discussed in detail in Chapter 6. This is related to the similar order of magnitude of the rates of electron impact reactions and of the radical-molecule reactions ( $k_2 n_e n_{\text{SiH}_4} / k_5 n_{\text{H}} n_{\text{SiH}_4} \approx 1$ ). However, the general tendency linking in a monotonic way the  $\Gamma_{\text{H}}/\Gamma_{\text{SiH}_x}$  ratio to the silane plasma concentration is still observable and this more general model does not put into question the simple analytical approach presented in Section 3.2.1. Indeed, the broadening of the  $\Gamma_{\text{H}}/\Gamma_{\text{SiH}_x}$  ratio as a function of  $c_p$  due to non-linear effects can be one of the sources of the relatively wide transition zone in Fig. 3.2.

The conclusion is that complicating the model by adding non-linear chemical reactions is not necessary to obtain a qualitative information on the species flux towards the surface within the pressure range investigated. Moreover, the use of numerical modeling alone does not bring any understanding of the physics behind experimental results. It is another way to perform experimental runs, with the same difficulty to link the input plasma parameters ( $P_{\text{RF}}$ ,  $p$ , etc.) to the output (densities, flux ratio, etc.) as for experiments performed in the laboratory.

	reaction	rate constant ( $\text{m}^3 \cdot \text{s}^{-1}$ )	Ref.
electron impact dissociation			
1.	$\text{SiH}_4 + e \rightarrow \text{SiH}_2 + 2 \text{H}$	$1.87 \cdot 10^{-17}$	[92]
2.	$\text{SiH}_4 + e \rightarrow \text{SiH}_3 + \text{H}$	$1.59 \cdot 10^{-16}$	[92]
3.	$\text{H}_2 + e \rightarrow 2 \text{H}$	$4.49 \cdot 10^{-18}$	[92]
4.	$\text{Si}_2\text{H}_6 + e \rightarrow \text{SiH}_4 + \text{SiH}_2$	$2.86 \cdot 10^{-16}$	[92]
reactions with radicals			
5.	$\text{SiH}_4 + \text{H} \rightarrow \text{SiH}_3 + \text{H}_2$	$2.8 \cdot 10^{-17} \exp(-1250/T_s)$	[55]
6.	$\text{SiH}_3 + \text{H} \rightarrow \text{SiH}_2 + \text{H}_2$	$5 \cdot 10^{-16}$	[55]
7.	$\text{SiH}_2 + \text{H}_2 \rightarrow \text{SiH}_4$	$3.2 \cdot 10^{-18} (1 - (1 + 0.024p)^{-1})$	[55]
8.	$\text{SiH}_4 + \text{SiH}_2 \rightarrow \text{Si}_2\text{H}_6$	$2.2 \cdot 10^{-16} (1 - (1 + 0.5p)^{-1})$	[55]
9.	$\text{Si}_2\text{H}_6 + \text{H} \rightarrow \text{SiH}_3 + \text{SiH}_4$	$8.16 \cdot 10^{-17} \exp(-1250/T_s)$	[55]
10.	$\text{Si}_2\text{H}_6 + \text{H} \rightarrow \text{Si}_2\text{H}_5 + \text{H}_2$	$1.58 \cdot 10^{-16} \exp(-1250/T_s)$	[55]
11.	$\text{SiH}_3 + \text{SiH}_3 \rightarrow \text{SiH}_2 + \text{SiH}_4$	$3.8 \cdot 10^{-16} (1 + 3.2/(1 + \exp(0.4p - 2.6)))$	[55]
12.	$\text{SiH}_3 + \text{Si}_2\text{H}_6 \rightarrow \text{SiH}_4 + \text{Si}_2\text{H}_5$	$4.1 \cdot 10^{-16} \exp(-2500/T_s)$	[55]
surface reactions			
13.	$\text{SiH}_2 \rightarrow \text{Si}_{\text{surf.}} + \text{H}_2$	$S_1$	
14.	$\text{SiH}_3 \rightarrow \text{Si}_{\text{surf.}} + 3/2 \text{H}_2$	$S_2$	
15.	$\text{Si}_2\text{H}_5 \rightarrow 2 \text{Si}_{\text{surf.}} + 5/2 \text{H}_2$	$S_3$	
16.	$\text{H} \rightarrow 1/2 \text{H}_2$	$R^{\text{II}}$	
17.	$\text{H} + 1/4 \text{Si}_{\text{surf.}} \rightarrow 1/4 \text{SiH}_4$	$G$	

**Table 3.4:** Reactions used and their rate constants for the 3<sup>rd</sup> model including non-linear effects caused by radical-radical reactions.

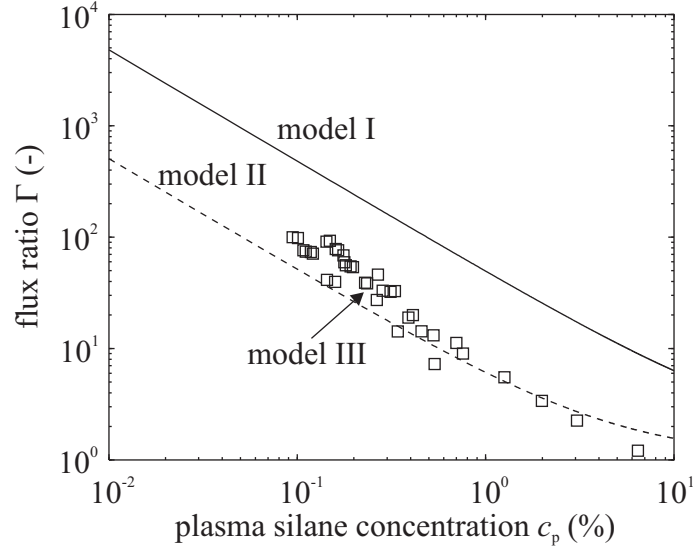


**Figure 3.10:** Numerical results of the effect of gas phase reactions addition to simple analytical models.

### 3.3 Relation between plasma and process parameters

We have seen in Section 3.1 that the silane concentration in the plasma,  $c_p$ , accounts for the effect of all the plasma input parameters, i.e. RF power, total flow rate, pressure, interelectrode distance, silane input concentration and excitation frequency. Since the silane concentration in the plasma is defined as a function of the "macro" characteristics of the plasma which are the silane input concentration,  $c$ , and the silane depletion fraction,  $D$ , we need to understand how the silane depletion fraction is affected by the "micro" plasma characteristics which are the residence times,  $1/a_{\text{SiH}_4}$  and  $1/a_{\text{H}_2}$ , and the gas dissociation frequencies,  $kn_e$  and  $k_{\text{H}}n_e$ . For this phenomenological interpretation, we will assume that silane and hydrogen have the same pumping speed  $a = a_{\text{SiH}_4} = a_{\text{H}_2}$ , and hence, that the silane input concentration,  $c$ , depends only on the input flow rates of silane and hydrogen, i.e.  $c = p_{\text{SiH}_4}^0 / (p_{\text{SiH}_4}^0 + p_{\text{H}_2}^0) = \Phi_{\text{SiH}_4} / (\Phi_{\text{SiH}_4} + \Phi_{\text{H}_2})$ . The silane depletion fraction,  $D$ , can be related to the silane dissociation frequency  $kn_e$  and to the pumping speed  $a$  from the chemical equilibrium presented in the Section 3.2.1. By summing Eqs. 3.7, 3.9 and 3.10 we obtain:

$$(\Phi_{\text{SiH}_4} + \Phi_{\text{H}_2}) + kn_en_{\text{SiH}_4} - (n_{\text{SiH}_4} + n_{\text{H}_2})a = 0 \quad (3.41)$$

with plasma ( $kn_e > 0$ ), and

$$(\Phi_{\text{SiH}_4} + \Phi_{\text{H}_2}) - (n_{\text{SiH}_4}^0 + n_{\text{H}_2}^0)a^0 = 0 \quad (3.42)$$

without plasma ( $kn_e = 0$ ). Equation 3.42 relates the input flow rates to the densities  $n_{\text{SiH}_4}^0$  and  $n_{\text{H}_2}^0$  before plasma ignition with pumping speed  $a^0$ , and Eq. 3.41 expresses the fact that, for this model, the net result of the dissociation and deposition of silicon from

silane releases two hydrogen molecules per silane molecule consumed, if the hydrogen incorporated in the film is neglected.

Working at constant pressure implies that the total number density is the same before ( $n_{\text{SiH}_4}^0 + n_{\text{H}_2}^0$ ) and after ( $n_{\text{SiH}_4} + n_{\text{H}_2}$ ) plasma ignition. By using the definition of  $c$ ,  $c_p$  and Eq. 2.7, equations. 3.41 and 3.42 give

$$\frac{a^0}{a} = 1 - \frac{kn_e}{a}(1 - D)c, \quad (3.43)$$

and equations. 3.7 and 3.42 give

$$\frac{a^0}{a} = \left( \frac{kn_e}{a} + 1 \right) (1 - D). \quad (3.44)$$

Hence we obtain  $D$  in terms of the ratio  $a/kn_e$  and the silane input concentration  $c$ :

$$D = \left( 1 + \frac{a/kn_e}{(1 + c)} \right)^{-1}. \quad (3.45)$$

The latter expression is useful to draw guidelines to understand the behavior of the silane depletion  $D$  as a function of the plasma input parameters; these can be divided into two categories: (i) Parameters which affect essentially the plasma dissociation rate  $kn_e$ , such as the RF power and the excitation frequency, and (ii) parameters which affect essentially the residence time  $1/a$ , such as the pressure, the total flow rate and the interelectrode distance.

### 3.4 Silane depletion as a function of the plasma parameters

Regarding the multi-parametric experimental problem of  $\mu\text{c-Si:H}$  deposition, the experimental results and the simple model presented in this chapter have permitted to reduce the number of process parameters from six (RF power, pressure, total flow rate, silane concentration, excitation frequency and interelectrode distance) to two: The silane depletion fraction,  $D$ , and the silane input concentration,  $c$ . However, the difficulty is that the silane depletion fraction,  $D$ , is not a simple input process parameter, but has to be measured experimentally. In our case, we have used the FTIR absorption spectroscopy technique, although in principle other techniques such as mass spectrometry or optical emission spectroscopy (see Chapter 2) can also be applied. Therefore, it is important for process optimization to measure how  $D$  is influenced by the process parameters.

Figure 3.11 shows the results of the measured silane depletion as a function of a process parameter (RF power, total flow rate, process pressure, silane concentration, interelectrode distance and excitation frequency) while the other parameters are kept constant. For each case, the solid line shows the estimated behavior deduced from Eq. 3.45. For these estimations, since the considered silane input concentrations remain small ( $c < 0.1$ ), we used for the pumping speed the approximate value obtained without plasma:

$$a \sim a^0 = \frac{\Phi_{\text{tot}}}{n_{\text{tot}}} = 6.1 \cdot 10^{-6} T \frac{F_{\text{tot}}}{pV}, \quad (3.46)$$



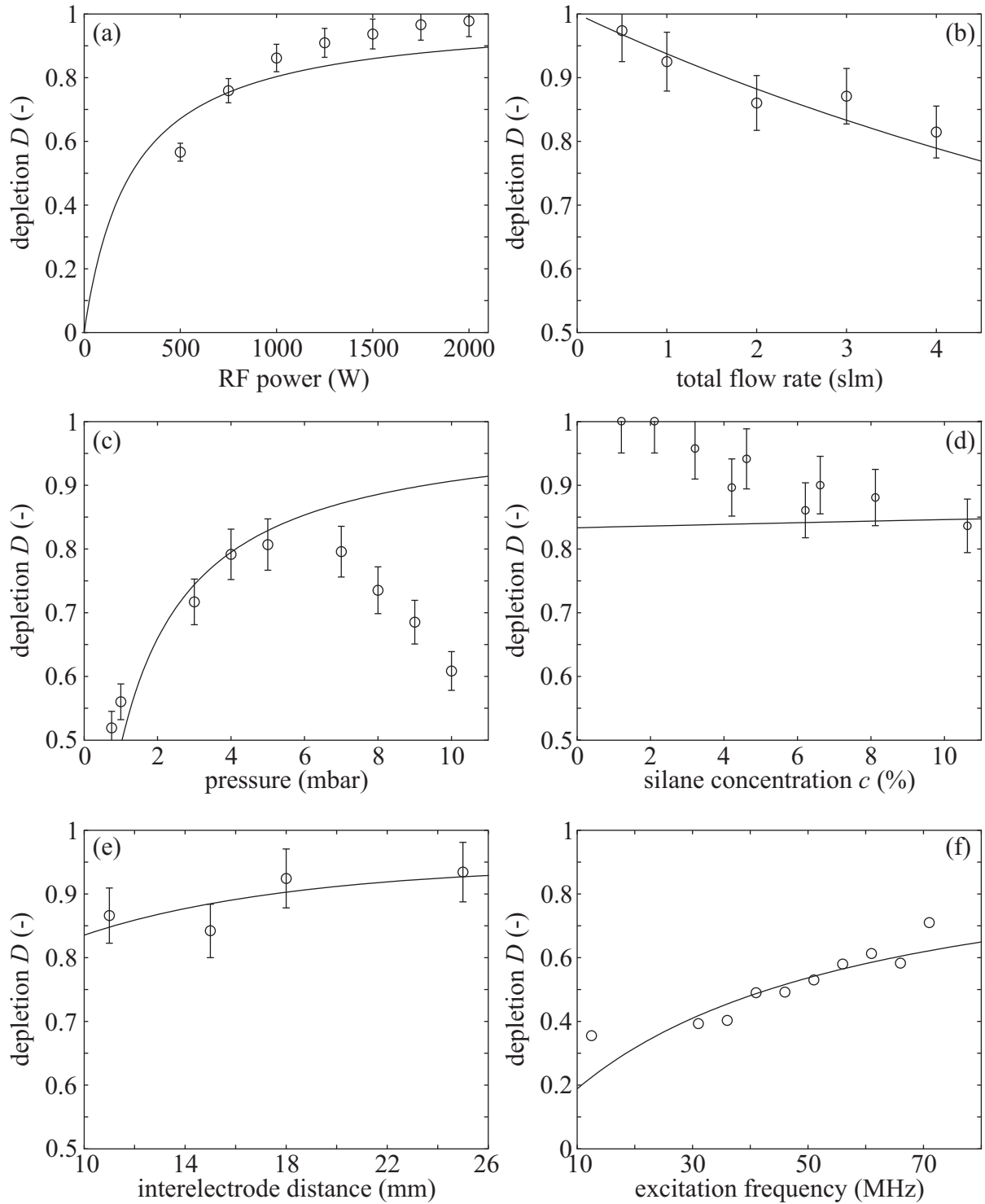


**Figure 3.11:** Silane depletion fraction as a function of (a) RF power, (b) total flow rate, (c) pressure, (d) silane concentration, (e) interelectrode distance and (f) excitation frequency (from Sansonnens *et al* [24]). Solid lines represent modeling assuming a linear dependence of the RF power and the excitation frequency with  $kn_e$ , and dependence on  $a$  by Eq. 3.46 for pressure, flow rates and interelectrode distance. Silane depletion as a function silane concentration is assumed with a constant  $kn_e/a$  ratio. Errors bars correspond to 5 %.

where  $a$  and  $a^0$  are in  $\text{s}^{-1}$ ,  $V$  the reactor volume in  $\text{m}^3$ ,  $p$  the total pressure in Pa,  $F_{\text{tot}}$  the total input flow rate in sccm and  $T$  the gas temperature in K. For the RF power and excitation frequency scans cases (Figs. 3.11 (a) and (f)), the model line is calculated assuming that the dissociation rate,  $kn_e$ , is simply proportional to the RF power and frequency, respectively, and the pumping speed  $a$  is constant. For all the other parameter scans (Figs. 3.11 (b)-(e)), the model lines are calculated from the variation of the pumping speed  $a$  as a function of the modified parameter (Eq. 3.46) and assuming a constant dissociation frequency  $kn_e$ .

As can be seen from Fig. 3.11, these simple estimations reproduce relatively well the behavior of the silane depletion as a function of the input parameters except for the pressure variation at pressures higher than 5 mbar. For the pressure dependence, the variation of the depletion in the low pressure range is well explained by the increase of the residence time, however at high pressure, a decrease of the depletion is observed while the residence time still increases. Such behavior of the silane consumption with pressure has already been reported by other groups [112]. This strong deviation between the simple model and the measurements may be due to the increasing importance of electron losses due to negatively charging of polysilanes and powder particles while increasing the pressure. This effect reduces the electron density at high pressure, when we account for a constant electron density in the simple model. Smaller deviations from this simple model and the experimental results are also observed for the RF power series and the silane concentration series. These deviations may be attributed to the fact that the silane dissociation rate has a more complicated behavior as the plasma composition changes than the simple assumption used here ( $kn_e$  proportional to the power for the power series and  $kn_e$  constant for the concentration series).

Results and simple modeling presented in Fig. 3.11 show that the behavior of the silane depletion as a function of the process parameters can be roughly estimated from simple assumptions on the dissociation frequency and pumping speed except for the high pressure case. These simple estimations are useful in order to give guidelines for the process optimization (see Chapter 4). However, the direct measurement of the silane depletion remains a diagnostic of choice to optimize the process.

### 3.5 Dissociation efficiency and deposition rate

As mentioned in the Chapter 1, thin films for PV solar cells should not only have the required microstructure, but they should also be produced efficiently (i.e. with the highest possible silane utilization fraction) and at deposition rate higher than  $10 \text{ \AA/s}$ .

For a uniform deposition on the reactor surfaces, the upper limit of the deposition rate  $R_{\text{max}}$  for a given silane flow rate will be reached when all the silicon atoms are incorporated in the thin film, and is given by:

$$R_{\text{max}} = \frac{\Phi_{\text{SiH}_4} V m_{\text{Si}}}{A \rho} \quad (\text{m/s}) = 0.00962 \frac{F_{\text{SiH}_4}}{A} \quad (\text{nm/s}) \quad (3.47)$$

where  $\rho \cong 2180 \text{ kg}\cdot\text{m}^{-3}$  [113] is the silicon thin film density (corresponding to a hydrogen content of 10 %),  $V$  and  $A$  are respectively the plasma reactor volume in  $\text{m}^3$  and surface

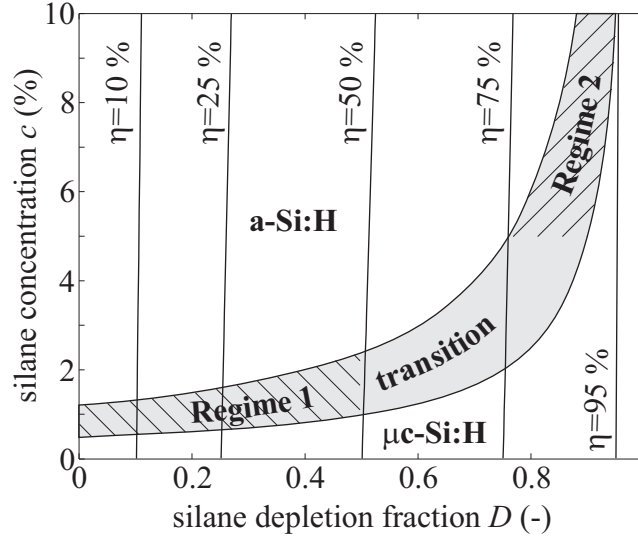


**Figure 3.12:** Silane dissociation efficiency as a function of silane depletion and concentration. The only way to deposit transitional material with high silane utilization is to work in the Regime 2 with high silane depletion and concentration.

of the electrodes facing the plasma in  $\text{m}^2$ ,  $m_{\text{Si}}$  is the mass in kg of a silicon atom, and  $F_{\text{SiH}_4}$  is the silane flow rate in sccm. In our large area reactor,  $R_{\text{max}}$  is  $16.4 \text{ \AA/s}$  for a silane flow rate of 100 sccm. This maximum possible deposition rate will be reached only if the silane is totally depleted ( $D = 1$ ), and if no silicon atoms are lost by pumping in the form of polysilane or powder particles. For processes having silane depletion less than 100 % ( $D < 1$ ), we can define the silane dissociation efficiency,  $\eta$ , as the ratio of the silane dissociation rate ( $kn_e n_{\text{SiH}_4}$ ) to the silane flow rate  $\Phi_{\text{SiH}_4}$  [19]. Using Eqs. 3.7 and 3.45, we have:

$$\eta = \frac{kn_e n_{\text{SiH}_4}}{\Phi_{\text{SiH}_4}} = \frac{kn_e}{kn_e + a} = \frac{D}{1 + (1 - D)c}. \quad (3.48)$$

In the range of validity of our simple plasma chemistry model,  $\eta$  is a function of  $c$  and  $D$  only, and for highly diluted silane plasma ( $c < 0.1$ ),  $\eta$  is almost equal to  $D$ , as shown in Fig. 3.12. Here, the silane dissociation efficiency,  $\eta$ , represents the fraction of the silane input flow rate which has been dissociated in the plasma and which can be deposited if there is no polysilane or powder particle formation. Therefore, the quantity  $R = \eta R_{\text{max}}$  represents the deposition rate which can be achieved as a function of the depletion  $D$  for a given input silane flow rate  $\Phi_{\text{SiH}_4}$  and silane concentration  $c$ .

In Fig. 3.12, contours of  $\eta$  have been plotted in the  $(D, c)$  plane together with the transition zone between the a-Si:H and  $\mu\text{c-Si:H}$  film growth. If the material of interest has to be deposited at this transition between a-Si:H and  $\mu\text{c-Si:H}$ , then we can distinguish two different regimes as before: In Regime 1, the low silane concentration regime ( $c < 2.5 \%$ ), growth in the transition region can be achieved with low silane depletion ( $D < 0.5$ ), as will be the case for a weak plasma. Since the corresponding value of  $\eta$  is also low ( $\eta < 50 \%$ ), high deposition rate in this regime could only be reached for high silane flow rate and

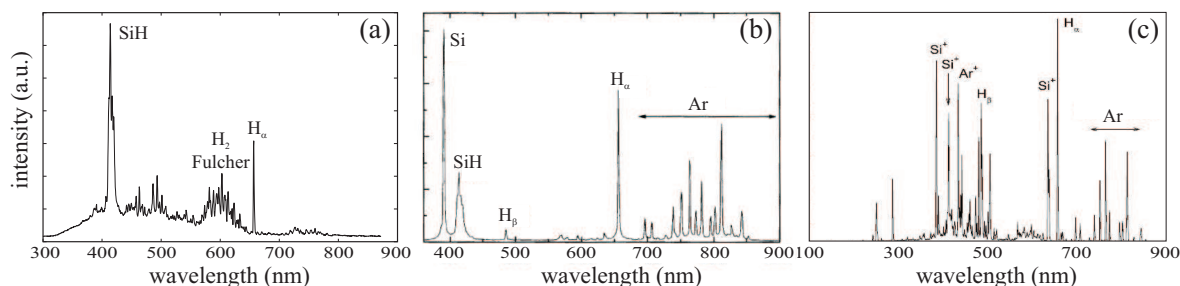


**Figure 3.13:** Optical emission spectra of different type of sources: (a) Large area RF, (b) high current DC arc (from Ref. [56]) and (c) low energy plasma DC arc (from Ref. [114]), leading respectively to molecular, atomic and ionic plasmas.

therefore very high hydrogen flow rate. As an example, to achieve a deposition rate of 10 Å/s with such conditions ( $\eta = 50\%$  and  $c < 2.5\%$ ), the silane flow rate has to be of 122 sccm, and the hydrogen flow rate higher than 4750 sccm. On the other hand, in Regime 2, the high concentration regime ( $c > 5\%$ ), growth in the transition region can only be achieved for high silane depletion  $D > 0.8$ , with a correspondingly high value for  $\eta$  ( $\eta > 80\%$ ). Hence, to achieve a deposition rate of 10 Å/s with these conditions ( $\eta = 80\%$  and  $c > 5\%$ ), only 76 sccm of silane are needed and the hydrogen flow rate can be lower than 1450 sccm. Therefore, in the Regime 2 it is possible to use lower silane and hydrogen flow rates compared to the high dilution regime in order to achieve a given deposition rate because of the higher efficiency of silane utilization.

### 3.6 Are there other interesting deposition regimes ?

The two deposition regimes described in the previous section stand in the transition zone between amorphous and microcrystalline regions where the deposited material shows the best properties for PV applications [40]. However, solar cells made of crystalline silicon or polycrystalline silicon show much higher conversion efficiencies up to 24.7 % and 19.8 % [115], respectively. Generally, these materials are produced by very different methods than for amorphous and microcrystalline silicon. Crystalline silicon is produced in the form of wafers cut in monocrystalline ingots produced by slow solidification from extremely pure liquid silicon. Monocrystalline silicon can also be produced using PECVD by epitaxial growth on monocrystalline silicon wafers [107]. To achieve such perfect arrangement at the atomic level, the dissociation source has to be very powerful in order to dissociate all the silicon and the hydrogen present in the gas phase. This makes RF sources inadequate to perform such deposition, because even if very high power density is used, the plasma will remain dominated by molecules as shown by optical emission spectroscopy (OES) in Fig. 3.13(a). This is confirmed by the difficulties to reach a total silane depletion ( $D = 1$ ) even with a favorable definition of the depletion (Eq. 2.6) considering a silane molecule to be depleted as soon as it loses a hydrogen atom. If sources with higher

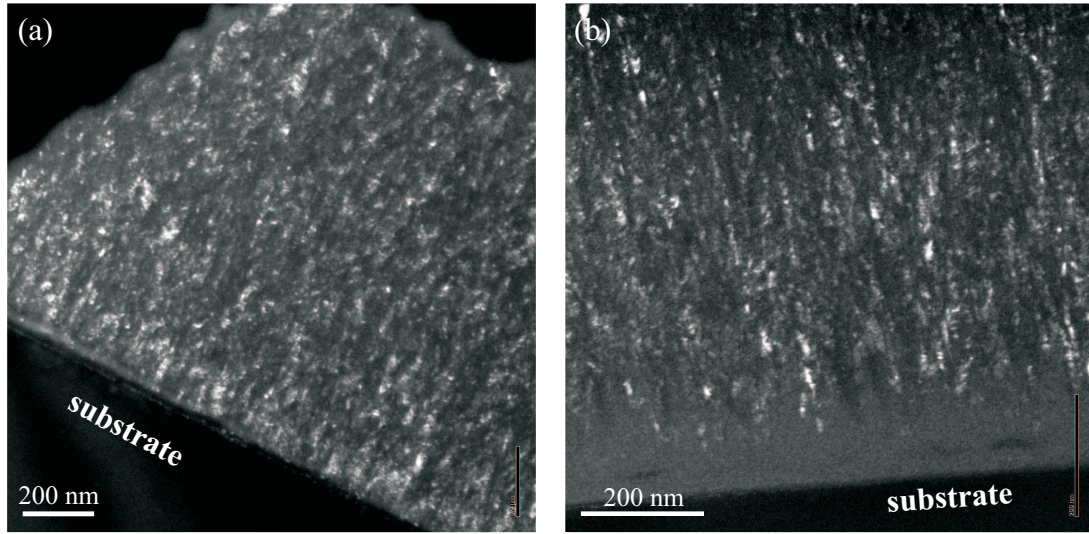


**Figure 3.14:** TEM pictures of microcrystalline silicon deposited in (a) a large area RF reactor (magn. 11.5 k $\times$ ) and (b) a low energy plasma (LEP) reactor (magn. 20 k $\times$ ).

dissociative power are used such as DC arc or low energy plasma (LEP) sources leading to plasma dominated by atoms (Fig. 3.13(b)) and ions (Fig. 3.13(c)), respectively, or such as expanding thermal plasma source [116] the silane depletion - as defined in this work - will always be equal to unity ( $D = 1$ ). Hence, a third deposition zone corresponding to polycrystalline or monocrystalline silicon deposition can be drawn in the  $(D, c)$  plane along the line  $D = 1$ . This zone could be of interest for a new type of PV solar cells made of polycrystalline or even monocrystalline silicon thin films deposited by PECVD, as opposed to PV solar cells made from monocrystalline silicon bulk material obtain from large ingots.

Up to now, such atomic or ionic sources have been used to produce microcrystalline silicon at very high deposition rates (up to 10 nm/s [56, 114]). The dissociation power of these sources has been used to dissociate a larger silane flow to improve the deposition rate, while keeping the silane concentration sufficiently low to deposit  $\mu c$ -Si:H. The film microstructure is then very similar, except for the amorphous incubation layer thickness (see Chapter 5), between a layer deposited from a molecular RF plasma in the transition zone (Fig. 3.14(a)) and a layer deposited from a ionic low energy plasma (LEP) (Fig. 3.14(b)).

To reach an eventual polycrystalline or monocrystalline growth regime, the high dissociation power has to be used in a different way. To increase the H atomic flux towards the growing film, an inlet flux of  $H_2$  has to be set and the  $H_2$  has to be dissociated. This seems exactly the same as the technique used up to now in RF plasmas to reach microcrystalline deposition: High  $H_2$  dilution of silane to reduce the silane concentration in the plasma (Regime 1). However, the case of high density sources for polycrystalline or monocrystalline deposition is very different, because we need to reach much higher values of the  $\Gamma_H/\Gamma_{SiH_x}$  ratio than the ones needed for microcrystalline silicon growth, making the

H<sub>2</sub> dilution probably a necessity. The H<sub>2</sub> dilution in the case of high dissociation power sources will not affect the dissociation efficiency, and hence the deposition rate, because of the total silane depletion (see Eq. 3.48). However, it may be necessary to reduce the silane flow rate to remain within a fully atomic or ionic plasma, making the deposition rate lower than the extremely high values (10 nm/s) reached nowadays for microcrystalline silicon with this type of sources.

To summarize, a new deposition regime could stand on the line corresponding to  $D = 1$ . This may correspond to polycrystalline or monocrystalline silicon growth and cannot be reached by using an RF excitation source such as the one used in this work. High density sources such as low energy DC plasmas have to be used and hydrogen dilution may be still necessary to increase the H to Si flux ratio to the surface in order to reach the very high values needed.

### 3.7 Conclusion

In this chapter, infrared absorption spectroscopy in the exhaust line of a large area PECVD reactor and deposited film characterization have been performed. It has been shown that the silane concentration *in the plasma* - as opposed to the silane input concentration or all other input plasma parameters - is a relevant parameter to determine the silicon thin film microstructure. The silane concentration in the plasma is determined by the silane input concentration and the fractional depletion of silane. Plasma chemistry modeling has shown that the silane concentration in the plasma is directly related to the ratio of atomic hydrogen and silane radical fluxes to the surfaces, which determines the microstructure of the growing film. This shows why the silane concentration in the plasma can be used to predict the transition between the amorphous and the microcrystalline microstructure of deposited silicon films. Moreover, it has been shown that simple analytical modeling is at least as relevant as more complicated models to show that the flux ratio towards the growing film surface is related to the silane concentration in the plasma. Finally, results have shown that the only way to produce μc-Si:H in the transition zone at high deposition rates with a silane gas utilization efficiency higher than 80 % is to work with silane concentration higher than 5 % and silane depletion higher than 0.8.

# Chapter 4

## $\mu\text{c-Si:H}$ deposition optimization: Towards pure silane plasmas

The phenomenological models (Section 1.3) and the results of Chapter 3 have shown that the flux of hydrogen atoms to the growing surface has to be large compared to the silane radical flux in order to grow crystalline material. In the hydrogen dilution technique, the large atomic hydrogen flux to the surface compared to the silane radical flux is guaranteed by the large initial pressure of  $\text{H}_2$  compared to the  $\text{SiH}_4$  partial pressure. However, nothing prevents  $\mu\text{c-Si:H}$  deposition from pure silane plasma, because the deposition conditions depend on the plasma composition [19], which is very different from the input silane concentration in highly depleted plasmas, as shown by crystalline material deposited by high power density PECVD in small size reactors [91, 117, 118, 119] from pure silane. In Chapter 3, it was shown that with a large initial silane concentration and a high depletion of silane in the plasma, the silane partial pressure in the plasma becomes as low as in strongly hydrogen-diluted plasmas. Hence, a similar ratio of atomic hydrogen to silane radical fluxes to the surface can be reached even with a large ( $> 10\%$ ) initial silane concentration.

The aim of this chapter is first to show the feasibility of the deposition of  $\mu\text{c-Si:H}$  from pure silane plasma on large area substrates with a high gas utilization efficiency. Secondly, a reactor-independent methodology is established to determine the optimum plasma conditions to come closer to an ultimate cost-effective process for mass production of PV solar cells.

### 4.1 From highly $\text{H}_2$ -diluted to pure silane regime

In spite of the promising gas utilization efficiency of pure silane processes [117], up to now  $\mu\text{c-Si:H}$  deposition over large areas has been investigated only for the conventional hydrogen-diluted regime [14, 120], and a pure silane process has never been tested in systems larger than small laboratory reactors. Even in small reactors, the highest deposition rate recorded is less than  $10\text{ \AA/s}$  although higher deposition rates of solar grade material have been demonstrated in the case of the hydrogen-diluted regime [121, 122, 123]. This section shows what are the conditions needed to perform microcrystalline silicon films

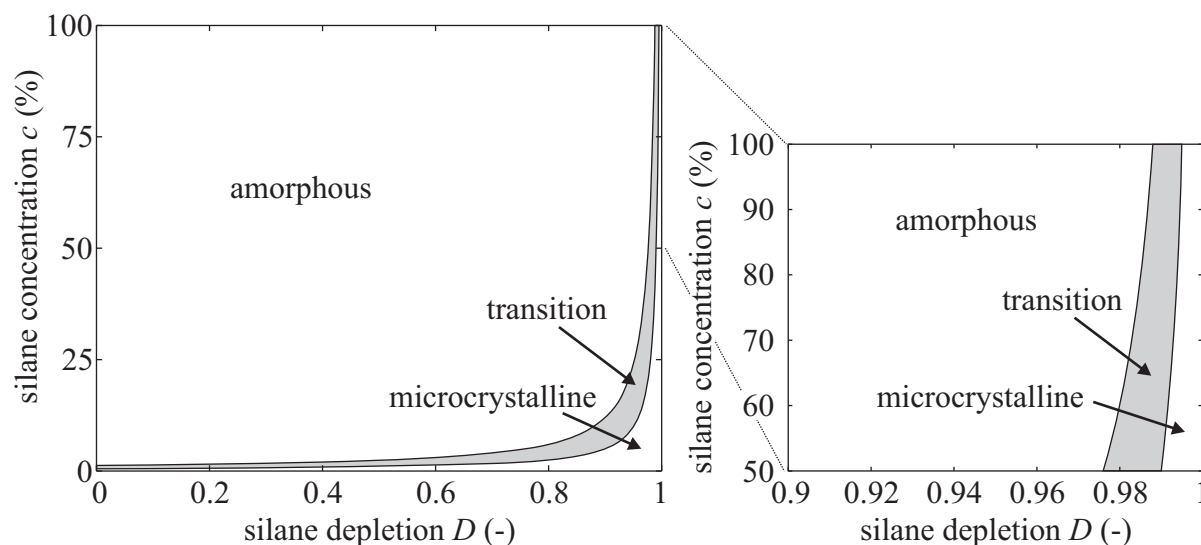


**Figure 4.1:** Representation of the three microstructure zones (amorphous, transition and microcrystalline) as a function of the silane depletion and concentration from highly  $\text{H}_2$ -diluted to pure silane. Microcrystalline silicon deposition is predicted by the model (Chapter 3) even from pure silane plasmas if the silane depletion is sufficiently high. The inset shows that the microcrystalline silicon zone is still present for silane concentration up to 100 %.

over large areas from pure silane, and compares them with the plasma chemistry model presented in the previous chapter.

#### 4.1.1 Effect of $\text{H}_2$ -dilution on the deposition rate and silane gas utilization fraction

The results of Chapter 3 have shown that the silane concentration in the plasma,  $c_p$ , is a relevant parameter for the determination of the microstructure transition, but the range in input silane concentration (0 - 10 %) was limited to concentrations conventionally used to deposit  $\mu\text{c-Si:H}$  films. However, Eq. 2.7 predicts  $\mu\text{c-Si:H}$  deposition even from a pure silane plasma ( $c = 1$ ), if the silane depletion  $D$  is sufficiently high ( $D > 0.995$ ) to maintain  $c_p < 0.5$  % as shown in Fig. 4.1. Physically, this is because a highly-depleted silane plasma consists mostly of hydrogen [19, 124] and therefore the plasma chemistry behaves similarly to a low depletion plasma with a strong hydrogen dilution. To reach such high silane depletion, the dissociation rate and the gas residence time have to be as high as possible. Moreover, with a high depletion plasma, the required silane flow rate to reach a target deposition rate is lower than for the deposition of transitional material from highly  $\text{H}_2$ -diluted silane plasma, because all the silane molecules are dissociated and deposited. Hence, using Eq. 3.47 the maximum possible deposition rate can be estimated for a given silane flow rate, assuming that every silicon atom flowing into the reactor is deposited uniformly on the reactor surface (no silane,  $\text{SiH}_x$  radical nor polysilane is



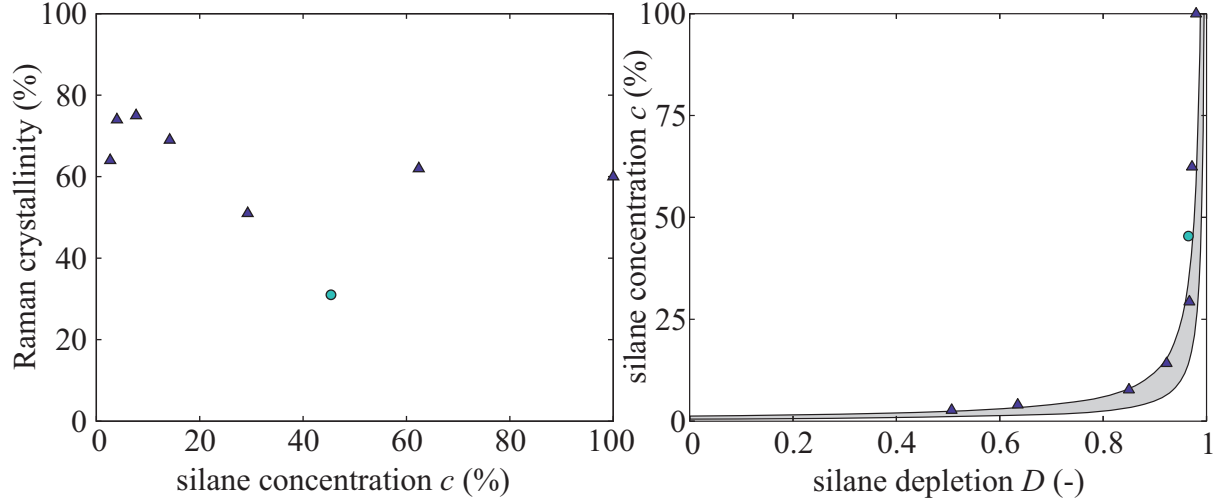


**Figure 4.2:** (a) Plot of the Raman crystallinity ( $\blacktriangle$  for  $\phi_c \geq 50\%$  and  $\circ$  for  $\phi_c < 50\%$ ) of samples deposited with constant pressure (2 mbar), RF power (1 kW) and silane flow rate (82 sccm), while varying the hydrogen (3000 - 0 sccm) flow rate to change the silane concentration (2.7 - 100 %). (b) All samples correspond to the transition material between amorphous and microcrystalline.

pumped out). Thus, if the target deposition rate is arbitrarily fixed at  $10 \text{ \AA/s}$  and a maximum loss fraction of 25 % of the input silane flow rate is assumed, the required input silane flow rate is 82 sccm for the KAI-S deposition reactor with an electrode area of  $0.593 \text{ m}^2$ . For all the following results, the silane flow rate is fixed at 82 sccm ( $R_{\max} = 13.3 \text{ \AA/s}$ ) and therefore, the only way to reach the pure silane regime from the standard highly H<sub>2</sub>-diluted one is by decreasing the H<sub>2</sub> flow and, hence, increasing the silane input concentration.

Results performed with an input power of 1000 W and a pressure of 2 mbar presented in Fig. 4.2(a) show that all samples from  $c = 2.7\%$  to  $100\%$  (H<sub>2</sub> flow from 3000 to 0 sccm) have a Raman crystalline fraction in the 30 - 75 % range and correspond to the microstructure transition region. Moreover, reduction of the hydrogen flow rate increases the deposition rate by a factor up to 3.5 (Fig. 4.3(b)). This increase of the deposition rate with the silane concentration (at a constant silane flow rate) can be explained by the reduction of silane pumping loss due to the increase of the gas residence time by reducing the total flow rate. The deposition rate and the silane depletion as a function of silane initial concentration can be deduced (solid lines in Fig. 4.3(a) and (b)) from the silane dissociation efficiency  $\eta$ , which corresponds to the ratio of the silicon deposition rate to the silane flow rate introduced by Howling *et al* [19] and developed in Section 3.5. This modeled behavior is obtained for constant pressure ( $p = n_{\text{tot}}k_B T = \text{constant}$ ) and silane flow rate ( $\Phi_{\text{SiH}_4} = \text{constant}$ ) which implies that

$$\frac{kn_e}{a^0} = \frac{kn_e}{\Phi_{\text{tot}}/n_{\text{tot}}} = \frac{kn_e}{\Phi_{\text{SiH}_4}/(p/k_B T)} \cdot c = B^{-1}c, \quad (4.1)$$

where  $B$  is constant for constant dissociation frequency ( $kn_e = \text{constant}$ ).

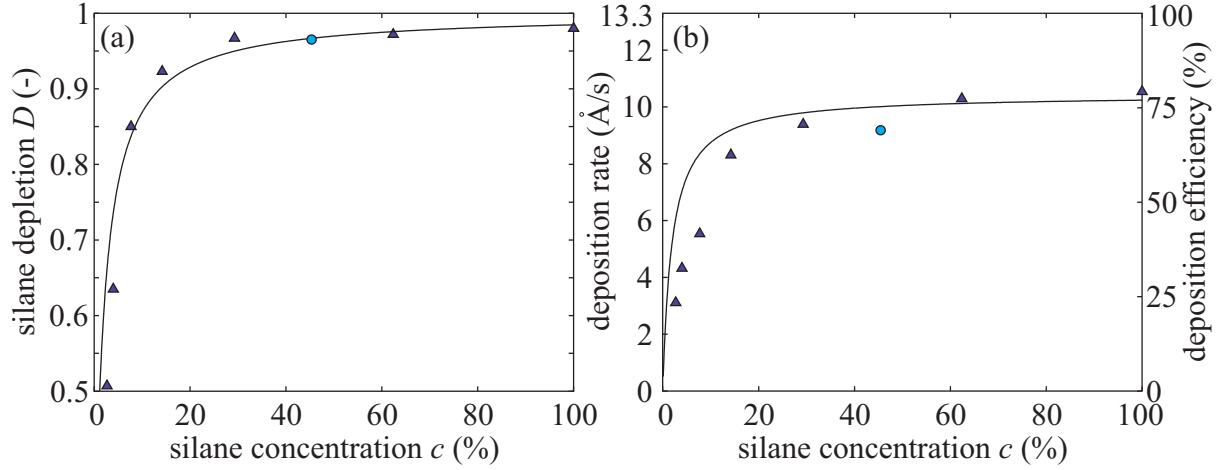


**Figure 4.3:** Dependence on the silane concentration of (a) the silane depletion and (b) the deposition rate and deposition efficiency with constant silane flow rate for microcrystalline (▲) and amorphous (○) silicon films. The solid lines represent modeling results (Eqs. 4.4 and 4.5) with  $B=0.02$ .

From equations 3.43 and 3.45 we obtain

$$\frac{kn_e}{a^0} = \frac{kn_e}{a} \cdot \frac{a}{a^0} = \frac{D}{(1-D)[1+c(1-D)]}. \quad (4.2)$$

Solving for  $B$  using the previous equation and Eq. 4.1 we have

$$B = \frac{c(1-D)[1+c(1-D)]}{D}. \quad (4.3)$$

The silane depletion,  $D$ , can be eliminated using Eq. 3.48 and by solving for  $\eta_{\text{iso-p}} = \eta_{\text{iso-p}}(c)$  we obtain

$$\eta_{\text{iso-p}} = \frac{-(1+B/c) + \sqrt{(1+B/c)^2 + 4B}}{2B}. \quad (4.4)$$

The silane depletion fraction plotted in Fig. 4.3(a) is then obtained using

$$D = 1 - \frac{B\eta_{\text{iso-p}}}{c} \quad (4.5)$$

with the free parameter  $B$  empirically set to 0.02. The deposition efficiency corresponding to the dissociated silane fraction which contributes to film growth and, hence to the deposition rate plotted in Fig. 4.3(b) are obtained through

$$R = R_{\text{max}}\eta_{\text{iso-p}}f \quad (4.6)$$

assuming a fraction  $f = 0.75$  of dissociated silane contributing to film growth (see Section 4.1.3).

The expression 3.48 can be re-written using Eq. 2.7 as

$$\eta = \frac{1 - c_p/c}{1 + c_p}, \quad (4.7)$$

showing that the maximum silane dissociation efficiency is reached for pure silane ( $c \rightarrow 1$ ) for a given material crystallinity (constant  $c_p$  [124]).

Moreover, experiments presented in Fig. 4.3 are in good agreement with the previous equations and clearly show that in terms of silane utilization efficiency, pure silane plasmas are the most efficient. Thus, microcrystalline silicon ( $\phi_c = 60$  %) has been deposited from a pure silane plasma at a rate of 10.5 Å/s corresponding to the target deposition rate fixed previously.

#### 4.1.2 Pure silane regime optimization

To optimize the pure silane regime, the only remaining adjustable process parameters are the RF power input and the working pressure, because the silane flow rate is fixed through Eq. 3.47 and the hydrogen flow rate is zero. The effects of the RF input power on the deposition rate and on the silane depletion (and thus on the crystallinity) are presented in Fig. 4.4(a). We can distinguish two different regimes separated by a maximum in the deposition rate (12.3 Å/s) at a RF power input of 500 W. For lower power densities, since the silane flow rate is constant, the deposition is rate-limited by the lack of availability of silane dissociation products for deposition, because the silane depletion fraction is low (down to 0.547 at 150 W in Fig. 4.4(a)) and the silane concentration in the plasma remains too high for  $\mu c$ -Si:H deposition for such low depletion. On the other hand, for higher power densities, when the silane depletion fraction approaches one, the deposition rate falls because part of the dissociation products are lost in the pumping line in the form of polysilane or powder. The transition from a-Si:H to  $\mu c$ -Si:H deposition in Fig. 4.4(a) takes place between 500 and 750 W, corresponding to a relatively low power density of 0.19 - 0.28 W·cm<sup>-2</sup>. Moreover, the deposition rate at the transition from a-Si:H to  $\mu c$ -Si:H, 11.5 Å/s, is the closest to the maximum possible deposition rate (13.3 Å/s if all silane is dissociated and deposited uniformly).

Results of deposition performed at a RF power of 1 and 2 kW for pressures from 0.5 to 4 mbar are presented in Fig. 4.4(b) and show a maximum in deposition rate for a pressure of 2 mbar. At higher pressures, for both power levels, deposition rates decrease slightly with pressure. We believe that this is mainly because of the higher powder formation caused by the increase of silane dissociation product density and not because of a pressure dependence of the power coupling since the silane depletion fraction is stable within 0.95 to 1 (center Fig. 4.4(b)). The strong decrease in deposition rate when the pressure is decreased from 2 to 1 mbar is also not attributable to a reduction of the silane depletion and has also been observed for H<sub>2</sub>-diluted plasmas [98, 121]; it could be caused by a nonuniform plasma in the reactor with a higher density plasma around the glass substrate at low pressure, hence consuming more silane without affecting in a significant manner the thickness uniformity over the substrate area. However, it seems to be unlikely because the silane depletion fraction is in the 0.95 - 1 range, making it necessary to have a

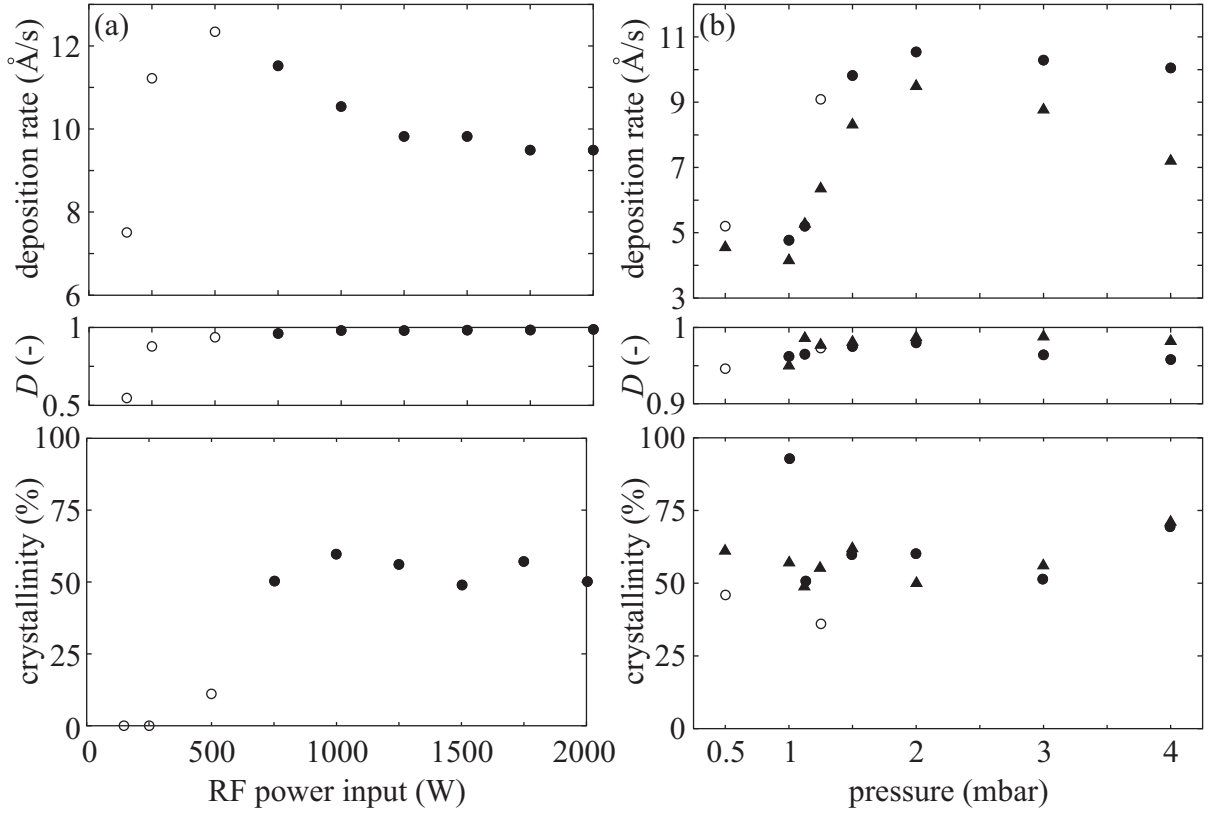


**Figure 4.4:** Deposition rate (top), silane depletion (center) and Raman crystallinity (bottom) as a function of (a) RF input power, performed at a pressure of 2 mbar, and (b) pressure, performed with RF power input of 1 (●) and 2 (▲) kW from pure silane plasmas. Silane flow rates were 82 sccm. Open and full symbols correspond to a-Si:H and  $\mu$ c-Si:H, respectively.

high silane depletion everywhere in the reactor in order to reach these high average values measured in the exhaust. Another possible cause of this strong increase in deposition rate is the role of disilane molecules. As shown by Hammad *et al* [125], a very small addition ( $\leq 0.6$  %) of disilane in the gas inlet drastically increases the deposition rate due to the increase of the contribution of higher-order silanes to the film growth. In the present case, no disilane was added in the gas inlet, but it may be produced directly in the discharge since we are concerned here with pure silane gas at relatively high working pressure.

The downward shift in deposition rate over the whole pressure range between the two curves performed at 1 and 2 kW can be plausibly attributed to the higher powder formation at higher power input [126] as deduced from Fig. 4.4(a). Even if the step in deposition rate between 1 and 2 mbar is not well understood, Fig. 4.4(b) confirms that the so-called "high-pressure depletion" regime [91, 121, 127] is interesting in terms of deposition rate and that - for the power inputs used - the pressure has no major effect on the crystallinity. Moreover, all  $\mu$ c-Si:H samples have a crystallinity factor between 50 to 60 % and even transition samples (○) contain a crystalline fraction of 46 and 36 % for the samples at 0.5 and 1.25 mbar (see Fig. 4.4(b)), respectively.

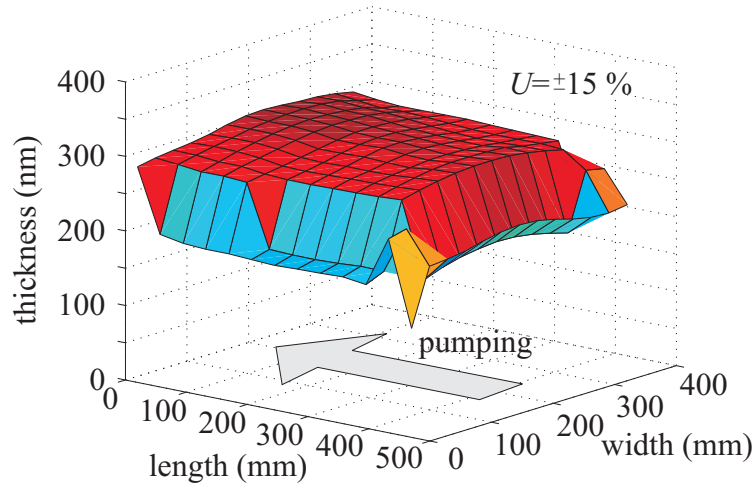


**Figure 4.5:** Thickness uniformity measured by light interferometry for deposition performed at 500 W at a pressure of 2 mbar and a silane flow rate of 82 sccm. The uniformity is of  $\pm 15\%$  over the whole substrate area and  $\pm 4\%$  with a 5 cm substrate edge exclusion.

### 4.1.3 Estimation of the polysilane or powder quantity

In Section 4.1.1, the silane flow rate was calculated in order to achieve a deposition rate of  $10 \text{ \AA/s}$ . For the estimate of 82 sccm, it was assumed that

1. almost all the silane is consumed in the plasma, but that a fraction of up to 25 % of the dissociation products may be lost in the pumping line in the form of powder or polysilane, and
2. the deposition rate (and thus the film thickness) is uniform over the whole electrode area including the substrate.

In a process totally free of polysilanes or powder (i.e. all  $\text{SiH}_4$  dissociated molecules contribute to film growth), with an input silane flow rate of 82 sccm, according to Eq. 3.47, the maximum achievable deposition rate is  $13.3 \text{ \AA/s}$  in the case of a fully-depleted silane flow (perfect dissociation efficiency  $\eta = 1$ ). Deposition rates above  $10 \text{ \AA/s}$  observed in Figs. 4.4(a) and (b) can be due either to processes producing a fraction of polysilanes less than 25 % or to a nonuniform deposition rate distribution over the electrode area, including the substrate.

Deposition at 500 W (2 mbar, 82 sccm of silane) shows that the film thickness uniformity, presented in Fig. 4.5, is  $\pm 15\%$  over the whole substrate area (including the nonuniformities due to the edge of the substrate and to the perturbation by the pumping side (see Fig. 4.5)). If only the central part ( $27 \times 37 \text{ cm}^2$ ) of the substrate is considered, the deposition rate nonuniformity falls to  $\pm 4\%$ . Similar uniformities have been found for depositions at different conditions (pressure, power, etc...) using pure silane. With regard to these observations, we can assume that the deposition rate is uniform over the whole substrate area in the range of around  $\pm 15\%$  taking into account the local effect of the

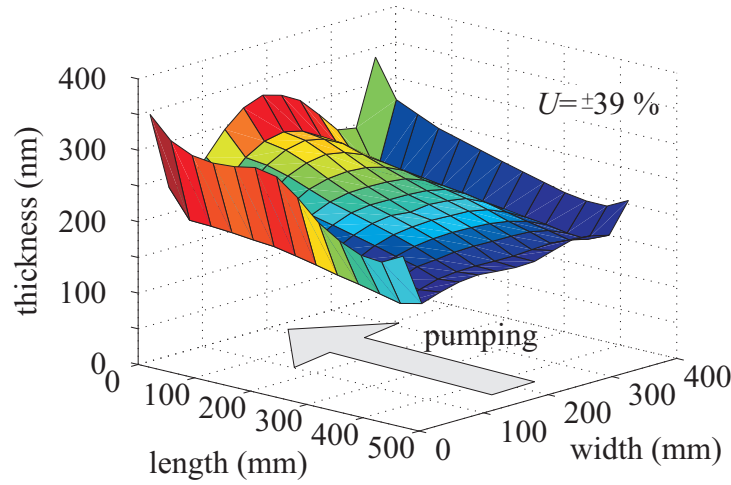


**Figure 4.6:** Thickness uniformity measured by light interferometry for deposition performed at 2000 W at a pressure of 2 mbar and a silane concentration of 6 %. The uniformity is of  $\pm 39$  % over the whole substrate area and 30 % with a 5 cm substrate edge exclusion.

substrate edge. Figure 4.6 shows that this good uniformity is not always achieved in this large area reactor, and that even with a uniform gas distribution over the large substrate area [60] we can observe, depending on the process parameters, influences of the pumping direction and lateral walls on the deposition uniformity. The increase in deposition rate at the substrate edges and in the pumping direction may be attributed to powder formation. Indeed, as shown by Hollenstein *et al* [69], powder forms preferably at RF electrode corner and at the glass edge where it is trapped around the substrate and induces an increase of the electron temperature [71, 128], hence locally increasing the silane dissociation and the deposition rate [129]. The increase of the deposition rate in the pumping direction may also be attributed to a cloud of negatively-charged particles whose density increases towards the pumping grid [69, 129].

Because of this good uniformity, the deposition rate measurement can be used together with the silane input flow rate and the depletion measurement to estimate the fraction of the input silane flow rate transformed into powder or polysilanes which are lost in the pumping line. In fact, the silane flowing into the reactor can be affected in three different ways:

1. a fraction  $(1 - \eta)$  of  $\text{SiH}_4$  is not dissociated and is pumped out without having any reaction with reactor walls or other gas molecules,
2. a fraction  $\eta f$  of  $\text{SiH}_4$ , where  $f$  is the deposition rate efficiency, i.e. the probability that silane dissociation products contribute to film growth, is dissociated and is deposited and thus contributes to the deposition rate, or
3. a fraction  $\eta(1 - f)$  of  $\text{SiH}_4$  is dissociated and is pumped out in the form of polysilane or dust particle.

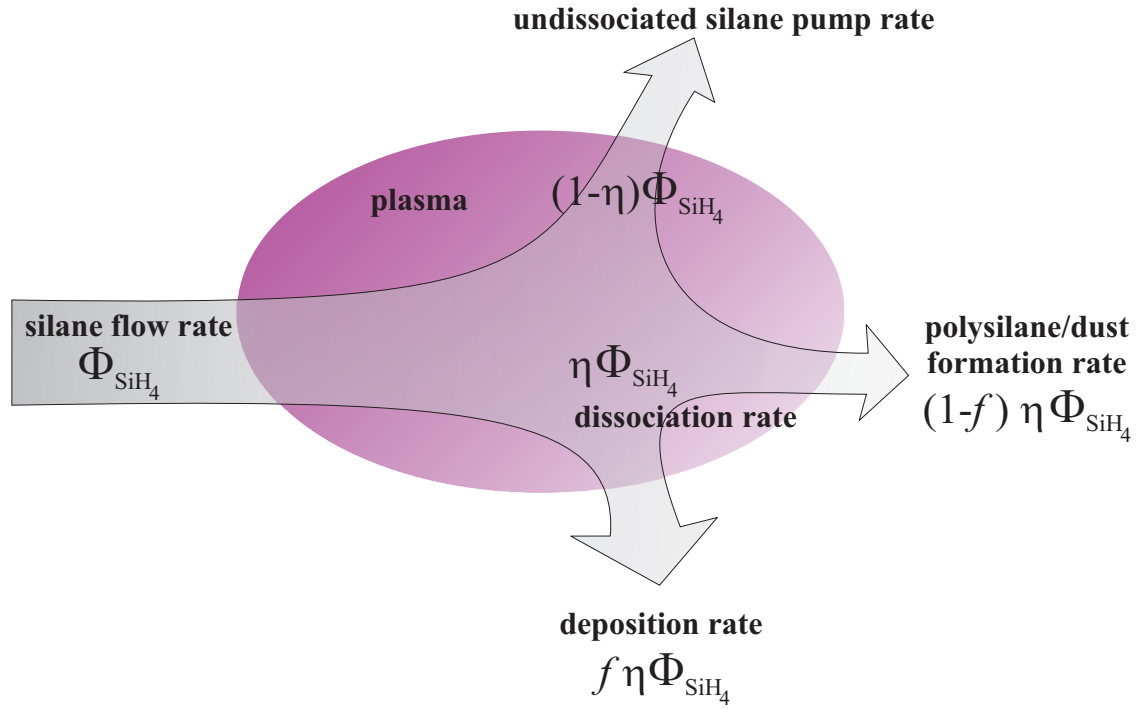


**Figure 4.7:** Schematic representation of overall silane utilization. An input silane molecule can be either undissociated, dissociated and transformed into polysilanes or powder, or dissociated and contribute to film growth.

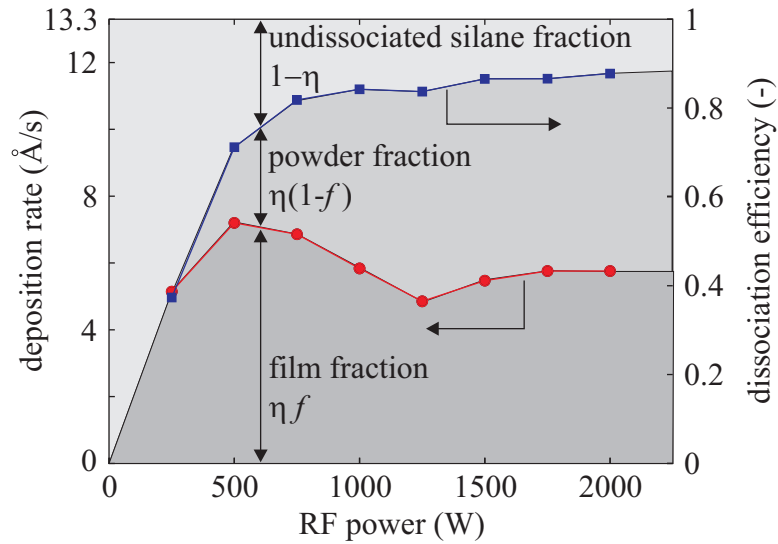


**Figure 4.8:** Graphic representation of the different utilizations of silane in the plasma using the deposition rate and the silane dissociation efficiency.

In fact, these estimations do not reflect exactly what happens in the reactor taken here as a "black-box". For example, the undissociated silane fraction ( $1 - \eta$ ) in fact takes

account also for dissociated silane which recombines back into silane and is pumped out. Following the same idea, the fraction  $f\eta$  of silane contributing to film growth also takes into account the polysilane and powder sticking onto the reactor walls, hence increasing the deposition rate.

The fraction  $f\eta$  of the silane flow which contributes to the film growth rate is represented by the ratio  $R/R_{\max}$  of the measured deposition rate to the maximum possible deposition rate (Eq. 3.47). Using the definition of  $\eta$  in Eq. 3.48, we finally obtain an experimental estimation of the fraction of the silane input flow transformed into polysilanes or powder which is pumped away:

$$(1 - f)\eta = \frac{D}{1 - (1 - D)c} - \frac{R}{R_{\max}}, \quad (4.8)$$

and can be schematized as in Fig. 4.8. According to the  $\pm 15$  % non-uniformity of the deposition rate mentioned previously, the maximum powder fraction for depositions performed at 500 W (a-Si-H, 12.3 Å/s, 2 mbar) and 750 W ( $\mu$ c-Si-H, 11.5 Å/s, 2 mbar) can be calculated as

$$[(1 - f)\eta]_{\max} = \frac{D}{1 - (1 - D)c} - \frac{(1 - U)R}{R_{\max}}, \quad (4.9)$$

with  $U$  the deposition uniformity. The polysilane or powder fraction is of  $\pm 9$  and  $\pm 19$  %, respectively, which remains below the initial assumed threshold value (25 %) of silane losses (Section 4.1.1). On the other hand, if the deposition is nonuniform the fraction of silane lost as powder is very difficult to estimate. For the film presented in Fig. 4.6 with a uniformity of  $\pm 39$  % the powder fraction stands between 25 and 44 % ( $R = 9.2$  Å/s,  $F_{\text{SiH}_4} = 120$  sccm,  $D = 0.719$  and  $c = 6.7$  %). Note that the powder fraction does not give any information about the size of the polysilanes or powder particles.

To summarize, both model and experiments have clearly shown that pure silane plasmas are the most efficient with regard to the silane dissociation efficiency and that the silane concentration in the plasma,  $c_p$ , can be low enough to deposit microcrystalline silicon from pure silane. That makes this type of process close to an ultimate cost-effective process for PV solar cells mass production. The only condition is that the silane flow rate has to be small enough to guarantee a very high dissociation efficiency necessary for microcrystalline silicon deposition, but the silane flow has to be sufficient to enable high deposition rate.

## 4.2 Optimization of the deposition efficiency of microcrystalline silicon

Previous results (Section 4.1) and simple plasma chemistry modeling (Section 3.2.1) have shown that high deposition efficiency, i.e. high gas utilization efficiency, can only be reached when high silane input concentration ( $> 30$  %) is used as shown in Fig. 4.3.



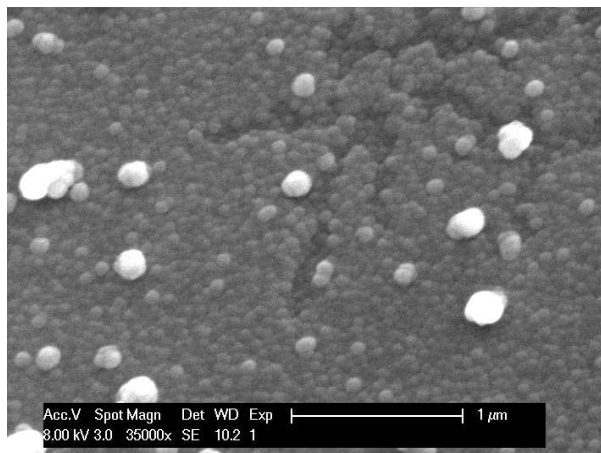


**Figure 4.9:** SEM imaging of dust contamination of microcrystalline film deposited from pure silane plasma.

Moreover, these results have shown that high input silane concentration was not incompatible with low silane concentration *in the plasma* [19, 124] because the silane is highly depleted for discharge conditions suitable for microcrystalline silicon deposition. However, it is probably not advisable to work with the extreme case of pure silane gas to obtain a material of good quality deposited at high rate. Polysilane and powder formation consuming silane in channels other than film growth [130] and possible contamination of final product with dust particles as shown in Fig. 4.9 may limit the use of very high silane concentrations.

The aim of this section is to establish a reactor-independent methodology to determine the optimum plasma conditions in terms of deposition rate, silane utilization fraction and material microstructure [131].

### 4.2.1 Initial process parameter selection: A short review

Before building any optimization procedure, we have to answer the question: Where should we start the optimization in the  $(D, c)$  plane? In other words, which are the plasma parameters (RF power, excitation frequency, interelectrode distance, gas flow rates and pressure) that will be adequate to start the procedure? This section makes a short review giving guidelines which should help to determine the most appropriate starting point of the process optimization technique presented in Section 4.2.2 for the deposition of films in the transition zone between amorphous and microcrystalline silicon where the material shows best performance for solar cell applications [40, 96].

#### RF power

Generally, the RF power input for  $\mu c$ -Si:H deposition is set to the maximum possible value for two main reasons:

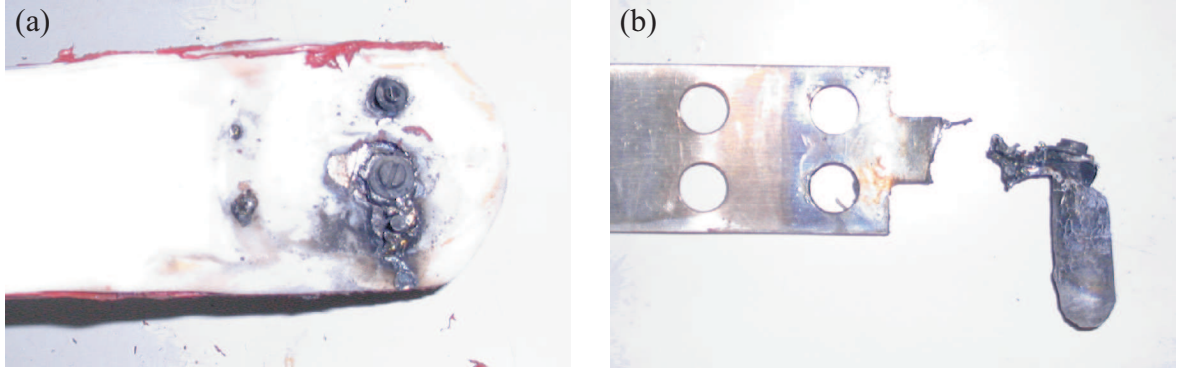


**Figure 4.10:** Results of too high power in the RF power stripline due to heating and melting of the imperfect electric contact.

1. The deposition rate increases with the RF power density [132] (in the absence of polysilane and powder formation) due to the increase of the silane depletion  $D$  (Sections 3.4 and 4.1.1);
2. for the same reason, the silane concentration in the plasma,  $c_p$ , is lower (Eq. 2.5) meaning that the silane in the plasma is more strongly-diluted with hydrogen, hence, the deposited material is more crystalline (Sections 3.4 and 4.1.1).

However, we have to take into account a potential up-scaling from this laboratory reactor to a larger area industrial reactor for mass production of solar cells. For example, a process developed in a small reactor with an excessively-high RF power density will not be suitable for solar cell production. The RF power input used here was 1000 W ( $0.37 \text{ W}\cdot\text{cm}^{-2}$ ), which is not the highest deliverable power of our generator (4 kW), nor the maximum power rating of our system including matching-box and reactor ( $\approx 3 \text{ kW}$ ), but corresponds to a power density which can be easily implemented in existing larger industrial reactors. The use of higher RF power will cause arcing problems [133], stripline heating (before melting as shown in Fig. 4.10) and other undesirable events which may abort the process, even if it was promising in a small laboratory reactor.

### Excitation frequency

According to previous studies, the excitation frequency should be set as high as possible, because of the higher deposition rates [23, 134] and higher silane depletion fractions [24] leading to films containing a larger crystalline fraction at very high frequencies (VHF) [124]. Moreover, the reduction of the ion bombardment energy of the film surface reduces the internal stresses of the film and improves the material quality [32]. However, as for the input RF power, up-scaling to industrial reactors limits the increase of the excitation frequency due to standing-wave nonuniformities as observed in large area reactors unless special precautions are taken [135]. For these reasons, an excitation frequency of 40.68 MHz has been chosen in this work because a quarter of the associated wavelength

( $\lambda/4 = c/4\nu_{RF} = 1.84$  m) is larger than the size of the KAI-S reactor (0.57 m), making the use of a lens-shaped electrode unnecessary.

### Interelectrode distance

The interelectrode distance is, in many cases, not really a variable because of the generally fixed geometry of the deposition apparatus. However - when possible - a reduction of the interelectrode distance may have some advantages when this reduction is associated with high pressures to reach the high-pressure-depletion regime [91, 136, 137] using narrow gap reactors to reduce the powder formation (see Chapter 6). Despite this interest, the effect of the interelectrode distance seems to be relatively small on plasma properties and results mainly in a shift of the plasma properties with regard to the pressure as it will be shown in Chapter 6. Effects of the interelectrode distance on discharge properties are not the concern of the present chapter and will be discussed more in detail in Chapter 6 dealing with powder formation, pressure and gap variation.

The interelectrode distance selected here was 18 mm (instead of the standard 25 mm) obtained by inserting a 7 mm aluminum plate on the grounded bottom part of the plasma reactor.

### Gas flow rates

The silane flow rate is a key parameter and has to be carefully chosen for two reasons: (i) A flow too small will limit the deposition rate due to the insufficient available raw material; (ii) on the other hand, a flow too high may lead to a low silane utilization efficiency and a large fraction of wasted raw material, increasing the cost of the final product. Hence, the choice of the silane flow rate will depend on the target deposition rate,  $R_{\text{target}}$ , the target silane utilization efficiency,  $u_{\text{target}}$ , and on the reactor size given by the total deposition area,  $A$ . Undissociated silane, polysilanes and powder formed in the plasma which are pumped out without contributing to the film growth, reduce the silane utilization efficiency  $u$  ( $u < 1$ ). Assuming that the film is uniformly deposited (see Section 4.1.1), the silane flow rate can be determined as follows [124, 130]:

$$F_{\text{SiH}_4}[\text{sccm}] = 104 \cdot \frac{R_{\text{target}}[\text{nm/s}]}{u_{\text{target}}} \cdot A [\text{m}^2]. \quad (4.10)$$

$R_{\text{target}}$  and  $u_{\text{target}}$  cannot be arbitrarily selected. If the chosen values are too high, it may be impossible to attain them, necessitating a new optimization with lower values of  $R_{\text{target}}$  and/or  $u_{\text{target}}$  as will be shown in Section 4.2.3. For the KAI-S reactor with a 18 mm interelectrode distance, for a target deposition rate of  $10 \text{ \AA/s}$ , the silane flow rate is 80 sccm if we suppose a silane utilization efficiency  $u_{\text{target}} = 0.75$ . If there were no silane wastage ( $u = 1$ ), the maximum possible deposition rate  $R_{\text{max}}$  would be  $13.3 \text{ \AA/s}$  for this example. The measured silane utilization efficiency is the ratio of the measured deposition rate to the maximum possible deposition rate ( $R/R_{\text{max}}$ ) as described in Section 4.1.3.

In order to start the optimization of the process in a powder free regime, the hydrogen flow has to be sufficiently high (i.e. the silane concentration sufficiently low) to begin in the standard highly hydrogen-diluted regime for transition material with silane concentration

typically less than 3 % [124]. It was fixed here at 2700 sccm, corresponding to an initial silane concentration of 2.9 %.

### Pressure

The deposition rate depends on the working pressure, especially around 1 - 2 mbar, where a strong increase with pressure has been observed in different reactors [98, 121, 130]. High pressure is also important in terms of crystallinity [88] due to the increase of the silane depletion fraction with pressure [124] due to a longer residence time. An additional advantage of high pressure is that the ion bombardment energy is reduced in a collisional sheath, and hence the film quality improved. However, to avoid powder formation, the working pressure should not be too high [138]. The starting point pressure was fixed at 2 mbar in order to benefit from the high deposition rate and to avoid powder formation. Note that the choice of the initial pressure depends on the interelectrode distance, for example, for a given RF power, the smaller the interelectrode distance, the higher the pressure needed to ignite the plasma as shown by Mai *et al* [122]. This observation is directly related to the Paschen law which links the discharge breakdown voltage to the product  $pd_{\text{gap}}$ , where  $p$  is the pressure and  $d_{\text{gap}}$  the interelectrode distance. To have a uniform plasma in the whole reactor - over and around the substrate - with a 18 mm gap and a RF power of 1000 W, the initial pressure should be 2 mbar or more.

To summarize, the chosen starting parameters were

- a RF power of 1000 W, corresponding to a power density of  $0.37 \text{ W}\cdot\text{cm}^{-2}$
- an excitation frequency of 40.68 MHz
- an interelectrode distance of 18 mm
- a silane flow rate of 80 sccm
- a hydrogen flow rate of 2700 sccm
- a pressure of 2 mbar.

Using these parameters, a film with a crystallinity of 55 % was deposited. The deposition rate was  $2.8 \text{ \AA/s}$ , corresponding to a silane utilization efficiency  $R/R_{\text{max}}$  of 21.4 %. The silane depletion was 0.31 positioning the starting point in the transition zone as presented in Fig. 4.11.

### 4.2.2 Optimization strategy

Since the material of interest for solar cell applications is  $\mu\text{c-Si:H}$  grown at the boundary zone between a-Si:H and  $\mu\text{c-Si:H}$  growth [40], the required process conditions are in the microstructure transition zone. We have seen in the previous section that the RF power, the excitation frequency, the interelectrode distance and the silane flow rate can be fixed, meaning that the only two remaining adjustable parameters are the pressure,  $p$ , and the

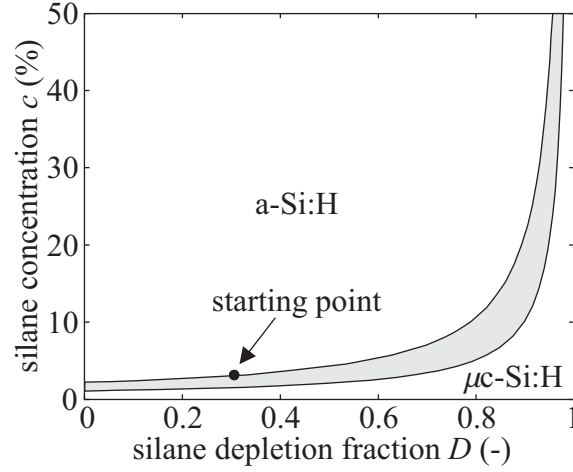


**Figure 4.11:** a-Si:H,  $\mu$ c-Si:H and transitional material (shaded) zones and position of the starting point for 1000 W, 2 mbar, 40.68 MHz, 18 mm interelectrode distance, 80 and 2700 sccm of  $\text{SiH}_4$  and  $\text{H}_2$ , respectively.

hydrogen flow rate,  $F_{\text{H}_2}$ . These two parameters can be varied independently and have effects on the deposition rate, deposition efficiency and film crystallinity.

Figure 4.12 shows that reducing the hydrogen flow rate, while keeping the silane flow rate and the pressure constant, increases the deposition rate and, hence, the silane utilization efficiency  $R/R_{\text{max}}$  from 21.4 % to 31.1 % for hydrogen flow rates of 2700 and 1000 sccm, respectively. This improvement of the silane utilization efficiency with silane input concentration is mainly because the total flow rate reduction, due to the decrease of  $F_{\text{H}_2}$  at constant  $F_{\text{SiH}_4}$ , increases the gas residence time and hence the silane depletion in the plasma. The variation of  $c$  and  $D$  with the hydrogen flow rate (Fig. 4.12(a)) can be deduced from the chemistry model presented in Chapter 3, for constant plasma

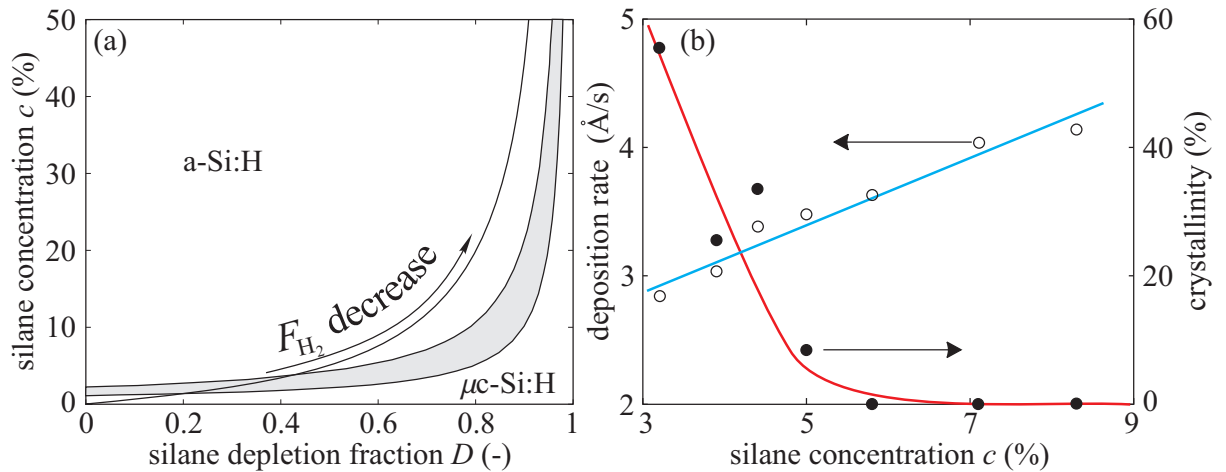


**Figure 4.12:** (a) Effect of  $\text{H}_2$  flow variation in the  $(D, c)$  space. (b) deposition rate (○) and Raman crystallinity (●) when the hydrogen flow is decreased, while the silane flow rate (80 sccm) and the pressure (2 mbar) are kept constant.

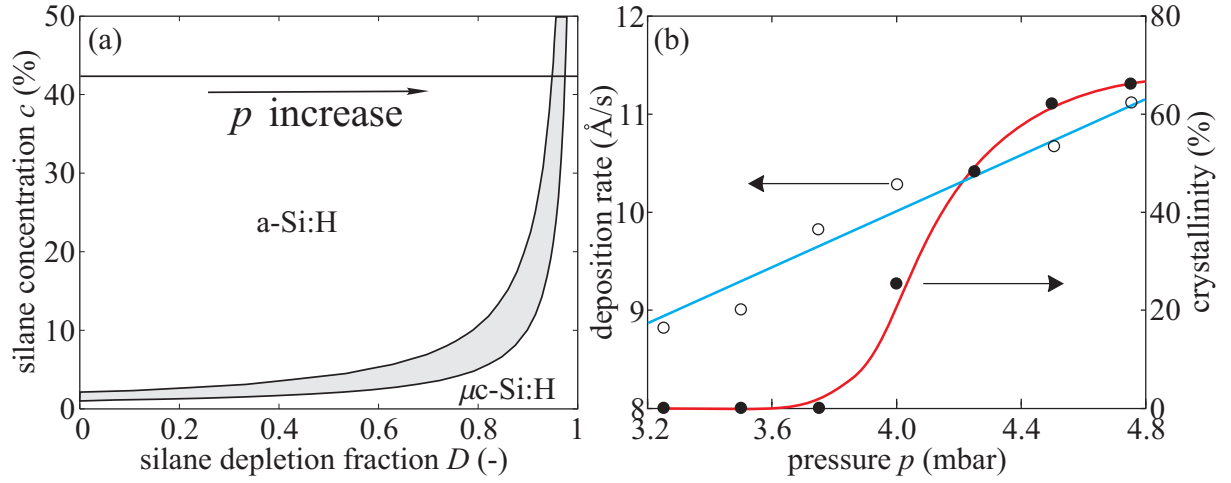


**Figure 4.13:** Effect of a pressure increase on (a)  $c$  and  $D$  and (b) deposition rate ( $\circ$ ) and Raman crystallinity ( $\bullet$ ) with constant silane and hydrogen flow rates of 80 and 150 sccm, respectively.

dissociation frequency, pressure and silane flow rate, as described in Section 4.1.1. The iso- $p$  curve presented in Fig. 4.12(a) correspond to  $B = 0.002$  (see Eqs. 4.1 and 4.3).

However, reducing the hydrogen flow rate does not guarantee a constant crystallinity of the deposited material. Indeed, by following the iso- $p$  curves from low to high silane concentrations, the contour moves away from the microstructure transition zone [124, 130], making the deposited material more amorphous as shown in Fig. 4.12(b), where decreasing the hydrogen flow rate from 2700 to 1000 sccm reduces the film crystallinity from 55 to 0 %.

The working pressure,  $p$ , which is the only other adjustable parameter, can be used to move back to the microstructure transition zone by changing the pumping speed while leaving the gas flow rates constant (Fig. 4.13(a)). This pressure variation changes the silane depletion fraction without changing the silane concentration as shown by the horizontal line in Fig. 4.13(a) and by the results of Chapter 3 (see Fig. 3.11(c)). This increase of the silane depletion fraction with the working pressure is mainly due to the increase of the gas residence time,  $\tau = 1/a$ , caused by the pumping speed reduction. Moreover, as shown in Fig. 4.13(b) the increase of the silane depletion with the pressure has two beneficial effects:

1. It increases the deposition efficiency and hence the deposition rate from Eq. 3.48 with increasing silane depletion,  $D$ , and constant silane concentration,  $c$ , and
2. the silane concentration in the plasma,  $c_p$ , is reduced, making the deposited material more crystalline.

However, as shown by Fig. 3.11(c), the measured silane depletion fraction goes through a maximum before decreasing back with increasing pressure, making the simple model - which predicts monotonic increase of  $D$  with pressure (solid line in Fig. 3.11(c)) - no longer correct for high pressures. To summarize, if, as recommended in Section 4.2.1, the starting point of the optimization is made at low pressure, increasing the pressure has

first a beneficial effect on both the deposition rate and the material crystallinity until a certain point before having a negative effect on the same parameters. This optimum pressure depends strongly on the interelectrode distance used [136, 139] and shifts to higher pressure while decreasing the interelectrode distance, explaining why high-pressure processes are generally performed in narrow gap reactors. Although this effect is not predicted by the analytical plasma chemistry model developed in Chapter 3, it has to be integrated into the optimization methodology because of its important effect on both the deposition rate and the film crystallinity. High pressure effects on the plasma chemistry model are described in more detail in Chapter 6.

Hence, by increasing the dissociation efficiency step-by-step by alternatively reducing the hydrogen flow rate  $F_{H_2}$  (at constant  $p$ ) and by increasing the pressure  $p$  (at constant  $F_{H_2}$ ) as shown in Fig. 4.14, it is possible to remain in the microstructure transition zone while increasing the deposition rate. This procedure is in agreement with a more descriptive approach by Mai *et al* [122].

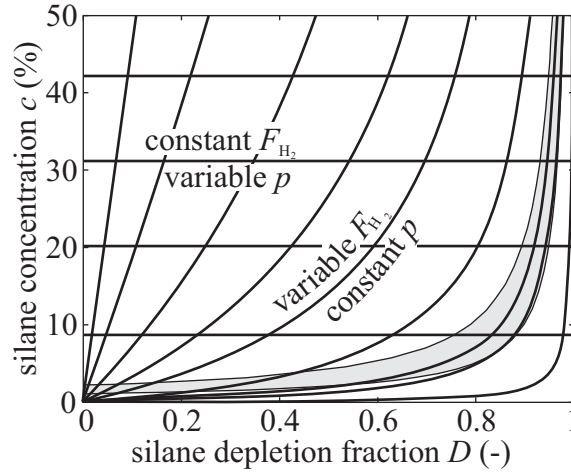


**Figure 4.14:** Iso- $p$  and iso- $F_{H_2}$  curves in the  $(D, c)$  plane.

### 4.2.3 Flow diagram

Following the conclusions of the previous section, a process flow diagram can be drawn up for the optimization of the deposition efficiency of microcrystalline silicon. In order for this flow diagram to be useful to operators having no silane depletion measurement, the only necessary equipment required to follow the flow diagram presented here are an *in situ* or *ex situ* deposition rate measurement and a film crystallinity measurement such as Raman spectroscopy or X-Ray diffraction (XRD). The method can be separated into two parts which are the selection of the initial parameters and the process optimization as sketched in Fig. 4.15.

The first step is to define the initial plasma parameters (RF power, excitation frequency, interelectrode distance and pressure) as reviewed in Section 4.2.1. The silane flow rate can be calculated using Eq. 4.10 and to start the optimization in a powder free

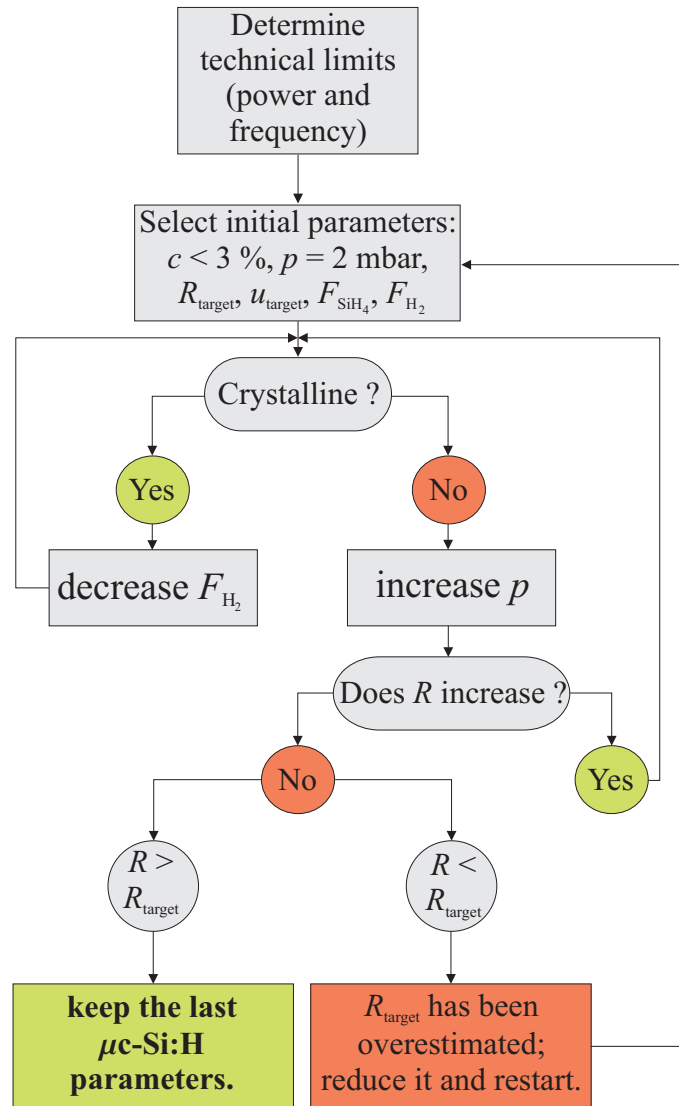


**Figure 4.15:** Flow diagram for  $\mu\text{c-Si:H}$  deposition optimization.

regime, a large hydrogen flow will be chosen, corresponding to a silane concentration lower than 3 %.

The optimization phase begins with the deposition of a film with the initial plasma parameters. Two cases can occur: The film can be microcrystalline or amorphous. In the first case, the deposition rate has to be increased by reducing the hydrogen flow rate, while keeping all the other plasma parameters constant. This reduction of  $F_{\text{H}_2}$  is continued until the deposited layer becomes amorphous as shown in Fig. 4.16(a), corresponding to the second case. To go back to the transition material from the amorphous region, the pressure has to be increased in order to reduce the silane concentration in the plasma by increasing



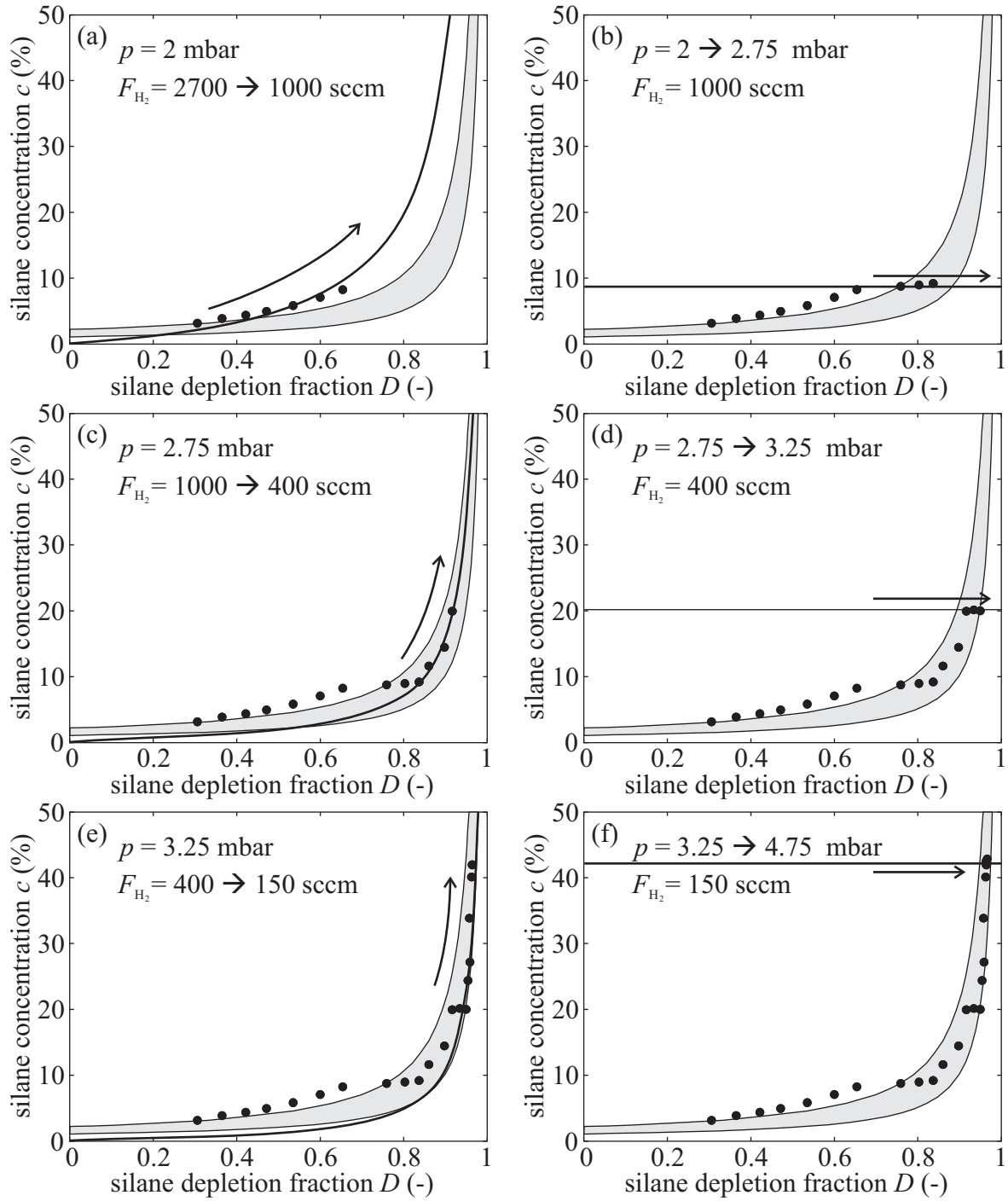


**Figure 4.16:** Multi-step experimental results following iso- $p$  (left column) and iso- $F_{H_2}$  (right column) curves.

the silane depletion as shown in the previous section and in Fig. 4.16(b). If the deposition rate increases, meaning that the silane depletion is still increasing with pressure, this step has to be repeated until the film again becomes microcrystalline, corresponding to the first case. The optimization is performed by alternating phases in which the hydrogen flow is reduced (Figs. 4.16(a), (c) and (e)) and phases in which the pressure is increased (Figs. 4.16(b), (d) and (f)) until the deposition rate no longer increases, meaning that the maximum value of  $D$  with pressure has been reached. In such a case, if the deposition rate is higher than the target deposition rate,  $R_{\text{target}}$ , all objectives are fulfilled and the last microcrystalline process conditions are maintained, or the optimization can be continued by using a higher target deposition rate. Otherwise, if the deposition rate,  $R$ , is lower than  $R_{\text{target}}$ , it means that the experimental silane utilization fraction,  $u$ , was smaller than the target utilization fraction,  $u_{\text{target}}$ , in Eq. 4.10. This can be due to undissociated silane, or to dissociated silane transformed into polysilanes and powder, which are pumped out of the system [130]. This means that  $R_{\text{target}}$  and/or  $u_{\text{target}}$  have been overestimated and cannot be attained for the deposition system used. Then  $R_{\text{target}}$  and/or  $u_{\text{target}}$  in Eq. 4.10 must be reduced, the silane flow rate updated, and the optimization restarted. Note that the deposition rate may be faster in reducing  $u_{\text{target}}$ , but that the silane utilization efficiency may be higher in reducing  $R_{\text{target}}$ .

Note that even if the plasma chemistry model on which this flow diagram has been constructed does not predict the decrease of the silane depletion fraction at high pressures, as mentioned previously, the optimization flow diagram accounts for this due to the test on the evolution of the deposition rate (see Fig. 4.15). However, to be sure that this optimization procedure works, the steps of both pressure and hydrogen flow rate have to be suitably small. Otherwise, it could happen that the deposition parameters are too far from the transition zone in the amorphous zone in the  $(D, c)$  plane, hence making impossible the return to the transition zone simply by increasing the pressure.

Following the optimization flow diagram presented in Fig. 4.15, the deposition rate, the deposition efficiency and the dissociation efficiency were monotonically increased over the 22 steps performed as shown in Fig. 4.17. The optimization procedure which started in the standard highly  $\text{H}_2$ -diluted regime with a measured silane concentration of 2.7 % finished in the high concentration regime with a final silane concentration of 43 %. This result confirms that, to achieve an efficient deposition process, we have to go towards pure silane, but not necessarily until pure silane. A microcrystalline silicon film with a Raman crystallinity of 66 % was deposited at a deposition rate of  $10.9 \text{ \AA/s}$  as shown in Fig. 4.17, which is higher than the initial target deposition rate ( $10 \text{ \AA/s}$ ), and corresponds to a silane utilization efficiency of 82.3 %, which is higher than the target utilization fraction (75 %). Moreover,  $\mu\text{c-Si:H}$  deposited in such a high concentration regime shows good electronic properties as demonstrated by a non-optimized single junction solar cell with a conversion efficiency of 6 % ( $V_{\text{oc}} = 492 \text{ mV}$ ,  $\text{FF} = 73 \%$ ,  $J_{\text{sc}} = 17 \text{ mA/cm}^2$ ) fabricated with a silane concentration of 50 % [140].

Note that the optimum reached using this procedure in a 18 mm interelectrode distance modified KAI-S reactor is reactor-dependent and the associated parameters cannot directly be used in another deposition reactor. However, this is not the fault of the optimization procedure itself, because it is only the final point which is reactor-dependent,

and not the method used to reach the optimum.

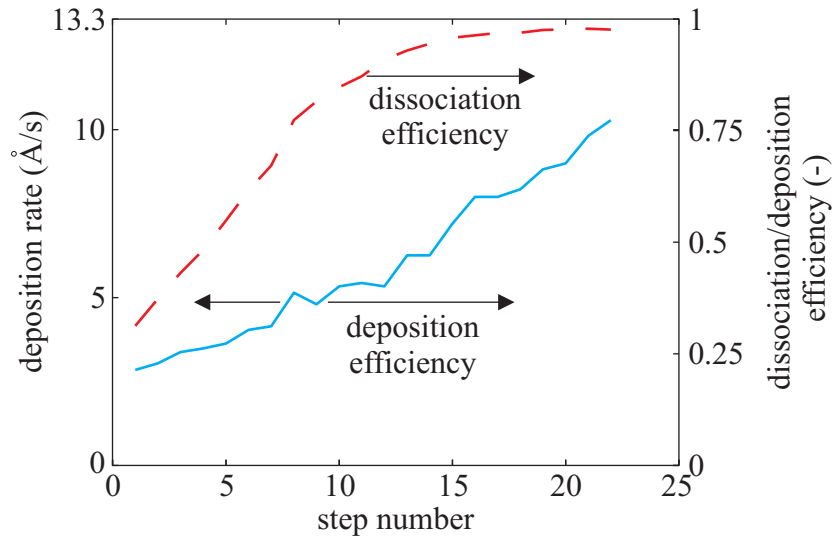


**Figure 4.17:** Measured deposition rate and efficiency (solid line) and dissociation efficiency (dashed line) as a function of the steps during the optimization based on the flow diagram presented in Fig. 4.15.

### 4.3 Conclusion

*In situ* FTIR absorption measurements have shown that the silane concentration in the plasma can be small enough even using pure silane in a RF discharge to allow microcrystalline silicon deposition as proven by *ex situ* Raman spectroscopy. To achieve such deposition without excessive RF input power, the silane flow rate has to be judiciously adjusted in order to have the lowest total flow rate as possible (the highest residence time), but with a sufficient silane flow rate to reach the target deposition rate. This approach fulfils the basic conditions of a suitable cost-effective process: A *uniform* layer ( $\pm 15\%$ ) of microcrystalline silicon has been deposited over a *large area substrate* ( $37 \times 47 \text{ cm}^2$ ) at *high rate* ( $11.5 \text{ Å/s}$ ) with an *efficient gas utilization* from a discharge producing a *low amount of powder* (19 % of silane input flow rate) with a *low power input* (750 W).

However, even with such a low amount of powder, substrate contamination can occur, meaning that the best process stands between the standard highly  $\text{H}_2$ -diluted regime and pure silane. An optimization procedure has been developed to determine the optimum plasma conditions in terms of deposition rate, silane utilization fraction and material crystallinity. Results have shown that if the initial plasma parameters are carefully selected, the deposition process can be optimized by varying only the working pressure and the hydrogen flow rate. The optimization methodology has been used to reach a process at a silane concentration of 46 % with a deposition rate of  $10.9 \text{ Å/s}$  of a material with a crystalline fraction of 66 % and a silane utilization efficiency of 82.3 %. A non-optimized single junction solar cell deposited with such conditions has shown a conversion efficiency of 6 %.



## Chapter 5

# Plasma and film growth at discharge ignition

In the previous chapters, the plasma was always considered to be in a chemical steady-state. From an experimental point of view, special care was taken to avoid perturbation from the transient plasma until steady-state equilibrium on the measured variables. First, the films produced were thicker than 200 nm to avoid perturbation of the Raman crystallinity measurement due to plasma-drift-induced amorphous incubation layer [141]; second, the plasma silane concentration measurements by IR absorption spectroscopy were performed several minutes after ignition. These precautions were motivated by times up to one minute or even more reported to reach chemical equilibrium, as by Feitknecht *et al* [118] and van den Donker *et al* [91].

The time necessary to reach plasma equilibrium is of great importance in the field of microcrystalline silicon solar cells, because the amorphous layer deposited before the silane is strongly depleted degrades the solar cell performances [141]. Moreover, the times reported by Feitknecht and van den Donker were measured in small laboratory reactors, therefore it might be expected that in large area production reactor it takes even longer to reach the steady-state. It is therefore crucial to choose an appropriate reactor design and plasma conditions that minimize the time until the final plasma composition suitable for the desired deposited film properties is reached. This chapter shows that large area, closed, directly-pumped, showerhead reactors can reach the theoretical minimum time to chemical equilibrium of less than one second [73].

### 5.1 Time-resolved plasma composition measurement

Steady-state equilibrium plasma silane concentration in previous chapters was determined using Fourier transform infrared (FTIR) absorption spectroscopy. This measurement was performed in the exhaust line (Fig. 2.6), therefore there was a delay corresponding approximately to the gas residence time between an event in the reactor and its detection. Moreover, the FTIR acquisition duration was about 90 seconds, making this technique inappropriate for fast time-resolved measurements. Optical emission spectroscopy (OES) has been used to determine the plasma evolution as a function of time, because it offers

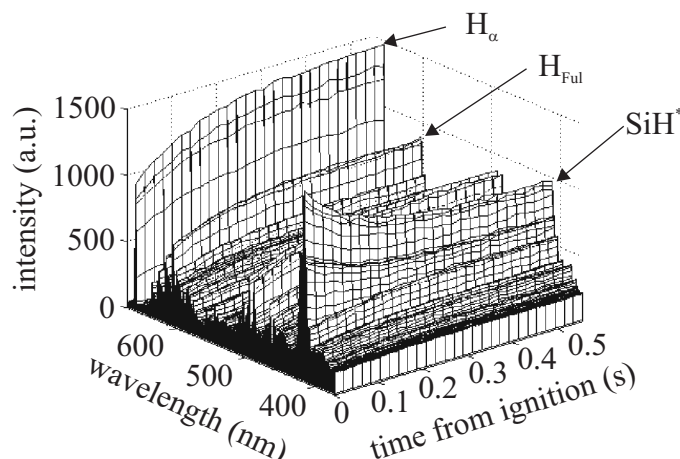


**Figure 5.1:** Emission spectrum of a  $\text{SiH}_4\text{-H}_2$  discharge with  $p = 0.4$  mbar and  $c = 5$  % during 0.5 s following plasma ignition.

two main advantages compare to FTIR: (i) It measures directly the plasma and not the gas in the exhaust, and (ii) the acquisition time can be very short, down to 20 ms with the spectrometer used, making possible time resolved experiments. The experimental arrangement and specifications are detailed in Section 2.2.3.

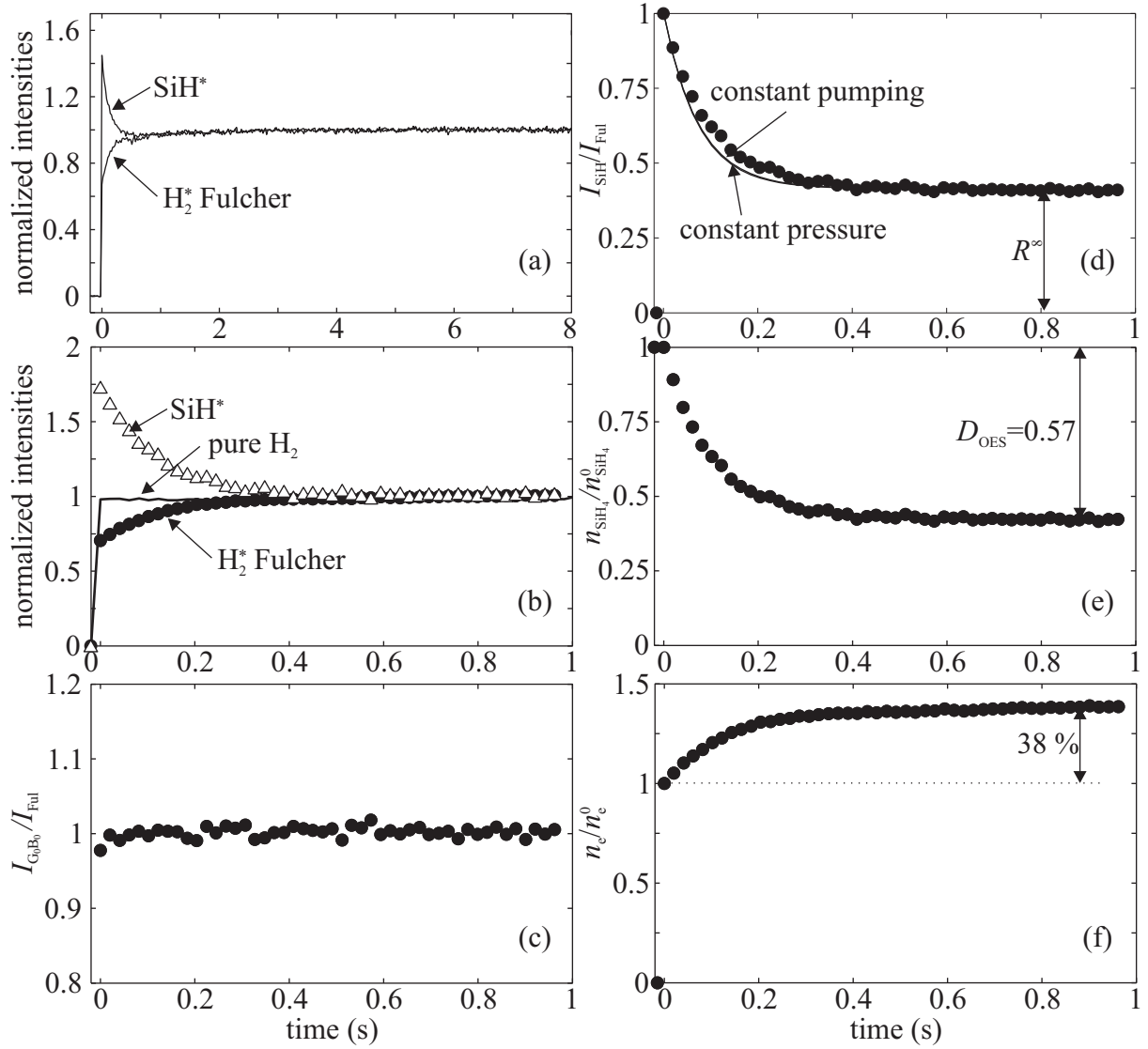
The experimental procedure was as follows: First, the plasma was ignited and the reflected power was set to zero during steady-state operation with the chosen plasma parameters. These settings were then fixed and the plasma turned off. Time-resolved OES data acquisition was then started and the RF power turned back on. This procedure makes adjustments of power matching unnecessary at plasma ignition.

## 5.2 OES measurements:

### I. Highly-diluted silane

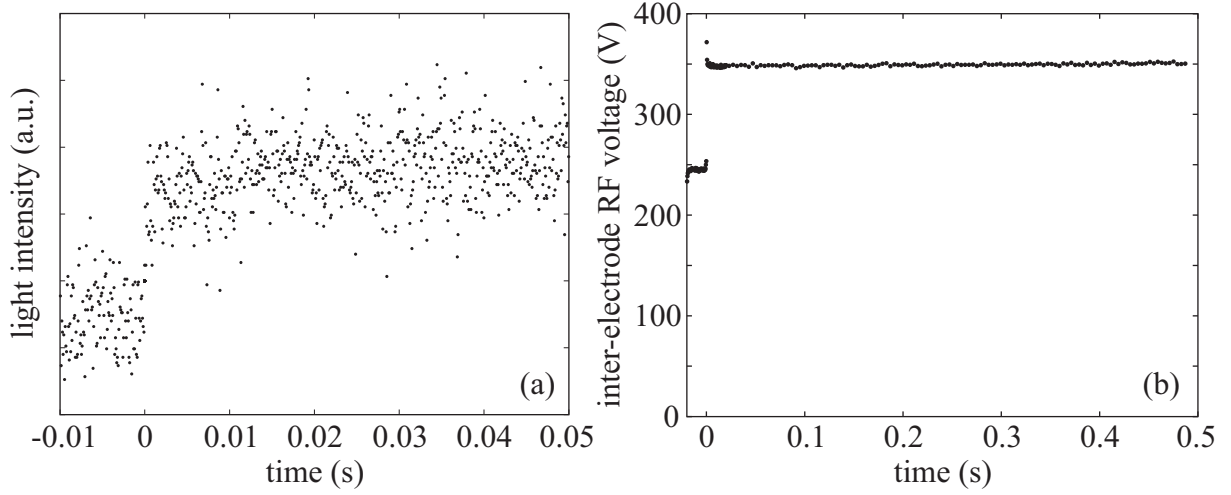
Figure 5.1 presents the time evolution over 0.5 seconds following plasma ignition of the optical emission spectrum of a mixture of 5 % silane (25 sccm) in hydrogen (475 sccm) at a pressure of 0.4 mbar and a RF power of 500 W. The relative intensity of the silane radical  $\text{SiH}^*$  and the hydrogen Fulcher  $\text{H}_2^*$  from the same data are plotted in Fig. 5.2(a) over 8 seconds after plasma ignition. The stable emission spectrum shows that there is no longer time variation. This very short time to equilibrium - much less than 1 second - contrasts with the results reported by Feitknecht *et al* [118] and van den Donker *et al* [91] which were performed in small laboratory reactors. In fact, the steady-state in the present work is reached before the second point is acquired in their study. This important difference is the center of interest of the present chapter and the following analysis and models are used to give a physical explanation of this phenomenon.

Figure 5.2(b) also presents the hydrogen Fulcher  $\text{H}_2^*$  relative emission for a pure hydrogen plasma for the same plasma conditions (500 sccm, 0.4 mbar, 500 W). In this pure  $\text{H}_2$



**Figure 5.2:** Time-resolved optical emission measurement and interpretation for a discharge performed at  $p = 0.4$  mbar,  $c = 5\%$ ,  $F_{\text{tot}} = 500$  sccm and  $P_{\text{RF}} = 500$  W. (a)  $\text{SiH}^*$  and  $\text{H}_2^*$  Fulcher emission intensities, (b) same emission intensities normalized and background subtracted, (c) hydrogen intensities ratio, (d)  $\text{SiH}^*$  to  $\text{H}_2^*$  Fulcher ignition normalized ratio, (e) silane density fraction and (f) electron density variation.

case, the time to steady-state equilibrium is shorter than the OES sampling time (20 ms), and as shown by the faster acquisition performed with a photomultiplier tube (Fig. 5.3(a)), it is even shorter than 1 ms. Hence, there are no significant unresolved time-dependent features within the first 20 ms sampling period of the optical spectrometer. This quasi-instantaneous response of the hydrogen plasma shows also that the RF power delivery is sufficiently fast to allow the observation of real time-evolution of the chemistry and not artifacts due to RF source time-variation, and this was confirmed by quasi-instantaneous



**Figure 5.3:** (a) Optical emission at ignition measured by a photomultiplier tube of a pure hydrogen discharge and (b) interelectrode voltage for the discharge containing 5 % of silane at  $p = 0.4$  mbar.

interelectrode RF voltage amplitude stabilization at final level (Fig. 5.3(b)).

The time response difference between plasmas with and without silane shows the difference between reactive and non-reactive plasmas. In pure hydrogen plasmas, the molecular hydrogen is dissociated by electron impact and recombines on reactor walls. In RF plasmas, the atomic hydrogen density is much less than the molecular density, therefore the emission spectrum does not show any time variation because the plasma composition is constant. On the other hand, once silane is dissociated by electron impact, it deposits on reactor walls and does not recombine into a silane molecule (since silicon etching is negligible [55]), hence the plasma composition varies as a function of time. In the extreme case of a pure silane without pumping and inlet flow, the silane concentration changes from 100 % down to 0 % (pure hydrogen), but it necessitates a certain time to consume all the silane molecules.

Using the OES analysis method presented in Section 2.2.3, the time development of the silane depletion fraction presented in Fig. 5.2(e) can be deduced from the ratio of normalized  $\text{SiH}^*$  and  $\text{H}_2^*$  intensities (Fig. 5.2(d)) from the emission spectra time-evolution given in Fig. 5.2(b). The time constant for an exponential fit of  $R^t$  and  $n_{\text{SiH}_4}^t$  is  $\sim 0.1$  s. At steady-state  $R^\infty = 0.41$  leading to a silane depletion at equilibrium measured by OES  $D_{\text{OES}} = 0.58$ . In this particular case of low pressure and low silane concentration, the value of  $D_{\text{OES}}$  cannot be compared to the one measured by FTIR,  $D_{\text{FTIR}}$ , because the partial pressure of silane at equilibrium ( $p_{\text{SiH}_4} = 0.008$  mbar) is at the limit of the detection with the FTIR setup used [142]. The comparison between  $D_{\text{OES}}$  and  $D_{\text{FTIR}}$  will be made for more adequate mixtures in the following sections.

Figure 5.2(c) shows that the electron temperature variation,  $T_e^t$ , which can be deduced from the ratio of  $I_{\text{G}_0\text{B}_0}^t/I_{\text{Ful}}^t$  is smaller than 4 %, corresponding to 0.1 eV, and therefore the elimination of  $X(T_e^t)$  to obtain  $R^t$  in Eq. 2.11 is legitimate. The electron density,



$n_e^t$ , varies in a much more significant manner of 38 % with a time constant of 0.13 s as shown by the ratio  $I_{\text{SiH}}^t/I_{\text{SiH}}^0$  in Fig. 5.2(f). This variation of electron density is probably due to the small interelectrode voltage variation at ignition (Fig. 5.3(b)) caused by a slow matching change due to plasma chemistry change. Moreover, the exponential fits of  $n_e^t$  and  $n_{\text{SiH}_4}^t$  are similar, probably because they are inter-dependent.

## 5.3 Time-resolved models

The zero-dimensional model presented in Chapter 3 was considered only in the case of a steady-state situation, i.e. it is valid only after several seconds (or more for open reactors) after plasma ignition. Although this model can be generalized by adding a time-dependence in the chemical system presented in Eqs. 3.7-3.10. The same assumptions have to be considered (see Chapter 3 for details):

1. The plasma is uniform over the whole electrode area, which is true when a shower-head Plasma-Box<sup>TM</sup> reactor is used [60].
2. The plasma is dominated by electron dissociation collisions, which is reasonable if the pressure is limited to low values where no powder is formed [74].
3. The pumping rate is the same for all gases.
4. The total pressure is the sum of the partial pressure of silane and hydrogen molecules, i.e. the partial pressure of radicals is negligible compared to those of molecules [20].

Then, the balance equations for silane and hydrogen molecules (Eqs. 3.8 and 3.9) with a time-dependency (denoted by the "t" exponent) become:

$$\Phi_{\text{SiH}_4} - (k^t n_e^t + a^t) n_{\text{SiH}_4}^t = \dot{n}_{\text{SiH}_4}^t \quad (5.1)$$

and

$$\Phi_{\text{H}_2} + 2k^t n_e^t n_{\text{SiH}_4}^t - a^t n_{\text{H}_2}^t = \dot{n}_{\text{H}_2}^t, \quad (5.2)$$

respectively, where  $\Phi_j$  refer to the inlet flow rate of silane and hydrogen in molecule·m<sup>-3</sup>·s<sup>-1</sup>,  $k^t$  the electron-temperature-dependent dissociation rate constant of silane in s<sup>-1</sup>,  $n_e^t$  the electron density in m<sup>-3</sup>,  $a^t$  the pumping rate in s<sup>-1</sup> and  $n_j^t$  the molecule density in m<sup>-3</sup>. The sum of the two previous equations gives the differential equation of the total density  $n_{\text{tot}}^t = n_{\text{SiH}_4}^t + n_{\text{H}_2}^t = p^t/(k_B T)$ :

$$\Phi_{\text{SiH}_4} + \Phi_{\text{H}_2} + k^t n_e^t n_{\text{SiH}_4}^t - n_{\text{tot}}^t a^t = \dot{n}_{\text{tot}}^t \quad (5.3)$$

This latter equation allows variations of both the total pressure (through the total density) and the pumping rate. Generally, all experiments or production processes are performed at constant pressure to guarantee reproducibility. This can be performed by using a butterfly valve to control the exhaust conductance or by varying the pumping speed by adjusting the speed of the pumps or the flow rate of ballast gas in the pumps. This constant pressure

case would mean that the time derivative of the total density is equal to zero,  $\dot{n}_{\text{tot}}^t = 0$ . However, the response of the experimental pressure control is not instantaneous and the constancy of the pressure cannot be guaranteed. At the other extreme, we can work at constant pumping rate,  $\dot{a}^t = 0$ , where the position of the butterfly valve, the speed of the pumps or the ballast flow rate is fixed and the pressure can freely change. In reality, all processes will stand between these two limits. Hence, by solving these two special cases we will obtain the upper and lower boundaries of all possible experimental situations.

From an experimental point of view, the constant pressure estimate of the silane depletion measured by OES,  $D_{\text{OES}}$ , presented in Section 2.2.3 has to be corrected for the case of constant pumping rate. This can be made by setting  $n_{\text{SiH}_4}^t = n_{\text{SiH}_4}^0 - \delta^t$  and  $n_{\text{H}_2}^t = n_{\text{H}_2}^0 + G\delta^t$ , where  $\delta^t$  is the time-dependent decrement of silane density, and  $G\delta^t$  the time-dependent increment of hydrogen density. For the case of constant pressure  $G = 1$ , and for the constant pumping rate case it can be easily shown, using Eqs. 5.1 and 5.2, that  $G = 2$ . For all intermediate cases of pressure variation without a constant pumping rate,  $G \in [1, 2]$ . Hence, from the definition of the silane concentration (Eq. 2.4) and normalized emission intensity ratio (Eq. 2.11), the estimated silane density variation is

$$\frac{n_{\text{SiH}_4}^t}{n_{\text{SiH}_4}^0} = \frac{1 + c(G - 1)}{Gc + (1 - c)/R^t}, \quad (5.4)$$

where  $G = 1$  gives the same expression as for constant pressure (Eq. 2.12), and  $G = 2$  gives the expression for constant pumping rate. The estimated steady-state silane depletion can be then determined from the value  $R^\infty$  at steady-state

$$D_{\text{OES}} = \frac{1 - R^\infty}{1 + G \frac{c}{1-c} R^\infty}. \quad (5.5)$$

This latest expression with  $G = 1$  is the same as the one for constant pressure presented in Section 2.2.3. This definition of the fraction of depleted silane shows that the two boundaries determined by the cases  $G = 1$  and  $G = 2$  may be very close from each other for both cases of low silane concentration and small emission ratio variation (i.e. low value of the silane depletion). This is due to the fact that  $G$  represents the silane contribution to the molecular hydrogen density. Hence, if the amount of input silane or the amount of dissociated silane is small, its contribution to molecular hydrogen density is negligible and working at constant pressure or constant pumping rate is almost the same.

### 5.3.1 Solution for constant pumping speed

For the case of constant pumping speed, the time evolution of the silane density,  $n_{\text{SiH}_4}^t$ , can be determined from Eq. 5.1 using a constant pumping rate  $a^t = a^0 = \Phi_{\text{SiH}_4}/n_{\text{SiH}_4}^0$  and a constant dissociation frequency  $k^t n_e^t = k n_e$ :

$$\frac{\dot{n}_{\text{SiH}_4}^t}{n_{\text{SiH}_4}^t - n_{\text{SiH}_4}^\infty} = - (k n_e + a^0), \quad (5.6)$$

where  $n_{\text{SiH}_4}^\infty = \Phi_{\text{SiH}_4} / (kn_e + a^0)$  is the silane density at steady-state<sup>1</sup>. Integrating Eq. 5.6 gives the silane number density

$$n_{\text{SiH}_4}^t = n_{\text{SiH}_4}^\infty + (n_{\text{SiH}_4}^0 - n_{\text{SiH}_4}^\infty) \exp \left[ - (kn_e + a^0) t \right]. \quad (5.7)$$

This corresponds to the results obtained by van den Donker *et al* [143] for their "local depletion" which corresponds to our "global" depletion since we are concerned here by the case of a closed Plasma-Box<sup>TM</sup> reactor which is not affected by silane back-diffusion (see Sec. 5.5 for details). Using the definition of the fractional silane depletion,  $D$ , the previous equation can be re-written as

$$n_{\text{SiH}_4}^t = n_{\text{SiH}_4}^0 - Dn_{\text{SiH}_4}^0 \left\{ 1 - \exp \left[ - (kn_e + a^0) t \right] \right\}, \quad (5.8)$$

and the corresponding solution for time-dependent molecular hydrogen density is

$$n_{\text{H}_2}^t = n_{\text{H}_2}^0 + 2Dn_{\text{SiH}_4}^0 \left\{ 1 - \exp \left[ - (kn_e + a^0) t \right] \right\}. \quad (5.9)$$

### 5.3.2 Solution for constant pressure

The initial conditions before ignition are the same for the present constant pressure case as for the previous constant pumping rate case, and the pre-ignition pumping speed is then  $a^0 = \Phi_{\text{SiH}_4} / n_{\text{SiH}_4}^0 = \Phi_{\text{H}_2} / n_{\text{H}_2}^0 = (\Phi_{\text{SiH}_4} + \Phi_{\text{H}_2}) / n_{\text{tot}}^0$ . But now the pressure is kept constant, hence  $\dot{n}_{\text{tot}}^t = 0$  in Eq. 5.3 and the pumping rate has to change instantaneously at ignition from  $a^0$  to  $a^{\text{ign}} = a^0 + kn_e c$  assuming that  $k^t n_e^t = kn_e$  is constant. The time-dependent pumping rate can be defined from its value at ignition as

$$a^t = a^{\text{ign}} - \Delta^t. \quad (5.10)$$

Inserting this latter in Eq. 5.3 and re-arranging, the time-dependent silane and hydrogen density for constant pressure are, respectively,

$$n_{\text{SiH}_4}^t = n_{\text{SiH}_4}^0 - \Delta^t \cdot \frac{n_{\text{tot}}}{kn_e} \quad \text{and} \quad n_{\text{H}_2}^t = n_{\text{H}_2}^0 + \Delta^t \cdot \frac{n_{\text{tot}}}{kn_e}. \quad (5.11)$$

Substituting these expressions in the silane balance equation (Eq. 5.1), we obtain the following non-linear first order equation for  $\Delta^t$ :

$$\dot{\Delta}^t = (\Delta^t)^2 - \Delta^t \left( kn_e + a^0 + \frac{kn_e}{p/k_B T} n_{\text{SiH}_4}^0 \right) + \frac{kn_e}{p/k_B T} [(kn_e + a^0) n_{\text{SiH}_4}^0 - \Phi_{\text{SiH}_4}]. \quad (5.12)$$

The latter can be solved by using boundary conditions on  $\Delta^t$ , which are  $\Delta^0 = 0$  and  $\dot{\Delta}^\infty = 0$ , and the general solution of this differential equation given by

$$\Delta^t = \frac{\Delta_1 \{1 - \exp [(\Delta_1 - \Delta_2)t]\}}{1 - \Delta_1/\Delta_2 \cdot \exp [(\Delta_1 - \Delta_2)t]}, \quad (5.13)$$

---

<sup>1</sup>In Chapter 3 this was defined as  $n_{\text{SiH}_4}$  without the " $\infty$ " superscript. This change in notation has been done in order to treat all variables as time-dependent and to avoid confusion between steady-state, initial and time-variable values.

where  $\Delta_1 = kn_e c D$  and  $\Delta_2 = kn_e(1+c) + a^\infty$  are the solutions of Eq. 5.12 at steady state ( $t \rightarrow \infty$ ) with  $\Delta_2 > \Delta_1$ . Using Eq. 3.45 linking  $D$  to  $kn_e$  and  $a^\infty$ , the final solution can be written as

$$\Delta^t = \frac{kn_e c D [1 - \exp(-t/\tau_p)]}{1 - \frac{cD^2}{1+c} \exp(-t/\tau_p)}, \quad (5.14)$$

where

$$\tau_p = \frac{1-D}{a^0} \cdot \frac{1+c(1-D)}{1+c(1-D^2)} \quad (5.15)$$

is the equilibration time constant for the case of constant pressure process. The time-dependent silane density is then

$$n_{\text{SiH}_4}^t = cn_{\text{tot}} \left[ 1 - D \frac{1 - \exp(-t/\tau_p)}{1 - \frac{cD^2}{1+c} \exp(-t/\tau_p)} \right], \quad (5.16)$$

and the time-dependent molecular hydrogen density

$$n_{\text{H}_2}^t = n_{\text{tot}} \left[ (1-c) + cD \frac{1 - \exp(-t/\tau_p)}{1 - \frac{cD^2}{1+c} \exp(-t/\tau_p)} \right]. \quad (5.17)$$

### 5.3.3 Comparison of model boundaries

Since both models for constant pressure and constant pumping rate presented in the previous sections are based on the same assumption of constant dissociation frequency,  $kn_e$ , the comparison between the two boundaries (constant  $a$  and constant  $p$ ) is valid. The normalized silane densities to initial value are:

$$\text{constant pumping speed : } n_{\text{SiH}_4}^t / n_{\text{SiH}_4}^0 = 1 - D [1 - \exp(-t/\tau_a)], \quad (5.18)$$

$$\text{constant pressure : } n_{\text{SiH}_4}^t / n_{\text{SiH}_4}^0 = 1 - \frac{D [1 - \exp(-t/\tau_p)]}{1 - \frac{cD^2}{1+c} \exp(-t/\tau_p)}, \quad (5.19)$$

where the  $\tau_a$  and  $\tau_p$  are the time constants for constant pumping speed and pressure, respectively, and are given by

$$\tau_a = \frac{1-D}{a^0} \quad \text{and} \quad \tau_p = \frac{1-D}{a^0} \cdot \frac{1+c(1-D)}{1+c(1-D^2)}. \quad (5.20)$$

The corresponding normalized molecular hydrogen density for both limits are:

$$\text{constant pumping speed : } n_{\text{H}_2}^t / n_{\text{H}_2}^0 = 1 + 2D \left( \frac{c}{1-c} \right) [1 - \exp(-t/\tau_a)], \quad (5.21)$$

$$\text{constant pressure : } n_{\text{H}_2}^t / n_{\text{H}_2}^0 = 1 + \left( \frac{c}{1-c} \right) \frac{D [1 - \exp(-t/\tau_p)]}{1 - \frac{cD^2}{1+c} \exp(-t/\tau_p)}. \quad (5.22)$$

The pressure variation,  $p^t$ , at constant pumping speed is given by

$$p^t = p^0 \{1 + cD [1 - \exp(-t/\tau_a)]\}, \quad (5.23)$$

and the pumping speed variation,  $a^t$ , at constant pressure by

$$a^t = a^0 + kn_e c \left[ 1 - D \frac{1 - \exp(-t/\tau_p)}{1 - \frac{cD^2}{1+c} \exp(-t/\tau_p)} \right]. \quad (5.24)$$

The inter-relation between the silane depletion,  $D$ , and the silane dissociation frequency,  $kn_e$ , is given by

$$\left[ \frac{kn_e}{a^0} \right]_a = \frac{D}{1-D} \quad \text{and} \quad \left[ \frac{kn_e}{a^0} \right]_p = \frac{D}{1-D} \cdot \frac{1}{1+c(1-D)}, \quad (5.25)$$

for constant pumping speed and pressure, respectively. Note that for the case of microcrystalline silicon deposition, which is the concern of this work, these two latter expressions are very close to each other because of the low silane concentration in the plasma,  $c_p = c(1-D)$ , needed to grow microcrystalline silicon (Chapter 3).

### 5.3.4 Comparison of the model with OES measurements

In order to determine the time evolution of silane and hydrogen normalized intensities given by Eqs. 5.18 - 5.22, the time constants  $\tau_a$  and  $\tau_p$  and therefore the pumping rate before ignition  $a^0$  have to be estimated. This can be performed through Eq. 3.46 ( $a^0 = 6.1 \cdot 10^{-6} T_{\text{gas}} F_{\text{tot}} / (pV)$ ) for given total gas inlet flow rate, pressure and temperature. For the conditions presented in Sec. 5.2, this gives a pumping speed of  $a^0 = 5.7 \text{ s}^{-1}$  and hence a gas residence time  $1/a^0 = 0.18 \text{ s}$ . The silane depletion fraction can be estimated by using Eq. 5.5 with  $R^\infty$  and is 0.58 for constant pressure ( $G = 1$ ) and 0.56 for constant pumping speed ( $G = 2$ ); the corresponding time constants are  $\tau_p = 0.074 \text{ s}$  and  $\tau_p = 0.077 \text{ s}$ . The difference between the two boundaries is very small because the silane is strongly diluted ( $c = 5 \%$ ) and therefore its contribution to total hydrogen outflow is weak, i.e.  $p^t$  is almost constant for constant  $a$ , and  $a^t$  is almost constant for constant  $p$ . The substitution of these values in Eqs. 5.18 - 5.22 allows to represent the modeled normalized intensity ratio in Fig. 5.2(d). The comparison between measurements and model shows a reasonably good agreement, hence validating once more the analytical plasma chemistry modeling approach presented in this work. Figure 5.2(d) shows that the modeled ratio is smaller than the measured ratio over the whole range between the normalization limits  $t = 0$  and  $t \rightarrow \infty$ . This is due to the electron density increase from ignition to steady-state (Fig. 5.2(f)), which makes the dissociation efficiency used at steady-state,  $kn_e$ , greater than the time-dependent dissociation efficiency,  $kn_e^t$ , overestimating the silane dissociation rate before the steady-state is reached.

This very short time response of the plasma at ignition in closed reactors is an important result for microcrystalline film manufacturing. It means that the plasma changes at ignition in such closed reactors are not the source of the generally observed amorphous incubation layer (see Fig. 3.6). Indeed, the time needed to reach plasma chemistry equilibrium is shorter than the time needed to grow a silicon monolayer ( $\approx 1.3 \text{ \AA}$ ) as shown in Fig. 5.4 and corresponding to about  $\sim 0.5 \text{ s}$  with a time-dependent deposition rate corresponding to  $R_{\text{max}} \cdot \eta^t$  as introduced in the previous chapters. Hence, amorphous

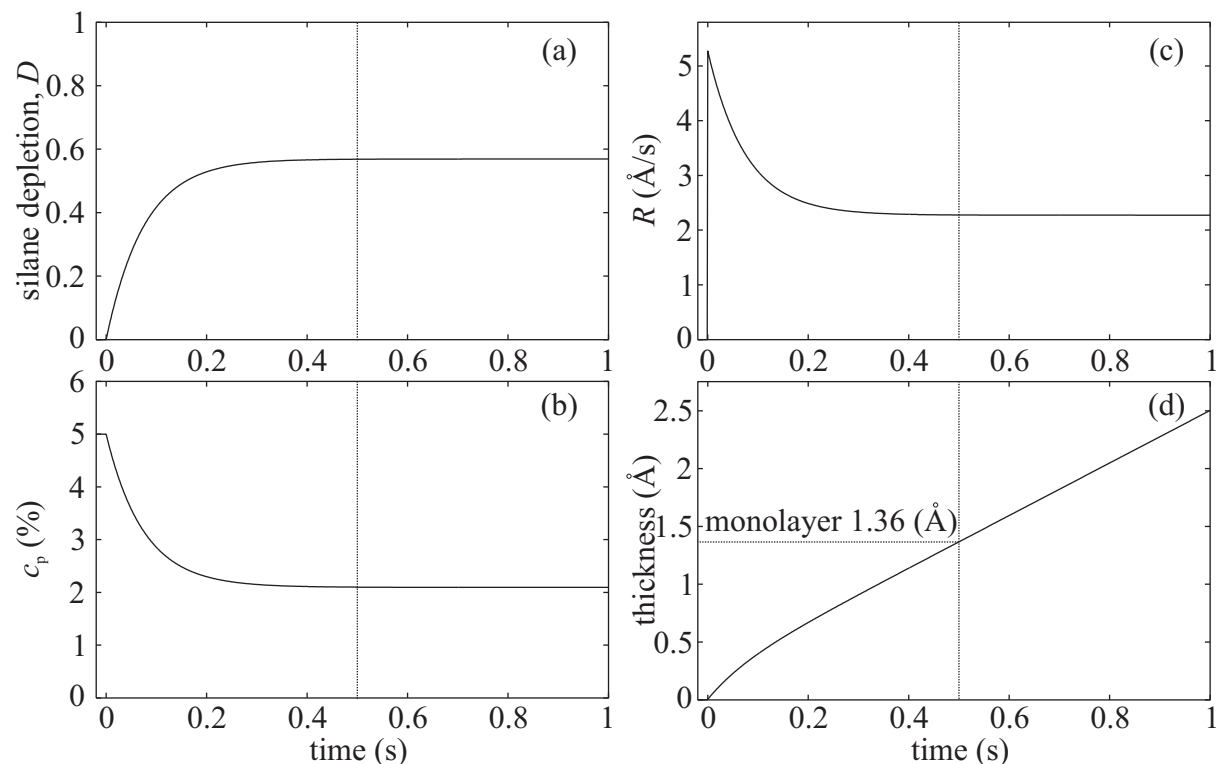


**Figure 5.4:** (a) Silane depletion fraction, (b) silane plasma concentration, (c) deposition rate and (d) film thickness as a function of time. The time necessary to deposit a silicon monolayer is longer than the time needed to reach equilibrium.

incubation layers with thickness of tens of nanometers are not due to plasma evolution from ignition to equilibrium, but have other sources such as substrate chemistry [144] or topology [44, 104]. This means that the time to reach the plasma steady-state equilibrium is shorter than the time needed to reach a steady-state film growth.

## 5.4 OES measurements

### II. Higher silane concentration and pressure

This section presents further experimental time-resolved OES measurements and modeling for processes with pressure up to 3 mbar and silane concentration up to 100 %. It will be shown that the plasma also has a very short equilibration time for these much more attractive processes in terms of process performance (Chapter 4) as for the previously discussed low pressure and low silane concentration process.

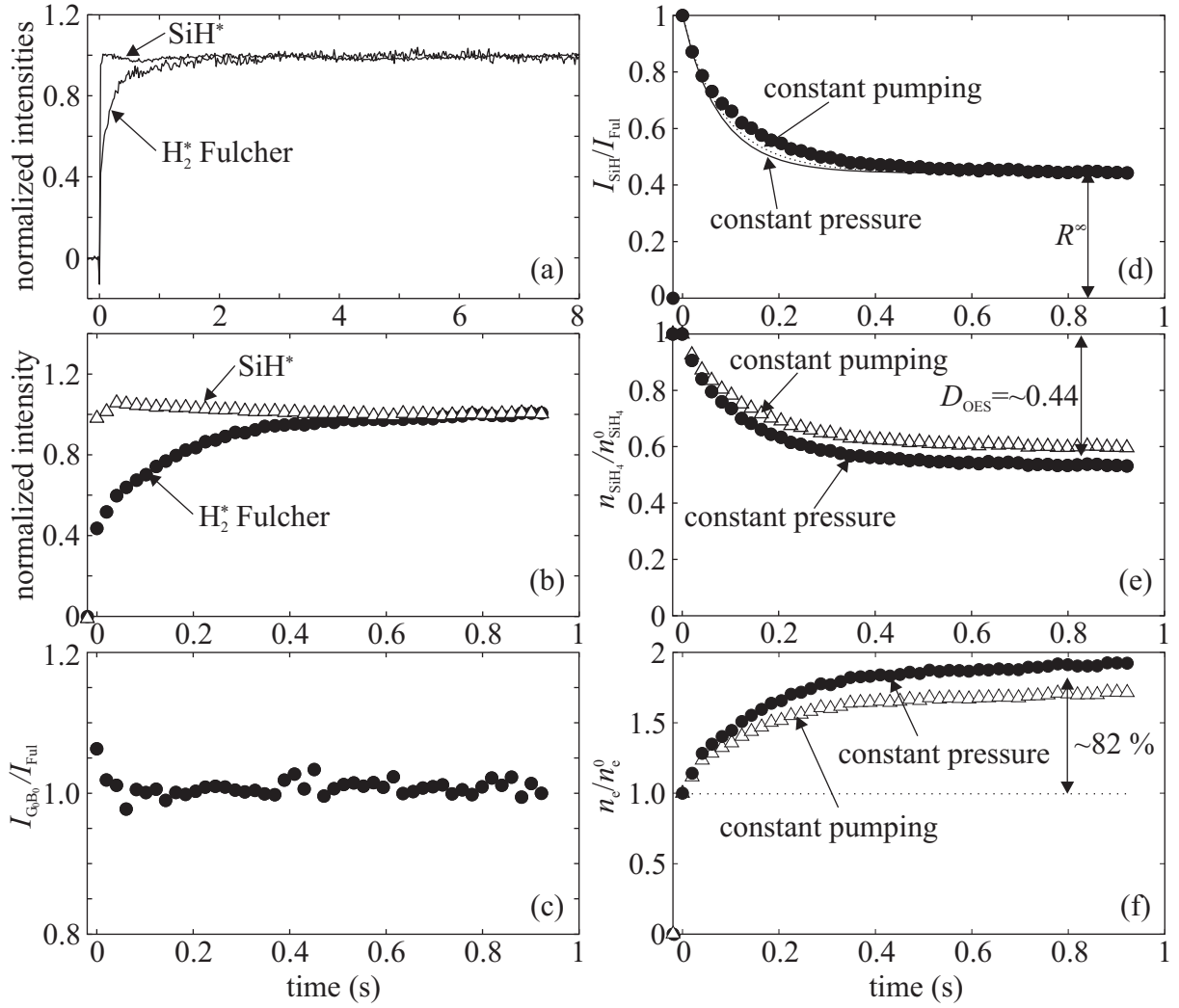
### 5.4.1 30 % silane concentration

Figure 5.5 presents the optical emission measurement (a-d) and interpretation (d-f) for a discharge performed with 30 % silane concentration and other parameters the same as for the previous case ( $p = 0.4$  mbar,  $F_{\text{tot}} = 500$  sccm,  $P_{\text{RF}} = 500$  W). When comparing the emission intensities of Figs. 5.5(a)-(b) with those of Figs. 5.2(a)-(b) performed with lower silane concentration, the  $\text{H}_2^*$  Fulcher intensities have similar behavior, but the  $\text{SiH}^*$  emission is surprisingly constant for the 30 % case. This might be misinterpreted as a constant silane and electron number density, but the variation of the  $\text{H}_2^*$  Fulcher emission over a 0.4 s time period clearly shows that the plasma parameters are not constant. The constancy of the  $\text{SiH}^*$  emission is in fact due to simultaneous and opposite variation of the silane density and the electron density making the silane dissociation rate,  $k^t n_e^t n_{\text{SiH}_4}^t$ , almost unchanged from ignition to steady-state equilibrium. Hence, the interpretation of a constant emission intensity of a single excited specy is not conclusive for the constancy of its density, and that using the time-variation of a unique emission line to determine the steady-state can be misleading. However, we have to note that the case of an almost-exact compensation between silane and electron density as reported here is purely coincidental.

Figure 5.5(c) shows that the ratio of  $I_{\text{GoB}_0}^t / I_{\text{Ful}}^t$  is constant from ignition to steady-state, hence allowing the hydrogen background subtraction and the post-treatment of the emission intensities to determine the time-dependent silane and hydrogen densities. It shows that even with high silane concentration, at least in the 5 to 30 % range, the electron temperature seems to be determined principally by the hydrogen density.

For results interpretation, the estimation of the pumping speed  $a^0$  is the same as for the previous case since the total flow rate (500 sccm), the pressure (0.4 mbar) and the gas temperature (230 °C) are the same. The measured steady-state intensity ratio  $R^\infty = 0.44$  gives a silane depletion value  $D_{\text{OES}}$  of 0.47 with  $\tau_p = 0.088$  s for the constant pressure limit case ( $G = 1$ ), and  $D_{\text{OES}}$  of 0.40 with  $\tau_a = 0.10$  s for the constant pumping limit case ( $G = 2$ ). The modeled intensity ratios for constant pressure and pumping speed are presented in Fig. 5.5(d). The difference between these two limiting cases is not important but more marked compared to the 5 % silane case (Fig. 5.2), due to the increased contribution of the silane to the molecular hydrogen outflow with  $c = 30$  %. The analytical solution is again in reasonably good agreement except for the above discussed dissociation frequency small overestimation, and the equilibration time is again much shorter than 1 s. It shows that it does not take more time to reach steady-state when the initial condition is far from equilibrium ( $c = 30\% \rightarrow c_p \approx 17\%$ ), and that the previous low silane concentration case was not an exceptional case. The deduced silane depletion has been confirmed by an independent measurement by IR absorption giving  $D_{\text{FTIR}} = 0.47 \pm 0.03$ , confirming the capability of time-resolved optical emission spectroscopy to accurately determine the silane depletion.

The increased contribution of the silane to the hydrogen outflow makes the calculated time-dependent silane and electron density presented in Figs. 5.5(e) and (f), respectively, more influenced by the type of exhaust boundary condition, i.e. constant pressure or pumping speed. The real silane and electron densities are expected to stand within these two extreme cases. Note that the electron density variation which is about  $n_e/n_e^0 \approx 82\%$  is much more important than for the 5 % silane concentration case.



**Figure 5.5:** Time-resolved optical emission measurement and interpretation for a discharge performed at  $p = 0.4$  mbar,  $c = 30\%$ ,  $F_{\text{tot}} = 500$  sccm and  $P_{\text{RF}} = 500$  W. (a)  $\text{SiH}^*$  and  $\text{H}_2^*$  Fulcher emission, (b) same emission intensities normalized and background subtracted, (c) hydrogen intensities ratio, (d)  $\text{SiH}^*$  to  $\text{H}_2^*$  Fulcher ignition normalized ratio, (e) silane density fraction and (f) electron density variation.

### 5.4.2 Higher pressures

Figure 5.6 presents the optical emission measurement (a-d) and interpretation (d-f) for a discharge performed at 3 mbar and other parameters the same as for the first case ( $c = 5\%$ ,  $F_{\text{tot}} = 500$  sccm,  $P_{\text{RF}} = 500$  W). As for the previous cases, the time to reach steady-state is short and is about one second. The initial pumping speed is no longer the same because of the higher pressure, and is  $a^0 = 0.76 \text{ s}^{-1}$  corresponding to a gas residence time of 1.3 s. This increase in residence time is at the origin of the much higher silane depletion level (see Fig.5.6(e)) than in the previous cases since the RF power has been held at the same level (500 W). The emission intensities ratio at equilibrium  $R^\infty = 0.15$



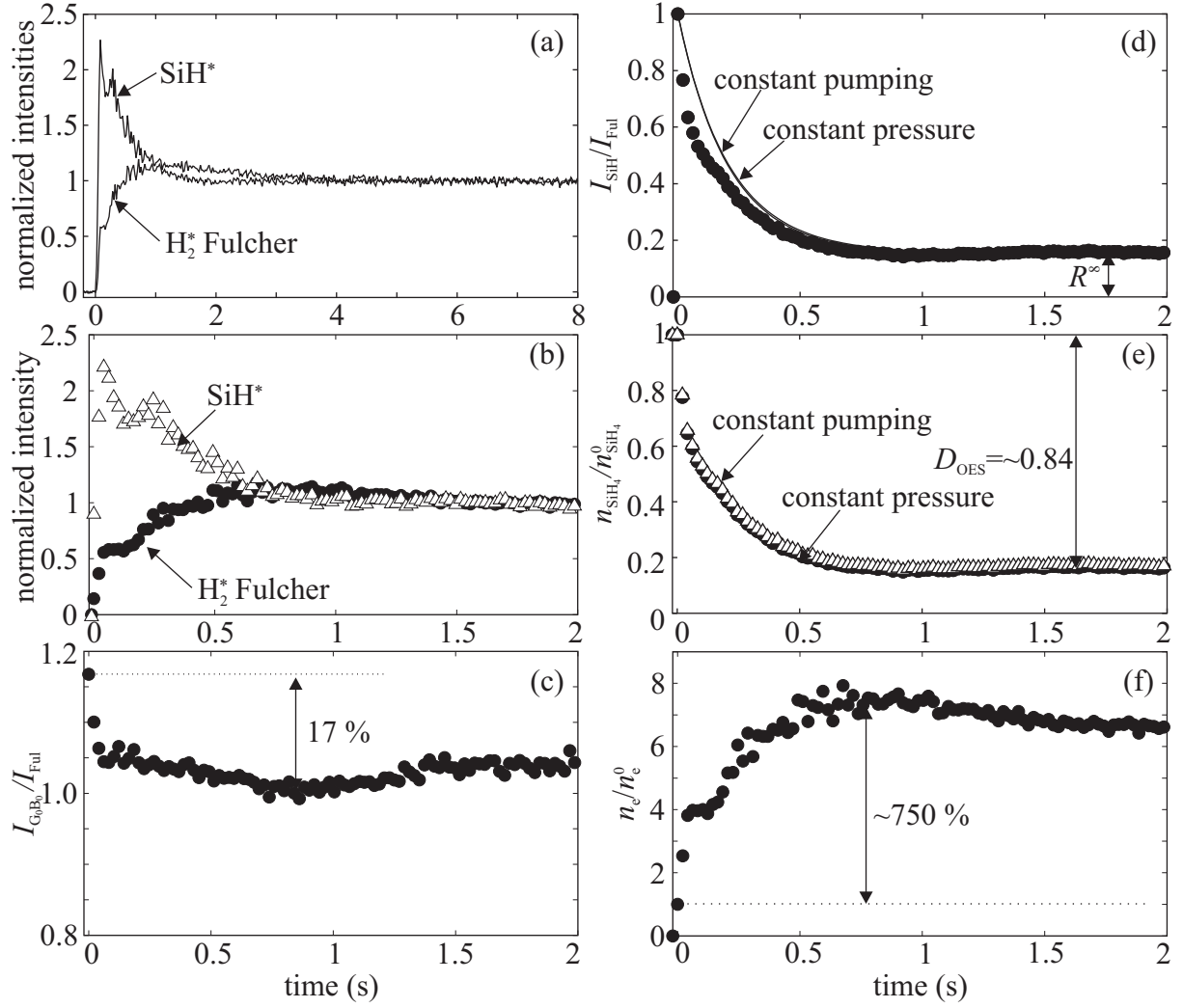


**Figure 5.6:** Time-resolved optical emission measurement and interpretation for a discharge performed at  $p = 3$  mbar,  $c = 5$  %,  $F_{\text{tot}} = 500$  sccm and  $P_{\text{RF}} = 500$  W. (a)  $\text{SiH}^*$  and  $\text{H}_2^*$  Fulcher emission intensities, (b) same emission intensities normalized and background subtracted, (c) hydrogen intensities ratio, (d)  $\text{SiH}^*$  to  $\text{H}_2^*$  Fulcher ignition normalized ratio, (e) silane density fraction and (f) electron density variation.

corresponds to silane depletion fraction  $D_{\text{OES}} = 0.83$  for constant pumping speed limit and  $D_{\text{OES}} = 0.84$  for constant pressure limit. These have been confirmed by silane depletion measurement by IR absorption that gives  $D_{\text{FTIR}} = 0.85 \pm 0.05$ . The high silane depletion fraction is responsible of the still short equilibration time by compensating the increase of the gas residence time due to the pressure increase from the first 0.4 mbar case (factor  $3/0.4 = 7.5$ ). The time constants  $\tau_a = 0.22$  and  $\tau_p = 0.21$  for constant pumping speed and pressure, respectively, are then not much larger than previously since  $\tau \approx (1 - D)/a^0$ . Figure 5.6(c) shows that the electron temperature is sensibly higher ( $\sim 0.4$  eV) than for the 0.4 mbar case and that it is constant within  $\sim 0.4$  eV, making the  $\text{H}_2^*$  background

subtraction applicable and emission intensities post-treatment accurate.

The electron density variation presented in Fig. 5.6(f) correlates with both  $\text{SiH}^*$  and  $\text{H}_2^*$  emission intensities time-variation and is much stronger than for the two previous low pressure cases with a variation amplitude up to about 750 %. From Figs. 5.2, 5.5 and 5.6 one can see that the increase in  $n_e/n_e^0$  is correlated to the reduction in silane density. This suggests that there is a loss rate of electrons associated with silane which diminishes as the silane density decreases. This electron loss might be due to dissociative attachment of silane [145] or negative charging of polysilanes, clusters or powder particles [146].

### 5.4.3 Pure silane

Figure 5.7 presents the optical emission measurement for a discharge performed with pure silane at 0.4 mbar pressure, 200 sccm flow rate of silane and 500 W RF power. Figure 5.7(a) shows that the intensity of the Fulcher  $\text{H}_2^*$  emission is zero at ignition; first, this means that the assumption stated in Sec. 2.2.3 on the fact that silane dissociation does not contribute to  $\text{H}_2^*$  emission is valid. Second, this makes the method for measuring the silane depletion by OES unusable, because the ratio  $I_{\text{SiH}}^t/I_{\text{Ful}}^t$  is then not defined at ignition ( $t = 0$ ). The silane intensity cannot be used alone to determine the silane depletion level, because nothing guarantees a constant electron density from ignition to

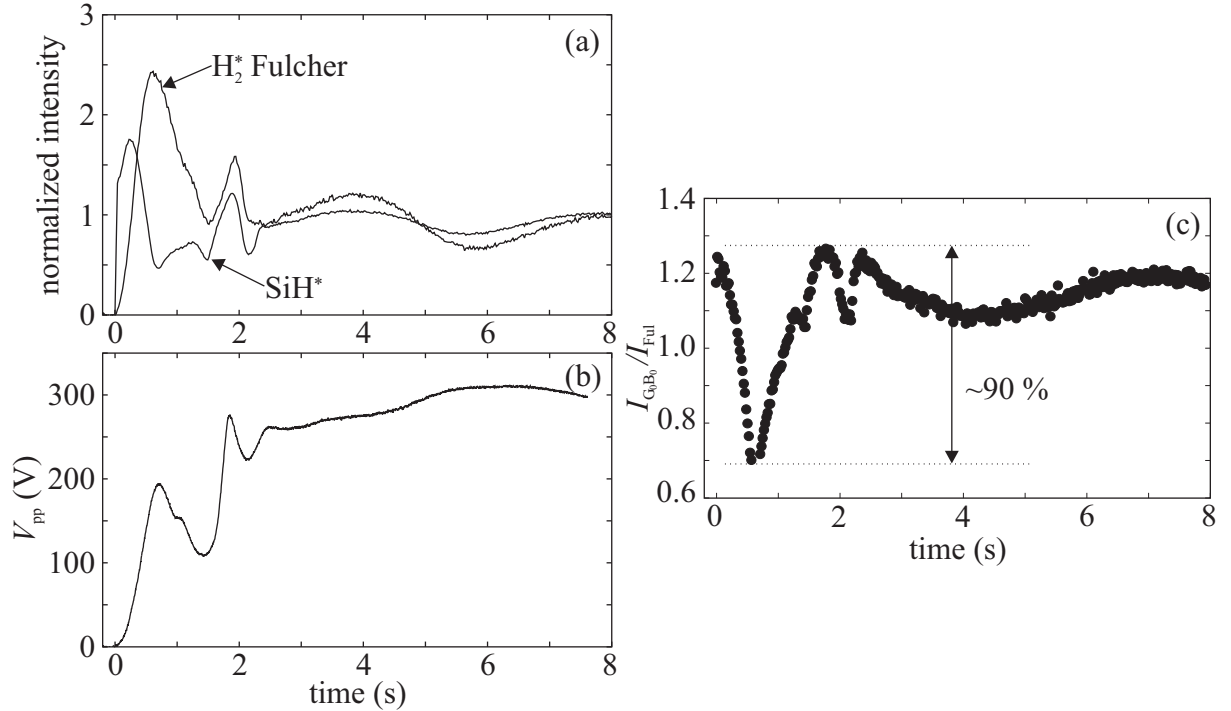


**Figure 5.7:** Time-resolved optical emission measurement and interpretation for a discharge performed at  $p = 0.4$  mbar,  $c = 100$  %,  $F_{\text{tot}} = 500$  sccm and  $P_{\text{RF}} = 500$  W. (a)  $\text{SiH}^*$  and  $\text{H}_2^*$  Fulcher emission intensities, (b) peak-to-peak interelectrode voltage, (c) hydrogen intensities ratio.

equilibrium, and previous experiments have shown that it is generally not the case. A possible way to permit depletion measurement by OES from pure silane plasma would be to perform time-resolved OES actinometry-like experiments [147] by adding a very small amount of hydrogen ( $< 1\%$ ), making the  $\text{H}_2^*$  intensity non-zero at ignition without affecting the pure silane character of the discharge.

The erratic behavior of the emission intensities (Fig. 5.7(a)) and of the hydrogen ratio  $I_{\text{G}_0\text{B}_0}^t/I_{\text{Ful}}^t$  (Fig. 5.7(c)) is roughly correlated with the interelectrode RF voltage amplitude in Fig. 5.7(b). This is probably because the plasma impedance variations perturb the matching accuracy and hence the delivered RF power. After approximately 3 seconds the plasma settles into slow oscillations which are characteristic of cycles of powder formation and ejection in dusty plasmas [128, 146, 148]. This powder formation may also be at the origin of the erratic plasma behavior from ignition to "steady-state" conditions. The strong variations of the electron temperature, as judged by the variation of the hydrogen ratio  $I_{\text{G}_0\text{B}_0}^t/I_{\text{Ful}}^t$ , makes the measurement post-treatment strategy invalid because of the non-constancy of the emission rate coefficient ratios, adding to the impossibility to determine the silane depletion fraction. Nevertheless, the time needed to reach equilibrium can be estimated to be about 3 s, which is still very fast compared to equilibration times reported until now [91, 118].

#### 5.4.4 Optimized conditions for microcrystalline silicon deposition

Figure 5.8 presents the optical emission measurement for a discharge performed with optimized parameters for microcrystalline silicon deposition as shown in Chapter 4: 2 mbar pressure, 50 % silane concentration, 186 sccm total flow rate and 1 kW RF power. The absence of erratic interelectrode RF voltage amplitude (Fig. 5.8(b)) behavior as observed for pure silane (Fig. 5.7(b)) indicates that excessive powder formation does not occur with such plasma parameters.

The electron temperature decreases strongly as shown by the variation of the  $I_{\text{G}_0\text{B}_0}^t/I_{\text{Ful}}^t$  ratio in Fig. 5.8(c), and so the background subtraction method is inaccurate. This is the reason why the background corrected  $\text{SiH}^*$  intensity becomes slightly negative and hence also the intensity ratio  $I_{\text{SiH}}^t/I_{\text{Ful}}^t$  given in Fig. 5.8(d). The fact that the ratio  $I_{\text{SiH}}^t/I_{\text{Ful}}^t \rightarrow 0$  shows that the silane is quasi-fully depleted and that the plasma is almost pure hydrogen after a plasma equilibration time of about one to two seconds, and this even if a high silane concentration is injected in the reactor. This strong depletion means that the  $R^\infty$  level is so close to zero that a small error may render it negative.

Even if the  $\text{H}_2^*$  background subtraction is approximative, an exponential fit of  $R^t$  can be performed and gives a time constant of only 0.15 s. The high pressure and low flow rate conditions make the residence time very long,  $1/a^0 = 2.4$  s, implying a very high silane depletion fraction  $D_{\text{OES}} \approx 0.94$ . Consequently, the silane concentration in the plasma is  $c_p = c(1 - D) \approx 3\%$ , even if the input silane concentration is 50 %. Using Eq. 5.5, the corresponding  $R^\infty$  will be 0.03 for constant pumping speed ( $G = 1$ ), and 0.02 for constant pressure ( $G = 2$ ), which are consistent with Fig. 5.8(d) within experimental error. This high silane depletion level deduced from OES measurements has been confirmed by IR absorption giving  $D_{\text{FTIR}} = 0.96 \pm 0.02$  ( $c_p = 2\%$ ).

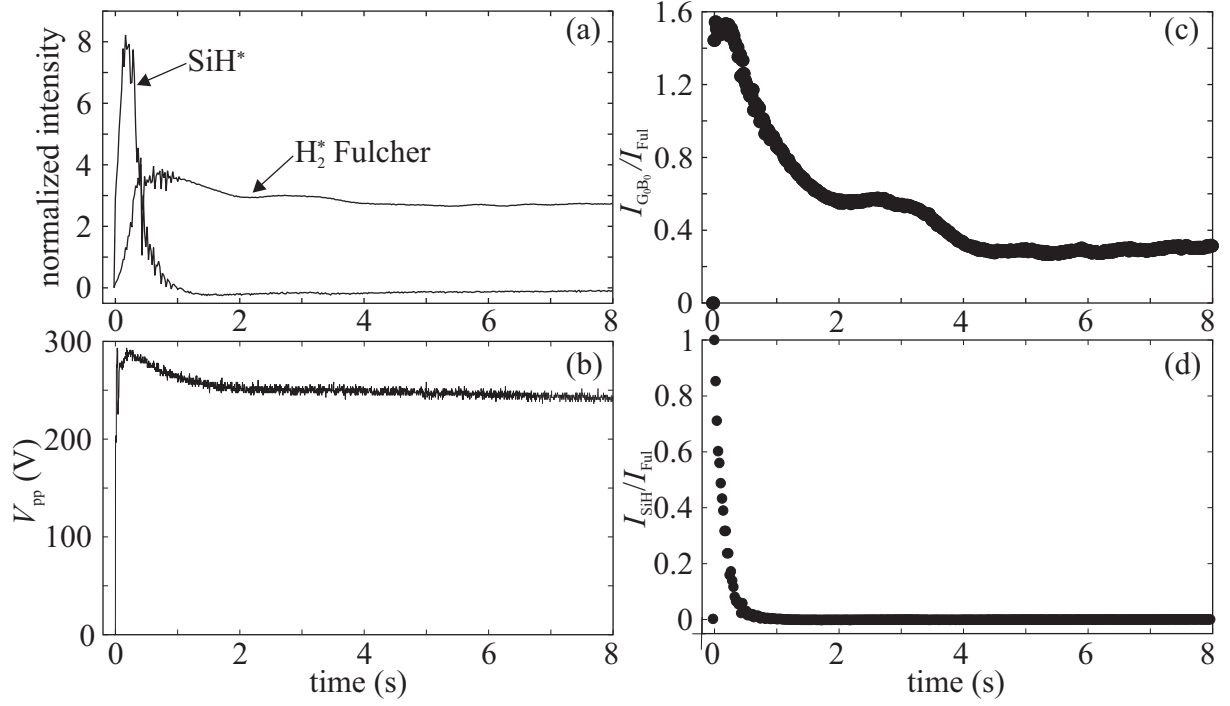


**Figure 5.8:** Time-resolved optical emission measurement and interpretation for a discharge performed at  $p = 2$  mbar,  $c = 50$  %,  $F_{tot} = 186$  sccm and  $P_{RF} = 1000$  W. (a) SiH\* and H<sub>2</sub>\* Fulcher emission intensities, (b) peak-to-peak interelectrode voltage, (c) hydrogen intensities ratio, (d) SiH\* to H<sub>2</sub>\* Fulcher ignition normalized ratio.

## 5.5 Large industrial vs small laboratory reactors

Up to now, only large area industrial Plasma-Box<sup>TM</sup> type reactors have been considered. This facilitates experiments and modeling because the assumption of plasma uniformity is valid [60]. However, this type of reactor is not widely used in research laboratories and this section will show that this is the cause of the large difference between the equilibration time reported here and the results obtained by Feitknecht *et al* [118] and van den Donker *et al* [91].

### 5.5.1 Silane back-diffusion

Generally, research laboratory reactors such as the one sketched in Fig. 5.9(b) consist of a small (typically 20 cm in diameter) plasma zone communicating with a large vacuum chamber where the pumps are connected. In such reactors the plasma equilibration time takes typically about one minute [91, 118], which is much longer than the  $\approx 1$  s equilibration time measured in closed reactor. The question therefore is not "Why is the equilibration time so short in closed reactors?", but rather, "Why is the equilibration time so long in open reactors?". Van den Donker *et al* [91, 143] show that back diffusion of silane gas from the surrounding vacuum chamber is responsible for this, and we will

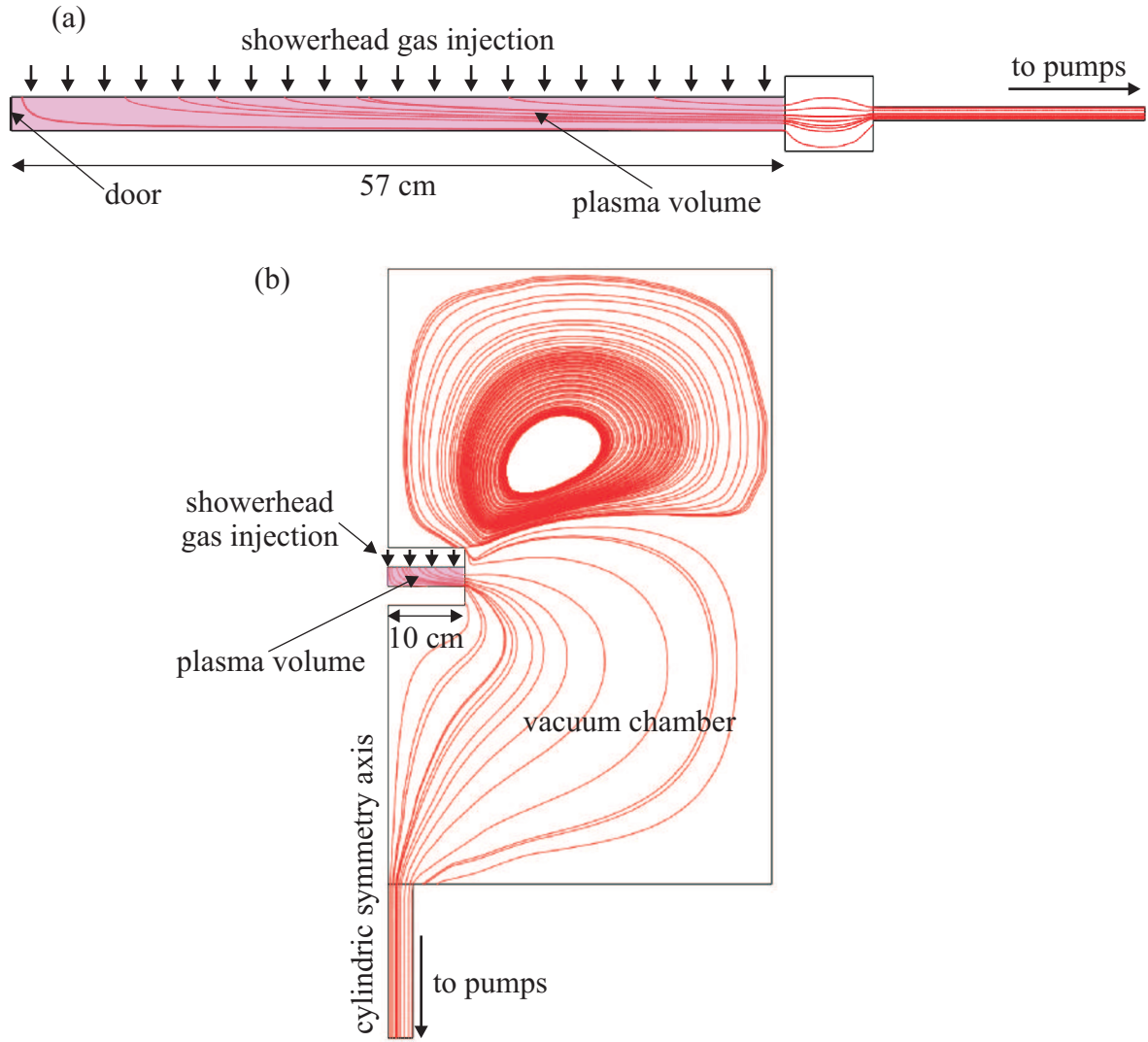


**Figure 5.9:** Plasma reactor geometry of (a) a large area, closed, directly-pumped reactor, and (b) a small, open laboratory reactor. These geometries have been used for the bi-dimensional modeling. The lines represent the flow velocity field.

compare open and closed reactors from this point of view.

The gas flow in the case of an open reactor communicating with a large vacuum chamber as the one presented in Fig. 5.9(b) is a complex three-dimensional transport problem with convective and diffusive gas flux in a complex reactor geometry. The silane number density  $n_{\text{SiH}_4}(\vec{r}, t)$  in the vacuum chamber after plasma ignition is time- as well as space-dependent and can be described by a binary transfer equation [149]

$$\frac{\partial n_{\text{SiH}_4}}{\partial t} + \nabla \cdot (n_{\text{SiH}_4} \vec{v}) + \nabla \cdot \vec{j} = 0, \quad (5.26)$$

where  $\vec{v}$  is the fluid velocity of the silane-hydrogen gas mixture and  $\vec{j} = -D_{\text{AB}} \nabla n_{\text{SiH}_4}$  is the silane diffusion flux in the  $\text{H}_2$  gas background. Note that in the plasma zone

the situation is even more complex because of the chemical reactions taking place due to non-zero electron density and reactions of radicals on the electrodes. Figure 5.9(b) shows the increased complexity of flow velocity fields in such open reactors compared to a closed Plasma-Box<sup>TM</sup> (Fig. 5.9(a)). Van den Donker *et al* [143] have constructed a zero-dimensional engineering model for the silane flow (the mass balance of hydrogen was not considered) in an open reactor, and we will consider their limit of "complete mixing".

If we consider the reactor geometry given in Fig. 5.9(a), the plasma volume is identical to the gas volume if the small downstream volume is neglected. If the plasma reactor is now open to a large surrounding vacuum chamber with a volume  $V_C$  as in Fig. 5.9(b), the total gas volume  $V_C$  is now larger than the plasma volume  $V_P$ , because of the reservoir in the "dead volume" of the vacuum chamber. In principle, the steady-state plasma conditions for identical plasma parameters (scaled in respect to electrode area) are unchanged, since at steady-state the gas composition is everywhere the same (in the reactor and in the vacuum chamber), and the only difference is that the gases are pumped at the chamber wall instead of directly at the plasma reactor (see Fig. 5.9). Hence, the silane dissociation rate,  $kn_en_{\text{SiH}_4}$ , is unchanged, and the silane pumping rate,  $an_{\text{SiH}_4}$ , to maintain the pressure constant is also unchanged. Therefore, the total silane molecule loss rate  $(kn_e + a)n_{\text{SiH}_4}$  is the same for open reactors as for closed reactors in steady-state conditions.

At equilibrium, the vacuum chamber standing between the plasma volume and the pumping aperture is simply a buffer zone with no influence on the steady-state conditions. However, at plasma ignition the whole initial quantity of silane,  $n_{\text{SiH}_4}V_C$ , has to be depleted although the dissociation rate is still the same in open reactor as for the closed reactor. The equilibration time  $\tau_{\text{open}}$  of a completely-mixed (perfectly-stirred) open reactor is therefore longer than  $\tau_{\text{closed}} = (kn_e + a)^{-1}$  for a closed reactor by the ratio of the volumes so that  $\tau_{\text{open}} = \tau_{\text{closed}}V_C/V_P$ . This is the result obtained by van den Donker *et al* [143] for their limit of "complete mixing". For small laboratory reactors, the ratio  $V_C/V_P$  can be very large; respectively 13 l/0.15 l  $\approx 87$  for van den Donker *et al* [91], and 60 l/0.3 l  $\approx 200$  for Feitknecht *et al* [118]. Taking the observed equilibration time  $\tau_{\text{closed}} = 0.1$  for the closed reactor in Sec. 5.2, this predicts  $\tau_{\text{open}} \approx 9$  s and  $\approx 20$  s respectively, which is roughly similar to the respective equilibration times reported [91, 118]. These estimations assume a perfectly-mixed volume, but if a diffusion timescale is accounted for, the equilibration times are even longer [143]. Special strategies such as  $\text{H}_2$  pre-dilution [91, 143] or  $\text{H}_2$  dilution profiling [141] are therefore necessary for open reactors to avoid long term drift in the plasma parameters and consequent variation in the film properties across its thickness [141].

The buffering effect of the vacuum chamber "dead volume" including complex convective and diffusive phenomena on the plasma composition can be determined by solving Eq. 5.26 numerically. This four-dimensional (3 in space and 1 in time) problem has been simplified to a time-resolved bi-dimensional space problem. The resolution of Eq. 5.26 in the plasma zone and vacuum chamber of the two geometries presented in Fig. 5.9 and detailed in the Appendix has been performed by using FEMLAB MultiPhysics<sup>TM</sup> solver coupled with Comsol Chemical Engineering Lab<sup>TM</sup> software for solving the chemical system presented in Sec. 3.2.2. The gases are injected through a showerhead electrode and the silane radical deposition and the hydrogen recombination on the electrodes was implicitly

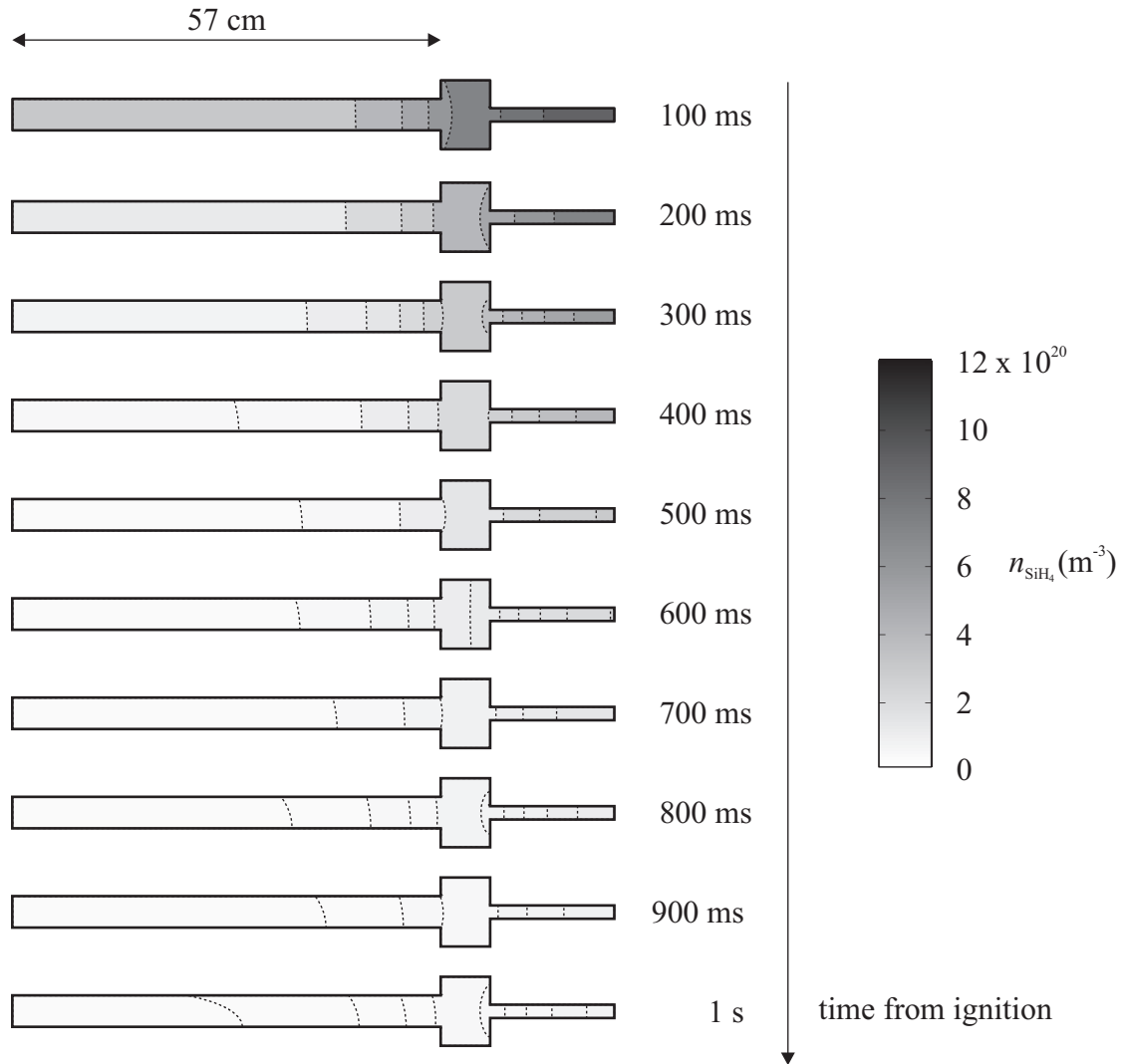


**Figure 5.10:** Two-dimensional modeling of silane density in a large area, closed, directly-pumped reactor. The whole plasma and pumping line volumes are depleted in less than 1 second.

calculated in the same manner as in the zero-dimensional model used in Sec. 3.2.2.

Results for large area, closed, directly-pumped reactor and small open reactor are given in Figs. 5.10 and 5.11, respectively. It shows that in the Plasma-Box<sup>TM</sup> reactor, the composition of the plasma volume is fully-depleted in less than 0.5 s, and that the pumping line itself is at quasi-equilibrium in less than 1 second. On the other hand, the plasma volume in the open reactor is still not at steady-state after 100 seconds, even if the electrode area is much smaller. Note that in Figs. 5.10 and 5.11 the color scales are similar. This shows that the pumping line itself in the case of a directly-pumped reactor does not act as a buffer volume as the vacuum chamber in the open configuration. Indeed, in the limit of a perfectly-stirred system (i.e. complete mixing due to infinitely-fast back diffusion,  $D_{AB} \rightarrow \infty$ ), the pumping line would behave exactly the same as the buffer zone

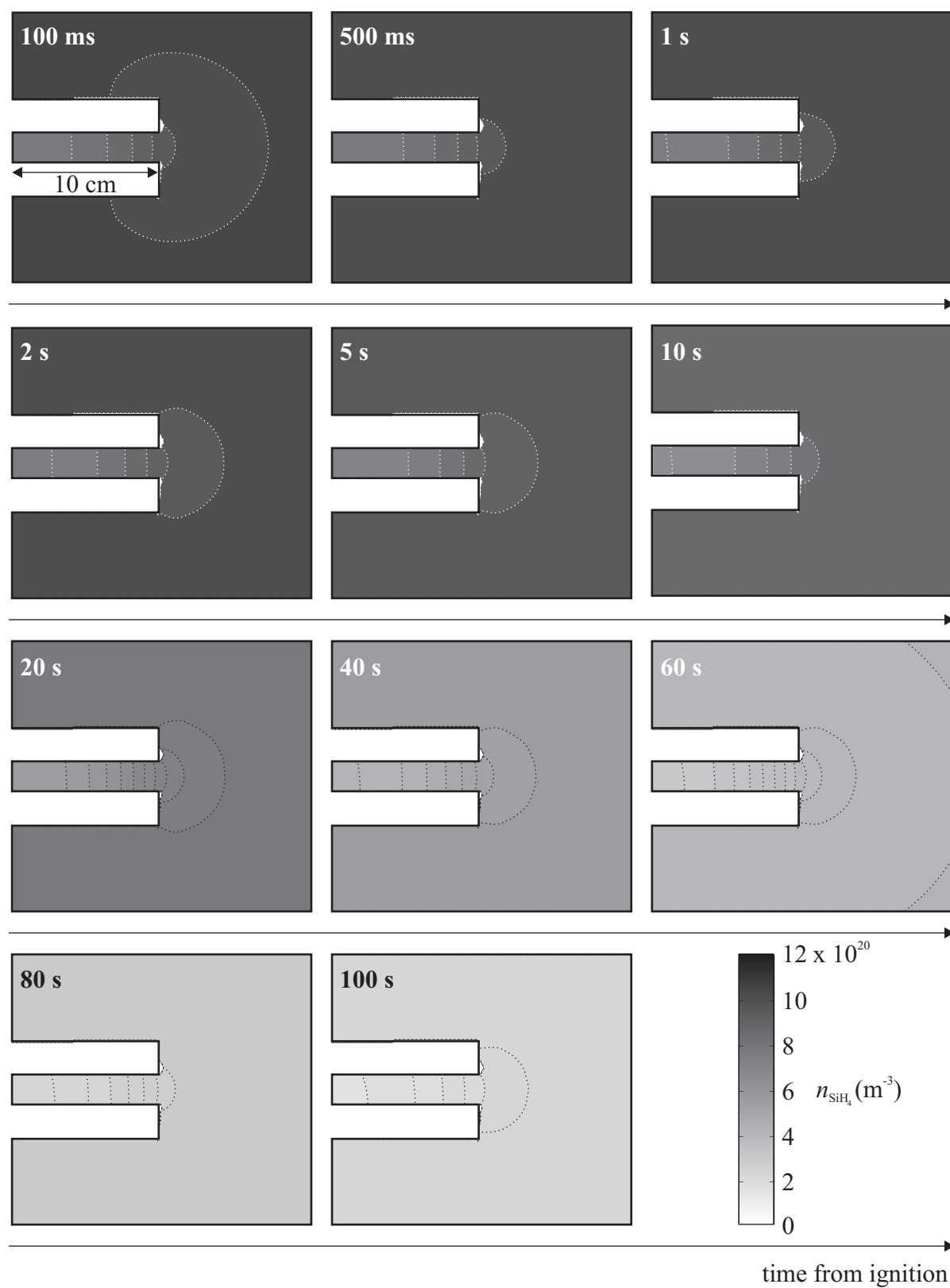


**Figure 5.11:** Two-dimensional modeling (zoom on the plasma region) of silane density in a small open reactor pumped at the vacuum chamber wall. The whole plasma and vacuum chamber volumes are not at steady-state even after 100 seconds.



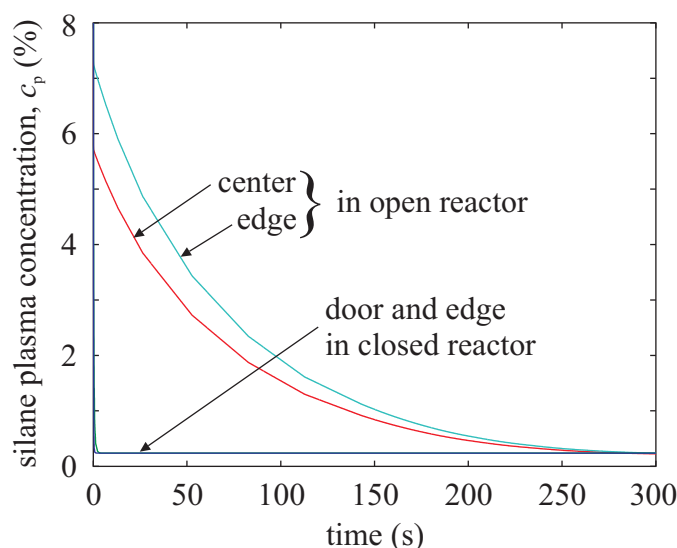


**Figure 5.12:** Comparison of silane concentration as a function of time after ignition for different positions in both type of reactor. The open reactor geometry takes more time to reach chemical equilibrium and is nonuniform in space during plasma drift.

of an open reactor. The important difference, however, is that the gas flow in the pumping line is a directed one-dimensional flow from the closed plasma reactor to the pumps, in contrast to the three-dimensional circulation of gas due to back-diffusion and convection in an open electrode system pumped indirectly at the vacuum chamber wall (see Fig. 5.9). In the opposite limit of a plug flow reactor (no diffusion,  $D_{AB} \rightarrow 0$ ), the silane concentration step created at ignition at the plasma zone boundary is instantaneously convected and dispersed downstream, away from the reactor pumping grid so that the back-diffusion into the reactor is rapidly eliminated [73]. This is valid even for an infinitely-long pumping line with infinite volume.

This negligible effect of back-diffusion in a directly-pumped closed reactor is shown in Fig. 5.12 where silane plasma concentrations at the pumping grid and at the reactor door (57 cm further in the plasma) are almost identical. In the case of the open reactor, before steady-state is reached (after  $\approx 300$  seconds), silane concentrations at the plasma-vacuum chamber boundary and at the center of the plasma (10 cm from plasma-vacuum chamber boundary) are different as shown in Fig. 5.12, even if only 10 cm separates these two positions. This spatial nonuniformity adds to the temporal nonuniformity and the uniformity of the deposited material is then not only affected across its thickness, but depends also on the position in the open reactor. In large area *open* reactors, only the edges will have a non-uniform plasma, since the effect of the back-diffusion is limited to a distance of the order of  $D_{AB}/v$  in the vicinity of the plasma boundary. This has been demonstrated by comparing film microstructure thickness profile of one sample placed at the reactor center, with another sample place next to the loading door which, exceptionally, was left open during a plasma normally appropriate for microcrystalline silicon deposition near the transition to amorphous silicon. Figure 5.13 shows that the amorphous incubation

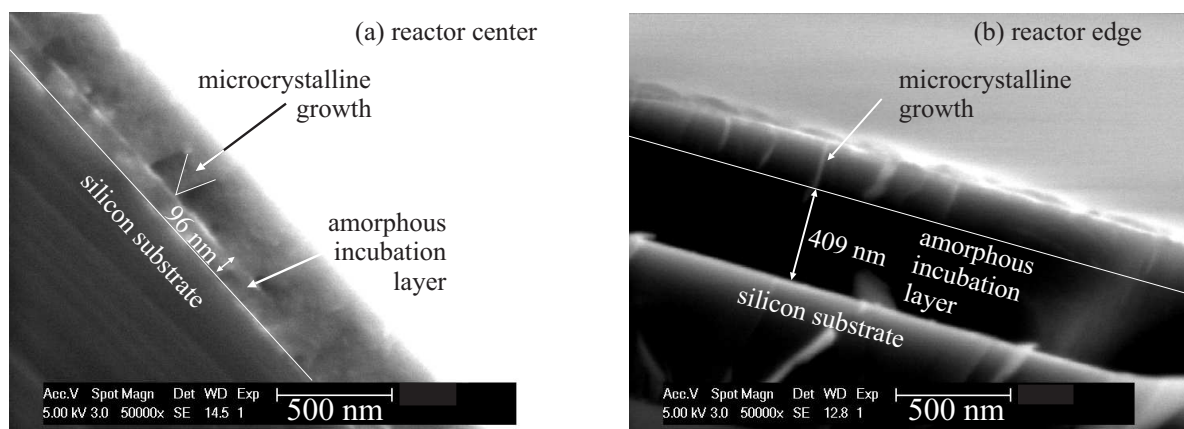


**Figure 5.13:** Cross-sectional scanning-electron microscopy (SEM) of sample positioned (a) next to the reactor edge with the door open and (b) at the center of the electrodes. The longer plasma drift at the edge causes a thicker amorphous silicon incubation layer before microcrystalline silicon nucleation.

layer is more than four times thicker for the sample next to the open door, because the necessary silane depletion took longer to occur due to silane back-mixing from the large vacuum chamber acting as a gas reservoir.

In summary, from the point of view of fast equilibration time, the flaw in the design of small laboratory open reactors is the lack of directed pumping. By pumping at the vacuum chamber wall, instead of directly at the plasma boundary of a closed reactor, the gases circulates by diffusion and convection between the plasma zone and the large "dead volume" of the vacuum chamber before evacuation. There is therefore a long equilibration time ( $\geq 1$  minute) before the composition is everywhere, in the vacuum chamber and the plasma zone, the same. Paradoxically, any arbitrarily-large area Plasma-Box<sup>TM</sup> reactor can reach steady-state conditions faster than an open reactor, such as a small laboratory reactor, typically by two orders of magnitude. There are two timescales for equilibration in closed plasma reactors: The plasma chemistry equilibration  $\approx 10^{-1}$  s, and the convective one-dimensional flow to convect the silane gas concentration gradient away down the pumping line, also  $\approx 10^{-1}$ . In an open reactor, the plasma chemistry equilibration time is the same, but the silane back-diffusion timescale is of the order of  $10^1$  s [91]. From the point of view of fast equilibration time, the ideal reactor configuration is therefore a closed, directly-pumped, uniform showerhead plasma reactor, where the plasma fills the whole reactor volume.

### 5.5.2 Hydrogen dilution profiling strategies

So far only ignition with fixed flow rates of silane and hydrogen was considered. This was made because in closed Plasma-Box<sup>TM</sup> reactors the time to chemical equilibrium is so short that less than one monolayer is deposited before the required steady-state

conditions are reached. Here, other situations are reviewed where, on the contrary, it is desirable to use a higher hydrogen flow rate initially:

1. Pre-dilution for open-reactors, where the initial gas composition is adjusted to be similar to the required final steady-state plasma composition [91, 143], because otherwise the equilibration time is long ( $\geq 1$  minute) and a thick amorphous silicon incubation layer is deposited;
2. Hydrogen dilution profiling, to promote initial nucleation of silicon crystallites in order to reduce the thickness of the intrinsic amorphous silicon incubation layer [141, 150, 151, 152, 153]; and
3. Pure hydrogen plasma cleaning of the substrate surface to improve the film adhesion.

In all these cases, the flow rates could be pre-programmed, controlled in real-time, or a combination of both. Ultimately, the required film properties, such as the crystallinity, would be monitored and controlled by a real-time feed-back to the silane and hydrogen flow rates to give the ideal plasma composition throughout the film growth. This could be achieved by adjusting the input gas concentration,  $c^t$ , with a fixed target plasma composition,  $c_p$ , as a function of the measured time-resolved silane depletion,  $D^t$ , in order to follow  $c^t = c_p / (1 - D^t)$ . The implementation of such a flow control would be simpler in a Plasma-Box<sup>TM</sup> configuration, since there is no external gas reservoir to take into account; but the equilibration time in this case of a close, directly-pumped reactor is so short that such dilution profiling is not necessary to guarantee a uniform plasma composition across time and space.

## 5.6 $H_2$ background subtraction

The  $H_2^*$  background subtraction method presented in Sec. 2.2.3 is fairly effective in eliminating the molecular hydrogen background emission over the whole acquisition wavelength range. However, as shown in Fig. 2.10(b) the  $H_\alpha$  and  $H_\beta$  atomic emissions are over-compensated and these become negative after  $H_2^*$  background subtraction. This effect is not trivial since we may think that the addition of silane in a hydrogen discharge would have the opposite effect by contributing to the H atomic emission by electron impact dissociation (which does not contribute to  $H_2^*$  emission as demonstrated in Sec. 5.4.3). Hence, this change in balance between atomic and molecular hydrogen in the plasma with the addition of silane has another origin(s) and is the focus of this section.

The emission spectra presented in this section were obtained by using a multiple grating liquid nitrogen cooled high resolution (0.18 nm) spectrometer (SpectraPro-750i by Acton Research Co.).

The fact that the atomic emissions are over-compensated by  $H_2$  background subtraction means that the fraction of atomic hydrogen is larger in pure hydrogen plasma than when silane is added. In other words, the addition of silane increases the atomic hydrogen recombination into molecular hydrogen. The hydrogen recombination in the gas phase is negligible since it is a three body reaction. Moreover, the mean free path for

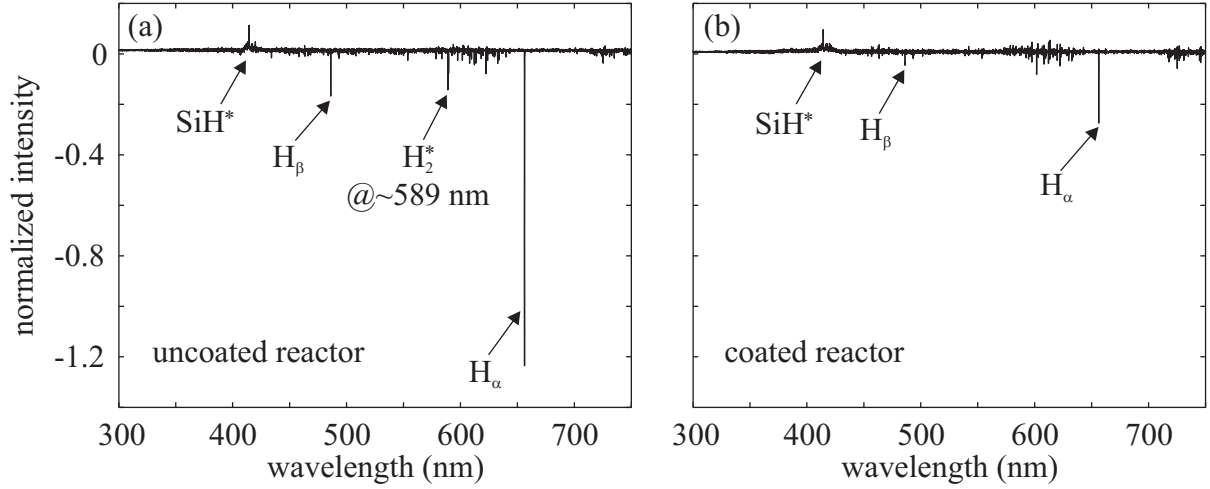


**Figure 5.14:** Emission spectrum of a silane-hydrogen discharge after  $H_2^*$  background subtraction from a  $H_2$  discharge reference spectrum performed in (a) a clean aluminum reactor and (b) a silicon coated reactor.

a collision between two H atoms is  $\lambda = 1/(\sqrt{2}\pi d_c^2 n_H) \approx 190$  m, with a binary collision diameter  $d_c = 2.44 \cdot 10^{-10}$  m [111] and a hydrogen density  $n_H \approx 2 \cdot 10^{16}$  m $^{-3}$  [55], which is much larger than the deposition reactor dimensions. The hydrogen recombination on the reactor surface is dominating as assumed from the beginning of this work, and the recombination frequency varies between a pure hydrogen plasma in a clean reactor and a plasma containing silane. This is due to the change in reactor surface chemistry from aluminum for pure hydrogen to silicon when silane is added, since silane radicals deposit onto the reactor walls. This effect of surface chemistry on the  $H \leftrightarrow H_2$  balance is shown in Fig. 5.14, where the emission spectra of the same silane-containing discharge has been corrected using a hydrogen plasma performed (a) in a clean aluminum reactor and (b) in a silicon coated reactor. The H atomic emission lines over-compensation is strongly reduced when the  $H_2$  reference discharge is performed in a silicon coated reactor, but they are not completely eliminated. The change in surface chemistry of the reactor between the hydrogen reference discharge and the silane-containing discharge is then not sufficient to completely explain this effect. However, the hydrogen surface recombination is known to have various efficiencies depending on the surface material [154, 155] and is very effective on silicon because it is fully covered by hydrogen bounded to surface silicon [156]. On the other hand, aluminum surfaces are not so effective to recombine hydrogen with a H atom loss probability approximately two times smaller than for silicon [157].

The residual change in  $H \leftrightarrow H_2$  balance may be explained by an effect comparable to the phenomenon of preferential electron impact dissociation seen in Ar-He plasmas. The more favorable dissociation of silane ( $E_{SiH_4} = 8.4$  eV  $<$  8.8 eV  $\leq E_{H_2}$  [158, 17]) reduces the quantity of high temperature electrons available for the dissociation of  $H_2$ . The overall H atom density is then reduced and the  $H \leftrightarrow H_2$  balance is displaced on the molecular side ( $\rightarrow$ ), making the  $H_2$  background subtraction not effective for both the molecular and atomic lines together.

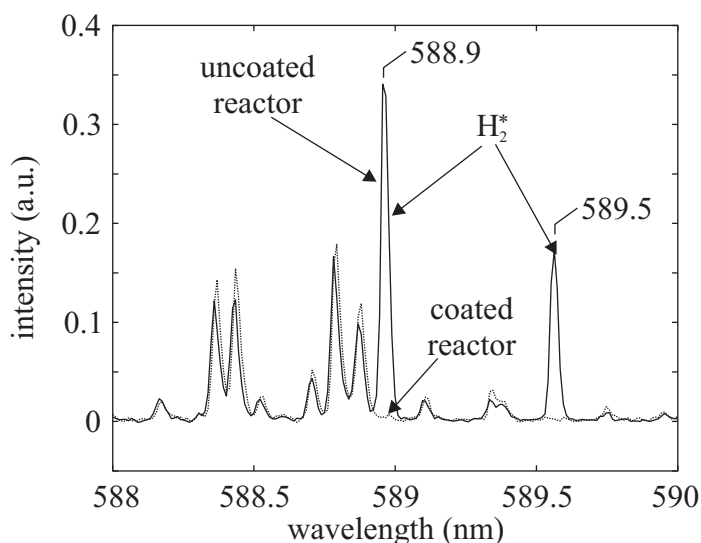


**Figure 5.15:** High resolution emission spectrum of  $\text{H}_2$  discharges performed in clean aluminum and silicon coated reactor.

The emission spectrum difference between a  $\text{H}_2$  reference discharge performed in a clean and a silicon coated reactor is not restricted to the change in the  $\text{H} \leftrightarrow \text{H}_2$  balance as shown in Figs. 5.14 and 5.15 with the appearance of two peaks at 588.9 and 589.5 nm in the case of a  $\text{H}_2$  discharge in a clean aluminum reactor. These two emissions are associated with excited molecular hydrogen  $\text{H}_2^*$ . They may be associated with specific  $\text{H}_2$  excited states resulting from a recombination of a gas phase H atom with hydrogen contained in an aluminum hydride group (AlH) on the reactor wall surface.

In summary, the  $\text{H}_2^*$  background subtraction method used to determine the  $\text{SiH}^*$  emission peak does not preserve the  $\text{H} \leftrightarrow \text{H}_2$  balance, and hence cannot be suitable to eliminate molecular and atomic lines both together. The  $\text{H}_2$  reference spectrum should be preferably performed in a silicon coated reactor to reduce the deviation caused by different H atom surface loss probability onto silicon and aluminum surfaces. However, the  $\text{H}_2^*$  background subtraction method is not affected if we consider wavelength ranges other than ones containing H atomic emissions.

## 5.7 Conclusion

Optical emission spectroscopy, analytical modeling and two-dimensional numerical modeling were used to show that the optimal reactor design for a fast chemical equilibration of silane-hydrogen RF discharge is a closed, directly-pumped, showerhead reactor. The time to reach equilibrium in such closed reactor is less than the gas residence time by a factor  $(1 - D)$ , where  $D$  is the silane depletion fraction at steady-state. This equilibration

<sup>2</sup>from the emission line identification software Plusus SpecLine version 1.3.

time is generally less than one second and does not depend on reactor size. Therefore, the amorphous silicon incubation layer is not due to plasma transient depletion at ignition, because the affected thickness is only about one monolayer thick.

The plasma-change at ignition in small open electrodes laboratory reactors with an indirect pumping at the vacuum chamber wall, in contrast, is one to two orders of magnitude longer, because of the silane back-diffusion between the relatively-small plasma volume and its surrounding large vacuum chamber.

Simple time-resolved optical emission spectroscopy of silane-hydrogen discharge was used to determine the absolute silane and hydrogen molecular density, the relative variation in electron density and qualitative information on any electron temperature variation. This was achieved with an inexpensive uncalibrated equipment, making OES a very attractive technique for plasma composition measurement with only few restrictive conditions: The electron temperature has to be verified constant and the emission intensities have to be followed from the plasma ignition, since the molecular densities are known at this instant.

Finally, it has been shown that the balance between atomic and molecular hydrogen in pure  $H_2$  discharges depends on the nature of the reactor walls. Silicon coated reactor walls improve significantly the hydrogen recombination frequency compared to uncoated, clean aluminum walls, hence reducing the fraction of atomic hydrogen in the plasma.

## Chapter 6

# Polysilane formation: Analytical model and process limitations

It has been shown in Chapters 4 and 5 that polysilane and powder formation during deposition lead to several problems such as film contamination by particles (Fig. 4.9), reduction of deposition efficiency (Fig. 4.7), non-uniform deposition [69] (Fig. 4.6), plasma time-instability (Fig. 5.7), down-time to clean/repair pumping system (Fig. 6.1) or potential health problems associated with fine particle handling [159]. All of these make the polysilane or powder formation a hot topic in the field of PV solar cell industrial production [105], since powder may make processes invalid even if they are promising at the research laboratory level. Moreover, it has been shown in Chapter 4 that for efficient deposition of  $\mu\text{c-Si:H}$  the silane input concentration and the working pressure have both to be increased, hence increasing the risk to form powder in the discharge. This is consistent with reported effects of plasma parameters on polysilane or powder formation in  $\text{SiH}_4\text{-H}_2$  discharges; it increases if the pressure [132, 160], the input RF power [132, 146] or the silane concentration [71] are increased or if the total flow rate [128, 146], the substrate temperature [146, 161, 162] or the excitation frequency [48] are reduced. Therefore, it is

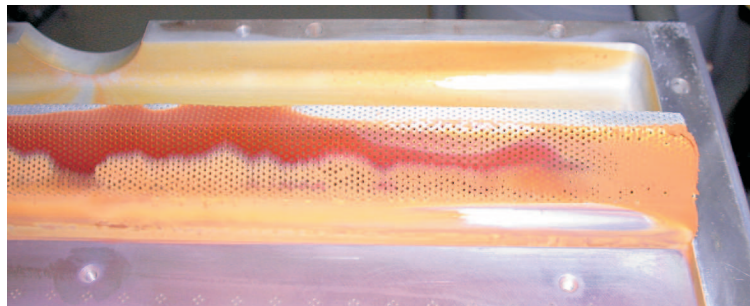


**Figure 6.1:** Powder pollution of the plasma reactor which necessitates intensive, time consuming cleaning.

crucial to understand the powder formation behavior as a function of the various plasma parameters, as has been done for the film crystallinity in Chapter 3, in order to find the limit between powder-free and dirty discharges. This understanding may also be helpful in order to develop new techniques to reduce or avoid powder formation, thereby extending the viable process window. Moreover, as shown in Chapter 3, including gas phase reactions in the plasma chemistry model adds some data scattering of the  $\Gamma_{\text{H}}/\Gamma_{\text{SiH}_x}$  flux ratio towards the film surface (see Fig. 3.10). This effect can be associated with the presence of polysilanes in the discharge which modifies the plasma composition and affects the crystallinity of the deposited layer, and hence, the analytical model presented in Chapter 3.

## 6.1 Plasma chemistry model including disilane

Up to now, the analytical plasma chemistry model presented in this work was limited to low pressures ( $< 2$  mbar), since no radical-molecule or radical-radical reactions were considered, because they are negligible for pressures lower than  $\approx 2$  mbar [74]. However, numerical modeling in Chapter 3 has already shown that adding radical gas phase reactions to the model does not change the general behavior of the plasma chemistry, but introduces a data scattering effect on the results as shown in Fig. 3.10. In this section, an extension including radical-molecule gas phase reactions on the basis of the previous analytical model will be presented. The polysilane/powder formation is associated here to the disilane density, which has been shown to be the precursor of higher order silane molecules [163]. In order to keep the linear character of the modeling presented in this work, no ions nor radical-radical reactions have been taken into account, even if they may play a role in the powder formation [74, 138, 145, 163, 164]. Therefore, the model discussed in this chapter does not pretend to describe dusty plasmas, nor powder formation processes. The model discusses the limit of validity of the simple analytical approach, where polysilanes become non-negligible, but complex phenomena occurring beyond this limit are not in the scope of this work since processes performed in such conditions are not interesting in term of industrial application. The plasma chemistry has been restricted to nine chemical reactions which are given in Table 6.1. There are three new contributions of radicals:

1. H abstraction leading to silane dissociation with the formation of a  $\text{H}_2$  molecule,
2. silane formation in the gas phase consuming molecular hydrogen and  $\text{SiH}_2$  radicals, and
3. polymerization of silane by the reaction between a radical  $\text{SiH}_2$  and a silane molecule forming  $\text{Si}_2\text{H}_6$ .

Note that  $\text{SiH}_3$  radicals do not contribute to silane polymerization and that all these three reactions modify the silane concentration *in the plasma*. Using the same approach as in Chapter 3, the chemical assessment over each species can be performed at chemical steady-state (no time-dependence) and is then



$$\text{SiH}_4 : \Phi_{\text{SiH}_4} + k_{\text{H}_2} n_{\text{H}_2} n_{\text{SiH}_2} - ((k_1 + k_2) n_e + a) n_{\text{SiH}_4} \quad (6.1)$$

$$-k_p n_{\text{SiH}_2} n_{\text{SiH}_4} = 0 \quad (6.2)$$

$$\text{SiH}_3 : k_2 n_e n_{\text{SiH}_4} + k_a n_{\text{H}} n_{\text{SiH}_4} - S_2 n_{\text{SiH}_3} = 0 \quad (6.3)$$

$$\text{SiH}_2 : k_1 n_e n_{\text{SiH}_4} - (k_{\text{H}_2} n_{\text{H}_2} + k_p n_{\text{SiH}_4} + S_1) n_{\text{SiH}_2} = 0 \quad (6.4)$$

$$\text{Si}_2\text{H}_6 : k_p n_{\text{SiH}_2} n_{\text{SiH}_4} - a n_{\text{Si}_2\text{H}_6} = 0 \quad (6.5)$$

$$\text{H}_2 : \Phi_{\text{H}_2} + S_1 n_{\text{SiH}_2} + 3/2 S_2 n_{\text{SiH}_3} + 1/2 R n_{\text{H}} + k_a n_{\text{H}} n_{\text{SiH}_4} \quad (6.6)$$

$$-k_{\text{H}} n_e n_{\text{H}_2} - k_{\text{H}_2} n_{\text{H}_2} n_{\text{SiH}_2} - a n_{\text{H}_2} = 0 \quad (6.7)$$

$$\text{H} : (2k_1 + k_2) n_e n_{\text{SiH}_4} + 2k_{\text{H}} n_e n_{\text{H}_2} - k_a n_{\text{H}} n_{\text{SiH}_4} - R n_{\text{H}} = 0, \quad (6.8)$$

where  $n_j$  is the  $j$  density in molecule·m<sup>-3</sup>,  $\Phi_j$  the  $j$  input flow rate in molecule·m<sup>-3</sup>·s<sup>-1</sup> and  $a$  the pumping rate in s<sup>-1</sup>. The pumping rate term of all species other than silane, disilane and hydrogen molecules have been neglected since they are very reactive and their density is small compared to stable molecules [20]. Assuming that the total density is governed by the hydrogen and silane densities, and using the fact that the silane and hydrogen density at equilibrium are  $c_p n_{\text{tot}}$  and  $(1 - c_p) n_{\text{tot}}$ , respectively, the disilane density can be calculated and is

$$n_{\text{Si}_2\text{H}_6} = \frac{k_1 n_e}{a} \cdot \frac{k_p c_p^2 n_{\text{tot}}^2}{S_1 + (k_{\text{H}_2} (1 - c_p) + k_p c_p) n_{\text{tot}}}. \quad (6.9)$$

In order to express the latter *only* as a function of the pressure, the silane input concentration,  $c$ , and fractional depletion,  $D$ , the electron density to pumping rate ratio  $n_e/a$  has to be expressed as a function of  $c$  and  $D$ . Following the same procedure as the

	reaction	reaction rate
electron impact dissociation		
1.	$\text{SiH}_4 + e \rightarrow \text{SiH}_2 + 2 \text{H}$	$k_1$
2.	$\text{SiH}_4 + e \rightarrow \text{SiH}_3 + \text{H}$	$k_2$
3.	$\text{H}_2 + e \rightarrow 2 \text{H}$	$k_{\text{H}}$
reactions with radicals		
4.	$\text{SiH}_4 + \text{H} \rightarrow \text{SiH}_3 + \text{H}_2$	$k_a$
5.	$\text{SiH}_2 + \text{H}_2 \rightarrow \text{SiH}_4$	$k_{\text{H}_2}$
6.	$\text{SiH}_4 + \text{SiH}_2 \rightarrow \text{Si}_2\text{H}_6$	$k_p$
surface reactions		
7.	$\text{SiH}_2 \rightarrow \text{Si}_{\text{surf}} + \text{H}_2$	$S_1$
8.	$\text{SiH}_3 \rightarrow \text{Si}_{\text{surf}} + 3/2 \text{H}_2$	$S_2$
9.	$\text{H} \rightarrow 1/2 \text{H}_2$	$R$

**Table 6.1:** Reactions used for the analytical plasma chemistry model. Only electron-molecule, radical-surface and radical-molecule reactions were considered.

one presented in Section 3.3, combining Eqs. 6.1, 6.7 and 6.8 gives

$$\frac{a}{a^0} = 1 + \frac{k_1 n_e}{a^0} \cdot \left[ c_p + \frac{k_a}{k_1} \cdot \frac{(2k_1 + k_2)c_p + 2k_H(1 - c_p)}{R + k_a c_p n_{\text{tot}}} - \frac{k_{H_2}(1 - c_p) + 2k_p c_p}{S_1 + (k_{H_2}(1 - c_p) + k_p c_p)n_{\text{tot}}} \right]; \quad (6.10)$$

and combining the balance on  $\text{SiH}_4$  (Eq. 6.1) with the case without plasma ( $k_j = 0$ ) linking the pumping rate, the total density and the input flow rates by  $a^0 n_{\text{tot}} = \Phi_{\text{SiH}_4} + \Phi_{\text{H}_2}$  gives

$$\frac{a}{a^0} = \frac{1}{1 - D} + \frac{k_1 n_e}{a^0} n_{\text{tot}} \cdot \left[ \frac{k_{H_2}(1 - c_p) - k_p c_p}{S_1 + (k_{H_2}(1 - c_p) + k_p c_p)n_{\text{tot}}} - \frac{k_a}{k_1} \frac{(2k_1 + k_2)c_p + 2k_H(1 - c_p)}{R + k_a c_p n_{\text{tot}}} - \frac{k_1 + k_2}{k_1 n_{\text{tot}}} \right]. \quad (6.11)$$

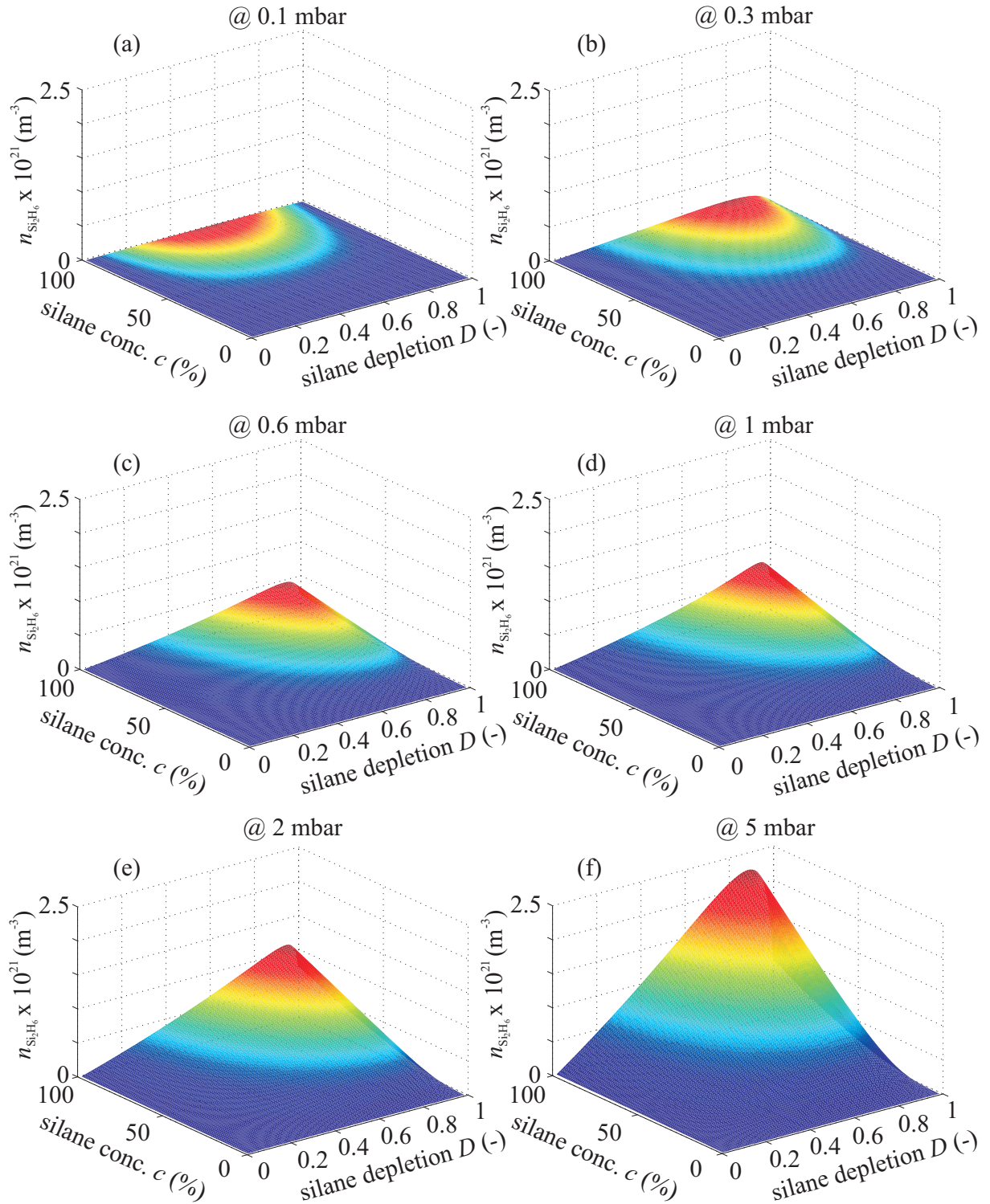
Using the identity of the two previous equations and re-arranging we obtain finally

$$\frac{k_1 n_e}{a^0} = \frac{1}{n_{\text{tot}}(1/D - 1)} \cdot \left[ \frac{k_1(c_p + 1) + k_2}{k_1 n_{\text{tot}}} - \frac{k_{H_2}(1 - c_p)(1 + c_p) + k_p c_p(2c_p - 1)}{S_1 + (k_{H_2}(1 - c_p) + k_p c_p)n_{\text{tot}}} + \frac{k_a(c_p + 1)}{k_1} \cdot \frac{(2k_1 + k_2)c_p + 2k_H(1 - c_p)}{R + k_a c_p n_{\text{tot}}} \right] \quad (6.12)$$

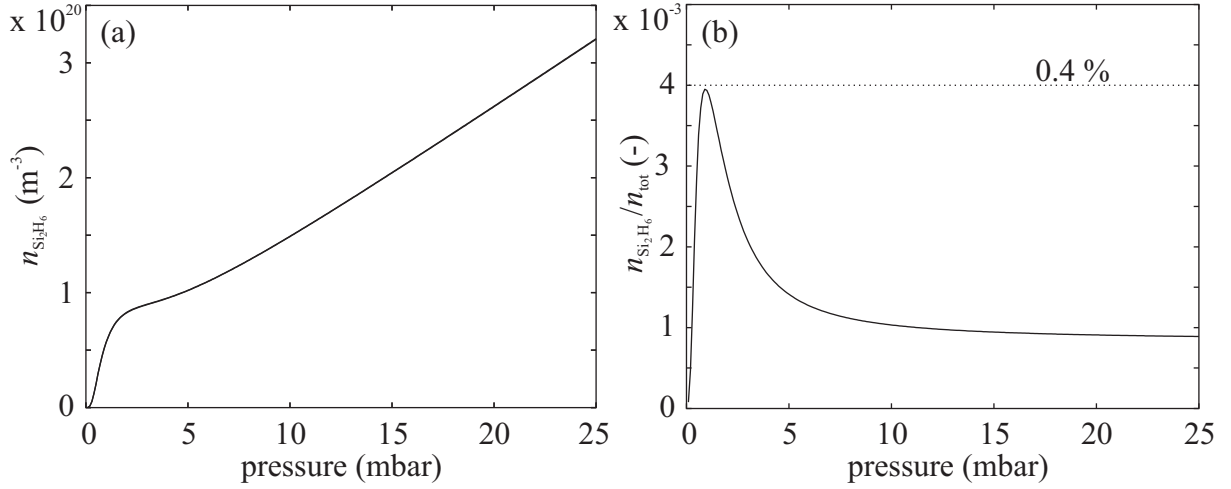
This latter expression does not give the exact solution when substituted into Eq. 6.9 since generally  $a \geq a^0$ . However,  $k_1 n_e/a$  can be determined by using Eqs. 6.10 and 6.12. The resulting formula is not presented here because of its unwieldy form.

Figure 6.2 presents the disilane density as a function of the silane concentration and depletion for various pressures ranging from 0.1 to 5 mbar. First of all, the pressure has a strong effect on the disilane density which increases from  $1.5 \cdot 10^{19}$  to  $2.3 \cdot 10^{21} \text{ m}^{-3}$  for its maximum value when the pressure is increased from 0.1 to 5 mbar (see also Fig. 6.3(a)). However, the normalized disilane density relative to the total density,  $n_{\text{tot}}$ , passes through a maximum as a function of pressure as shown in Fig. 6.3(b). This behavior shows that at low pressure the discharge is free of disilane; when the pressure is raised, a threshold is crossed and disilane appears suddenly. For higher pressures, the rate of disilane formation is reduced, even if its density increases linearly with pressure (Fig. 6.3(a)). These results seems to be in good agreements with observation of powder formation in  $\text{SiH}_4$ - $\text{H}_2$  discharges, even if the model contains only disilane and not higher-order polysilanes. Therefore, results are certainly valid for the threshold of polysilane appearance, but not for the case of powdery discharge above this threshold, due to complex phenomena involved in dusty plasmas such as ion chemistry [145, 164], ion trapping [128, 146, 164] or particle agglomeration [162, 165]. Therefore, the behavior above the maximum in Fig. 6.3(b) might be different from the one proposed here.

Second, the position of the maximum stands on the line  $c = 100 \%$ , but the position relative to the  $D$ -axis is pressure-dependent. At low pressure the maximum in disilane



**Figure 6.2:** Disilane density as a function of the silane depletion and concentration for pressures ranging from 0.1 mbar (a) to 5 mbar (f).



**Figure 6.3:** (a) Absolute and (b) relative disilane density variation as a function of pressure for a depletion  $D = 0.85$  and a silane concentration  $c = 10 \%$  ( $c_p = 0.85 \%$ ).

density stands at  $D = 0.5$  and shifts to higher values when the pressure is raised, before going back to the lower values as shown in Fig. 6.4(a). According to powder formation observations, polysilane density is expected to increase with silane concentration [71] with a maximum for pure silane, which agrees with the present result. On the other hand, an increase in polysilane density is also expected while the silane depletion is increased as shown by power series experiment [146], but Fig. 6.4(a) shows that the disilane density is lower for  $D = 1$  than for intermediate value of  $D$ . Physically this is due to the fact that the silane concentration in the plasma is very low for high values of the silane depletion. It slows down the polysilane production rate, since it is governed by the product  $n_{\text{SiH}_2} \cdot n_{\text{SiH}_4} = n_{\text{SiH}_2} \cdot c(1 - D)n_{\text{tot}}$ , which agrees with the results of Kessels *et al* [20]. For this reason, the silane density can be the limiting factor of polysilane formation, even for a pure silane plasma, showing once more that the plasma composition is much more relevant than the initial input composition. When speaking about RF capacitively-coupled discharges, having lower powder density at higher silane depletion, i.e. higher power level for example, does not seem intuitive. This is due to the fact that it is usually difficult to reach very high levels of silane depletion fraction by using a RF source of excitation. But if much more powerful sources are used such as a low energy plasma (LEP) DC arc source, powder-free plasma discharges can be performed and this even from pure silane gas [107]. Moreover, the reactor configuration of this latter technique has a very large volume:surface ratio. Therefore, the reactor geometry is not at all in favor of powder-free processes, making the strong plasma dissociation fully responsible for the cleanliness of the discharge.

Following the same idea, for low values of the silane depletion, the disilane production rate is also low, since for this case the limiting factor is the  $\text{SiH}_2$  radical density which is too low due to the low silane dissociation rate. It results that the maximum in disilane density stands in between these two extremes.

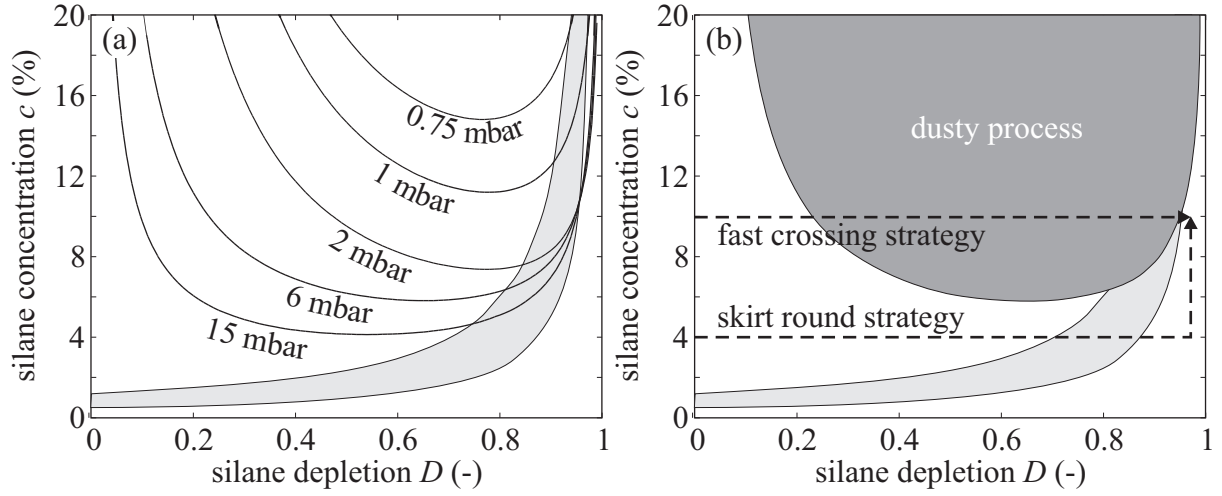


**Figure 6.4:** (a) Iso-disilane density ( $n_{\text{Si}_2\text{H}_6} = 7 \cdot 10^{19} \text{ m}^{-3}$ ) curves for various pressures in the  $(D, c)$  plane. When the pressure is increased, the powder-free process window for transitional material is reduced to lower silane concentration or very high silane depletion. (b) Schematic representation of the possible strategies to avoid powder formation while working in Regime 2.

Iso-disilane curves in Fig. 6.4 have been calibrated on the basis of the observation of powder appearance by laser scattering for a silane concentration of 10 %, a pressure of 2 mbar and a measured silane depletion of 0.47, corresponding to a modeled disilane density of  $7 \cdot 10^{19} \text{ m}^{-3}$ . The position of the iso-disilane density in Fig. 6.4(a) makes the process window for transitional material at high silane concentration disadvantageous. The pressure has to be limited to low values to avoid powder formation, and even if this precaution is taken, the polysilane formation threshold may be crossed at plasma ignition, while increasing RF power at constant silane input concentration as shown in Fig. 6.4(b). If the duration of the trip in the high disilane density region is too long, it may be impossible to reach a powder free process [146, 162], and this even if the silane depletion fraction is sufficiently high. Two different countermeasures could be used in order to avoid polysilane formation while igniting the plasma. (i) A pre-matching can be used as described in Chapter 5. If the matching network is set at the equilibrium position before plasma ignition, and the full RF power delivered directly, the equilibration time is so fast that no polysilane could form before steady-state is reached. Of course, this technique is only valid if the plasma reactor is closed and directly pumped (see Chapter 5). (ii) Hydrogen dilution profiling can also be used to avoid polysilane formation. The disilane threshold can be skirted round by igniting the plasma with a silane concentration lower than the lowest value of the threshold. The high silane depletion level is then reached by increasing the RF power input, and finally the silane input concentration is raised to the final level as sketched in Fig. 6.4(b). This second technique can be used in all types of reactors, i.e. open or closed, since the time to reach equilibrium is not important in this case, for both the crystallinity and the polysilane formation, because the silane concentration in the plasma remains always low.

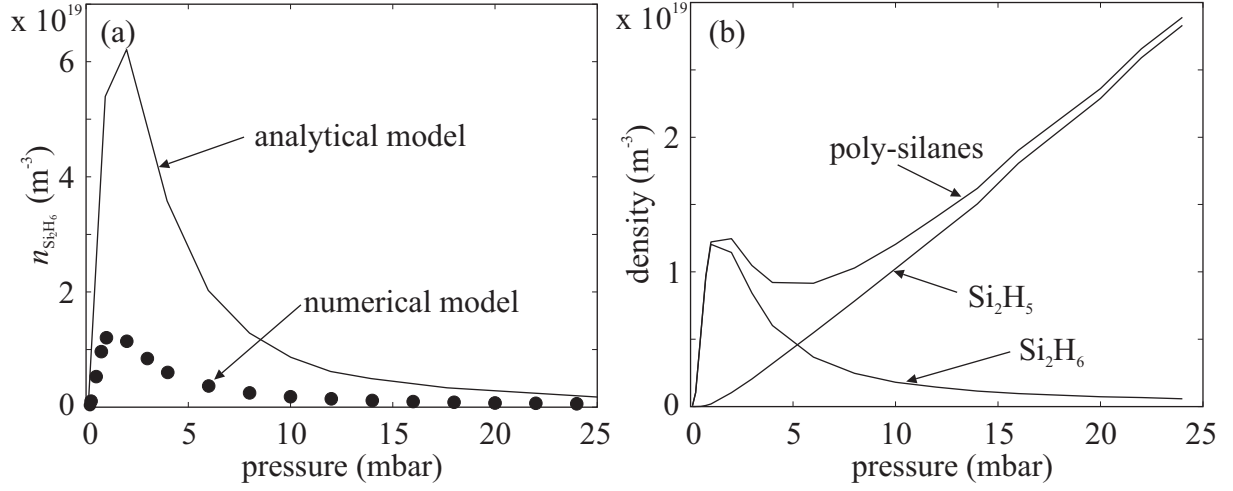


**Figure 6.5:** (a) Comparison of the analytical and numerical models for the disilane density as a function of the pressure, while other parameters are kept constant. The silane depletion is pressure dependent and is an output of the numerical model. The depletion has then been used in the analytical model as an input to draw the corresponding curve. (b)  $\text{Si}_2\text{H}_6$ ,  $\text{Si}_2\text{H}_5$  and total disilane densities obtained by numerical computing as a function of the pressure

## 6.2 Numerical model

The analytical model presented in the previous section includes only disilane molecule specie ( $\text{Si}_2\text{H}_6$ ) as a marker for higher-order polysilane formation. Other type of polysilanes have not been taken into account for, because radical-radical or radical-disilane reactions introduce non-linearity into the equation system, making the analytical resolution impossible without using numerical routines. Therefore, the analytical plasma chemistry model including disilane has been compared to the numerical model presented in Section 3.2.2 including the  $\text{Si}_2\text{H}_5$  specie and five radical-radical or radical-molecule reactions.

Figure 6.5(a) presents the disilane density,  $n_{\text{Si}_2\text{H}_6}$ , as a function of the pressure calculated with the numerical and the analytical models for a gas mixture with a silane concentration  $c = 10 \%$ , a total flow rate of 500 sccm and an electron density  $n_e = 10^{17} \text{ m}^{-3}$  (interelectrode distance  $d_{\text{gap}} = 25 \text{ mm}$ ). It shows that the analytical model overestimates by a factor of about 5 the disilane density compared to the density given by the numerical zero-dimensional model. This difference is due to the absence of loss term on the  $\text{Si}_2\text{H}_6$  specie other than pumping loss in the analytical model. The numerical model takes into account for additional losses of  $\text{Si}_2\text{H}_6$  by electron impact or H abstraction dissociation or reaction with  $\text{SiH}_3$  radicals (see Table 3.4), hence lowering the disilane density. However, when summing disilane molecule and radical  $\text{Si}_2\text{H}_6$  and  $\text{Si}_2\text{H}_5$ , respectively, the relative polysilane density has a different behavior than for the analytical model while the pressure is increased. The polysilane appearance threshold is similar for both models, but the numerical model predicts a more or less constant relative polysilane density ( $1 - 1.5 \cdot 10^{19} \text{ m}^{-3}$ ) in the 2 - 15 mbar pressure range and a linear increase for higher pressures. On the other hand, the analytical model predicts a decrease of the relative disilane density for

pressures higher than  $\approx 2$  mbar. This is in agreement with the main conclusion of the previous section stating that the analytical model is valid for the position of the polysilane appearance threshold, but is not able to describe phenomena occurring above this limit. The numerical model presented here has also such a limitation, because the limited number of species and reactions chosen here are not sufficient to describe what happens at higher pressures where higher order polysilanes and dust form. However, the numerical routine predicts a more or less constant polysilane density after its appearance up to 15 mbar as shown in Fig. 6.5(b). Therefore, it is more in agreement with general observation of powder formation than the analytical model which predicts a decrease of the polysilane density when the pressure is increased in the 2 - 15 mbar pressure range (for  $p$ -dependent silane depletion), which is in fact where most of the process for microcrystalline silicon are performed.

Note that the pressure dependence of the disilane densities given in Figs. 6.3 and 6.5 present different behavior. This is due to the fact that in the case of Fig. 6.3 the pressure increase was performed while the silane depletion (and hence also  $c_p$ ) was kept constant, hence following the horizontal line in Fig. 6.6 and increasing monotonically the disilane density. In the second case presented in Fig. 6.5, the silane depletion fraction increases with the pressure while the electron density is kept constant, due to the variation of the residence time. The silane depletion fraction is a result of the numerical routine and cannot be fixed arbitrarily. Therefore, the silane depletions obtained by numerical simulation were re-injected as an input in the analytical model to be able to compare both models. The path followed in Fig. 6.6 in this case is no longer horizontal since the silane concentration in the plasma is not constant and decreases with pressure. This explains why we can observe a decrease of the disilane absolute density while the pressure is increased, fact which is not intuitive at first sight.

## 6.3 Gap reduction

It has been shown from the plasma chemistry model that polysilane formation, which is rapidly followed by powder formation [163], limits the process window for microcrystalline silicon deposition. Moreover, polysilane formation occurs preferentially in Regime 2, i.e. at high silane concentration, where the deposition is the more efficient, making powder formation a real limitation for high rate deposition of microcrystalline silicon with a high deposition efficiency. Therefore, it is necessary to eliminate, or at least limit, polysilane formation in order to permit the increase of the input silane concentration to improve the deposition efficiency [130].

As shown by Eq. 6.9, the disilane density depends on the silane concentration in the plasma and on the total density as discussed above, but also on the surface reaction rates of  $\text{SiH}_2$  radicals,  $S_1$ , and of atomic hydrogen,  $R$ . These are pressure-dependent, as well as the reaction rate coefficient  $k_{\text{H}_2}$  and  $k_p$ , and are also dependent on the reactor geometry as shown in Sec. 3.2.2. This dependence is shown in Fig. 6.7 for a constant plasma silane concentration of 1.5 % ( $c = 10$  %,  $D = 0.85$ ) for interelectrode gaps from 5 to 25 mm as a function of the pressure. For all interelectrode distances the disilane density increases monotonically with the pressure as shown in Fig. 6.7(a). When comparing the different

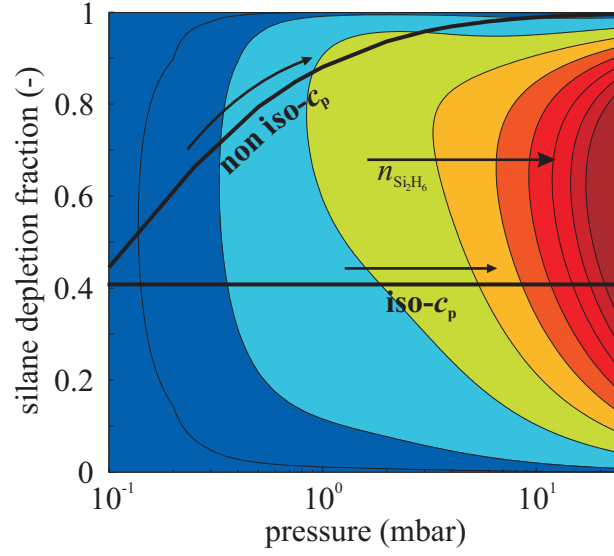


**Figure 6.6:** Contour of iso-disilane density in the the  $(p, D)$  plane. Curves represent the path followed when the pressure is increased for constant  $c_p$  (iso- $D$  in Fig. 6.3) and variable  $c_p$  (variable  $D$  in Fig. 6.5).

reactor geometries on the basis of the relative disilane density (Fig. 6.7(b)), we can see that the maximum is almost at the same level ( $\approx 0.4$  %) for all gaps, but the position is gap-dependent. Note that the disilane relative density above its maximum is somewhat speculative since no radical-radical reactions leading to higher-order polysilanes formation are taken into account as discussed in the previous section. Therefore, the effect of the

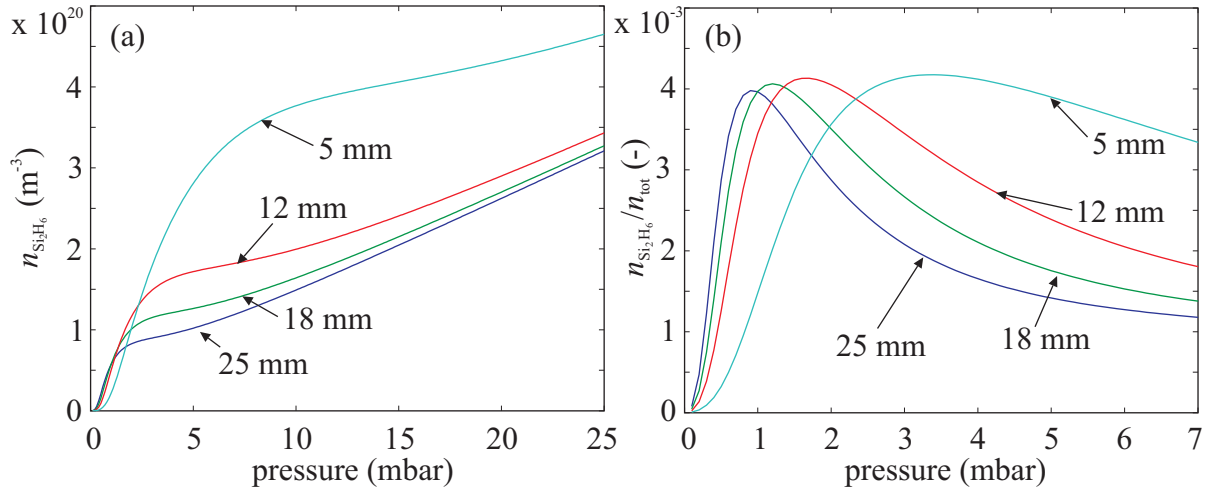


**Figure 6.7:** Analytical results of (a) absolute and (b) relative disilane density variation as a function of pressure for a depletion  $D = 0.85$  and a silane concentration  $c = 10$  % ( $c_p = 0.85$  %) for interelectrode distance ranging from 5 to 25 mm.



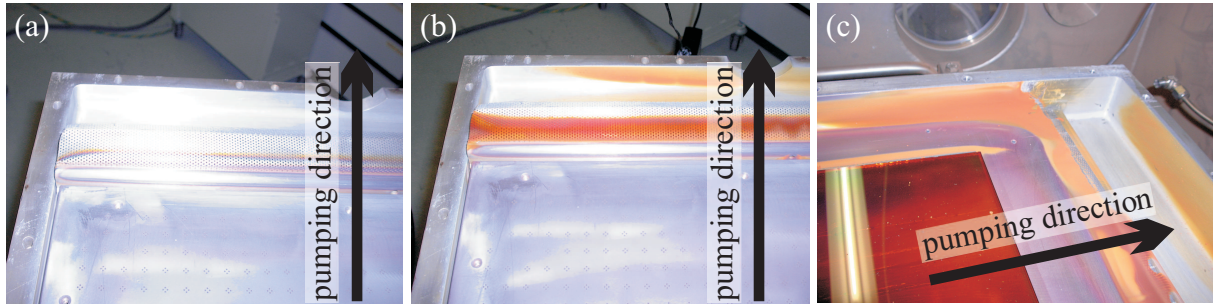


**Figure 6.8:** Picture of the inside of the reactor after processes producing (a) no powder, (b) powder only on the pumping grid and (c) powder on the electrodes in the deposition area.

gap estimated from the model at high pressure, i.e. above 3 mbar for  $d_{\text{gap}} = 5$  mm, is not representative of what occurs in the discharge. However, for pressures lower than these maxima it is clear that the disilane formation is shifted to higher pressure when the interelectrode distance is reduced. This can be interpreted by the change in the distribution between surface and volume reactions of the  $\text{SiH}_2$  radicals when the gap is varied. In parallel plate reactors, the surface to volume ratio follows  $2/d_{\text{gap}}$ , where  $d_{\text{gap}}$  is the interelectrode distance. Since the radical mean free path is not gap-dependent, the surface reaction probability for a radical,  $\text{SiH}_x$  or  $\text{H}$ , is higher while  $d_{\text{gap}}$  is reduced. Therefore, the powder formation is reduced in narrow gap reactors, only because of a geometrical effect.

Results of the models including polysilane formation presented in this work are difficult to validate experimentally since the detection of polysilane is extremely complex. Different diagnostics have been tried to estimate the polysilane density or relative density variation, but all were unable to give relevant information. Mass spectroscopy is inadequate to measure low-order polysilanes in the gas exhaust, and laser scattering in the exhaust line is sensitive only to "large" particles ( $> 10 - 20$  nm depending on the laser wavelength) which are difficult to correlate with low-order polysilanes. However, the most problematic sources of experimental difficulties are not technical but physical. First of all, the polysilane density is not only pressure,  $c_p$  and gap-dependent, but depends strongly on time with cycles of powder growth and ejection out of the plasma zone [128, 165]. These cycles are strongly parameter-dependent in terms of period and amplitude [128] making difficult a general approach as the one presented here. Second, the polysilane formation may be strongly nonuniform for both low-order polysilane and powder particles. Indeed, polysilanes could form preferentially in the vicinity of intense plasma zone at the edge of the reactor where the RF and the ground electrodes are separated only by 2-3 mm [69]. It could also form just at the back of the pumping grid where the vertical space is larger, reducing the surface to volume ratio, and where the electrode heating is less efficient, favoring the polysilane formation [71, 146, 161, 162, 165]. The door of the reactor could also be a source of powder formation, since it is not directly heated as for the zone at the back of the pumping grid. For all these reasons, polysilane and powder formation characterization in the gas exhaust is not necessarily representative of what is occurring

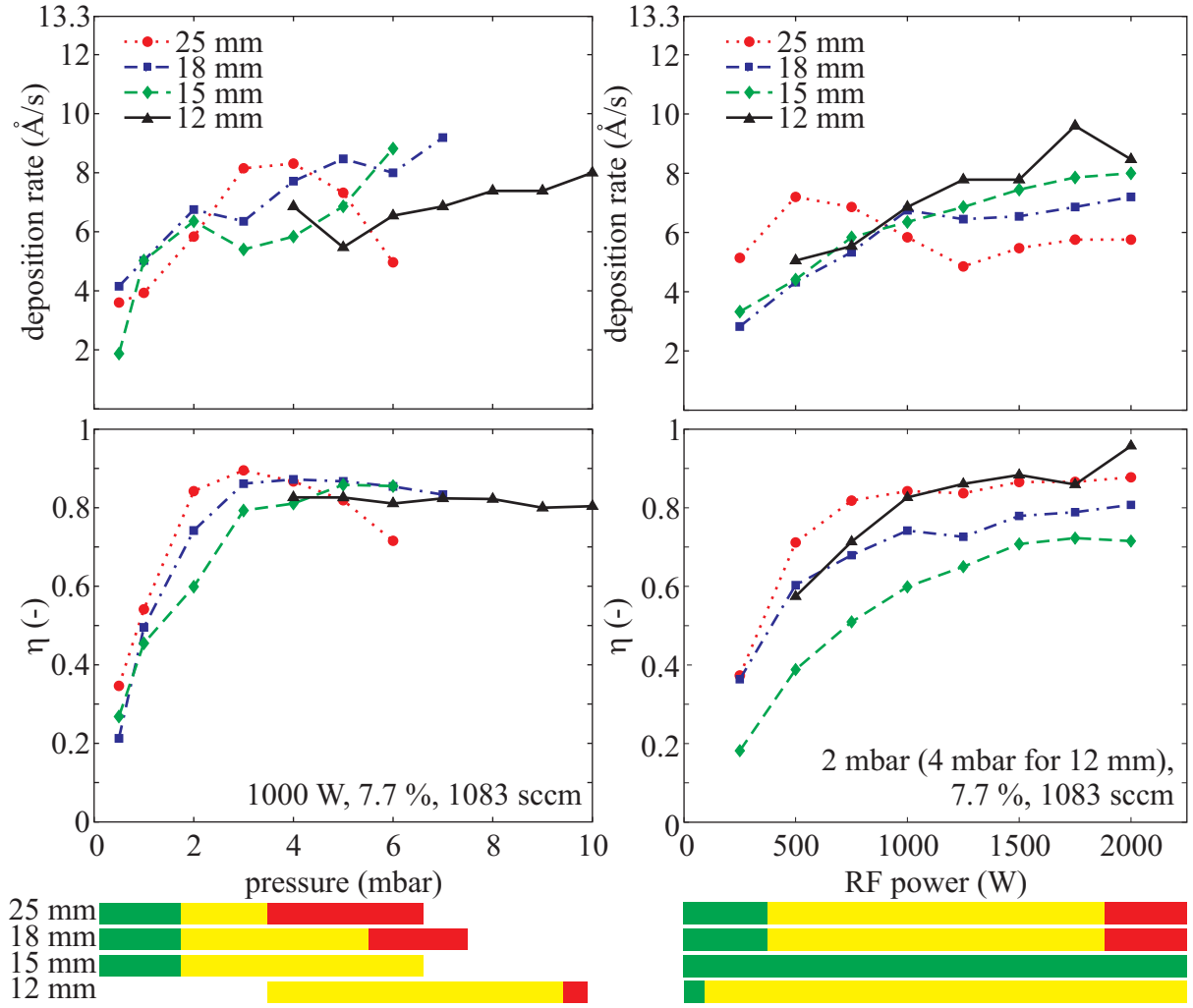


**Figure 6.9:** Deposition rate (top), silane dissociation efficiency (center) and powder contamination of the reactor (bottom) for pressure (left) and power (right) series for interelectrode distance of 12, 15, 18 and 25 mm. Constant silane flow rate of 82 sccm ( $R_{\max} = 13.3$  Å/s) has been used. The power series for the 12 mm gap has been performed at 4 mbar (2 mbar for the others) since plasma ignition did not occur for lower pressures. The powder contamination has been estimated by eye after each deposition and has been graded as green for powder free, yellow for powder only on pumping grid and red for powder on the electrodes.

over the deposition area and could be misinterpreted.

However, a purely qualitative technique has been used to quantify polysilane and powder formation as a function of the different discharge parameters. This was performed by checking visually if there was powder in the reactor after a discharge. A deposition process was considered as powder free if no powder residue could be seen in the reactor, including the pumping grid as shown in Fig. 6.8(a). Processes after which powder could be seen only on the pumping grid (Fig. 6.8(b)) are acceptable since no contamination over the deposition area occurs, but processes involving powder deposition in the reactor

(Fig. 6.8(c)) are not acceptable. This classification has been used for pressure and RF power series for interelectrode distance of 12, 15, 18 and 25 mm which are given in Fig. 6.9. The pressure series clearly shows that the lower the interelectrode gap, the higher the pressure at which powder starts to form. For the RF power series, the powder is not reduced in a significant manner when the gap is reduced from 25 to 18 mm, but no powder forms over the 0 to 2 kW range for a gap of 15 mm. For the 12 mm gap, powder was observed only on the pumping grid over the whole power range, but the pressure (4 mbar) was higher than for the other gaps (2 mbar) because of the absence of uniform plasma for lower pressures for such a narrow gap configuration. These observations confirm that reducing the interelectrode distance shifts the polysilane and powder appearance to higher pressures, as found on the basis of the plasma chemistry model.

Moreover, figure 6.9 shows that the deposition rate and dissociation efficiency,  $\eta$ , depend on the interelectrode distance. With a 25 mm gap configuration, the deposition rate and dissociation efficiency do not increase monotonically with the pressure and pass through a maximum. These are inter-related and the decrease of the dissociation efficiency at high pressure is probably associated with electron attachment onto powder particles which results in a reduction of the electron density [71, 128]. For this wide gap, the powder formation significantly influences also the power series by reducing the deposition rate at high power because of silane radical consumption by gas phase reactions. Note that the silane dissociation efficiency is not reduced in this case, probably because the RF power increases more the electron density than electron attachment on particle decreases the electron density for such discharge parameters.

The reduction of the dissociation efficiency in the power series while the gap is decreased can be explained by the fact that the residence time is reduced because of the reactor volume reduction while all other plasma parameters are held constant. The reduction of both the deposition rate and the dissociation efficiency at high pressure is not observed for interelectrode distance lower than 25 mm, even if the dissociation efficiency saturates around 0.8 for all gaps. However, a behavior similar to the one of the 25 mm gap has been reported by Graf [139] for lower interelectrode distance. In his case the maximum in deposition rate was shifted to higher pressures when the gap was reduced. This is probably related to the results of the plasma chemistry model presented above.

To summarize, reducing the interelectrode distance may help to reduce polysilane and powder formation when working at high pressure. This has been shown by plasma chemistry modeling and by qualitative observation of powder in the deposition reactor which agree that the lower the interelectrode distance, the higher the pressure at which powder starts to form. However, the use of a narrow gap reactor forces to work at very high pressures in order to have a uniform plasma over the deposition area, therefore it could eliminate the benefit of interelectrode distance reduction by permitting only processes where powder forms.

## 6.4 Flux ratio dependence on pressure

Polysilane and powder formation not only reduce the process window because of film contamination or reactor dirtying as shown in the previous section. A discharges which contains polysilanes has quite obviously a different composition compared to a discharge free of polysilane such as the ones treated in all the previous chapters. This change in plasma composition may affect the  $\Gamma_{\text{H}}/\Gamma_{\text{SiH}_x}$  flux ratio towards the growing film surface, and hence affect the position of the transition zone from amorphous to microcrystalline silicon deposition.

By using the analytical plasma chemistry model which includes disilane ( $\text{Si}_2\text{H}_6$ ) presented in Table 6.1, the flux of hydrogen which recombines onto the film surface,  $\Gamma_{\text{H}}$ , and the flux of silane radicals sticking on the film surface,  $\Gamma_{\text{SiH}_x} = \Gamma_{\text{SiH}_3} + \Gamma_{\text{SiH}_2}$ , can be deduced from Eqs. 6.3, 6.4 and 6.8, respectively, and the flux ratio is then given by

$$\frac{\Gamma_{\text{H}}}{\Gamma_{\text{SiH}_3} + \Gamma_{\text{SiH}_2}} = \frac{[(2k_1 + k_2)n_{\text{SiH}_4} + 2k_{\text{H}}n_{\text{H}_2}]n_{\text{e}} - k_{\text{a}}n_{\text{H}}n_{\text{SiH}_4}}{(k_1 + k_2)n_{\text{SiH}_4}n_{\text{e}} + k_{\text{a}}n_{\text{H}}n_{\text{SiH}_4} - (k_{\text{H}_2}n_{\text{H}_2} + k_{\text{p}}n_{\text{SiH}_4})n_{\text{SiH}_2}}. \quad (6.13)$$

The  $\text{SiH}_2$  and the atomic hydrogen number densities can be obtained from Eqs. 6.4 and 6.8 and correspond, respectively, to

$$n_{\text{SiH}_2} = \frac{k_1}{S_1 + k_{\text{H}_2}n_{\text{H}_2} + k_{\text{p}}n_{\text{SiH}_4}} \cdot n_{\text{e}} \quad (6.14)$$

and

$$n_{\text{H}} = \frac{(2k_1 + k_2)n_{\text{SiH}_4} + 2k_{\text{H}}n_{\text{H}_2}}{R + k_{\text{a}}n_{\text{SiH}_4}} \cdot n_{\text{e}}. \quad (6.15)$$

In the expression 6.13, the additional effects due to radical-molecule reactions are the three terms containing  $n_{\text{H}}$  either  $n_{\text{SiH}_2}$ . If these terms are neglected, the flux ratio is then the one deduced from the simplest analytical case given in Eq. 3.13. In the present case, the  $\Gamma_{\text{H}}/\Gamma_{\text{SiH}_x}$  flux ratio depends no longer only on the silane concentration in the plasma, but also on the total density, i.e. the working pressure  $p = n_{\text{tot}}k_{\text{B}}T$ . This dependence is shown by Eq. 6.16, where the pressure has an obvious effect on the total density,  $n_{\text{tot}}$ , but also on the values of the surface reaction rates,  $S_1$  and  $R$ , discussed in Sec. 3.2.2, and finally on the gas phase reaction rates  $k_{\text{p}} = 2.2 \cdot 10^{-16}(1 - (1 + 0.5p)^{-1})$  [55] and  $k_{\text{H}_2} = 3.2 \cdot 10^{-16}(1 - (1 + 0.024p)^{-1})$  [55]. Despite the unwieldy form of the expression of the flux ratio in Eq. 6.16, the numerator (first line) has the same form as the general expression for the simple model given by  $2\kappa(c_{\text{p}}^{-1} - 1) + \text{constant}$ .

$$\begin{aligned} \frac{\Gamma_{\text{H}}}{\Gamma_{\text{SiH}_x}} = & \left\{ 2 \frac{k_{\text{H}}}{k} \left[ 1 - \left( \frac{R}{c_{\text{p}}n_{\text{tot}}} + k_{\text{a}} \right)^{-1} \right] (c_{\text{p}}^{-1} - 1) + \frac{2k_1 + k_2}{k} \left[ 1 - k_{\text{a}} \left( \frac{R}{c_{\text{p}}n_{\text{tot}}} + k_{\text{a}} \right)^{-1} \right] \right\} \cdot \\ & \cdot \left[ 1 - \frac{k_1}{k} \cdot \frac{k_{\text{p}} + k_{\text{H}_2}(c_{\text{p}}^{-1} - 1)}{\frac{S_1}{c_{\text{p}}n_{\text{tot}}} + k_{\text{H}_2}(c_{\text{p}}^{-1} - 1) + k_{\text{p}}} + \frac{k_{\text{a}}}{k} \cdot \frac{(2k_1 + k_2) + 2k_{\text{H}}(c_{\text{p}}^{-1} - 1)}{\frac{R}{c_{\text{p}}n_{\text{tot}}} + k_{\text{a}}} \right]^{-1} \end{aligned} \quad (6.16)$$

The resulting flux ratio towards the surface of the growing film as a function of pressure is given in Fig. 6.10 for a silane concentration of 10 % and an interelectrode distance of

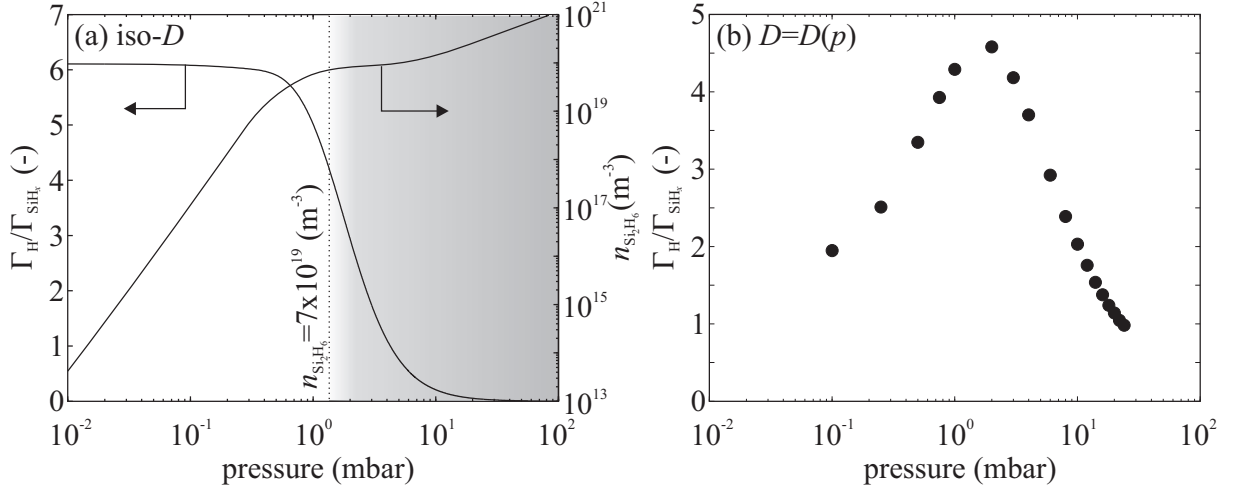


**Figure 6.10:** Pressure effect ( $n_e = \text{constant}$ ) on the  $\Gamma_H/\Gamma_{SiH_x}$  flux ratio for (a) constant silane depletion and (b) variable depletion as a function of the pressure. The constant silane depletion case is the results of the analytical model, and the pressure dependent depletion case of the zero-dimensional numerical model.

25 mm. Figure 6.10(a) assumes a constant silane depletion of  $D = 0.9$ , i.e. a constant silane plasma concentration  $c_p = 1\%$ , whereas Fig. 6.10(b) takes into account the silane depletion variation while the pressure increases. This has been performed by using the results of the numerical model for the pressure dependence of the silane depletion, which has been used as an input in the analytical model presented here. Figure 6.10(a) shows that for low pressures ( $p < 0.3$  mbar), the flux ratio is not affected by the pressure variation, since for such pressures radical reactions are concentrated on the reactor walls due to the long collision mean free path. For higher pressures, the volume reactions between radical and molecules are no longer negligible and affect the fluxes towards the film surface. The appearance of polysilanes in the discharge reduces the hydrogen to silicon radical flux ratio while the pressure increases, hence reducing the ability of the plasma to deposit microcrystalline silicon films. The threshold value of the disilane density corresponding to  $7 \cdot 10^{19} m^{-3}$  stands at a higher pressure ( $\approx 2$  mbar) than the pressure at which the first effect on the flux ratio is observed. This means that already for pressures lower than at which powder is observed by eye in the discharge, the flux towards the surface is affected. For higher pressures (shaded zone in Fig. 6.10(a)), the effect on the flux ratio might be very different from the one exposed here, because of particles larger than  $Si_2H_6$  and more complex chemical channels such as electron attachment or negative particle trapping which are not taken into account here.

The pressure effect on the flux ratio towards the surface is somewhat different when the depletion is not fixed, but pressure-dependent as shown in Fig. 6.10(b). When the silane depletion depends on the pressure, there are two competing phenomena: (i) The silane depletion increases with pressure due to the increase of the residence time, and (ii) the flux ratio is lowered with the no-longer negligible gas phase chemical reactions between radicals and molecules. First, the increase of the flux ratio with the silane depletion

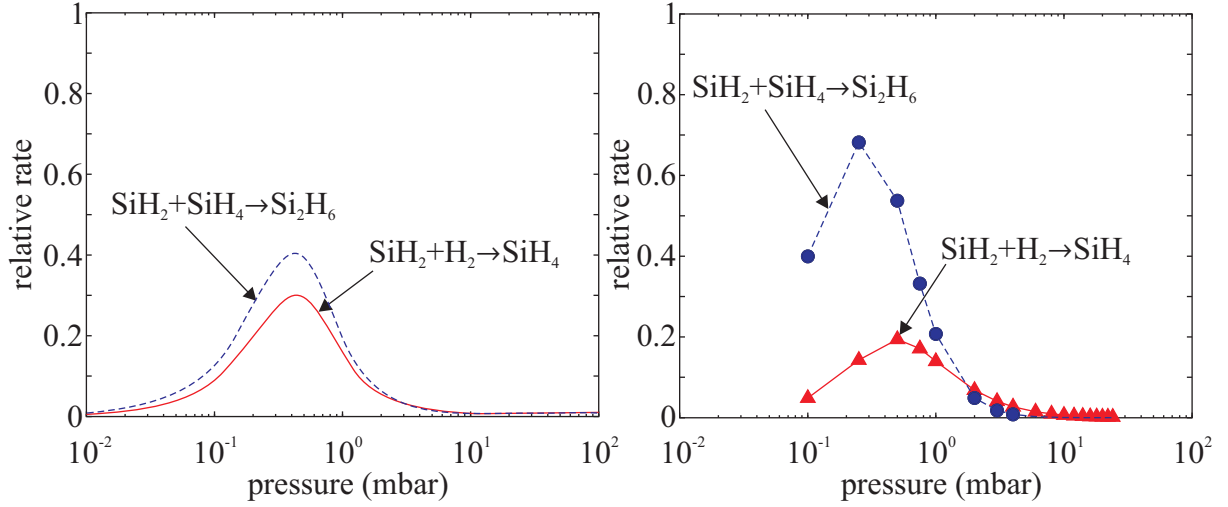


**Figure 6.11:** Reaction rates of  $\text{SiH}_2$  gas recombination ( $k_{\text{H}_2}n_{\text{SiH}_2}n_{\text{H}_2}$ ) and silane polymerization ( $k_{\text{p}}n_{\text{SiH}_2}n_{\text{SiH}_4}$ ) reactions relative to the hydrogen abstraction reaction rate ( $k_{\text{a}}n_{\text{H}}n_{\text{SiH}_4}$ ) for (a) constant silane depletion ( $D = 0.9$ ) and (b) pressure-dependent silane depletion with a silane concentration of 10 %.

dominates until a maximum is reached around 2 mbar. The value of 2 mbar at which gas phase reactions becomes non-negligible is consistent with values found by Amanatides *et al* [74]. For higher pressures, the reduction of the flux ratio due to hydrogen consumption by gas phase reactions is dominant. Note that the disilane density in the case of pressure-dependent silane depletion is lower than  $3 \cdot 10^{19} \text{ m}^{-3}$  over the whole  $10^{-2}$  to  $10^2$  mbar pressure range, due to the lower rate of polysilane formation for very high depletion ( $D \rightarrow 1$ ) [20].

As mentioned before, the reason for the effect of the addition of radical-molecule gas phase reactions is the balance between surface and volume chemical reactions. In fact, the negative effect of high pressures - from the point of view of  $\mu\text{c-Si:H}$  deposition - is not surprising. As soon as the pressure is sufficiently high to make the radical-molecule reaction rates non-negligible, an additional sink for atomic hydrogen and a source of silane radical appear. The reaction (4) in Table 6.1 removes one hydrogen atom and produces one silane radical. The other gas phase reactions ((5) and (6) in Table 6.1) consume  $\text{SiH}_2$  radicals, but these reactions have much lower rates compared to the hydrogen abstraction reaction (reaction (4)), as shown by the reaction rates  $k_{\text{H}_2}n_{\text{SiH}_2}n_{\text{H}_2}$  and  $k_{\text{p}}n_{\text{SiH}_2}n_{\text{SiH}_4}$  relative to the hydrogen abstraction rate  $k_{\text{a}}k_{\text{H}}k_{\text{SiH}_4}$  in Fig. 6.11. This is valid for both constant silane depletion (Fig. 6.11(a)) and pressure-dependent silane depletion (Fig. 6.11(b)) over the  $10^{-2}$  to  $10^2$  mbar pressure range. As for the flux ratio, the relative importance of the gas phase reactions presented in Fig. 6.11 do not account for more complex and more realistic gas phase chemistry and may deviate for pressures higher than about 2 mbar. However, the resulting change in  $\Gamma_{\text{H}}/\Gamma_{\text{SiH}_x}$  flux ratio towards the growing film surface makes iso- $c_{\text{p}}$  curves in the  $(D, c)$  plane no longer iso-material quality. The iso- $\Gamma_{\text{H}}/\Gamma_{\text{SiH}_x}$  curves, which are iso-material quality, shift towards the microcrystalline deposition region

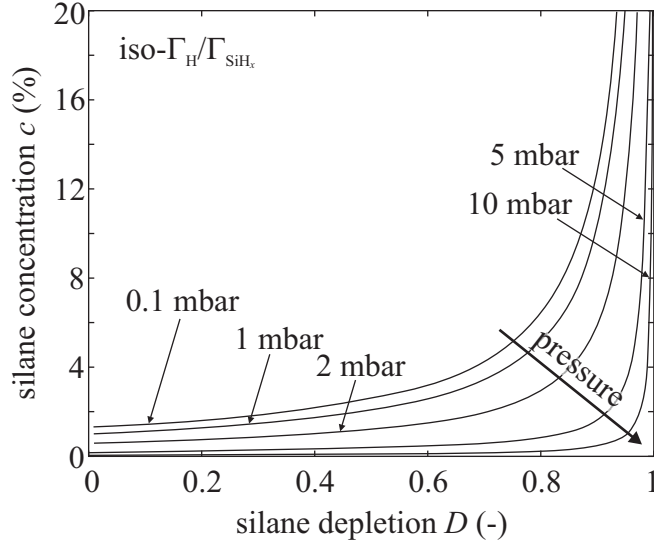


**Figure 6.12:** Pressure effect on  $\text{iso-}\Gamma_{\text{H}}/\Gamma_{\text{SiH}_x}$  flux ratio in the  $(D, c)$  plane. Curves correspond to  $\Gamma_{\text{H}}/\Gamma_{\text{SiH}_x} = 5$ , which is representative of the transitional material.

when the pressure increases, making the process window for microcrystalline silicon deposition smaller for higher pressures as shown in Fig. 6.12 for a flux ratio  $\Gamma_{\text{H}}/\Gamma_{\text{SiH}_x} = 5$ , corresponding to transitional material. This shift of the transition zone from amorphous to microcrystalline silicon deposition implies that the higher the pressure, the lower has to be the input silane concentration to deposit  $\mu\text{c-Si:H}$  in the Regime 1, and the higher should be the silane depletion to deposit  $\mu\text{c-Si:H}$  in the Regime 2. The combination of Figs. 6.4 and 6.12 could be at the origin of powder-free  $\mu\text{c-Si:H}$  depositions at high pressure in the so-called high-pressure-depletion regime [74], since the fact that  $\mu\text{c-Si:H}$  is deposited seems to guarantee to keep off the high disilane density zone, even if the pressure is increased.

## 6.5 Conclusion

Low-order polysilane formation has been discussed on the basis of analytical and numerical modeling. Results have shown that polysilanes are the origin of some limitations for microcrystalline silicon manufacture. First, polysilane, which leads rapidly to powder, forms preferentially in the Regime 2, i.e. at high silane concentration, where processes are interesting in terms of deposition rate and efficiency for microcrystalline silicon films. This means that the increase of the silane concentration in order to increase the deposition efficiency cannot be performed indefinitely. Moreover, the maximum possible silane concentration while remaining powder free is pressure dependent: The higher the pressure, the lower the maximum permissible concentration.

It is obvious that the presence of polysilanes modifies the plasma composition, therefore it affects the atomic hydrogen to silane radical flux ratio toward the surface. This ratio

is no longer only  $c_p$ -dependent, when polysilanes are taken into account for, but it depends also on the pressure and the interelectrode distance. At constant silane concentration in the plasma, increasing the pressure decreases the  $\Gamma_H/\Gamma_{SiH_x}$  ratio making the deposited film more amorphous. This is because the dominant radical-radical and radical-molecule gas phase reaction consumes atomic hydrogen and creates silicon radicals.

Finally, it has been shown that reducing the interelectrode distance in large-area parallel plate reactors is able to reduce powder formation and shifts its negative effects to higher pressures. Another possibility to reduce powder formation is to work with very highly depleted discharges ( $D \rightarrow 1$ ), since in this case the deposited layer is microcrystalline and the silane density in the plasma is so low that it limits the powder formation rate.



# Chapter 7

## Reactor geometry and uniformity

In recent years it has been shown that electromagnetic nonuniformity may affect the plasma uniformity and hence the deposited layer uniformity. For PV solar cells applications, the film thickness uniformity has to be better than  $\pm 10\%$  over the whole substrate area [58]. Moreover, when involved with Tandem solar cell structure, the crystallinity of the  $\mu c$ -Si:H intrinsic layer has to be as uniform as possible. This is of great importance since the material of interest lies in the transition zone, where the material is very sensitive to the plasma composition. Many theoretical works [166, 167, 168, 169, 170, 171, 172] have shown that the two main electromagnetic nonuniformities are the so-called Telegraph and standing-wave effects. In particular, it has been demonstrated by Sansonnens *et al* [171] that these two effects are the two only solutions of the electromagnetic field equation. Therefore, they are necessary and sufficient to describe the electromagnetic field everywhere in the plasma reactor, except for the immediate vicinity of the reactor walls, where secondary effects can be observed. These two effects have no influence on each other, therefore they can be treated separately [171, 172]. Moreover, these models have been validated experimentally separately by measuring plasma properties such as the optical emission [135, 173, 174, 175], the plasma potential [174, 176, 177, 173] or the ion flux towards the electrodes [135, 173]. However, effects of electromagnetic nonuniformity on film deposition have not been yet demonstrated, except for the influence of the standing-wave on the film thickness uniformity evidenced by Sansonnens *et al* [174, 175] and the effect of the Telegraph on the film thickness [176] which is detailed in this chapter.

This chapter reviews the theoretical aspects of electromagnetic nonuniformity important for the purpose of this work (Sec. 7.1). The influence of the Telegraph effect on film thickness uniformity is discussed in Sec. 7.2.1 and the influence of a variation of the RF voltage amplitude on both the thickness and the microstructure uniformity is presented in Sec. 7.2.2.

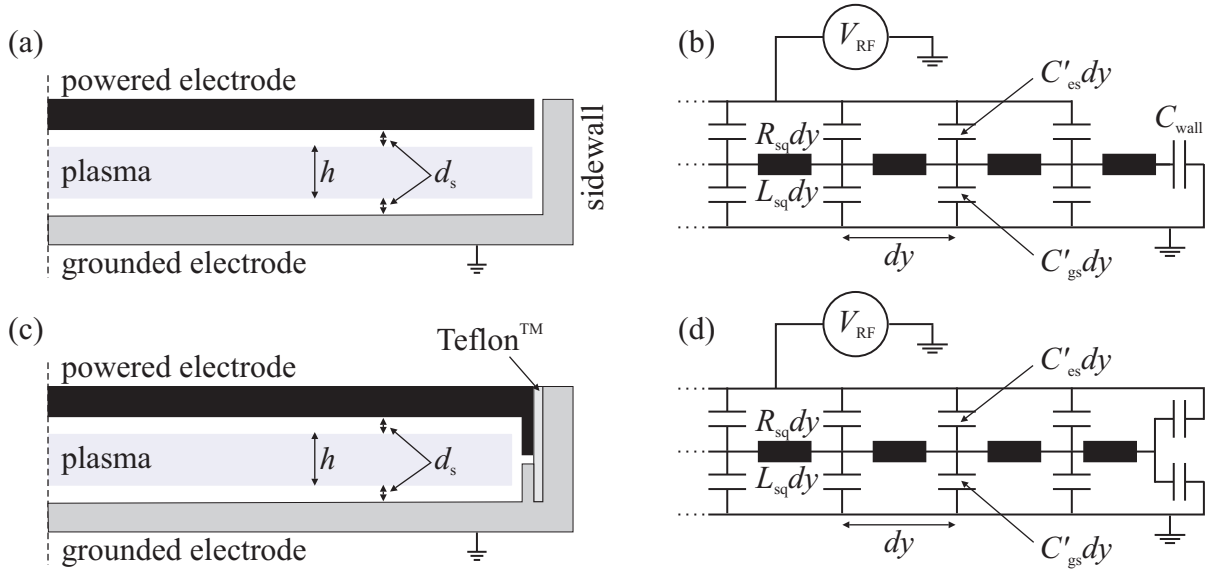


**Figure 7.1:** (a) Schematic representation of the asymmetric KAI reactor. (b) Planar equivalent circuit with the contribution of the sidewall for the derivation of the Telegraph effect. (c) Symmetrized KAI reactor and (d) its planar equivalent circuit.

## 7.1 Theoretical considerations on electromagnetic uniformity

### 7.1.1 The Telegraph effect

The Telegraph effect is observed in asymmetric capacitively-coupled RF reactors such as the one considered in this work and sketched in Fig. 7.1(a). This asymmetry is at the origin of a lateral RF current that propagates from the asymmetric vertical sidewalls into the plasma and is redistributed to the electrodes through the capacitive sheaths. This lateral RF current is necessary in order to conserve the RF displacement current between the powered and the grounded electrodes [166]. This causes a perturbation  $V(x, y)$  of the plasma potential near the edge of the reactor compared to the symmetric part at the center of a large area parallel plate reactor. Assuming a  $e^{i\omega t}$  time harmonic dependence for RF voltage and current, where  $\omega$  is the angular excitation frequency, the RF plasma potential complex amplitude  $\tilde{U}_p$  can be written as

$$\tilde{U}_p = V_{\text{RF}}/2 + V(x, y), \quad (7.1)$$

where  $V_{\text{RF}}$  is the interelectrode RF voltage amplitude. The perturbation  $V(x, y)$  can be calculated using the equivalent planar circuit [166, 173] described in Fig. 7.1(b) and from the two-dimensional Telegraph equation

$$\nabla^2 V + \omega^2 L_{\text{sq}} C' V - i\omega R_{\text{sq}} C' V = 0, \quad (7.2)$$

and the boundary condition at the sidewall

$$\nabla V \cdot \mathbf{n}|_{\text{wall}} = -i\omega R_{\text{sq}} C_{\text{wall}} (1 + i\omega/\nu_m) \tilde{U}_{\text{p}}|_{\text{wall}}. \quad (7.3)$$

In these expressions,  $R_{\text{sq}} = m_e \nu_m / n_e e^2 h$  and  $L_{\text{sq}} = R_{\text{sq}} / \nu_m$  are, respectively, the resistance and inductance per square of the plasma bulk.  $C' = C_{\text{gs}} + C_{\text{es}} = 2\epsilon_0/d_s$  is the combined sheath capacitance per unit length and  $\mathbf{n}$  is the unit vector perpendicular to the side walls and directed outward from the plasma volume. In the equivalent circuit model described in Fig. 7.1(b), we assume a uniform plasma slab and that the vertical impedance of the plasma is dominated by the sheath capacitance  $C_{\text{es}}$  and  $C_{\text{gs}}$ . Therefore, the applied voltage on the RF electrode,  $V_{\text{RF}}$  is taken as uniform and the inductance of the electrode is neglected. This restricts the validity of the equivalent circuit to cases where the standing-wave is negligible [166]. Substituting the expressions of  $R_{\text{sq}}$ ,  $L_{\text{sq}}$  and  $C'$  in Eq. 7.2 we obtain

$$\nabla^2 V = \frac{2}{\delta^2} \left( i - \frac{\omega}{\nu_m} \right) V, \quad (7.4)$$

where  $\delta$  is the damping scale length in m for the perturbation and is given by

$$\delta = \sqrt{\frac{2}{\omega R_{\text{sq}} C'}} = \omega_{\text{pe}} \sqrt{\frac{h d_s}{\omega \nu_m}}, \quad (7.5)$$

where  $\omega_{\text{pe}} = \sqrt{n_e e^2 / \epsilon_0 m_e}$  is the electron plasma frequency,  $h$  and  $d_s$  the plasma bulk and sheath height, respectively (see Fig. 7.1(a)) [166]. Assuming that the RF voltage drop across the plasma bulk height  $h$  is negligible compared to the voltage drop across the sheaths, the RF voltage across the ground sheath is then  $\tilde{U}_{\text{gs}} = |V_{\text{RF}}/2 + V(x, y)|$  and the RF voltage across the RF sheath is  $\tilde{U}_{\text{es}} = |V_{\text{RF}}/2 - V(x, y)|$ . Figure 7.2 shows that these two perturbations are asymmetric with a strong decrease at the edge of the grounded electrode and a strong increase at the edge of the powered electrode. This is the main characteristic of the Telegraph effect in large area reactors, since all other effects such as fringing fields or, as it is shown in the next section, the standing-wave have symmetric effect on both electrodes.

The Telegraph effect has been demonstrated experimentally by Howling *et al* [177] for non-reactive Ar plasmas using sheath voltage probes mounted in the grounded electrode of a KAI-S reactor. Results have shown that the experiments were in good agreement with voltage simulations. Moreover, it has been shown that when the reactor edges were symmetrized (see Fig. 7.1(c)), the Telegraph effect was eliminated, since the sum of the injected ground and excitation RF currents from equal-height sidewalls is zero [166, 176].

### 7.1.2 The standing-wave effect

Sansonnens *et al* [171] have shown that the electromagnetic field equation has two solutions, if we neglect the direct vicinity of the reactor edges. The first one is the Telegraph effect, and the second one is the so-called standing-wave effect. The standing-wave effect is observed in large area capacitively coupled parallel-plate reactors when very high excitation frequencies are used. The standing-wave is observed when the reactor size is larger than about a tenth of the vacuum wavelength of the excitation frequency [172]. Therefore,

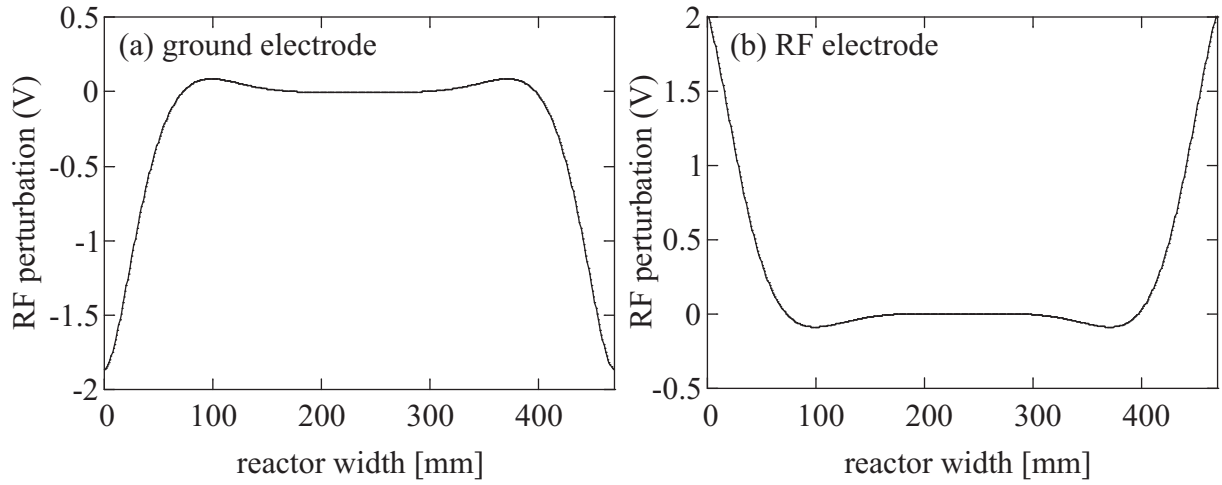


**Figure 7.2:** Variation across the width of the reactor of the RF voltage perturbation across (a) the ground sheath and (b) the RF sheath, calculated from the Telegraph equation assuming a damping length of 33 mm.

the correction of the standing-wave effect is of great importance when processing  $\mu\text{c-Si:H}$  for the PV industry, since the dimension of the reactors is nowadays about  $1 \text{ m}^2$  to reduce the production costs and the excitation frequencies are in the range of 40 to 100 MHz to improve the deposition rate [23, 24, 134, 178] and to reduce the film bombardment by energetic ions [23, 83, 178].

The standing-wave effect, as opposed to the Telegraph effect, is only little damped, therefore it influences the whole deposition area. Moreover, it does not affect only the plasma potential, as for the case of the Telegraph effect, but it affects the RF voltage amplitude across the plasma. The vertical electric field in the reactor is then perturbed as shown by vacuum measurements, i.e. without plasma, performed by Schmidt et al [135] and presented in Fig. 7.3(a). It results in a variation of the plasma intensity across the area of the reactor as shown for non-reactive plasma in Fig. 7.3(b) [135]. This plasma nonuniformity affects the gas dissociation rate uniformity over the substrates, hence, films deposited in the presence of the standing-wave nonuniformity have a nonuniform thickness profile (Fig. 7.3(c) [175]) which is related to the profile of the RF voltage.

Sansonnens *et al* [168] have shown that shaping one or both electrodes can be done in order to compensate the higher RF voltage amplitude at the center of the reactor due to the standing-wave. The shaping has to be filled or screened by a dielectric in order to permit a capacitive division of the interelectrode RF voltage amplitude, hence reducing the potential drop across the plasma [179]. The profile of the shaping can be calculated quite easily to compensate the interelectrode RF voltage amplitude in circular reactor under vacuum conditions (without plasma) [135]. But it is rather difficult to calculate and build a shaped electrode which takes into account the plasma and the glass substrate in large area rectangular reactors [175].

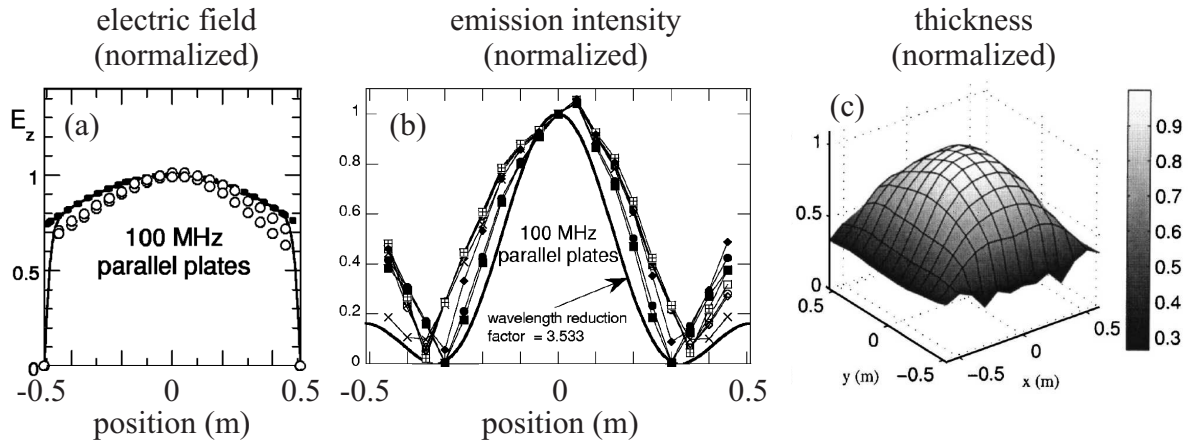


**Figure 7.3:** Standing-wave effect in parallel plate reactor evidenced by (a) vertical electric field [135], (b) plasma emission intensity [135] and (c) film thickness [175] measurements.

## 7.2 Results

### 7.2.1 Edge uniformity: the Telegraph effect

The influence of the Telegraph effect on the deposited silicon film has been studied. This was performed by characterizing the film thickness deposited directly on both ground and excitation electrodes, i.e. without any substrate. This was done to prevent any effects of the substrate on the plasma uniformity in the vicinity of the substrate edge. Figure 7.4 presents the film thickness profile on both electrodes across the width of the KAI-S reactor for amorphous silicon thin films. These were deposited using pure silane at 0.3 mbar, 100 sccm flow rate, 24 W RF power, 27.12 MHz excitation frequency and 200 °C reactor temperature with an asymmetric (Fig. 7.4(a)) and symmetric (Fig. 7.4(b)) reactor configuration. For these conditions, no powder is formed in the plasma, and nonuniformities due to standing-wave effect are negligible ( $\lambda_{\text{RF}}/0.57 \approx 20$ ). The symmetric configuration has been built by adding extra sidewalls on the RF and the ground electrodes as sketched in Fig. 7.1(c). Teflon<sup>TM</sup> (poly-tetra-fluoro-ethylene) strips were used to avoid parasitic plasmas behind these extra-sidewalls.

In the asymmetric configuration presented in Fig. 7.4(a), the thicknesses are similar in the symmetric central part of the reactor on both electrodes. When approaching the reactor edges, the film thickness increases strongly on the excitation electrode, while it decreases strongly on the grounded bottom electrode. The difference between both film thicknesses (dotted lines) eliminates all symmetric effects, hence only the Telegraph effect remains. In contrast to the asymmetric case, the symmetric case in Fig. 7.4(b) presents similar thickness across the whole reactor width on both electrodes. The resulting difference profile is almost equal to zero across the whole reactor.

This difference close to the reactor edge between symmetric and asymmetric reactor configuration can be interpreted in terms of the perturbation of the RF potential described by the Telegraph equation. As shown by the Telegraph effect model [166] and

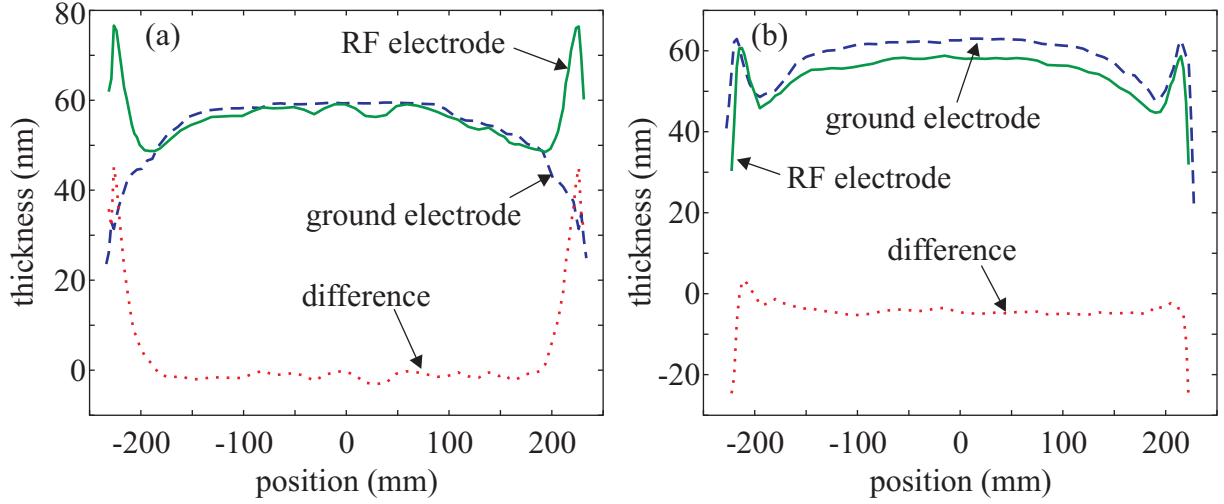


**Figure 7.4:** Thickness profiles of a-Si:H films deposited on RF and ground electrodes in (a) asymmetric and (b) symmetric KAI-S reactor.

by voltage probe measurement in non-reactive plasmas [173, 176, 177], the redistribution of the sidewall RF current in the asymmetric wall configuration causes a decrease of the voltage amplitude across the ground sheath  $\tilde{U}_{gs}$  towards the reactor edge, and an increase of the voltage amplitude across the excitation sheath  $\tilde{U}_{es}$ . Since most of the electron impact dissociation in RF capacitively-coupled plasmas occurs in the sheaths and at the bulk-sheath transition, this sheath voltage amplitude perturbations affects locally the dissociation rates, making them nonuniform across the plasma height. Therefore, the higher silane dissociation rate in front of the RF electrode makes the silane radical density higher than in front of the grounded electrode, where the dissociation rate is lowered by the Telegraph effect. This film asymmetry is expected to extend into the reactor from the reactor sidewalls over a distance to be about  $2\delta$ . Therefore, on the basis of Fig. 7.4(a), the damping scale length  $\delta$  can be estimated to be about 2.5 cm.

In the case of the symmetric configuration, the amplitude of the RF plasma potential perturbation vanishes, and therefore, similar deposition rates on both electrodes are observed. The remaining nonuniformity should be attributed to other nonuniformity sources. A possible source may be a nonuniformity of the gas showerhead injection through the powered electrode near the reactor edge.

For both reactor configuration, we can observe a decrease of the film thickness on both electrodes in the close vicinity of the reactor edge. This decrease is due to the presence of the sidewalls that acts as additional surfaces on which radicals deposit. Therefore, this radical sink consumes silane dissociation products making them less available for film growth on the electrodes.

Figure 7.4 demonstrates the importance of the Telegraph effect on film uniformity. These experiments here were carried in a large area reactor, therefore making the Telegraph effect an edge effect since it is no longer observed in the central part of the reactor. However, laboratory reactors are not generally as large as the KAI-S reactor and have

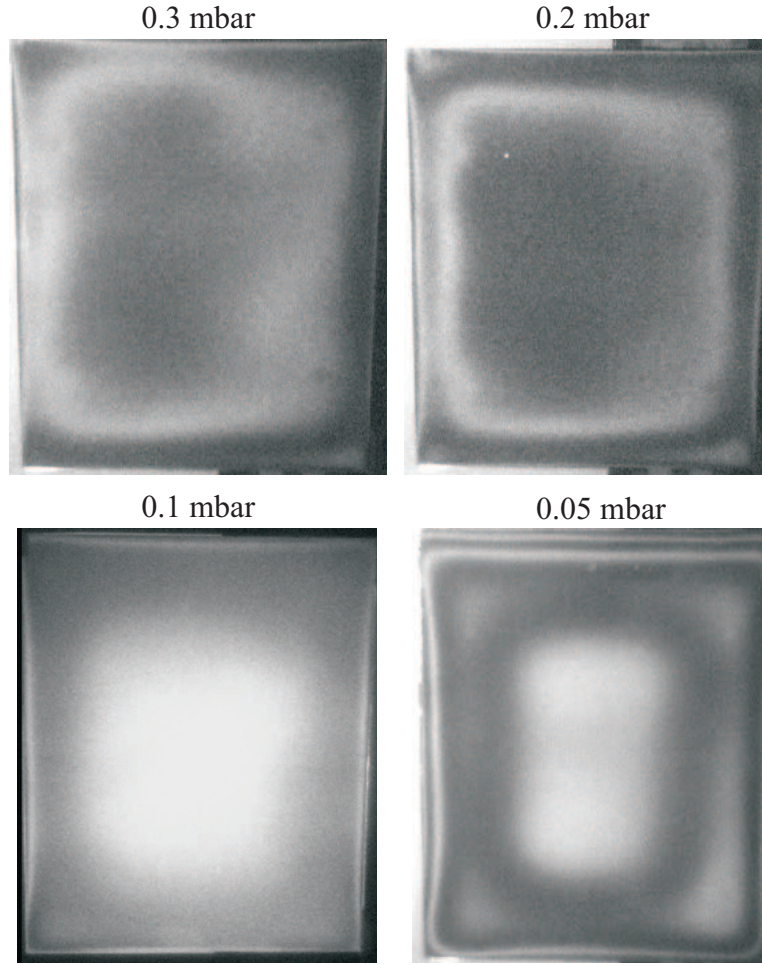


**Figure 7.5:** Thickness profiles by monochromatic light interferometry imaging of a-Si:H films deposited at various pressures on 1 mm thick glass substrates. The Telegraph effect affects more the film uniformity over the substrate as the pressure is reduced.

circular electrodes with typical diameter of about 20 cm. The Telegraph effect is then no longer an edge effect and affects the whole deposition area. However, even in large area reactors the use of substrate smaller than the electrodes does not guarantee to stand away from the zone where the Telegraph effect has an influence. Indeed, the damping scale length  $\delta$  depends on the plasma parameters, and especially on the working pressure with a  $\delta \propto 1/\sqrt{p}$  dependence as demonstrated by Howling *et al* [177]. This inverse dependence on pressure is principally due to the collision frequency  $\nu_m$  in Eq. 7.5 which decreases while decreasing the pressure. Therefore, even if the substrate edge is 5 cm away from the reactor edge, the Telegraph effect perturbation is observed on the substrate for low working pressures as shown by interferometry pictures of film deposited on 1 mm thick glass substrates in Fig. 7.5. Moreover, the zone of influence of the Telegraph effect increases while decreasing the pressure.

The plasma conditions used here for the demonstration of the Telegraph effect are rel-

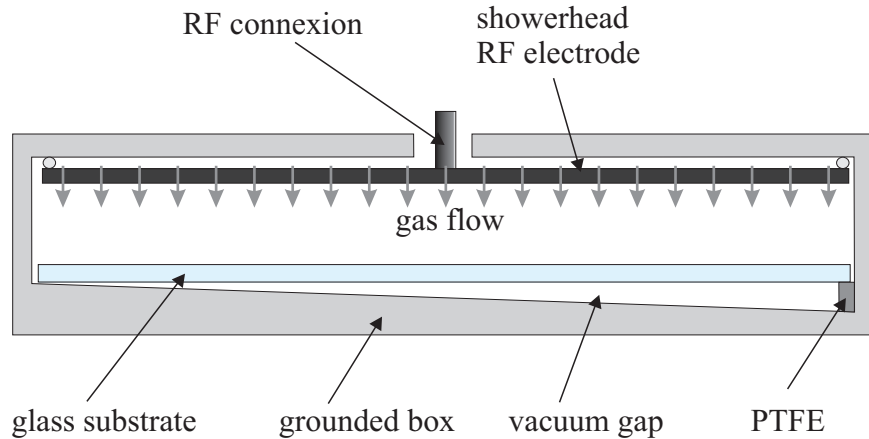


**Figure 7.6:** Modification of the KAI-S reactor with a wedge electrode. The interelectrode distance varies from 19 to 22 mm while the plasma height is maintained constant at 16 mm between the glass substrate ( $46 \times 56 \text{ cm}^2$ ) and the powered electrode.

actively far-away from interesting conditions for microcrystalline silicon processing. However, even if the use of higher pressures will reduce the damping length, the much higher RF input power density used in the case of  $\mu\text{c-Si:H}$  processing has an opposite effect by increasing the electron density [166, 177]. Therefore, the Telegraph effect may perturb the thickness uniformity over the substrate even for plasma conditions adequate for  $\mu\text{c-Si:H}$  deposition, i.e. at high pressure and high RF power. Moreover, in the case of Tandem PV solar cells based on an amorphous and microcrystalline silicon multi-junction design, the Telegraph effect has to be corrected by symmetrizing the reactor edges, since the a-Si:H layer is generally performed, in the same reactor, in low pressure conditions where the influence of the Telegraph effect is strong.

### 7.2.2 RF voltage non-uniformity

When very-high frequency ( $> 13.68 \text{ MHz}$ ) sources are used in large area parallel plate reactors, a problem of plasma nonuniformity known as standing-wave appears as described in Section 7.1. Generally, when dealing with nonuniformities in deposition device, one associates plasma uniformity with the uniformity of the layer thickness over the substrate. This is also the case for the standing-wave, which has been reported as a source of thickness nonuniformity [174, 175]. However, the plasma does not affect only the deposition rate, as shown from the beginning of this work, but also the properties of the deposited film such as the crystallinity. Moreover, the intrinsic microcrystalline silicon layer of silicon thin film based photovoltaic solar cells has to be deposited at the transition between amorphous and microcrystalline silicon, where the crystallinity may be very sensitive to the plasma as shown by the wide range of crystallinity in the transition zone in Fig 3.2. Therefore, this section will show that the material crystallinity sensitivity to plasma uniformity depends essentially on the input silane concentration.

For such a purpose, a controlled nonuniform voltage distribution was created in the



KAI-S reactor by modifying the grounded electrode across the width of the reactor as shown in Fig. 7.6. In this way, the interelectrode distance varied from 19 to 22 mm perpendicular to the pumping direction, while the distance between the substrate and the powered electrode was fixed at 16 mm by using a PTFE strip as sketched in Fig. 7.6. The 3 mm glass substrate for these experiments was 56 cm long and 46 cm wide, hence covering almost the whole electrode area ( $57 \times 47 \text{ cm}^2$ ). This strategy of controlling the interelectrode voltage distribution by using a wedge electrode was chosen because of its simplicity and because of the similarity of creating a nonuniform voltage by changing the reactor geometry or by generating a standing-wave. Indeed, to observe a significant effect of the standing-wave in the KAI-S reactor, the excitation frequency would have to be increased up to about 130 MHz ( $\approx c/(4 \cdot 0.57)$ ), hence generating important RF power matching problems. The resulting difference in interelectrode distance of 3 mm creates an estimated variation of the power dissipation of about 70 % across the reactor width as shown in Fig. 7.7 according to a relation between the dissipated power and the tension across the plasma following  $P_{\text{RF}} \propto U_p^2$ . The relative voltage drop across the plasma,  $U_p$ , has been calculated on the basis of a simple plasma sheath model presented in Fig. 7.7. It assumes constant capacitance of the two plasma sheaths of 3 mm height and a variable capacitance due to the variable wedge gap,  $d_w$ , between the glass substrate and the bottom grounded electrode.

Figure 7.8 presents the thickness uniformity of two films deposited in the wedge electrode reactor. In both cases, the deposition time was set to 60 minutes after having deposited a SiC thin layer for adhesion improvement during 15 minutes. The film of Fig. 7.8(a) was deposited in the Regime 1, i.e. with a low silane input concentration

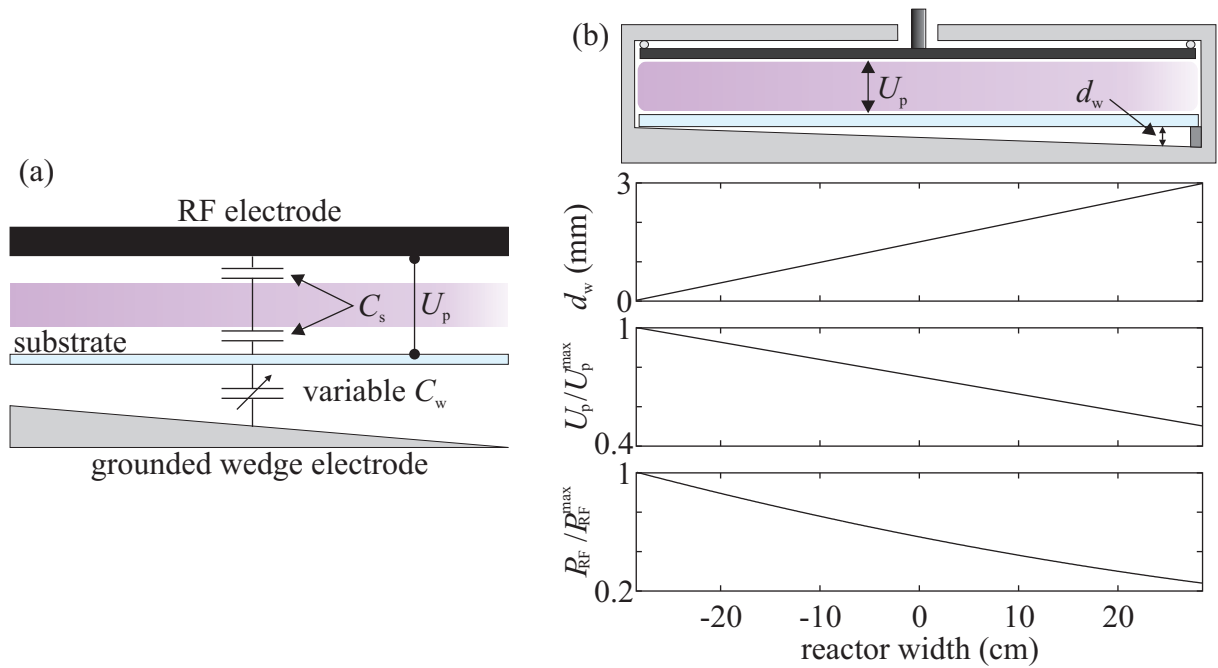


**Figure 7.7:** RF voltage and power distribution across the width of the wedge reactor.

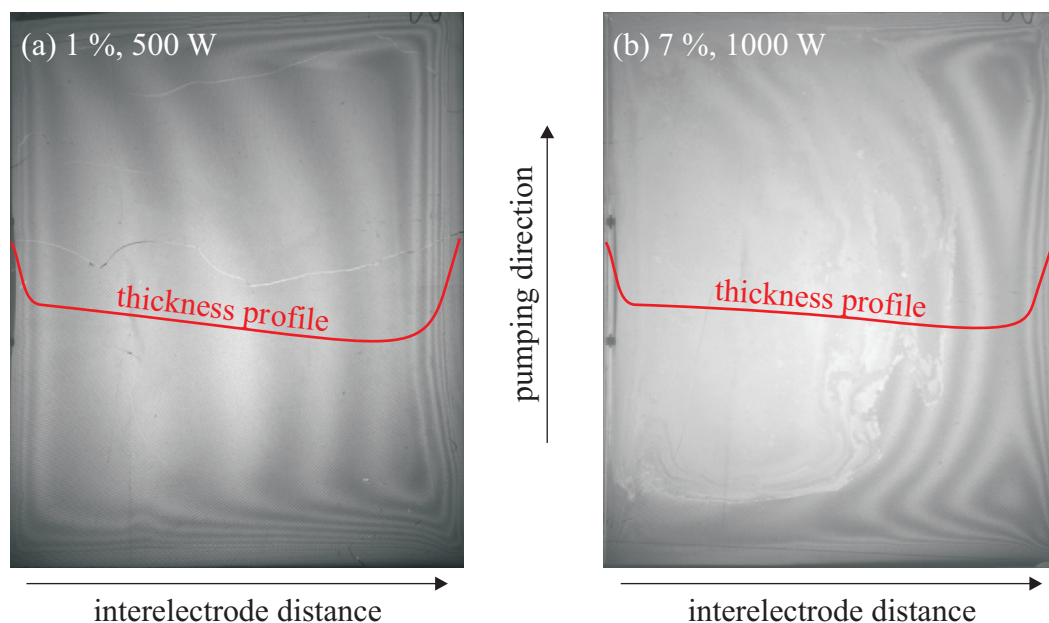


**Figure 7.8:** Thickness uniformity by light interferometry (filtered at 720 nm) of film deposited on 46 x 56 cm<sup>2</sup> glass with the wedge electrode reactor configuration for (a) highly-diluted Regime 1 (1 %, 500 W, 2 mbar, 20 sccm silane) and (b) high concentration Regime 2 (7 %, 1000 W, 2 mbar, 20 sccm silane).

( $c = 1\%$ ) and a low power (500 W). On the other hand, the film presented in Fig. 7.8(b) was deposited in the Regime 2, i.e. with a high silane input concentration ( $c = 7\%$ ) and a high power (1000 W). As expected, the nonuniformity introduced by the wedge electrode creates a nonuniform film thickness across the width of the substrate. At all four edges, the strong film thickness increase within about 6 cm from glass edge is probably the result of intense plasmas at the RF electrode edges, since here the substrate covers the whole electrode area. Except for these edge effects, the film thickness decreases in a monotonic way as the interelectrode distance increases. This is well correlated with the variation of the power dissipation across the reactor shown in Fig. 7.7 due to capacitive division of the voltage across the plasma. Note that in the case of Regime 2 the film thickness variation in the central part of the substrate is weaker than for the Regime 1, even if the general behavior is similar.

Even if the film thickness uniformity is affected by the wedge electrode configuration, the effect is not significantly affected by the regime in which the film is deposited. On the other hand, Fig. 7.9 shows that the wedge electrode has a huge effect on the Raman crystallinity of the film and the effect depends strongly on the deposition regime. In Regime 1 ( $\triangle$ , low silane concentration and depletion), the film is microcrystalline across the whole substrate, with a Raman crystallinity everywhere higher than 50 %. In Regime 2 ( $\bullet$ , high silane concentration and depletion), the film is crystalline for small interelectrode distance, and suddenly becomes totally amorphous at about 10 - 15 cm from the substrate edge for higher interelectrode distance. In both cases the variation in crystallinity cannot

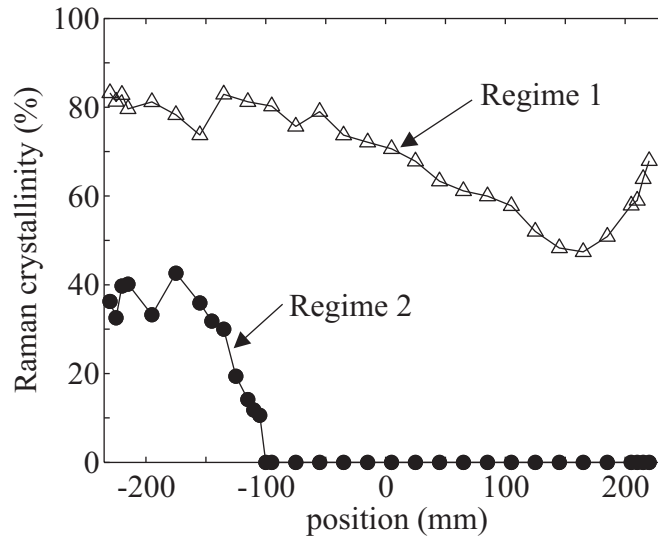


**Figure 7.9:** Raman crystallinity across the width of the  $46 \times 57 \text{ cm}^2$  substrate for two different conditions: Regime 1 with  $c = 1 \%$ , 500 W, 2 mbar and Regime 2 with  $c = 7 \%$ , 1000 W, 2 mbar.

be attributed to film thickness variation, even if, at first sight it seems to have a relation for the Regime 1 by comparing the profiles given in Figs. 7.8(a) and 7.9. However, the silane flow rate used was 20 sccm and the deposition time 60 minutes, implying that the film can be estimated by Eq. 3.47 to be thicker than 250 nm everywhere on the substrate, according to a silane depletion as low as 0.25. This thickness is sufficiently important to be out of the influence of the amorphous incubation layer which is very thin in a closed Plasma-Box<sup>TM</sup> reactor (see Chapter 5). In the case of Regime 2, the microcrystalline to amorphous silicon transition takes place in a region where the film thickness is almost uniform as shown by the absence of interference fringe in the central part of Fig. 7.8(b), hence it is obvious that the film thickness and crystallinity are not related.

The variation of the film crystallinity has for origin the silane concentration in the plasma, exactly as for the case presented in Chapter 3. In the present case, the silane input concentration is uniform over the whole substrate area (1 % for Regime 1 and 7 % for Regime 2), but due to the nonuniform power dissipation, the silane depletion is not uniform and hence, the silane concentration in the plasma is also nonuniform across the width of the reactor. This is schematized in Fig. 7.10 where in the  $(D, c)$  plane the deposition processes are now represented by iso- $c$  segments and not by points, because the reactor is no longer uniform since the electric field is not uniform. Therefore, the  $\Gamma_H/\Gamma_{\text{SiH}_x}$  flux ratio towards the growing film surface is not uniform according to Chapter 3. In the case of the Regime 1 at low silane concentration this nonuniformity does not have a strong effect on the Raman crystallinity since the corresponding segment is almost parallel to iso- $c_p$  curves. Hence, it does not cross many of them and the resulting microstructure inhomogeneity is not important. In the case of Regime 2 at high silane input concentration, the inhomogeneity of the silane depletion has a dramatic effect on

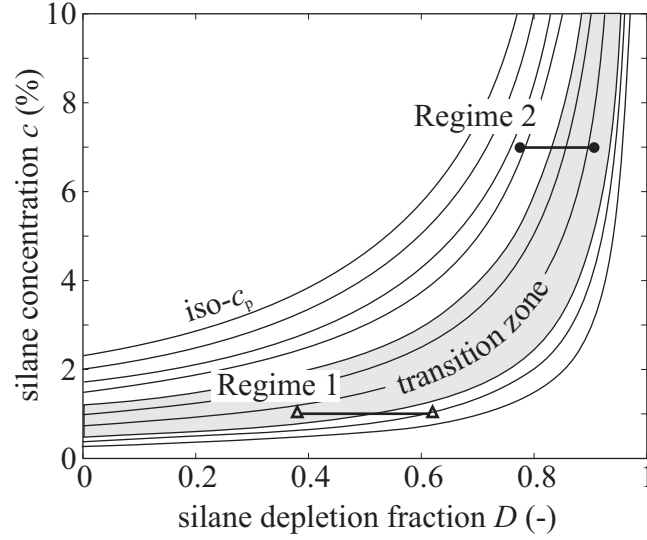


**Figure 7.10:** Variation of the plasma composition in the  $(D, c)$  plane for two different conditions corresponding to the two Regimes 1 and 2. Experiments have to be represented with iso- $c$  segments due to non-uniform silane depletion fraction.

the crystallinity, since the segment is almost perpendicular to iso- $c_p$  curves. Hence, the  $\Gamma_H/\Gamma_{SiH_x}$  flux ratio varies strongly from one side to the other of the substrate, significant affecting the film crystallinity. This variation is so strong that the segment covers a range over all the three microstructure regions  $\mu c$ -Si:H, transitional and a-Si:H. We may expect a transition from  $\mu c$ -Si:H to a-Si:H over a wide region on the substrate since the transition zone is not a thin line, but a wide region in Fig. 3.2. However, this transition zone has been determined using many different experiments (see Chapter 3) and includes many secondary effects. Therefore this zone should probably be narrower for experiments made in conditions close to each other. This may explain the abrupt fall of the crystallinity over a distance of only about 50 mm.

Note that the length of the segments in Fig. 7.10 are different for Regime 1 and 2. These have been set arbitrarily because we do not know the silane depletion level, but this difference is justified by the relation between the silane depletion and the electron density introduced in Eq. 3.45 and plotted in Fig. 7.11(a). Fully depleted silane is reached asymptotically, therefore a similar power dissipation nonuniformity, i.e. a similar electron density perturbation, has different consequences on the uniformity of the silane depletion if we consider a plasma with a high or a low level of silane depletion. Consequently, if the objective is to deposit  $\mu c$ -Si:H in the Regime 2 with silane input concentration about 10 %, because of the interest in high gas utilization efficiency associated with high silane concentration, the electric field has to be very uniform over the whole electrode area in order to assure a uniform microstructure of the deposited film. This is because for such intermediate silane concentrations, the silane depletion uniformity still depends strongly on the RF power dissipation uniformity (Fig. 7.11(a)) while the width of the transition zone is smaller than for deposition in the Regime 1 (Fig. 7.11(b)). However, for higher

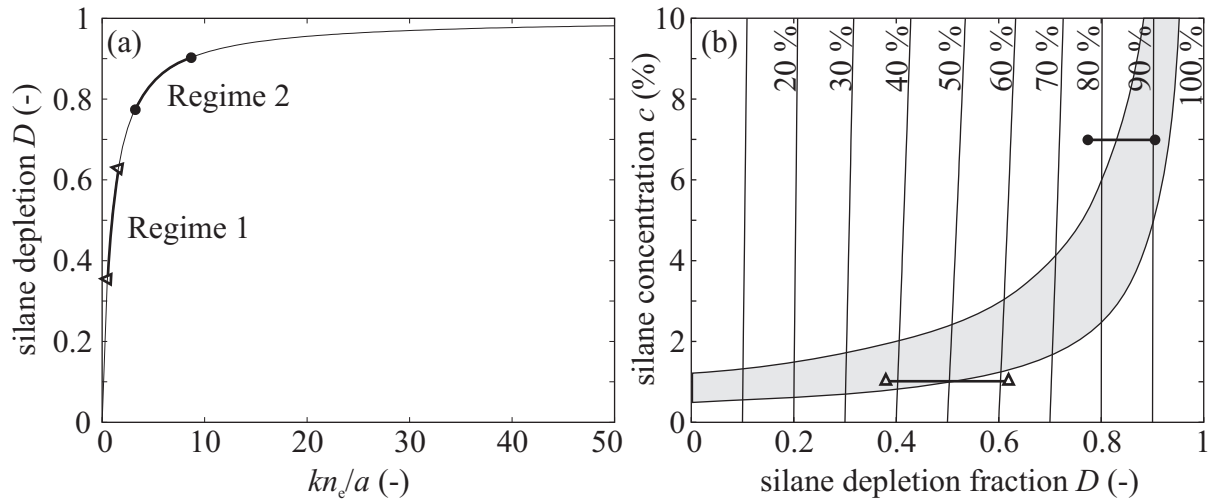


**Figure 7.11:** (a) Asymptotic behavior of the silane depletion fraction as a function of  $kn_e/a$ . (b) Effect of silane depletion non-uniformity on the deposition efficiency for the two Regimes 1 and 2.

silane concentrations, the tolerance on the silane depletion for a uniform microstructure is even narrower, but the silane depletion uniformity only weakly depends on the power distribution uniformity as shown for high value of  $kn_e/a$  in Fig. 7.11(a). Therefore, the microcrystalline silicon microstructure uniformity is less sensitive to electric field variation when deposited at very high silane concentration ( $c > 10$  %). However, when working at such high silane concentrations, one has to pay attention to avoid powder formation which is another source of plasma and film nonuniformity [69]. At the other extreme, in the low silane concentration Regime 1, where the deposition efficiency is less attractive, the plasma composition is less sensitive to variation of the electric field, even if the silane depletion fraction depends strongly on the electric field. Therefore, for Regime 1 the reactor geometry has not to be designed with tolerance as small as for the case of intermediate silane concentrations in order to guarantee a uniform film microstructure over the whole substrate area.

This different amplitude of the silane depletion perturbation is probably also the reason for the small difference of the thickness uniformity between the two deposition regimes. Indeed, the segment associated with Regime 2 covers a smaller range of dissociation efficiency  $\eta$  than the one associated with Regime 1, as shown in Fig. 7.11(b). Therefore, the variation in deposition rate across the electrode width is less important at high silane concentration and depletion.

To summarize, as expected, the interelectrode electric field uniformity influences the film homogeneity in terms of thickness and microstructure. However, this influence depends on the deposition regime, i.e. on the silane input concentration. For low silane concentrations (Regime 1), the electric field nonuniformity affects essentially the thickness uniformity and weakly the film crystallinity. On the other hand, for intermediate

silane concentrations (Regime 2), the electric field nonuniformity affects essentially the crystallinity uniformity and weakly the film thickness. As a consequence, if we want to benefit from the high silane deposition efficiency encountered within the Regime 2, the reactor has to be very well designed and the correction of the standing-wave nonuniformity in large area reactors has to be almost perfect and account for plasma and substrate.

### 7.3 Conclusion

Electromagnetic sources of plasma nonuniformity, which are due to the Telegraph and the standing-wave effects, have been reviewed and their effects on silicon film deposition have been studied. It has been shown that the Telegraph effect has an opposite effect on film thickness profile on the RF and the ground electrode in the vicinity of the edge of the deposition area. For grounded sidewalls, the film thickness decreases on the ground electrode when approaching the edge and it increases symmetrically on the powered electrode. It has been shown that the zone of influence of the Telegraph effect increases towards the electrode center when the pressure is decreased, because of the increase of the damping scale length. The Telegraph effect can be totally eliminated by symmetrizing the edges of the reactor, since the RF plasma potential variation at the edge vanishes for such a configuration.

The standing-wave effect has been simulated experimentally by generating a controlled variation of the interelectrode RF voltage amplitude by using a wedge electrode in the KAI-S reactor. Results have shown that depending on the deposition regime, the influence of the voltage amplitude variation on the film microstructure is very different. For the Regime 1, at low silane concentration and depletion, the crystallinity is almost uniform and higher than 50 % across the whole reactor width. On the other hand, in Regime 2, at intermediate silane concentration and high silane depletion, the microstructure varies from microcrystalline to fully amorphous silicon across the width of the reactor. It shows that for silane concentrations in the 0 to 10 % range, the higher the silane concentration, the better has to be the plasma uniformity, which agrees with the simple plasma chemistry model. For silane input concentrations higher than 10 %, the microstructure uniformity is less sensitive to the power distribution uniformity, but processes are less attractive because of powder formation when working at high silane concentration.

From the point of view of the film uniformity, the best reactor design is a symmetric, closed and directly-pumped reactor with perfect lens-shaped electrode. This is in order to guarantee uniform film at the edge, across the thickness and over the substrate, respectively. Moreover, the tolerance on the design of the shaped electrode in order to guarantee a uniform film microstructure becomes more and more critical as the process for  $\mu\text{c-Si:H}$  deposition is performed at input silane concentration closer to 10 %.

# Final conclusion and outlook

This thesis has focused on the study of the deposition of silicon thin films by plasma-enhanced chemical vapor deposition in large area, capacitively-coupled radio frequency reactor. Special attention has been paid to the inter-relation between the plasma properties and the crystallinity of the deposited films in order to understand the relevant parameters which govern the transition from amorphous to microcrystalline silicon growth.

Infrared absorption spectroscopy in the exhaust of a large area PECVD reactor has been used to measure the plasma composition. These measurements have been combined with crystallinity measurement of the deposited films by micro-Raman spectroscopy. It has been shown that the *silane concentration in the plasma*, as opposed to the input silane concentration in the inlet flux, is the relevant parameter which determines the film microstructure. Microcrystalline material grows when the silane plasma concentration is lower than 0.5 %. This can be explained by the fact that the silane concentration in the plasma determines the atomic hydrogen to silane radical flux ratio towards the surface as shown by an analytical plasma chemistry model and confirmed by a more general numerical model. This conclusion is in agreement with all existing phenomenological models of microcrystalline silicon growth. The silane concentration in the plasma can be expressed as a function only of the input silane concentration and the fractional silane depletion in the plasma, which takes into account all the other plasma parameters.

On the basis of the analytical plasma chemistry model, it has been shown that to increase the deposition rate of silicon while remaining at the boundary between amorphous and microcrystalline silicon, where the material shows the best PV properties, the silane depletion has to be higher than 0.8 and the silane input concentration higher than 5 %. Moreover, it has been shown theoretically and experimentally that the optimum tends towards pure silane, where microcrystalline silicon can be deposited at high rate ( $> 10 \text{ \AA/s}$ ) without using excessive RF power if the silane flow rate is judiciously adjusted. These conditions lead to a quasi-fully depleted silane fraction by means of a long residence time as opposed to a high electron density usually provided by high RF power density. This has been used to develop an optimization strategy by varying only the pressure and the hydrogen flow rate and by measuring only the deposition rate and the film crystallinity. It would be of interest to look at the dependence of the electronic quality of the film on the plasma composition as a function of the silane concentration and depletion to refine the optimization strategy. Nevertheless, a non-optimized single-junction microcrystalline silicon solar cell has been manufactured following the proposed optimization flow diagram with a silane input concentration of 46 %. The conversion efficiency was 6 %. This process is close to an ultimate cost-effective production of microcrystalline silicon by combining

*large area* ( $47 \times 57 \text{ cm}^2$ ), *high deposition rate* ( $10.9 \text{ Å/s}$ ), *high gas utilization efficiency* ( $> 80 \%$ ), *low power input* ( $1000 \text{ W}$ ) and *adequate film crystallinity* ( $\phi_c = 66 \%$ ).

Optical emission spectroscopy (OES) has been combined with analytical and two-dimensional numerical plasma chemistry modeling to study the plasma and the film growth at plasma ignition until steady-state. This study was motivated by the necessity to optimize the time needed to reach plasma chemical equilibrium, which was reported to be about 1 minute or even more, therefore significantly affecting the beginning of the crystallites growth. It has been shown that OES can be used to measure the silane depletion fraction only if two conditions are fulfilled: (i) The acquisitions have to be performed as a function of time from plasma ignition with a short integration time ( $\approx 20 \text{ ms}$ ), and (ii) the electron temperature has to be stable from ignition to steady-state. This second condition can be checked by a careful analysis of the optical emission spectra. Results have shown that in closed, directly-pumped showerhead reactors the time to reach steady-state is less than 1 second, which corresponds to the theoretical value. The much longer time observed in small, open laboratory reactors can be explained by the back-diffusion of silane from the large vacuum chamber surrounding the plasma volume. In open reactors, strategies such as  $\text{H}_2$ -dilution profiling are necessary to control the plasma composition directly from plasma ignition, to avoid a plasma-induced growth of an amorphous silicon incubation layer which deteriorates the solar cell performance. Such strategies are not necessary in large area, closed, directly-pumped reactors since the plasma fills the whole reactor volume in Plasma-Box<sup>TM</sup> reactors.

Analytical and numerical modeling have been used to study the formation of polysilanes in  $\text{SiH}_4\text{-H}_2$  discharges. The disilane density has been used as a marker of higher-order polysilanes and powder formation. It has shown that the polysilane formation occurs at high input silane concentration and depletion, where the deposition conditions are interesting in terms of deposition rate and efficiency. This means that there is a competition when silane input concentration is increased between a positive effect on the deposition efficiency increase, and a negative effect on powder formation which consumes silane radicals in a channel other than film growth. Therefore, the silane concentration increase to enhance the deposition efficiency cannot be performed indefinitely, while remaining in powder free discharge. Moreover, the higher the pressure, the lower the maximum silane concentration to avoid powdery regime. It has also been shown that the formation of polysilane in the plasma affects the plasma composition, making the deposited film more amorphous because of the consumption of atomic hydrogen by gas phase reactions, hence reducing the  $\text{H}$  to  $\text{SiH}_x$  flux ratio towards the surface of the growing film. However, the powder formation can be reduced by decreasing the interelectrode distance or by working with very high silane depletion ( $D \rightarrow 1$ ), where the silane density becomes a limiting factor in the powder formation kinetics. However, the passage from the amorphous silicon solar cell generation to the amorphous/microcrystalline Tandem generation needs further investigations. The powder formation has still to be understood and controlled in order to push the limit to higher silane concentrations and pressures to benefit from interesting deposition regime with high deposition efficiency. This will need time-consuming and tricky experiments and numerical modeling.

Finally, the effects of the electromagnetic nonuniformities in large area reactors have



been studied by means of thickness and crystallinity measurements on the deposited layers. It has been shown that the Telegraph effect affects essentially the zone near the edge of asymmetric reactors. It has an opposite effect on the thickness of the film deposited on the RF and the ground electrodes and can be eliminated by symmetrizing the electrodes. The standing-wave has been experimentally simulated by generating a controlled variation of the interelectrode RF voltage distribution across the width of the reactor. It has been shown that the impact of this RF voltage perturbation on the film crystallinity depends strongly on the deposition regime. At low silane input concentration and depletion (Regime 1), the film crystallinity is almost uniform across the width of the reactor. On the other hand, at high silane concentration and depletion (Regime 2), the film microstructure varies from microcrystalline to amorphous. It shows that, for silane concentrations in the 0 to 10 % range, the higher the input silane concentration, the higher has to be the electric field uniformity. The main conclusion on film uniformity is that the ideal reactor has to be *symmetric* to avoid the Telegraph effect, with a *perfect lens-shaped electrode* to provide a uniform deposition in the Regime 2 and has to be *closed and directly-pumped with a showerhead gas injection* to guarantee a uniform microstructure across the thickness of the film without using special strategies at plasma ignition.

This work has shown that to improve plasma processing techniques, one has to perform a multidisciplinary approach, combining plasma physics, chemistry and material sciences. Simple plasma characterization techniques have been combined with thin film characterization in order to understand the inter-relation between the plasma properties and the resulting film microstructure. This has been used to improve the plasma process parameters as well as the deposition reactor, coming closer to an ultimate cost-effective production of microcrystalline silicon.



# Appendix A

## Two-dimension numerical modeling

Numerical modeling of plasma chemical composition has been performed for the two geometries presented in Figs. A.1 and A.2. The large area, closed, directly-pumped KAI-S reactor has been taken as a semi-infinite (along  $y$ ) parallel plate problem, with a plasma volume 57 cm in length, 25 mm in height, limited at  $x = 0$  m by the closed loading-door (no-slip boundary condition) and at  $x = 0.57$  m by a virtual pumping grid with an infinite gas conductance. On the upper part the plasma is bounded by a showerhead electrode with a uniform gas injection (vertical gas velocity and initial silane and hydrogen concentration boundary conditions), and on the lower part by the grounded electrode (no-slip boundary condition). The plasma has been taken as uniform (constant  $n_e$  in the whole volume) and the reaction of radicals with walls has been taken into account as volume reactions, as for the zero-dimensional modeling case presented in Sec. 3.2.2. The outflow was controlled by fixing the pressure and assuming a convective flux boundary condition for all gases. The only difference between the plasma volume and the pumping line is that no molecule dissociation reactions occur in the pumping line.

The height of the pumping line has been calculated in order to account for a finite gas conductance of a cylindrical pipe of 70 mm in diameter, which is the real dimension of the exhaust line used in the experiments (see Fig. 2.1). Indeed, if the thickness of the exhaust was taken to be 70 mm, the semi-infinite configuration of the modeling geometry would induce an over-estimation of the conductance of the exhaust, even though the cross-section geometry would be respected. The conductance of a cylindrical pipe is given by

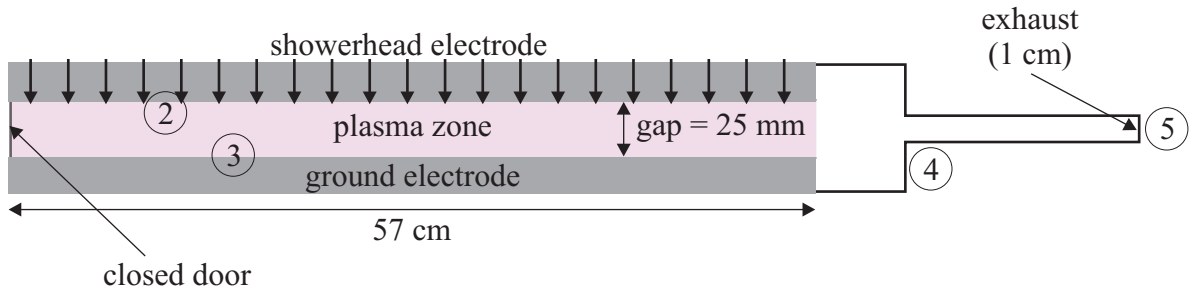


**Figure A.1:** Geometry of the simulated closed, directly pumped large area reactor.

boundary	Navier-stokes	diffusion and convection
1.	no slip	insulation/symmetry
2.	flow velocity	normal flux
3.	no slip	insulation/symmetry
4.	no slip	insulation/symmetry
5.	pressure	convective flux

**Table A.1:** Boundary conditions for the large area closed reactor. The number of the boundaries corresponds to the ones in Fig. A.1.

the Hagen-Poiseuille law [180]

$$C_{\circ} = \frac{\pi d^4}{128 \eta L} \cdot p, \quad (\text{A.1})$$

where  $d$  and  $L$  are the pipe diameter and length, respectively,  $\eta$  the gas viscosity and  $p$  the pressure. For a pipe with a rectangular cross-section, the conductance is given by [180]

$$C_{\square} = \frac{4}{48} \frac{ab^3}{\eta L} \cdot p\psi, \quad (\text{A.2})$$

where  $a$  and  $b$  are the lateral dimension of the pipe ( $a \leq b$ ) and  $\psi$  a correction factor depending on the  $a/b$  ratio. This ratio can be estimated as  $a/b \rightarrow 0$ , since the width of the pumping line has to be identical to the width of the reactor ( $b = 0.47$  m). Therefore,  $\psi \approx 0.002$  [180] and the thickness of the semi-infinite pumping line is  $a \approx 1$  cm.

The small open-electrode laboratory reactor geometry presented in Fig. A.2 has been built on the same basis as the closed, directly-pumped reactor. The only changes are the position of the pumping orifice at the wall of a large vacuum chamber ( $V_C \approx 630$  l) and the lateral dimension of the plasma volume ( $V_P \approx 0.8$  l). Note that this geometry has a cylindric symmetry. Therefore, the diameter of the exhaust can be taken as 70 mm as in the experiment in this case. The numerical modeling boundaries conditions for the Navier-Stokes and the diffusion-convection equations are given in Tables A.1 and A.2 for the closed and open geometries, respectively.

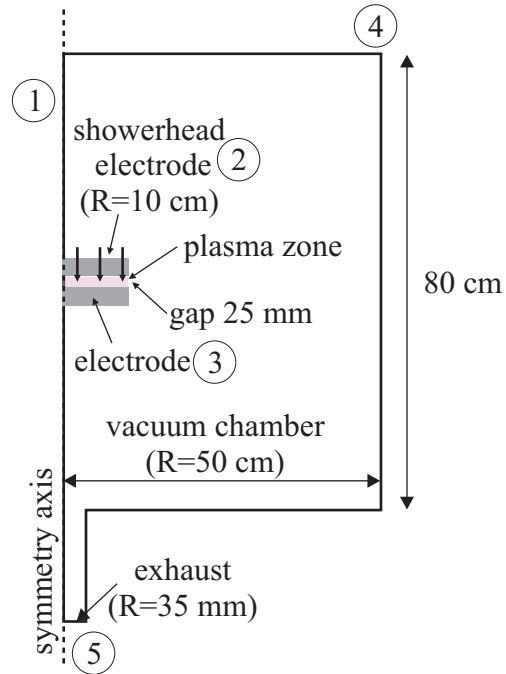


**Figure A.2:** Geometry of the simulated open laboratory reactor.

boundary	Navier-stokes	diffusion and convection
1.	axial symmetry	insulation/symmetry
2.	flow velocity	normal flux
3.	no slip	insulation/symmetry
4.	no slip	insulation symmetry
5.	pressure	convective flux

**Table A.2:** Boundary conditions for the open laboratory reactor. The number of the boundaries corresponds to the ones in Fig. A.2.



# Bibliography

- [1] K.R.G. Hein, “Future energy supply in Europe: Challenge and chances”, *Fuel*, **84**, 1189–1194 (2005).
- [2] Intergovernmental Panel on Climate Change (IPCC). “4<sup>th</sup> Assessment Report”, (2007).
- [3] N. Stern, *The Economics of Climate Change: The Stern Review*, Cambridge Univ. Press (2007).
- [4] [www.infoplease.com](http://www.infoplease.com).
- [5] Energy Information Administration. [www.eia.gov](http://www.eia.gov).
- [6] European Photovoltaic Industry Association. [www.epia.org](http://www.epia.org).
- [7] K.L. Shum and C. Watanabe, “Photovoltaic deployment strategy in Japan and the USA - an institutional appraisal”, *Energy Policy*, **35**, 1186–1195 (2007).
- [8] [www.solarbuzz.com](http://www.solarbuzz.com).
- [9] Observatoire des Energies Renouvelables. “Baromètre photovoltaïque 2006”, (2006).
- [10] J. Albrecht, “The future role of photovoltaics: A learning curve versus portfolio perspective”, *Energy Policy*, **35**(4), 2296–2304 (2007).
- [11] A. Shah, J. Meier, A. Buechel, U. Kroll, J. Steinhauser, F. Meillaud, H. Schade, and D. Dominé, “Towards very low-cost mass production of thin film Si PV solar modules on glass”, *Thin Solid Films*, **502**, 292–299 (2006).
- [12] S. Ito, N.-L. Cevy Ha, G. Rothenberger, P. Liska, P. Comte, S.M. Zakeeruddin, P. Péchy, M.K. Nazeeruddin, and M. Grätzel, “High-efficiency (7.2 %) flexible dye-sensitized solar cells with Ti-metal substrate for nanocrystalline-TiO<sub>2</sub> photoanode”, *Chem. Commun.*, **38**, 4004–4006 (2006).
- [13] M.A. Green, K. Emery, Y. Hisikawa, and W. Warta, “Solar cell efficiency tables (Version 30)”, *Prog. Photovoltaics: Res. Appl.*, **15**, 425–430 (2007).

- [14] J. Meier, U. Kroll, J. Spitznagel, S. Benagli, T. Roschek, G. Pfanner, Ch. Ellert, G. Androustopoulos, A. Hügli, M. Nagel, C. Bucher, L. Feitknecht, G. Büchel, and A. Buechel, “Progress in up-scaling of thin film silicon solar cells by large-area PECVD KAI systems”, in *Proc. 31st IEEE Photovoltaic Specialists Conference, Orlando (USA)*, 1464–1467, (2005).
- [15] A. Shah, P. Torres, R. Tscharnner, N. Wyrsh, and H. Keppner, “Photovoltaic technology: The case for thin-film solar cells”, *Science*, **285**, 692–698 (1999).
- [16] Oerlikon-Solar GmbH. [www.oerlikon.com](http://www.oerlikon.com).
- [17] M.A. Lieberman and A.J. Lichtenberg, *Principles of plasma discharges and material processing*, Wiley (1994).
- [18] National Research Council of the National Academies. “Plasma Science Advancing Knowledge in the National Interest”, (2007).
- [19] A.A. Howling, L. Sansonnens, J. Ballutaud, F. Grangeon, T. Delachaux, Ch. Hollenstein, V. Daudrix, and U. Kroll, “The influence of plasma chemistry on the deposition of microcrystalline silicon for large area photovoltaic solar cells”, in *16th European Photovoltaic Solar Energy Conference, Glasgow (UK)*, 375–379, (2000).
- [20] W.M.M. Kessels, K. Nadir, and M.C.M. van den Sanden, “SiH<sub>x</sub> film growth precursors during high rate nanocrystalline silicon deposition”, *J. Appl. Phys.*, **99**, 076110 (2006).
- [21] N. Itabashi, N. Nishiwaki, M. Magane, T. Goto, A. Matsuda, C. Yamada, and E. Hirota, “SiH<sub>3</sub> radical density in pulsed silane plasma”, *Jpn. J. Appl. Phys.*, **29**(3), 585–590 (1990).
- [22] T. Shirafuji, K. Tachibana, and Y. Matsui, “Measurement and calculation of SiH<sub>2</sub> radical density in SiH<sub>4</sub> and Si<sub>2</sub>H<sub>6</sub> plasma for deposition of hydrogenated amorphous silicon thin films”, *Jpn. J. Appl. Phys.*, **34**(8A), 4239–4246 (1995).
- [23] A.A. Howling, J.-L. Drier, Ch. Hollenstein, U. Kroll, and F. Finger, “Frequency effects in silane plasmas for plasma enhanced chemical vapor deposition”, *J. Vac. Sci. Technol. A*, **10**(4), 1080–1085 (1992).
- [24] L. Sansonnens, A.A. Howling, and Ch. Hollenstein, “Degree of dissociation measured by FTIR absorption spectroscopy applied to silane plasmas”, *Plasma Sources Sci. Technol.*, **7**, 114–118 (1998).
- [25] W. Schwarzenbach, A.A. Howling, M. Fivaz, S. Brunner, and Ch. Hollenstein, “Sheath impedance effects in very high frequency plasma experiments”, *J. Vac. Sci. Technol. A*, **14**(1), 132 (1996).
- [26] A. Madan, “Flexible displays and stable high efficiency four terminal solar cells using thin film silicon technology”, *Surf. Coating Technol.*, **200**, 1907–1912 (2005).



- [27] M.N. van den Donker, A. Gordijn, H. Stiebig, F. Finger, B. Rech, B. Stannowski, R. Bartl, E.A.G. Hamers, R. Schlattmann, and G.J. Jongerden, “Flexible amorphous and microcrystalline silicon tandem solar modules in the temporary superstrate concept”, *Solar Energy Mater. Solar Cells*, **91**, 572–580 (2007).
- [28] J. Krč, M. Zeman, F. Smole, and M. Topič, “Optical modeling of a-Si:H solar cells deposited on textured glass/SnO<sub>2</sub> substrates”, *J. Appl. Phys.*, **92**(2), 749–755 (2002).
- [29] J.W. Mayer, “Characteristics of p-i-n junctions produced by ion-drift techniques in silicon”, *J. Appl. Phys.*, **33**(9), 2894–2902 (1962).
- [30] D.E. Carlson and C.R. Wronski, “Amorphous silicon solar cell”, *Appl. Phys. Lett.*, **28**(11), 671–673 (1976).
- [31] D.L. Staebler and C.R. Wronski, “Reversible conductivity changes in discharge-produced amorphous Si”, *Appl. Phys. Lett.*, **31**(4), 292–294 (1977).
- [32] A. Matsuda, “Microcrystalline silicon: Growth and device application”, *J. Non-Cryst. Solids*, **338-340**, 1–12 (2004).
- [33] P. Stradins, “Light-induced degradation in a-Si:H and its relation to defect creation”, *Solar Energy Mater. Solar Cells*, **78**, 349–367 (2003).
- [34] C.R. Wronski, “Amorphous silicon technology: Coming of age”, *Solar Energy Mater. Solar Cells*, **41-42**, 427–439 (1996).
- [35] B. Rech and H. Wagner, “Potential of amorphous silicon for solar cells”, *Appl. Phys. A: Mater. Sci. Processing*, **69**, 155–167 (1999).
- [36] J. Meier, S. Dubail, R. Flückiger, D. Fischer, H. Keppner, and A. Shah, “Intrinsic microcrystalline silicon ( $\mu\text{c-Si:H}$ ) - A promising new thin film solar cell material”, in *1<sup>st</sup> World Conference on Photovoltaic Energy Conversion, Hawai (USA)*, volume 1, 409–412, (1994).
- [37] J. Meier, R. Flückiger, H. Keppner, and A. Shah, “Complete microcrystalline p-i-n solar cell - Crystalline or amorphous cell behavior?”, *Appl. Phys. Lett.*, **65**(7), 860–862 (1994).
- [38] A. Shah, J. Meier, E. Vallat-Sauvain, N. Wyrsh, U. Kroll, C. Droz, and U. Graf, “Material and solar cell research in microcrystalline silicon”, *Solar Energy Mater. Solar Cells*, **78**(1-4), 469–491 (2003).
- [39] A. Shah, J. Meier, E. Vallat-Sauvain, C. Droz, U. Kroll, N. Wyrsh, J. Guillet, and U. Graf, “Microcrystalline silicon and ‘micromorph’ tandem solar cells”, *Thin Solid Films*, **403-404**, 179–187 (2002).
- [40] O. Vetterl, F. Finger, R. Carius, P. Hapke, L. Houben, O. Kluth, A. Lambertz, A. Mück, B. Rech, and H. Wagner, “Intrinsic microcrystalline silicon: A new material for photovoltaics”, *Solar Energy Mater. Solar Cells*, **62**, 97–108 (2000).

- [41] J.P.M. Schmitt, “Amorphous silicon deposition: Industrial and technical challenges”, *Thin Solid Films*, **174**, 193–202 (1989).
- [42] T. Ohira, O. Ukai, and M. Noda, “Fundamental processes of microcrystalline silicon film growth: A molecular dynamics study”, *Surf. Sci.*, **458**(1-3), 216–228 (2000).
- [43] G. Ganguly and A. Matsuda, “Defect formation during growth of hydrogenated amorphous silicon”, *Phys. Rev. B*, **47**(7), 3661–3670 (1993).
- [44] H. Fujiwara, M. Kondo, and A. Matsuda, “Microcrystalline silicon nucleation sites in the sub-surface of hydrogenated amorphous silicon”, *Surf. Sci.*, **497**(1-3), 333–340 (2002).
- [45] J. Robertson, “Growth mechanism of hydrogenated amorphous silicon”, *J. Non-Cryst. Solids*, **266-269**, 79–83 (2000).
- [46] A. Matsuda, “Growth mechanism of microcrystalline silicon obtained from reactive plasmas”, *Thin Solid Films*, **337**(1-2), 1–6 (1999).
- [47] C.C. Tsai, G.B. Anderson, R. Thompson, and B. Wacker, “Control of silicon network structure in plasma deposition”, *J. Non-Cryst. Solids*, **114**, 151–153 (1989).
- [48] R. Terasa, M. Albert, H. Grüger, A. Haiduk, and A. Kottwitz, “Investigation of growth mechanisms of microcrystalline silicon in the very high frequency range”, *J. Non-Cryst. Solids*, **266-269**, 95–99 (2000).
- [49] R. Terasa, M. Albert, J.W. Bartha, H. Brechtel, and A. Kottwitz, “Time-resolved layer thickness behavior of microcrystalline and amorphous silicon samples after switching on a hydrogen/silane VHF plasma”, *J. Non-Cryst. Solids*, **299-302**, 58–62 (2002).
- [50] H. Shirai and T. Arai, “Role of hydrogen in the growth of  $\mu\text{c-Si:H}$ ”, *J. Non-Cryst. Solids*, **198-200**(2), 931–934 (1996).
- [51] S. Vepřek and V. Mareček, “The preparation of thin layers of Ge and Si by chemical hydrogen plasma transport”, *Solid-State Electronics*, **11**, 683–684 (1968).
- [52] R. W. Collins, A. S. Ferlauto, G. M. Ferreira, Chi Chen, Joohyun Koh, R. J. Koval, Yeeheng Lee, J. M. Pearce, and C. R. Wronski, “Evolution of microstructure and phase in amorphous, protocrystalline and microcrystalline silicon studied by real time spectroscopic ellipsometry”, *Solar Energy Mat. Solar Cells*, **78**, 143–180 (2003).
- [53] R.C. van Oort, M.J. Geerts, J.C. van den Heuvel, and J.W. Metselaar, “Hydrogen plasma etching of amorphous and microcrystalline silicon”, *Electronic Lett.*, **23**(18), 967–968 (1987).
- [54] K. Nakamura, K. Yoshida, S. Takeoka, and I. Shimizu, “Roles of atomic hydrogen in chemical annealing”, *Jpn. J. Appl. Phys.*, **34**(2A), 442–449 (1995).

- [55] O. Leroy, G. Gousset, L.L. Alves, J. Perrin, and J. Jolly, “Two-dimensional modelling of  $\text{SiH}_4\text{-H}_2$  RF discharges for a-Si:H deposition”, *Plasma Sources Sci. Technol.*, **7**(3), 348–358 (1998).
- [56] D. Franz, F. Grangeon, T. Delachaux, A.A. Howling, Ch. Hollenstein, and J. Karner, “Rapid deposition of hydrogenated microcrystalline silicon by a high current DC discharge”, *Thin Solid Films*, **383**, 11–14 (2001).
- [57] J. Perrin, J.P.M. Schmitt, Ch. Hollenstein, A.A. Howling, and L. Sansonnens, “The physics of plasma-enhanced chemical vapor deposition for large-area coating: Industrial application to flat panel displays and solar cells”, *Plasma Phys. and Controlled Fusion*, **42**, B353–B363 (2000).
- [58] J.P.M. Schmitt, M. Elyaakoubi, and L. Sansonnens, “Glow discharge processing in the liquid crystal display industry”, *Plasma Sources Sci. Technol.*, **11**(3A), 206–209 (2002).
- [59] H. Takatsuka, Y. Yamauchi, K. Kawamura, H. Mashima, and Y. Takeuchi, “World’s largest amorphous silicon photovoltaic module”, *Thin Solid Films*, **506-507**, 13–16 (2006).
- [60] L. Sansonnens, A.A. Howling, and Ch. Hollenstein, “A gas flow uniformity study in large-area showerhead reactors for RF plasma deposition”, *Plasma Sources Sci. Technol.*, **9**(2), 205–209 (2000).
- [61] J. Ballutaud, *Study of radio-frequency plasma deposition of amorphous silicon for improvement of solar cell production*, PhD thesis, Ecole Polytechnique Fédérale de Lausanne (EPFL) (2004).
- [62] L. Sansonnens, *Déposition assistée par plasma radiofréquence dans un réacteur de grande surface: Effets de la contamination particulaire et de la fréquence d’excitation*, PhD thesis, Ecole Polytechnique Fédérale de Lausanne (EPFL) (1998).
- [63] P.R. Griffiths and J.A. de Haseth, “Fourier transform infrared spectrometry”, in *Chemical analysis*, volume 83, Wiley (New-York) (1986).
- [64] N.B. Colthup, L.H. Daly, and S.E. Wiberley, *Introduction to Infrared and Raman Spectroscopy*, Academic Press Inc, San Diego (1990).
- [65] B. Gupta, J. Hilborn, Ch. Hollenstein, C.J.G. Plummer, R. Houriet, and N. Xanthopoulos, “Surface modification of polyester films by RF plasma”, *J. Appl. Polym. Sci.*, **78**, 1083–1091 (2000).
- [66] J. Pironon, R. Thiery, M. Aytougoudal, S. Teinturier, G. Beaudoin, and F. Walgenwitz, “FT-IR measurements of petroleum fluid inclusions : Methane, *n*-alkanes and carbon dioxide quantitative analysis”, *Geofluids*, **1**, 2–10 (2001).
- [67] J. Osswald and K.T. Fehr, “FTIR spectroscopic study on liquid silica solutions and nanoscale particle size determination”, *J. Mater. Sci.*, **41**, 1335–1339 (2006).

- [68] M. Goujon, T. Belmonte, and G. Henrion, "OES and FTIR diagnostics of HMDSO/O<sub>2</sub> gas mixtures for SiO<sub>x</sub> deposition assisted by RF plasma", *Surface Coatings Technol.*, **188-189**, 756–761 (2004).
- [69] Ch. Hollenstein, A.A. Howling, C. Courteille, J.-L. Drier, L. Sansonnens, D. Magni, and H. Müller, "Dust particle diagnostics in RF plasma deposition of silicon and silicon oxide films", in *MRS Symp. Proc.*, volume 507 of *Amorphous and Microcrystalline Silicon Technology*, 547–557, (1998).
- [70] U. Fantz, "Spectroscopic diagnostics and modelling of silane microwave plasmas", *Plasma Phys. Control. Fusion*, **40**, 1035–1056 (1998).
- [71] M. Takai, T. Nishimoto, M. Kondo, and A. Matsuda, "Effect of higher-silane formation on electron temperature in a silane glow-discharge plasma", *Appl. Phys. Lett.*, **77**, 2828–2830 (2000).
- [72] U. Fantz, "Basics of plasma spectroscopy", *Plasma Sources Sci. Technol.*, **15**, S137–S147 (2006).
- [73] A.A. Howling, B. Strahm, P. Colsters, L. Sansonnens, and Ch. Hollenstein, "Fast equilibration of silane/hydrogen plasmas in large area RF capacitive reactors monitored by optical emission spectroscopy", *accepted in Plasma Sources Sci. Technol.*, (2007).
- [74] E. Amanatides, A. Hammad, E. Katsia, and D. Mataras, "High pressure regime of plasma enhanced deposition of microcrystalline silicon", *J. Appl. Phys.*, **97**, 073303 (2005).
- [75] R.L. McCreery, "Chemical Analysis", in *Raman spectroscopy for chemical analysis*, volume 157, Wiley (2000).
- [76] B. Schrader, editor, *Infrared and Raman spectroscopy: Methods and applications*, VCH Publisher (New-York) (1995).
- [77] D.A. Long, *Raman spectroscopy*, McGraw-Hill Inc. (1977).
- [78] C. Droz, E. Vallat-Sauvain, J. Bailat, L. Feitknecht, J. Meier, and A. Shah, "Relationship between Raman crystallinity and open-circuit voltage in microcrystalline silicon solar cells", *Solar Energy Mater. Solar Cells*, **81**, 61–71 (2004).
- [79] S. Mukhopadhyay, C. Das, and S. Ray, "Structural analysis of undoped microcrystalline silicon thin films deposited by PECVD technique", *J. Phys. D: Appl. Phys.*, **37**(13), 1736–1741 (2004).
- [80] C. Droz, *Thin Film Microcrystalline Silicon Layers and Solar Cells: Microstructure and Electrical Performances*, PhD thesis, Université de Neuchâtel (2003).

- [81] U. Kroll, J. Meier, A. Shah, S. Mikhailov, and J. Weber, "Hydrogen in amorphous and microcrystalline silicon films prepared by hydrogen dilution", *J. Appl. Phys.*, **80**(9), 4971–4975 (1996).
- [82] H. Shanks, C.J. Fang, L. Ley, M. Cardona, F.J. Demond, and S. Kalbitzer, "Infrared spectrum and structure of hydrogenated amorphous silicon", *Phys. Stat. Sol. (b)*, **100**, 43–56 (1980).
- [83] F. Finger, U. Kroll, V. Viret, A. Shah, W. Beyer, X.-M. Tang, J. Weber, A.A. Howling, and Ch. Hollenstein, "Influences of high excitation frequency (70 MHz) in the glow discharge technique on the process plasma and the properties of hydrogenated amorphous silicon", *J. Appl. Phys.*, **71**(11), 5665–5674 (1992).
- [84] G. Socrates, *Infrared characteristic group frequencies: Tables and charts*, Wiley, 2<sup>nd</sup> edition (1997).
- [85] A.A. Howling. "Interference, transmittance and reflectance for thin films". January (2006).
- [86] B. Rech, T. Repmann, M.N. van den Donker, M. Berginski, T. Kilper, J. Hüpkes, S. Calnan, H. Stiebig, H. Stiebig, and S. Wieder, "Challenges in microcrystalline silicon based solar cell technology", *Thin Solid Films*, **511-512**, 548–555 (2006).
- [87] N. Pinto, M. Ficcadenti, L. Morresi, R. Murri, G. Ambrosone, and U. Coscia, "Electrical transport properties of microcrystalline silicon grown by PE-CVD", *J. Appl. Phys.*, **96**(12), 7306–7311 (2004).
- [88] M. Fukawa, S. Suzuki, L. Guo, M. Kondo, and A. Matsuda, "High rate growth of microcrystalline silicon using a high-pressure depletion method with VHF plasma", *Solar Energy Mater. Solar Cells*, **66**, 217–223 (2001).
- [89] L. Qing-Song, W. Zhi-Meng, G. Xin-Hua, Z. Ying, and X. Jian-Ping, "Influence of deposition parameters on the transition region of hydrogenated silicon film growth", *Chin. Phys.*, **14**(11), 2342–6 (2005).
- [90] J. Kočka, T. Mates, H. Stucklíková, J. Stuchlík, and A. Fejfar, "Characterization of grain growth, nature and role of grain boundaries in microcrystalline silicon - review of typical features", *Thin Solid Films*, **501**, 107–112 (2006).
- [91] M.N. van den Donker, B. Rech, F. Finger, W.M.M. Kessels, and M.C.M. van de Sanden, "Highly efficient microcrystalline silicon solar cells deposited from a pure SiH<sub>4</sub> flow", *Appl. Phys. Lett.*, **87**, 263503 (2005).
- [92] M.J. Kushner, "A model for discharge kinetics and plasma chemistry during plasma enhanced chemical vapor deposition of amorphous silicon", *J. Appl. Phys.*, **63**(8), 2532–2551 (1988).

- [93] E. Amanatides, S. Stamou, and D. Mataras, "Gas phase and surface kinetics in plasma enhanced chemical vapor deposition of microcrystalline silicon: The combined effect of rf power and hydrogen dilution", *J. Appl. Phys.*, **90**(11), 5786–5798 (2001).
- [94] E. Amanatides, D. Mataras, and D.E. Rapakoulias, "Surface simulation of PECVD of microcrystalline silicon thin films", in *15<sup>th</sup> Intl. Symp. Plasma Chemistry* (Orleans, 2001).
- [95] J. Perrin, C. Böhm, R. Etemadi, and A. Lioret, "Possible routes for cluster growth and particle formation in RF silane discharges", *Plasma Sources Sci. Technol.*, **3**, 252–261 (1994).
- [96] U. Kroll, J. Meier, P. Torres, J. Pohl, and A. Shah, "From amorphous to microcrystalline silicon films prepared by hydrogen dilution using the VHF GD technique", *J. Non-Cryst. Solids*, **227-230**, 68–72 (1998).
- [97] G.M. Ferreira, A.S. Ferlauto, C. Chen, R.J. Koval, J.M. Pearce, C. Ross, C.R. Wronski, and R.W. Collins, "Kinetics of silicon film growth and the deposition phase diagram", *J. Non-Cryst. Solids*, **338-340**, 13–18 (2004).
- [98] B. Rech, T. Roschek, J. Müller, S. Wieder, and H. Wagner, "Amorphous and microcrystalline silicon solar cells prepared at high deposition rates using RF (13.56 MHz) plasma excitation frequencies", *Solar Energy Mater. Solar Cells*, **66**, 267–273 (2001).
- [99] L. Guo, M. Kondo, M. Fukawa, K. Saitoh, and A. Matsuda, "High rate deposition of microcrystalline silicon using conventional plasma-enhanced chemical vapor deposition", *Jpn. J. Appl. Phys.*, **37**, L116–L118 (1998).
- [100] P. Torres, H. Keppner, J. Meier, U. Kroll, N. Beck, and A. Shah, "Fast deposition of  $\mu$ c-Si:H by restrictive dilution and enhanced HF-Power", *Physica status solidi (a)*, **163**(2), R9–R10 (1997).
- [101] J. Farjas, C. Rath, P. Roura, and P. Roca i Cabarrocas, "Crystallisation kinetics of hydrogenated amorphous silicon thick films grown by PE-CVD deposition", *Appl. Surf. Sci.*, **238**, 165–168 (2004).
- [102] E.A.T. Dirani, A.M. Andrade, L.K. Noda, F.J. Fonseca, and P.S. Santos, "Effect of the substrate on the structural properties of low temperature microcrystalline silicon films - a Raman spectroscopy and AFM investigation", *J. Non-Cryst. Solids*, **273**(1-3), 307–313 (2000).
- [103] C. Ross, J. Herion, R. Carius, and H. Wagner, "Nucleation and growth of low-temperature fine-crystalline silicon: A scanning probe microscopy and Raman spectroscopy study of the influence of hydrogen and different substrates", *Mater. Sci. Engineering*, **B72**(1), 1–6 (2000).

- [104] X. Zhang, Y. Zhao, F. Zhu, C. Wei, C. Wu, Y. Gao, J. Sun, G. Hou, X. Geng, and S. Xiong, "A combinatorial analysis of deposition parameters and substrates on performance of  $\mu\text{c-Si:H}$  thin films by VHF-PECVD", *Appl. Surf. Sci.*, **245**, 1–5 (2005).
- [105] B. Rech, T. Roschek, T. Repmann, J. Müller, R. Schmitz, and W. Appenzeller, "Microcrystalline silicon for large area thin film solar cells", *Thin Solid Films*, **427**, 157–165 (2003).
- [106] S. Klein, F. Finger, R. Carius, and M. Stutzmann, "Deposition of microcrystalline silicon prepared by HW-CVD: The influence of deposition parameters on the material properties and solar cell performance", *J. Appl. Phys.*, **98**, 024905 (2005).
- [107] C. Rosenblad, H.R. Deller, A. Domman, T. Meyer, P. Schroeter, and H. von Känel, "Silicon epitaxy by low-energy plasma enhanced chemical vapor deposition", *J. Vac. Sci. Technol. A*, **16**(5), 2785–2790 (1998).
- [108] D.B. Graves and D. Humbird, "Surface chemistry associated with plasma etching processes", *Appl. Surf. Sci.*, **192**, 72–87 (2002).
- [109] W. Schwarzenbach, A.A. Howling, M. Fivaz, S. Brunner, and Ch. Hollenstein, "Sheath impedance effects in very high frequency plasma experiments", *J. Vac. Sci. Technol. A*, **14**(1), 132–138 (1996).
- [110] P.J. Chantry, "A simple formula for diffusion calculations involving wall reflection and low density", *J. Appl. Phys.*, **62**(4), 1141–1148 (1987).
- [111] J. Perrin, O. Leroy, and M.C. Bordage, "Cross-sections, rate constants and transport coefficients in silane plasma chemistry", *Contrib. Plasma Phys.*, **36**(1), 3–49 (1996).
- [112] D. Mataras, "Exploration of deposition limits of microcrystalline silicon", *Pure Appl. Chem.*, **77**(2), 379–389 (2005).
- [113] *Properties of Amorphous Silicon*, volume 1, INSPEC, London (1989).
- [114] M. Chesaux. "Déposition de silicium microcristallin par plasma DC à haut courant d'arc". Master's thesis, Ecole Polytechnique Fédérale de Lausanne (EPFL), (2007).
- [115] M.A. Green, K. Emery, D.L. King, S. Igari, and W. Warta, "Solar efficiency tables (Version 17)", *Prog. Photovoltaics: Res. Appl.*, **9**, 49–56 (2001).
- [116] W.M.M. Kessels, R.J. Severens, A.H.M. Smets, B.A. Korevaar, G.J. Adriaenssens, D.C. Schram, and M.C.M. van de Sanden, "Hydrogenated amorphous silicon deposited at very high growth rates by an expanding  $\text{Ar-H}_2\text{-SiH}_4$  plasma", *J. Appl. Phys.*, **89**(4), 2404–2413 (2001).
- [117] T. Roschek, B. Rech, J. Müller, R. Schmitz, and H. Wagner, "Influence of the total gas flow on the deposition of microcrystalline silicon solar cells", *Thin Solid Films*, **451-452**, 466–469 (2004).

- [118] L. Feitknecht, J. Meier, P. Torres, J. Zürcher, and A. Shah, “Plasma deposition of thin film silicon: Kinetics monitored by OES”, *Solar Energy Mater. Solar Cells*, **74**, 539–545 (2002).
- [119] M. Sheib, B. Schröder, and H. Oechsner, “Deposition of nanocrystalline silicon films (nc-si:H) from a pure ECWR-SiH<sub>4</sub> plasma”, *J. Non-Cryst. Solids*, **198-200**, 895–898 (1996).
- [120] B. Rech, T. Repmann, S. Wieder, M. Ruske, and U. Stephan, “A new concept for mass production of large area thin-film silicon solar cells on glass”, *Thin Solid Films*, **502**, 300–305 (2006).
- [121] U. Graf, J. Meier, U. Kroll, J. Bailat, E. Vallat-Sauvain, and A. Shah, “High rate growth of microcrystalline silicon by VHF-GD at high pressure”, *Thin Solid Films*, **427**, 37–40 (2003).
- [122] Y. Mai, S. Klein, R. Carius, J. Wolff, A. Lambertz, F. Finger, and X. Geng, “Microcrystalline silicon solar cells deposited at high rates”, *J. Appl. Phys.*, **97**, 114913 (2005).
- [123] A. Gordijn, J.K. Rath, and R.E.I. Schropp, “High efficiency  $\mu$ c-Si Solar cells made by very high frequency PECVD”, *Prog. Photovoltaic: Res. Appl.*, **14**, 305–311 (2006).
- [124] B. Strahm, A.A. Howling, L. Sansonnens, and Ch. Hollenstein, “Plasma silane concentration as a determining factor for microcrystalline to amorphous silicon transition in SiH<sub>4</sub>/H<sub>2</sub> discharges”, *Plasma Sources Sci. Technol.*, **16**, 80–89 (2007).
- [125] A. Hammad, E. Amanatides, D. Mataras, and D. Rapakoulis, “PECVD of hydrogenated silicon thin films from SiH<sub>4</sub>+H<sub>2</sub>+Si<sub>2</sub>H<sub>6</sub> mixtures”, *Thin Solid Films*, **451-452**, 255–258 (2004).
- [126] J.-L. Dorier, Ch. Hollenstein, A.A. Howling, and U. Kroll, “Powder dynamics in very high frequency silane plasmas”, *J. Vac. Sci. Technol.*, **A 10**(4), 1048–1052 (1992).
- [127] E. Katsia, E. Amanatides, D. Mataras, A. Soto, and G.A. Voyiatzis, “Total SiH<sub>4</sub>/H<sub>2</sub> pressure effect on microcrystalline silicon thin films growth and structure”, *Solar Energy Mater. Solar Cells*, **87**, 157–167 (2005).
- [128] W.W. Stoffels, E. Stoffels, G.M.W. Kroesen, and F.J. de Hoog, “Electron density fluctuations in a dusty Ar/SiH<sub>4</sub> rf discharge”, *J. Appl. Phys.*, **78**(8), 4867–4872 (1995).
- [129] A. Maçarico, M. Vieira, A. Fantoni, P. Louro, A. Sêco, R. Martins, and Ch. Hollenstein, “On the a-Si:H film growth: The role of the powder formation”, *J. Non-Cryst. Solids*, **198-200**, 1207 (1996).



- [130] B. Strahm, A.A. Howling, L. Sansonnens, Ch. Hollenstein, U. Kroll, J. Meier, Ch. Ellert, L. Feitknecht, and C. Ballif, “Microcrystalline silicon deposited above 10 Å/s from pure silane RF-capacitive discharge”, *Solar Energy Mater. Solar Cells*, **91**, 795–502 (2007).
- [131] B. Stahm, A.A. Howling, L. Sansonnens, and Ch. Hollenstein, “Optimization of the microcrystalline silicon deposition efficiency”, *J. Vac. Sci. Technol. A*, **25**(4), 1198–1202 (2007).
- [132] R.C. Ross and J. Jaklik Jr, “Plasma polymerization and deposition of amorphous hydrogenated silicon from rf and dc plasmas”, *J. Appl. Phys.*, **55**(10), 3785–3794 (1983).
- [133] Y. Yin, M.M.M. Bilek, D.R. McKenzie, R.W. Boswell, and C. Charles, “Microarcing instability in RF PECVD plasma system”, *Surf. Coating Technol.*, **198**, 379–383 (2005).
- [134] E. Amanatides, D. Mataras, and D. E. Rapakoulias, “Deposition rate optimization in SiH<sub>4</sub>/H<sub>2</sub> PECVD of hydrogenated microcrystalline silicon”, *Thin Solid Films*, **383**(1-2), 15–18 (2001).
- [135] H. Schmidt, L. Sansonnens, A.A. Howling, and Ch. Hollenstein, “improving plasma uniformity using lens-shaped electrodes in a large area VHF reactor”, *J. Appl. Phys.*, **95**(9), 4559–4564 (2004).
- [136] Y. Nakano, S. Goya, T. Watanabe, N. Yamashita, and Y. Yonekura, “High-deposition-rate of microcrystalline silicon solar cell by using VHF PECVD”, *Thin Solid Films*, **506-507**, 33–37 (2006).
- [137] E. Amanatides, D. Mataras, and D.E. Rapakoulias, “Combined effect of electrode gap and radiofrequency on power deposition and film growth kinetics in SiH<sub>4</sub>/H<sub>2</sub> discharge”, *J. Vac. Sci. Techol. A*, **20**(1), 68–75 (2002).
- [138] M.N. van den Donker, E.A.G. Hamers, and G.M.W. Kroesen, “Measurements and semi-empirical model describing the onset of powder formation as a function of process parameters in an RF silane-hydrogen discharge”, *J. Phys. D: Appl. Phys.*, **38**, 2382–2389 (2005).
- [139] U.S. Graf, *Single-chamber process development of microcrystalline silicon solar cells and high-rate deposited intrinsic layers*, PhD thesis, Université de Neuchâtel (2005).
- [140] L. Feitknecht, F. Freitas, C. Bucher, J. Bailat, A. Shah, C. Ballif, J. Meier, J. Spitznagel, U. Kroll, B. Strahm, A.A. Howling, L. Sansonnens, and Ch. Hollenstein, “Fast growth of microcrystalline silicon solar cells on LP-CVD ZnO in industrial KAI PECVD reactors”, in *21st European Photovoltaic Solar Energy Conference and Exhibition, Dresden (Germany)*, (2006).

- [141] M.N. van den Donker, B. Rech, W.M.M. Kessels, and M.C.M. van de Sanden, "Deposition of highly efficient microcrystalline silicon solar cells under conditions of low  $H_2$  dilution: The role of the transient depletion induced incubation layer", *Prog. Photovoltaics: Res. Appl.*, **15**(4), 291–301 (2007).
- [142] B. Strahm, A.A. Howling, and Ch. Hollenstein, "Plasma diagnostics as a tool for process optimization: The case of microcrystalline silicon deposition", *submitted to Plasma Phys. Controlled Fusion*, (2007).
- [143] M.N. van den Donker, B. Rech, W.M.M. Kessels, and M.C.M. van de Sanden, "Transient depletion of source gases during materials processing: A case study on the plasma deposition of microcrystalline silicon", *to appear in J. Appl. Phys.*, (2007).
- [144] M.M. Giangregorio, M. Losurdo, A. Sacchetti, P. Capezzuto, F. Giorgis, and G. Bruno, "An optical study of the correlation between growth kinetics and microstructure of  $\mu c$ -Si grown by  $SiH_4$ - $H_2$  PECVD", *Appl. Surf. Sci.*, **253**, 287–291 (2006).
- [145] A. Gallagher, A.A. Howling, and Ch. Hollenstein, "Anion reactions in silane plasma", *J. Appl. Phys.*, **91**, 5570–5580 (2002).
- [146] A. Bouchoule, A. Plain, L. Boufendi, J. Ph. Blondeau, and C. Laure, "Particle generation and behavior in a silane-argon low-pressure discharge under continuous or pulsed radio-frequency excitation", *J. Appl. Phys.*, **70**(4), 1991–2000 (1991).
- [147] R.A. Gottscho and V.M. Donnelly, "Optical emission actinometry and spectral line shapes in rf glow discharges", *J. Appl. Phys.*, **56**(2), 245–250 (1984).
- [148] F. Grangeon, C. Monard, J.-L. Drier, A.A. Howling, Ch. Hollenstein, D. Romanini, and N. Sadeghi, "Applications of the cavity ring-down technique to a large-area rf-plasma reactor", *Plasma Sources Sci. Technol.*, **8**, 448–456 (1999).
- [149] J.C. Slattery, *Advanced transport phenomena*, Cambridge University Press (1999).
- [150] J. Gu, M. Zhu, L. Wand, Zhau B. Liu, F. and, K. Ding, and G. Li, "High quality microcrystalline Si films by hydrogen dilution profile", *Thin Solid Films*, **515**, 452–455 (2006).
- [151] P. Roca i Cabarrocas, N. Layadi, T. Heitz, B. Drévillon, and I. Solomon, "Substrate selectivity in the formation of microcrystalline silicon: Mechanisms and technological consequences", *Appl. Phys. Lett.*, **66**(26), 3609–3611 (1995).
- [152] H. Fujiwara, J. Koh, and R.W. Collins, "Depth-profiles in compositionally-graded amorphous silicon alloy thin films analyzed by real-time spectroscopic ellipsometry", *Thin Solid Films*, **313–314**, 474–478 (1998).
- [153] Q. Wang, E. Iwaniczko, J. Yang, K. Lord, and S. Guha, "High-Quality 10 Å/s amorphous silicon germanium alloy solar cells by hot-wire CVD", in *NCPV Program Review Meeting, Lakewood (USA)*, (2001).

- [154] U. Fantz, “Emission spectroscopy of molecular low pressure plasmas”, *Contrib. Plasma Phys.*, **44**(5-6), 508–515 (2004).
- [155] A. Drenik, A. Vesel, and M. Mozetic, “Measurements of probability for heterogeneous recombination of hydrogen atoms on surfaces of fusion relevant materials”, *33rd EPS Conference on Plasma Phys. Rome (Italy)*, **301**, 5.170–174 (2006).
- [156] A. Bouchoule and P. Ranson, “Study of volume and surface processes in low pressure radio frequency plasma reactors by pulsed excitation methods. I. Hydrogen-argon plasma”, *J. Vac. Sci. Technol. A*, **9**, 317–326 (1991).
- [157] A.D. Tserepi and T.A. Miller, “Two-photon absorption laser-induced fluorescence of H atoms: A probe for heterogeneous processes in hydrogen plasmas”, *J. Appl. Phys.*, **75**, 7231–7236 (1994).
- [158] L. Sansonnens, A.A. Howling, Ch. Hollenstein, J.-L. Dorier, and U. Kroll, “The role of metastable atoms in argon-diluted silane radiofrequency plasmas”, *J. Phys. D: Appl. Phys.*, **27**, 1406–1411 (1994).
- [159] L. Massolo, A. Müller, M. Tueros, M. Rehwagen, U. Franck, A. Ronco, and O. Herbarth, “Assessment of mutagenicity and toxicity of different size fractions of air particulates from La Plata, Argentina, and Leipzig, Germany”, *Environ. Toxicol.*, **17**, 219–231 (2002).
- [160] D. Hegemann, “Influence of pressure on an asymmetric RF discharge with methane”, *Thin Solid Films*, **515**, 2173–2178 (2006).
- [161] Y. Maemura, H. Fujiyama, T. Takagi, R. Hayashi, W. Futako, M. Kondo, and A. Matsuda, “Particle formation and a-Si:H film deposition in narrow-gap RF plasma CVD”, *Thin Solid Films*, **345**, 80–84 (1999).
- [162] L. Boufendi and A. Bouchoule, “Particle nucleation and growth in a low-pressure argon-silane discharge”, *Plasma Sources Sci. Technol.*, **3**, 262–267 (1994).
- [163] G. Bano, P. Horvath, K. Rozsa, and A. Gallagher, “The role of higher silane in silane-discharge particle growth”, *J. Appl. Phys.*, **98**, 013304 (2005).
- [164] A.A. Howling, C. Courteille, J.-L. Dorier, L. Sansonnens, and Ch. Hollenstein, “From molecules to particles in silane plasmas”, *Pure Appl. Chem.*, **68**(5), 1017–1022 (1996).
- [165] M. Sorokin, G.M.W. Kroesen, and W.W. Stoffels, “Temperature dependence and silane consumption during particle formation in Ar-Silane RF capacitively coupled plasma”, *IEEE Transaction Plasma Sci.*, **32**(2), 731–737 (2004).
- [166] A.A. Howling, L. Sansonnens, J. Ballutaud, Ch. Hollenstein, and J.P.M. Schmitt, “Non-uniform rf plasma potential due to edge asymmetry in large-area rf reactor”, *J. Appl. Phys.*, **96**, 5429–5443 (2004).

- [167] P. Chabert, J.L. Raimbault, J.M. Rax, and M.A. Lieberman, “Self-consistent non-linear transmission line model of standing-wave effects in a capacitive discharge”, *Phys. Plasmas*, **11**(5), 1775–1785 (2004).
- [168] L. Sansonnens and J.P.M. Schmitt, “Shaped electrode and lens for a uniform radio-frequency capacitive plasma”, *App. Phys. Lett.*, **82**(2), 182–184 (2003).
- [169] M.A. Lieberman, J.P. Booth, P. Chabert, J.M. Rax, and M.M. Turner, “Standing wave and skin effects in large-area, high-frequency capacitive discharge”, *Plasma Sources Sci. Technol.*, **11**(3), 283–293 (2002).
- [170] L. Sansonnens, J. Bondkowski, S. Mousel, J.P.M. Schmitt, and V. Cassagne, “Development of a numerical simulation tool to study uniformity of large area PECVD film processing”, *Thin Solid Films*, **427**(1-2), 21–26 (2003).
- [171] L. Sansonnens, A.A. Howling, and Ch. Hollenstein, “Electromagnetic field nonuniformities in large area, high-frequency capacitive plasma reactors, including electrode asymmetry effects”, *Plasma Sources Sci. Technol.*, **15**, 302–313 (2006).
- [172] A.A. Howling, L. Sansonnens, and Ch. Hollenstein, “Electromagnetic sources of nonuniformity in large area capacitive reactors”, *Thin Solid Films*, **515**, 5059–5064 (2007).
- [173] J. Ballutaud, Ch. Hollenstein, A.A. Howling, L. Sansonnens, H. Schmidt, and J.P.M. Schmitt, “Consequences of non-uniform RF plasma potential in large-area capacitive reactors”, in *16th Intl. Symp. Plasma Chemistry, Taormina (Italy)*, (2003).
- [174] L. Sansonnens, A. Pletzer, D. Magni, A.A. Howling, Ch. Hollenstein, and J.P.M. Schmitt, “A voltage uniformity study in large-area reactors for RF plasma deposition”, *Plasma Sources Sci. Technol.*, **6**(2), 170–178 (1997).
- [175] L. Sansonnens, H. Schmidt, A.A. Howling, Ch. Hollenstein, Ch. Ellert, and A. Buechel, “Application of the shaped electrode technique to a large area rectangular capacitively coupled plasma reactor to suppress standing wave nonuniformity”, *J. Vac. Sci. Technol.*, **A 24**, 1425–1430 (2006).
- [176] L. Sansonnens, B. Strahm, L. Derendinger, A.A. Howling, Ch. Hollenstein, Ch. Ellert, and J.P.M. Schmitt, “Measurements and consequences of nonuniform radio frequency plasma potential due to surface asymmetry in large area radio frequency capacitive reactors”, *J. Vac. Sci. Technol. A*, **23**(4), 922–926 (2005).
- [177] A.A. Howling, L. Derendinger, L. Sansonnens, H. Schmidt, Ch. Hollenstein, E. Sakanaka, and J.P.M. Schmitt, “Probe measurements of plasma potential nonuniformity due to edge asymmetry in large-area radio-frequency reactors: The Telegraph effect”, *J. Appl. Phys.*, **97**, 123308 (2005).
- [178] F. Finger, P. Hapke, M. Luysberg, R. Carius, H. Wagner, and M. Scheib, “Improvement of grain size and deposition rate of microcrystalline silicon by use of very high frequency glow discharge”, *Appl. Phys. Lett.*, **65**(20), 2588–2590 (1994).

- [179] H. Meiling, W.G.J.H.M. van Sark, J. Bezemer, and W.F. van der Weg, “Deposition-rate reduction through improper substrate-to-electrode attachment in very-high-frequency deposition of a-Si:H”, *J. Appl. Phys.*, **80**(6), 3546–3551 (1996).
- [180] A. Roth, *Vacuum technology*, Morth-Holland (1976).



# Acknowledgments/Remerciements

Before switching to French to conclude this manuscript, I wish to thank the Jury of my thesis, Profs. Michel Rappaz, Christophe Ballif and Paul Muralt and Dr Friedhelm Finger for their precious time they have offered to me.

Nous voici à la fin de cet épisode et c'est le moment de remercier toutes les personnes qui ont participé de près ou de loin à cette aventure - j'espère en n'oubliant personne - avant de continuer à participer à cette extraordinaire histoire sans fin qu'est la science.

En tête de liste se trouvent les membres du groupe des plasmas industriels du CRPP. Christoph, moteur inébranlable du groupe, je ne te remercie pas seulement pour m'avoir accueilli dans ton groupe et pour m'avoir fait découvrir ce monde passionnant bien qu'immatériel, mais également pour ta manière de gérer le groupe. Merci de nous faire une telle confiance et de nous laisser libre de tester et bricoler selon nos envies et intuitions, malgré les casses occasionnées de temps en temps... Merci également de nous servir de bouclier quasi-permanent aux attaques administratives, nous permettant ainsi de passer notre temps à faire ce que l'on aime : produire de la science.

Un merci tout particulier à Alan qui ne se montre jamais avare d'explications et d'idées, et qui a participé de manière très active à ce manuscrit en tant que correcteur de fond et de forme.

Je tiens également à remercier tout les membres actuels et passés du groupe pour les coups de mains variés (labo, théorie, modélisation), le partage de leurs connaissances et pour les bons moments passés. Un merci tout particulier au Dr Alban pour son soutien en tant que spécialiste en écriture de thèse

Cette thèse a avant tout été expérimentale avec quantité de casses et de modifications. Réparations et tuning de réacteur n'auraient pas pu être effectués avec rapidité et précision sans les compétences des membres des différents ateliers (construction, mécanique, électrotechnique, électronique, vide), ainsi que de Christian, spécialiste du tuning extrême ne reculant devant aucuns défis. Merci à vous tous qui tenez une place importante dans la réussite de ce travail.

Je remercie également toute l'équipe du secrétariat, bien qu'elle soit plutôt habituée aux stylos qu'aux clés à molette.

Pour finir du côté scientifique, je tiens à remercier les membres d'Oerlikon-Solar AG (Drs. Kroll, Ellert, Meier, ainsi que Arthur Buechel), de l'IMT (Institut de Microtechnique de l'Université de Neuchâtel), l'équipe du CIME (Centre Interdisciplinaire de Microscopie Electronique) et Evelyn pour les discussions intéressantes et le travail de caractérisation des dépôts.

Sortons des plasmas pour d'autres états de la matière plus classiques. Merci à vous tous qui autour d'un verre ou d'une assiette m'avez apporté votre soutien aux travers de votre intérêt pour ce travail qui, dans la plupart des cas, vous semblait incompréhensible.

Merci enfin à ma famille et en particulier à maman qui m'a aidé en permanence pour pouvoir faire ce qui me plaisait et pour son soutien sur le chemin de ces longues années d'études.

Et le meilleur pour la fin...merci à toi Sofia pour m'avoir supporté (dans tous les sens du terme) durant ce travail...je t'aime.

Benjamin



# Curriculum Vitae

**Benjamin STRAHM**

Né le 12 septembre 1978 à Lausanne (VD),  
de nationalité suisse et originaire de Leysin (VD).

## FORMATION

---

- |             |   |
|-------------|---|
| 2004 - 2007 | <b>Thèse de doctorat</b><br>effectuée dans le groupe des plasmas industriels,<br>Centre de Recherches en Physique des Plasmas (CRPP),<br>Ecole Polytechnique Fédérale de Lausanne (EPFL).<br>Assistant pour divers cours de Physique générale et analyse<br>mathématique.   |
| 1998 - 2004 | <b>Diplôme d'ingénieur en science et génie des matériaux</b> ,<br>Ecole Polytechnique Fédérale de Lausanne (EPFL).<br>Travail de diplôme effectué au laboratoire d'analyse de surface<br>de l'institut des matériaux, "Surface modification and charac-<br>terization of modified intubation devices: RF-plasma prepara-<br>tion and surface characterization of PVC" |

## PUBLICATIONS

---

B. Strahm, A.A. Howling and Ch. Hollenstein, "Plasma diagnostics as a tool for process optimization: The case of microcrystalline silicon deposition", to appear in *Plasma Phys. Controlled Fusion* (2007).

A.A. Howling, B. Strahm, P. Colsters, L. Sansonnens and Ch. Hollenstein, "Fast equilibration of silane/hydrogen plasmas in large area RF capacitive reactors monitored by optical emission spectroscopy", *Plasma Sources Sci. Technol.* **16** 679-696 (2007).

B. Strahm, A.A. Howling, L. Sansonnens and Ch. Hollenstein, "Optimization of the microcrystalline silicon deposition efficiency", *J. Vac. Sci. Technol. A*, **25**(4), 1198-1202 (2007).

B. Strahm, A.A. Howling, L. Sansonnens, Ch. Hollenstein, U. Kroll, J. Meier, Ch. Ellert, L. Feitcknecht and C. Ballif, "Microcrystalline silicon deposited above 10 Å/s from pure silane RF-capacitive discharge", *Solar Energy Mater. Solar Cells*, **91**, 795-502 (2007).

B. Strahm, A.A. Howling, L. Sansonnens and Ch. Hollenstein, "Plasma silane concentration as a determining factor for microcrystalline to amorphous silicon transition in  $\text{SiH}_4/\text{H}_2$  discharges", *Plasma Sources Sci. Technol.*, **16**, 80-89 (2007).

L. Feitknecht, F. Freitas, C. Bucher, J. Bailat, A. Shah, C. Ballif, J. Meier, J. Spitznagel, U. Kroll, B. Strahm, A.A. Howling, L. Sansonnens, Ch. Hollenstein, "Fast growth of microcrystalline silicon solar cells on LP-CVD ZnO in industrial KAI PECVD reactors", in Proc. *21st European Photovoltaic Solar Energy Conference and Exhibition*, Dresden (Germany) (2006).

L. Sansonnens, B. Strahm, L. Derendinger, A.A. Howling, Ch. Hollenstein, Ch. Ellert and J.P.M. Schmitt, "Measurements and consequences of nonuniform radio frequency plasma potential due to surface asymmetry in large area radio frequency capacitive reactors", *J. Vac. Sci. Technol. A*, **23**, 922-926 (2005).

## CONFERENCES

---

Invited talk at *European Physical Society conference on plasma physics*, "Plasma diagnostics as a tool for process optimization: The case of microcrystalline silicon deposition", Warsaw (Poland), July 2007.

Talk at *American Vacuum Society conference*, "Optimization of the microcrystalline silicon deposition efficiency", San Francisco (USA), November 2006.